A novel approach towards electrode openings for flexible neural implants

Dissertation
der Mathematisch-Naturwissenschaftlichen Fakultät
der EBERHARD KARLS UNIVERSITÄT Tübingen
zur Erlangung des Grades eines
Doktors der Naturwissenschaften
(Dr. rer. nat.)

vorgelegt von
Markus Westerhausen
aus Stuttgart

Tübingen
2017

Gedruckt mit Genehmigung der Mathematisch-Naturwissenschaftlichen
Fakultät der Eberhard Karls Universität Tübingen.

Tag der mündlichen Qualifikation: 13.07.2018

Dekan:	Prof. Dr. Wolfgang Rosenstiel
1. Berichterstatter:	Prof. Dr. Boris Hofmann
2. Berichterstatter:	Prof. Dr. Dieter Kern

Ich erkläre hiermit, dass ich die zur Promotion eingereichte Arbeit mit dem Titel: „A novel approach towards electrode openings for flexible neural implants“ selbständig verfasst, nur die angegebenen Quellen und Hilfsmittel benutzt und wörtlich oder inhaltlich übernommene Zitate als solche gekennzeichnet habe. Ich erkläre, dass die Richtlinien zur Sicherung guter wissenschaftlicher Praxis der Universität Tübingen (Beschluss des Senats vom 25.05.2000) beachtet wurden. Ich versichere an Eides statt, dass diese Angaben wahr sind und dass ich nichts verschwiegen habe. Mir ist bekannt, dass die falsche Abgabe einer Versicherung an Eides statt mit Freiheitsstrafe von bis zu drei Jahren oder mit Geldstrafe bestraft wird.

Tübingen, den 02.07.2018 Markus Westerhausen

FÜR SIBEL

I. TABLE OF CONTENTS

I. Table of Contents VII

II. List of Abbreviations XI

III. List of Symbols XIII

IV. Abstract XV

V. Kurzbeschreibung XVII

1. Introduction 1

2. Background Theory 5

  2.1. Medical Implants 5

    2.1.1. Medical Background and Overview 5

    2.1.2. Flexible Implants and their Hermeticity 7

    2.1.3. Biocompatibility and Biostability 8

    2.1.4. Defect Mechanisms 13

  2.2. Physical Manufacturing Processes 15

    2.2.1. Optical Lithography 16

    2.2.2. Physical Vapor deposition Techniques 16

    2.2.3. Reactive Ion Etching 17

    2.2.4. Ion Beam Etching 18

    2.2.5. Atomic Layer Deposition 19

  2.3. Measurement Techniques 20

    2.3.1. Ion and Electron Currents 20

    2.3.2. DC Measurements 25

    2.3.3. AC Measurements 26

    2.3.4. Electrical Strain Gauges 29

3. Materials and Fabrication Processes 31

  3.1. Materials 31

3.1.1. Polyimide 2611 31

3.1.2. Metals 35

3.1.3. Chemicals 37

3.1.4. Titanium Oxide 38

3.2. Fabrication Processes 38

3.2.1. Wafer Dicing 39

3.2.2. Optical Lithography and Chromium Masks 39

3.2.3. Vapor Deposition Techniques 43

3.2.4. Sputtering 45

3.2.5. Spin Coating Polyimide and Temperature Curing 46

3.2.6. Plasma Etching by RIE 48

3.2.7. Atomic Layer Deposition 50

3.2.8. Ion Beam Etching 51

4. Results and Discussion 55

4.1. Fabrication of Devices 55

4.1.1. Non-Flexible Multilayer Samples 56

4.1.2. Flexible Polyimide Samples and Electrode Layout 65

4.1.3. Flexible Multi-Layer Samples 72

4.2. Measurement Setups 76

4.2.1. Setup Requirements 77

4.2.2. Manufacturing and Software Programing 80

4.2.3. Validation and Verification 89

4.3. Assessment of Manufactured Samples 97

4.3.1. Delamination of Multilayer Samples 97

4.3.2. Etching of Polyimide 100

4.3.3. Electrical Stability of Polyimide 102

4.3.4. Chemical Stability of Polyimide 108

4.3.5. Bending of Thin Polyimide Foils 110

4.3.6. DC measurements while Bending flexible Samples 114

4.3.7. Influence of Polyimide Tempering on the Circuitry 118

4.4. Assessment of TiO_2 as Electrode Side Wall Passivation Material 119

4.4.1. Optical and Electrical Validation 120

4.4.2. Evaluation of Surface stability of TiO_2 Layers 124

4.5. Electrode Side Wall Passivation 126

4.5.1. Verification and Validation of electrode side wall passivation on non-flexible samples 126

4.5.2. ALD coating of electrodes on Flexible Samples 132

4.5.3. Validation of Side Wall passivation on flexible Samples 134

5. Conclusion 141

6. Outlook 145

7. References 147

I. List of Figures 163

II. List of Tables 169

III. Appendix 171

II. LIST OF ABBREVIATIONS

A

a.U.: arbitrary Unit 44
AC: Alternating Current 26
ALD: Atomic Layer Deposition 19, 50
ASIC: Application-specific integrated circuit 8
Au: Gold 35

C

CNS: Central Nervous System 5
COM-Port: Communication Port 81
CVD: Chemical Vapor Deposition XV

D

DC: Direct Current 25

E

EBPVD: Electron Beam Physical Vapor Deposition 43
EDX: Energy-Dispersive X-Ray spectroscopy 108
EIS: Electrochemical Impedance Spectroscopy 26
EKG: Electrocardiography 1

F

FDA: Food and Drug Administration 9
FIB: Focused Ion Beam 97
Flex-MEA: Flexible Multi Electrode Array 55
FMS: Fluidic Measurement Setup 77

G

GPC: Growth Per Cycle 50
GPIB: General Purpose Interface Bus 80

I

IBE: Ion Beam Etching XV, 51
IHP: Inner Helmholtz Plane 23

L

Lisa$^+$: Center for Light-Matter Interaction, Sensors & Analytics 36

M

MEA: Multi Electrode Array 55
MFCS: Mass-Flow-Controller-System 85

O

OHP: Outer Helmholtz Plane 23

P

PCB: Printed Circuit Board 84
PDMS: Polydimethylsiloxan 82
PEALD: Plasma enhanced ALD 20
PI: Polyimide (2611) 31
PMMA: Polymethylmethacrylat 83
PNS: Peripheral Nervous System 5
PP: Polypropylene 111
PVD: Physical Vapor Deposition XV

R

RF: Radio Frequency 48
RIE: Reactive Ion Etching XV

S

sccm: standard cubic centimeter 47
SDK: Software Development Kit 80
SMU: Source Measurement Unit 80

T

Ti: Titanium 36

U

UHV: ultra-high vacuum 35

III. LIST OF SYMBOLS

Symbol	**Unit**	**Description**
A^*	$\frac{A}{m^2 kg}$	Richardson Constant $\left(A^* = 1.20173 \cdot 10^6 \frac{A}{m^2 kg}\right)$
C	F	Capacity
E	V	Voltage
f	Hz	Frequency
G	$\frac{g}{cm^2 s}$	Rate of evaporation
I	A	Current
k_b	$\frac{J}{K}$	Boltzmann constant ($k_b = 1.3806488 \cdot 10^{-23}$ J/K)
λ_D/κ^{-1}	m	Debye length
l	m	Length
M		Molecular weight
m_e	kg	Electron mass ($m_e = 9.10938356 \cdot 10^{-31}$kg)
N_A	mol^{-1}	Avogadro Constant ($N_A = 6.022140857 \cdot 10^{23} mol^{-1}$)
P/p	Pa/Torr	Pressure
R	Ω	Frequency independent Impedance (Resistivity)
ρ_e	$\frac{C}{m^3}$	Charge density
ρ_S	Ω cm	Solution resistivity
T	K or °C	Temperature
t	s	Time
ε_0	$\frac{F}{m}$	Vacuum permittivity $\left(\varepsilon_0 = 8.854\,187\,817 \cdot 10^{-12} \frac{F}{m}\right)$
ε_l	%	Linear expansion
ε_r	none	Relative permittivity
ω	Hz	Circular frequency
Z	Ω	Impedance

IV. ABSTRACT

With the ongoing technological advances in the field of medical applications, there is an evolving market for micro medical implants, capable of simultaneously detecting neural activities and, if required, stimulating the human tissue. Retina Implants, which stimulate the degenerated retina and brain implants for treatment of Parkinson's disease are only two of many examples, where neurological defects can be treated by modern, electrically active implants.

In contrast to conventional implants like the cochlea implants or cardiac pacemakers, which are all encapsulated by a stiff ceramic or metal housing, modern implants must be flexible, while remaining biocompatible and biostable. Cardiac Pacemakers e.g. usually contain their electronics in a ceramic or metal housing, while only the stimulating electrodes are fed through the encapsulation. This setup is not feasible for modern, flexible implants, where not only the opened stimulation and recording electrodes but also the electronics themselves remain on a flexible, but hermetically shielded substrate.

The suitable, flexible materials for encapsulation are polyimide and parylene. Both, however, are water vapor permeable, which leads to several defect mechanisms like corrosion and layer delamination. A common solution to this problem is the incorporation of metal layers into the encapsulation which act as water vapor barriers. These metal layers are exposed to the tissue at the electrode openings, leading to possible electrical short circuits and corrosion. In addition, the electrode side walls offer a great attack surface for negative effects such as layer delamination and -degradation. Thus, an electrode side wall passivation was developed and is introduced in this thesis.

Flexible as well as not-flexible samples on a polyimide base were created in a clean room environment, utilizing physical vapor deposition (PVD) techniques, while the circuitry was self-designed and realized by lithography procedures. A multilayer, consisting of titanium and gold, was chosen as feed line as well as electrode material. As a result, the adhesion to the surrounding polyimide was enhanced. The electrode openings were realized by reactive ion etching (RIE) and finally cleaned by ion beam etching (IBE).

To characterize the produced samples, two measurements setups were created, established, validated and finally combined to one complete fully autonomous setup. The first one is capable of detecting (leakage-) currents down to $1 \cdot 10^{-12}\,\mathrm{A}$ over several electric measurement channels, as two multiplexers were utilized. The second setup simulates mechanical stress onto the flexible samples, as would occur in the human body by bending the samples in a fluid medium. Additionally, harsh material stress tests are possible. Both setups were combined, allowing completely autonomous electrical measurements of flexible samples, while being mechanically tested. At the time of this thesis, this was the first setup to simulate induced motions onto flexible (neural) samples in a fluid electrolyte medium.

Thin titanium dioxide layers created by Atomic Layer Deposition have been thoroughly tested in respect to their electrical capabilities as well as the layer homogeneity. After positive evaluation of titanium dioxide as an electrode side wall passivation, the enhanced electrode side wall passivation was analyzed.

The enhancement of the biostability of flexible electrically active samples by such a treatment is successfully shown in this thesis with several possible applications of the newly created multilayered passivation given.

V. KURZBESCHREIBUNG

Der anhaltente technologische Fortschritt, lässt sich auch im medizinischen Bereich feststellen und führt zu einem wachsenden Markt für mikro-medizinische Implantate, die simultan neurologische Signale detektieren, wie auch das umliegende Gewebe stimulieren können. Als Beispiel für elektrisch aktive Implantate in der medizinischen Anwendung sind Retina-Implantate und Gehirnimplantate zu nennen. Während Erstere die degenerierte Retina des menschlichen Auges ersetzen und so Augenlicht wiederherstellen, stimulieren Letztere das menschliche Gehirn von Parkinson-Patienten und unterdrücken erfolgreich den resultierenden Tremor.

Im Gegensatz zu herkömmlichen medizinisch elektrisch aktiven Implantate wie dem Cochlea-Implantat oder Herzschrittmachern, sind moderne neurologische Implantate nicht von einem starren Keramik- oder Metallgehäuse umgeben, aus dem lediglich die Elektroden herausgeführt werden. Stattdessen verweilt die Elektronik bei modernen Implantaten neben den Elektrodenöffnungen auf einem flexiblen Substrat und ist dennoch hermetisch gegenüber dem Gewebe abgeschirmt, während die Elektroden geöffnet bleiben und so ein elektrischer Kontakt zum Gewebe hergestellt wird.

Als flexible, biokompatible und biostabile Materialien haben sich Parylen und Polyimid durchgesetzt. Beide sind allerdings wasserdampfdurchlässig, was negative Effekte wie Korrosion und Lagenablösung zur Folge hat. Durch Einbringen von Metalllagen in die Passivierung soll eine Wasserdampfundurchlässigkeit garantiert werden. Diese Metalllagen sind an den Elektrodenöffnungen exponiert und können dort zu Kurzschlüssen führen. Gleichzeitig ist die Elektrodenseitenwand selbst ungeschützt gegenüber negativen Effekten wie Korrosion und Lagendelamination. Daher wurde eine Möglichkeit der Elektrodenseitenwandpassivierung entwickelt und ist in dieser Arbeit vorgestellt.

Dazu wurden sowohl nicht-flexible wie auch flexible polyimid-basierte Testsubstrate mikrotechnologisch unter Verwendung von Reinraumtechnologie und Verfahren der physikalischen Gasphasenabscheidung entwickelt und hergestellt. Ein Multilayer, bestehend aus Titan und Gold wurde als Leiterbahnmaterial gewählt, um die Haftung der Leiterbahnen an das umgebende passivierende Polyimid herzustellen. Die Elektrodenöffnungen wurden per reaktivem Ionenstrahlätzen, sowie Ionendünnung realisiert.

Neben der Herstellung neuartiger Substrate wurden auch zwei Messaufbauten entwickelt, angefertigt, validiert und zu einem komplett automatisierten Messstand kombiniert. Die erste Messanordnung kann (Leck-) Ströme in der Größenordnung von $1 \cdot 10^{-12}$ A über mehrere Kanäle hinweg detektieren. Der zweite Messaufbau simuliert kleinste flüssigkeits-induzierte mechanische Bewegungen auf flexible Substrate, wie sie auch im menschlichen Körper auftreten. Aber auch Materialtests bis an die Grenzen der flexiblen Substrate sind möglich. Durch die Kombination beider Aufbauten ist eine komplett autonome elektrische Analyse flexibler Substrate möglich, während sie parallel mechanisch definiert belastet werden. Zum Zeitpunkt dieser Arbeit existiert keine vergleichbare Messanordnung.

Atomlagenabscheidung wurde genutzt, um dünne Titandioxid Schichten herzustellen, die ausgiebig auf ihre elektrischen Eigenschaften wie auch Schichtbegebenheit getestet wurden. Die Biokompatibilität von diesen Schichten ist bekannt und viele Arbeitsgruppen haben eine Steigerung der Biostabilität von Substraten durch die Nutzung dieser bestätigt. Nach Prüfung aller Voraussetzungen wurden Elektrodenseitenwände hergestellter Substrate mit Titandioxid passiviert und analysiert.

Die Steigerung der Biostabilität von elektrisch aktiven, flexiblen, Implantat-ähnlichen Substraten durch die Passivierung der Elektrodenseitenwand wird in dieser Arbeit zusammen mit einigen Anwendungen der neuartigen Passivierung vorgestellt.

1. INTRODUCTION

With the great advances in medical technologies over the last years, more and more diseases can be treated with implants. The most commonly known medical implant to remain in the human body is the cardiac pacemaker. It stimulates the heart muscles periodically and newer versions also gather neuronal feedback by Electrocardiography (EKG). However, these traditional implants contain all their electronics in a stiff encapsulated housing, while only the stimulation and detection electrodes are fed through the encapsulation [1], [2]. Modern implants, like retina implants which aim to restore eye vision or brain implants which are being used in the treatment of Parkinson's disease cannot be realized with an inflexible and big housing, ensuring the hermetical shielding from the tissue with single electrodes fed through. Instead, they are all based on the same principle of containing all electrodes on a flexible substrate. By doing so, not only the electrode density can be increased, but also the traumatization for the human body is minimized, if the implant's electrodes can follow the body's movement.

While researching these modern implantation devices, it must be kept in mind that these devices persist in the human body, preferably for several decades or even a lifetime. As a result, the implants must be shielded from the body's electrolyte fluids, while remaining stable in this harsh physiologic environment without degenerating or delaminating. In addition, it is a necessity for the complete implant to have a non-toxic effect on the tissue or organ. If this is not possible, due to the need of toxic materials, the implant must be encapsulated with a non-toxic material, serving as a barrier layer between the implant and the body and vice versa. [3]–[5]

Modern flexible materials, such as parylene and polyimide, have shown promising results as such possible encapsulation materials for these modern flexible implants, as Richardson et al. as well as Akin et al. conclude [6], [7]. Both materials have shown to be biostable as well as biocompatible. They are, however, water vapor permeable, which leads to several negative effects like corrosion of the electrical circuitry or even delamination of the complete passivation. As metal and many ceramics are water vapor impermeable, it has become a standard, to include thin films into the passivation of such an implant [8]. Figure 1 shows such a multilayered passivation with included metal layers. Such passivation systems combine the biocompatibility of parylene and polyimide, while maintaining water vapor impermeability.

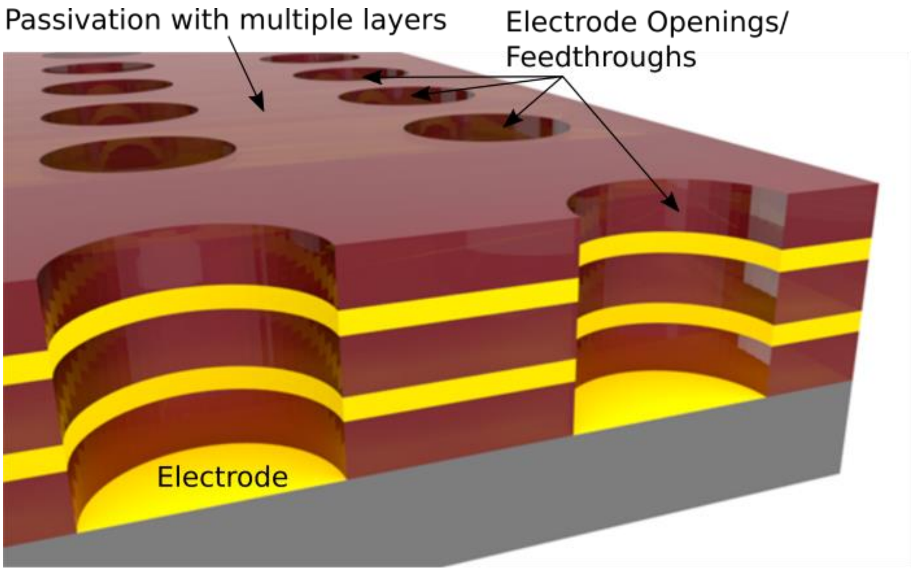

Figure 1: Sketch of Multilayer System with Electrode Openings

However, incorporation of metal layers into the passivation has a serious drawback, which can also be seen in figure 1. All electrodes are electrically connected to each other via the embedded metal layers leading to internal short circuits. In addition, the electrode openings represent an artificial discontinuity of the otherwise intact encapsulation (Figure 2) and are the main starting point of layer delamination and -degradation. [9]

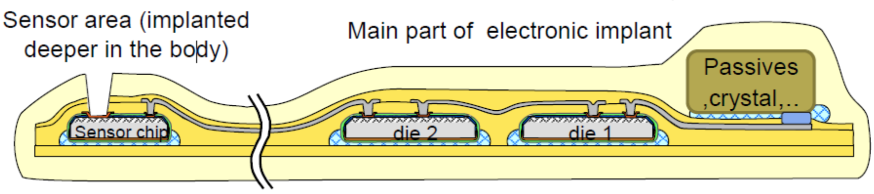

Figure 2: Schematic of electric active implant. Clearly visible is the artificially created opening in the passivation layer to create an electric access from the electrode to the tissue [10]

Thus, this work focuses on an annular side wall passivation of the electrode openings with the aim to protect the electrodes against the environmental conditions in the human body as well as to shield the electrode side walls against embedded metal layers.

Beginning with the creation of polyimide-based multichannel-arrays with clean room technology and PVD methods, first delamination measurements evaluate the current state so far. Incorporation of metal layers into the passivation created a multilayered passivation system with annular side wall electrodes, which allowed the electrical characterization of the electrode side wall. On this basis, an electrode side wall passivation was developed and characterized (see figure 3 for schematic). Utilizing atomic layer deposition techniques, it was possible to create a 100 nm thin electrode side wall passivation of TiO_2, which shows very promising results in its electrical as well as mechanical properties.

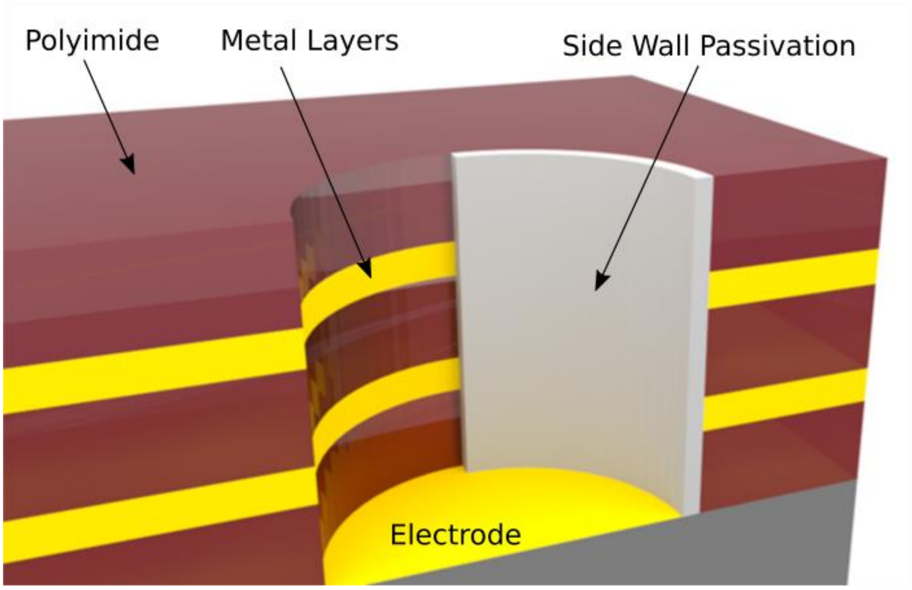

Figure 3: Electrode Side Wall Passivation

As the tissue is in permanent motion due to the blood pressure, mechanical stress tests were necessary to further evaluate the stability of the electrode side wall passivation. Thus, a fluid-based measurement setup, capable of bending the samples while gaining electrical (leakage-) data completely autonomously, was developed and manufactured. This setup allows the detection of currents down to $1 \cdot 10^{-12}$ A along 10x10 channels.

2. BACKGROUND THEORY

This chapter summarizes the necessary theoretical background for a better understanding of this work. Firstly, medical implants, together with the biological background and challenges to face when creating them are described. Chapter 2.2 provides a brief overview of physical processes, which were frequently used during this work. Fundamentals about utilized measurement techniques are given in Chapter 2.3.

2.1. MEDICAL IMPLANTS

Medical background is given in chapter 2.1.1, alongside with a quick introduction to implants. Most devices implanted today are still not flexible, as flexibility brings some difficulties concerning the hermeticity of the device, which is discussed in chapter 2.1.2. The overall biocompatibility and biostability concerns and requirements are summarized in chapter 2.1.3, with several possible defect mechanisms introduced in the final subchapter 2.1.4

2.1.1. MEDICAL BACKGROUND AND OVERVIEW

The human nervous system is made up of single neurons, which can be divided into two groups in respect of their position inside of the body. The central nervous system (CNS), consisting of the brain and the spinal cord, consists of neurons with a very high density and an extremely large number of interconnections, the so-called synapses. The peripheral nervous system (PNS), connects all muscles and sensors to the CNS. Here, the neurons form long nerve fibers, the fascicles, with few interconnections. Neurons transfer electric signals by propagating their action potential, which is the electric potential difference across the cell membrane. In equilibrium, it amounts to approx. -70 mV in the human body. In case of an action potential, this potential difference drops several mV[1] within of few milliseconds with a maximum frequency of subsequent action potential of roughly 1 kHz. The complete electrical signal is pulse-density coded and the pulse density and signal value are not linearly correlated. These signals propagate with 0.5 m/s up to 120 m/s in the PNS along the axon of the neuron. [11]

---

[1] An action potential itself can be measured to be 30 mV [56]

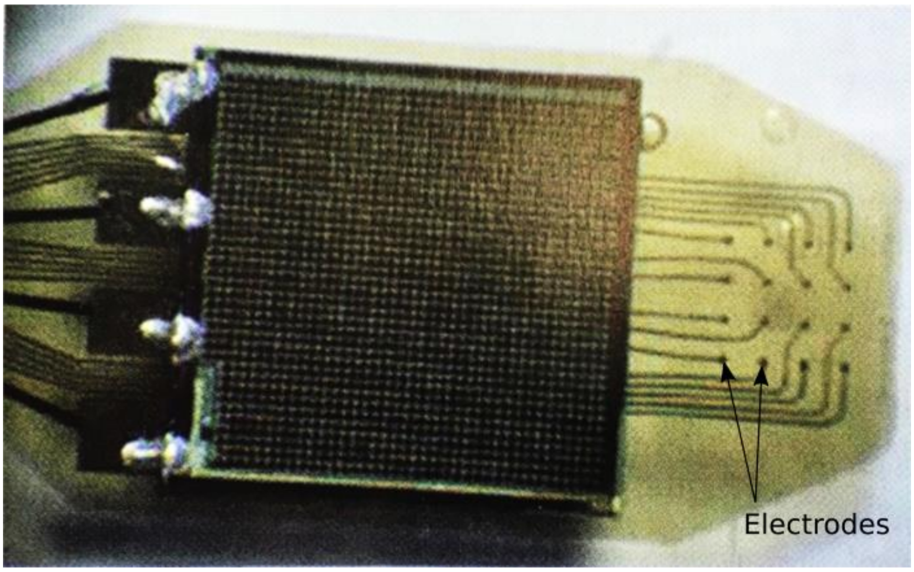

Figure 4: hybrid sub retinal device with both micro photodiodes and microelectrodes, embedded in a polyimide encapsulation. Developed by Retina Implant AG, Reutlingen, Germany and Zrenner, et al. [12]

An industrial retina implant, displayed in figure 4, is shown as an example. It shows electrodes, embedded in polyimide with an additional active micro photodiode array. A good overview over implant types and their respective function is given in the work of DiLorenzo [13] and Horch [14].

Every implant has direct contact with the body’s tissue and must therefore be heavily regulated, concerning biocompatibility and biostability. These are both topics of the norm DIN ISO 10993, the norm DIN ISO 13485 (quality management and corresponding general aspects for medical devices) as well as DIN ISO 27186 (active implantable medical devices).

2.1.2. FLEXIBLE IMPLANTS AND THEIR HERMETICITY

As all implanted devices remain in a wet environment and are exposed to moisture, the capability of the implants' housing to hinder water vapor from entering is crucial for the functionality of the implant, as the presence of water leads to failure of electric components. This ability of prohibiting molecules from entering an enclosed structure is called hermeticity, which is only 100 % reachable in theory, as all known materials allow a certain transmission. [15]

In general, an implant's housing is called hermetic when a sufficiently low humidity is ensured inside over several years, which is most commonly achieved by housings out of glass, ceramic or metal. Figure 5 shows the time it needs for housings of different materials and varying wall thickness to let enough water pass through, so that a hermeticity level of 50 % is reached. Only the previously noted materials ensure a long enough time spans with sufficiently low wall thicknesses. [15]

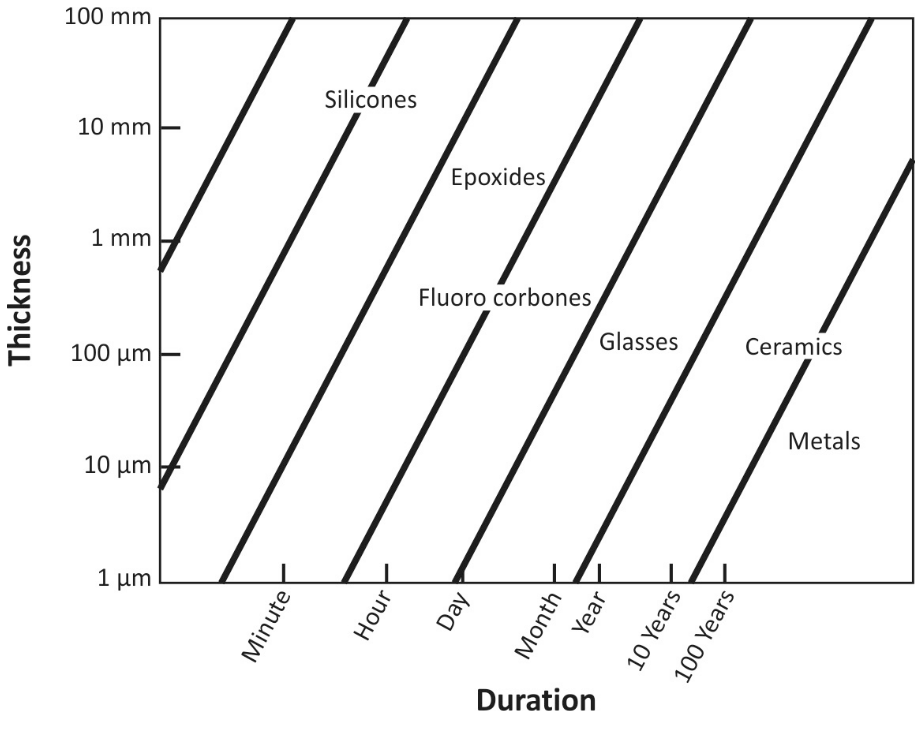

Figure 5: Water permeability of different materials; the lines depict the timespan in which a humidity of 50 % inside a closed housing of the given material with the respected wall thickness is reached [15], [16]

Although diffusion coefficients differ for several polyimides, all of them allow diffusion of water vapor over time spans of some years, which is why no polyimide-based encapsulations can reach this level of hermeticity. Complete hermeticity, needed for medical applications, is only reachable with crack-free housings of glass, metal and ceramics. [17]

However, only polymers allow the creation of flexible implants, which adapt better to the biological tissue. As only the semiconducting components of an implant are sensitive to humidity, which results in failure of these components, they are encapsulated in a stiff, rigid, hermetic housing, while the passive electrical components such as current leading paths, capacitors, resistors and the electrodes themselves may be encapsulated in a flexible, non-hermetic housing. As such, the flexible implant is locally separated from the non-flexible part, inheriting the ASICs and connected by so-called feedthroughs.

2.1.3. BIOCOMPATIBILITY AND BIOSTABILITY

A good definition of biocompatibility is given by Park and Lakes as the “acceptance of an artificial implant by surrounding tissues and by the body as a whole. The implant should be compatible with tissues in terms of mechanical, chemical, surface, and pharmacological properties.” [18]

In general, the biocompatibility of medical products is regulated in the norm ISO 10993, which defines various testing methods for implantable materials and medical devices regarding their application. Figure 6 shows a schematic, given in the annex B of the norm, which helps manufactures of medical devices with the decision, regarding the necessity of biocompatibility tests.

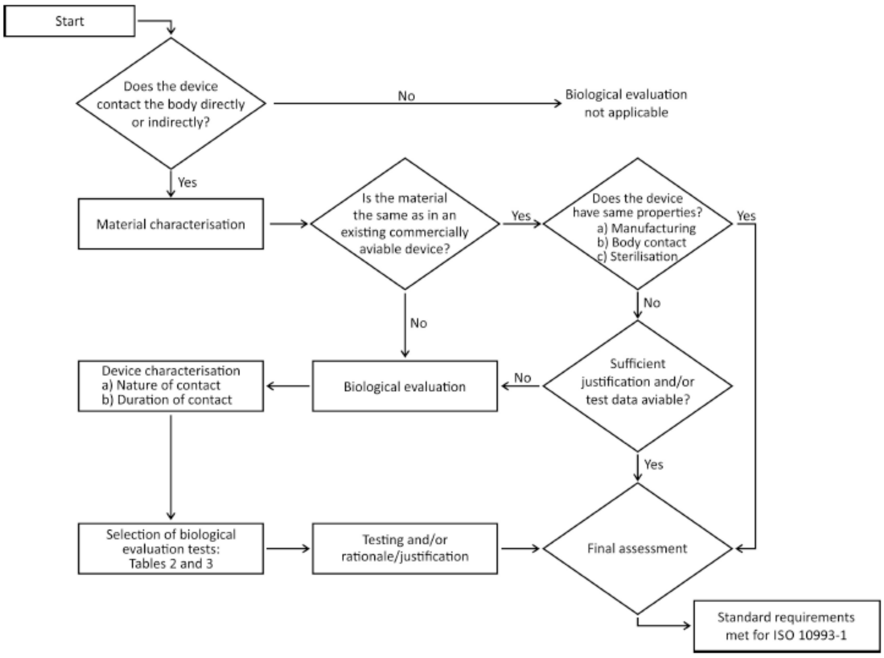

Figure 6: Schematic to evaluate the need for material tests [19]

Dependent on the type of medical device, different kinds of tests are necessary and listed in table 1 and table 2 with the tests for long term (neural) implants highlighted. Similar tests are required by the FDA (Food and Drug Administration) for approval of medical devices in the USA. An introduction to in-vivo and in-vitro analysis as well as biostability concerns is subsequently given on page 12.

Table 1: Overview of material tests regarding the biocompatibility according to DIN EN ISO 109931-1

Medical device categorized by			Biological effect							
Nature of body Contact		Contact duration A: limited (<24 h) B Prolonged (24 h to 30 d) C: permanent (> 30 d)	Cytotoxy	Sensitisation	Irritation of intracutaneous reactivity	Subacute and subchronic toxicity	Systematic toxicity (acute)	Genotoxicity	Implantation	Haemocompatibility
Category	Contact									
Surface device	Skin	A	X	X	X					
		B	X	X	X					
		C	X	X	X					
	Mucosal membrane	A	X	X	X					
		B	X	X	X					
		C	X	X	X		X	X		
	Breached of compromised surface	A	X	X	X					
		B	X	X	X					
		C	X	X	X		X	X		
External communicating device	Blood path, indirect	A	X	X	X	X				X
		B	X	X	X	X				X
		C	X	X		X	X	X		X
	Tissue / Bone / Dentine	A	X	X	X					
		B	X	X	X	X	X	X	X	
		C	X	X	X	X	X	X	X	
	Circulating blood	A	X	X	X	X				X
		B	X	X	X	X	X	X	X	X
		C	X	X	X	X	X	X	X	X
Implant Device	Tissue / Bone	A	X	X	X					
		B	X	X	X	X	X	X	X	
		C	X	X	X	X	X	X	X	
	Blood	A	X	X	X	X	X		X	X
		B	X	X	X	X	X	X	X	X
		C	X	X	X	X	X	X	X	X

Table 2: Overview of additional material tests according to DIN EN ISO 10993-1

Medical device categorized by			Biological effect			
Nature of body Contact		Contact duration A: limited (<24 h) B Prolonged (24 h to 30 d) C: permanent (> 30 d)	Cytotoxy	Carcinogenicity	Reproductive / developmental	Biodegration
Category	Contact					
Surface device	Skin	A				
		B				
		C				
	Mucosal membrane	A				
		B				
		C				
	Breached of compromised surface	A				
		B				
		C				
External communicating device	Blood path, indirect	A				
		B				
		C	X	X		
	Tissue / Bone / Dentine	A				
		B				
		C	X	X	X	
	Circulating blood	A				
		B				
		C	X	X		
Implant Device	Tissue / Bone	A				
		B				
		C	X	X		
	Blood	A				
		B				
		C	X	X		

In-Vitro-Tests

Before testing materials or devices on animals, crucial evaluations such as cytotoxicity and haemotoxicity, as well as tests regarding immune reactions and carcinogenicity are performed in vitro on cell cultures to evaluate the biocompatibility of the implanted material.

Cytotoxicity

The tested material is brought in direct or indirect contact to a cell culture of the type, that will surround the implant after implantation. After a certain incubation time[1], the viable cells are counted. In addition to the number of viable cells, their shape as well as adhesion and distribution over the tested material is taken into consideration for material toxicity.

Haemocompatibility

Instead of cell culture, the tested material is brought in direct contact with blood to analyze the adhesion of blood cells to the material. In general, those materials which do not support adhesion of blood cells are suitable for implantation in blood circulation environment.

In-Vivo-Tests

If the in-vitro tests leave no further concern, animal trials (in-vivo-tests) are conducted to prove the material's biocompatibility in a living environment. The material-tissue contact is assured by skin contact, injection or implantation of the material, while the final immune reaction, toxicity and carcinogenicity is analyzed by biopsy or histology after the animals (artificial) death.

(Paragraphs based on [20])

Biostability Concerns

As implants stay in the human body for a long time span and even if batteries should be renewed every 5 to 10 years, the implanted electrodes themselves remain in contact with the tissue. As a result, biostability is a necessity and describes several chemical and physical aspects of material stability in order to ensure system integrity. [21]–[23]

---

[1] 24 h have shown to be a viable standard incubation time

2.1.4. DEFECT MECHANISMS

Mechanisms leading to device failure can be primarily divided into process-related induced weak points, leading to device failure at production stage on the one hand and physical/chemical failure mechanisms on the other hand. Prohibiting the incorporation of particles and artificial impurities into the passivating layers during production is a common necessity as particles lead to a greatly reduced adhesion. While producing thin film layers, the maximum service temperature of the used materials must not be exceeded, as temperature induced material transition is to be avoided. In addition, high production temperatures, as in sputtering and chemical processes during the polyimide curing process result in high intrinsic stress, due to different thermal material coefficients and, thus, weaken the adhesion of different layers [24]. These aspects must be considered during the manufacturing stage and a possible annealing process can help reduce existing intrinsic stress (see also chapter 4.3.7).

Incorporating more than one metal into a multilayered device leads to a possible galvanic corrosion if they are in direct contact and have direct access to water due to a defect in the passivation layer [25]. This possibility is also given, if one of the metals acts as an adhesion layer and is only several nm thick.

Delamination

When in contact with moisture, such as by implantation into a biological milieu, the difference in the concentration gradient drives water ions into the previously dry, passivating polyimide layer. For single polyimide layers, this process stops when the maximal water uptake with a homogenous water concentration inside of the polyimide is reached. The osmotic pressure, driving water out of the polyimide, comes to an equilibrium with the ion concentration gradient, driving water into it. However, in the case of a polyimide layer with a poor adhesion to another layer, uptaken water vapor condenses in existing voids between the polyimide and the adhering layer. Any dissolved ions, impurities and particles in this void create another concentration gradient, driving more water into the void, thus enlarging the water pressure inside of it and finally also the volume. A burst of the encapsulating polyimide layer is the final worst case, but also short circuits and corrosion may occur prior to failure due to insufficient adhesion. [26]

Corrosion

With the previously described failures of the encapsulation, corrosion effects are likely to occur as an exchange of charge carriers has become possible. Several corrosion mechanisms, likely to happen in multilayered system with a passivation layer, are given in the following paragraphs.

Voltage induced Corrosion

Two metals of the same kind, set at different electric potentials and separated by an electrolyte, corrode if a voltage is applied. While the anode[1] dissolves over time, according to eq. (1), the negatively charged cathode dissolves water and oxidizes hydrogen, according to eq. (2) and eq. (3) with the cathode itself, however, not being negatively influenced.

$$Me \rightarrow Me^{+} + e^{-} \tag{1}$$

$$2H^{+} + 2e^{-} \rightarrow H_2 \tag{2}$$

$$O_2 + 2H_2O + 4e^{-} \rightarrow 4OH^{-} \tag{3}$$

Medical implants with their electrically active metal layers, suffer from this type of corrosion, while being placed in an electrolyte fluid.

Galvanic Corrosion

If two different kinds of metal are brought together by an electrolyte, a standard battery is formed. The difference in the standard potentials drives ions from the less noble metal electrode, thus dissolving it (eq. (2)), to the other, nobler one, forming an anode and a cathode. The standard potential for gold lies in in the range between +1.40 V[2] to +1.69 V[3] whereas titanium has a standard potential between -1.21 V for Ti^{3+} to -1.77 V for Ti^{2+}, potentially leading to galvanic corrosion. [27]

---

[1] *Me* is exemplified for any kind of metal, as seen in eq. (1)

[2] for the oxidized form Au^{2+}

[3] for the oxidized form Au^{+} (Au^{3+} has a standard potential of +1.42 V)

Crevice corrosion

Many metals form passivating oxide layers on their own due to their extremely low standard potential, preventing further corrosion. Titanium, which is used as an adhesive layer in this work, is a good example, as it forms a thin passivating titanium oxide layer. In the case of a broken passivation due to impurities or external deformation, the now opened, bare metal may act as an anode against the passivation, which works as the counter cathode. If the bare metal is being prevented from forming its passivating oxide layer due to the lack of oxygen, crevice corrosion may lead to high current densities, as the ratio of the passivated material is high compared to the non-passivated bare metal. [28], [29]

Polymeric Degradation

Electrical Degradation

Several studies have shown a decrease in resistivity of polymeric insulations in wet conditions under the influence of electric fields. Critical current breakthrough measurements with a DC BIAS indicate the electrical strength of insulations. However, with AC currents applied, the resistivity decrease is a gradual process, described as *water treeing* in literature [30], [31], where small water filled voids are formed. These voids with diameters in ranges of micrometers are then connected to each other by small channels in the range of nanometers, which let ions propagate [32]. The necessary currents however, are much higher than acceptable for medical implants.

Hydrolytic Degradation

Degradation by hydrolysis and hydrolytic reactions in polyimides is described by the workgroups of Hoagland, Deiasi and Stephans [33]–[35]. Ultimately, the loss of insulation capabilities and change in mechanical properties is reported due to dissolution of bulk material and changes in the polymeric structure.

(Subchapter based on [16])

2.2. PHYSICAL MANUFACTURING PROCESSES

The following chapters provide a brief overview of the backgrounds of the used techniques, arranged by the order of appearance during sample manufacturing. Thus, optical lithography is firstly discussed in chapter 2.2.1, followed by the theory of thermal evaporation and sputtering, both being enclosed in chapter 2.2.2. After a multilayer sample is produced, the electrode openings are etched with reactive ion etching, of which a theoretical description can be found in Chapter 2.2.3. Ion Beam Etching is not only used for cleaning processes, but also to etch the layers, created by atomic layer deposition and is thus discussed in 2.2.4. The Theory about Atomic Layer Deposition is placed at the end in chapter 2.2.5.

2.2.1. OPTICAL LITHOGRAPHY

Photolithography is a broadly used process in the micro technological industry to definably pattern a surface via ultra-violet (UV) light. The pattern is transferred from a shadow mask to a light-sensitive polymeric photo-resist, which is applied prior by spin coating onto a substrate. The type of applied photoresist differentiates the two main types of photolithographic processes. A positive resist increases its solubility when exposed to UV light, whereas a negative resist forms cross-linked structures during exposure, hence, becoming more stable.

After exposure, the soluble exposed (for positive resists) or unexposed (negative resist) part of the resist is washed away in a developer solution, leaving the transferred pattern on the sample. [36]–[38]

2.2.2. PHYSICAL VAPOR DEPOSITION TECHNIQUES

Sputtering and evaporation are the most common Physical Vapor Deposition Techniques (PVD) and broadly used in this thesis. All PVD techniques are vacuum based and translate material from its condensed phase into a vapor phase, letting it condense on a target material as a thin film. [39]

Thermal Evaporation

A source material is thermally evaporated, by increasing its temperature until its vapor pressure reaches 10^{-2} Torr. The evaporation rate is derived from the kinetic gas theory and calculated by Langmuir [40] as

$$\mathrm{G} = 5.83 \cdot 10^{-2}\, \alpha\, \mathrm{P}\, (\mathrm{M}/\mathrm{T})^{1/2} \tag{4}$$

with G as the rate of evaporation in $[\frac{\mathrm{g}}{\mathrm{cm}^2 \cdot \mathrm{s}}]$, P the vapor pressure in Torr at the Temperature T (measured in K), M the molecular weight and a sticking coefficient α. Primarily, the evaporation rate is determined by the source temperature. In the case of filament evaporation, the material is located in a so-called *boat*, through which a high current is lead, thus heating the source. [41], [42]

Electron beam physical vapor deposition (EBPVD)

Similar to thermal evaporation, the source material is heated to its vapor pressure. However, this is now done by an electron beam, being magnetically guided to the source. A normal acceleration voltage[1] of 10 kV with a current of 0.1 A delivers 1 kW of power to the source, thus heating the material which is contained in a water-cooled crucible, preventing its own destruction. As the electron beam needs a minimal time of flight, before reaching the crucible, recipient pressures of 10^{-2} Pa or lower are needed. [43]

Sputtering

The coating material, called target, is bombarded with ions, which are generated from a separate ion source or by plasma discharge and accelerated towards the target within an electric field [44]. Typically, the inert gas argon is used for plasma creation. The ions directly break atoms out of the target, by transferring their impulse onto a target atom. The now mobile atoms condense on the surface of the material to be coated. The resulting coating morphology is strongly dependent on substrate temperature and argon pressure, as described by Thornton in 1974 with his structure zone model [45]. There are several possibilities of plasma ignition, however, as HF-sputtering (high-frequency) is the most common and utilized during this work, it is further described.

A high-frequency field is coupled into the chamber, ionizing the process gas. As electrons follow the high frequency due to their small mass, they collide with the target and it becomes negatively charged. The positively charged argon ions are not influenced by the high-frequency due to their much higher mass, but are only accelerated towards the negatively charged target, knocking target atoms out of the solid material.

2.2.3. REACTIVE ION ETCHING

A Reactive Ion Etching (RIE) unit consists of a sample plate and a chamber, which form the cathode and the anode of the electrical system (Figure 7). After a defined atmosphere, consisting of the active process gases, is reached, a plasma is ignited by applying a high

---

[1] In this thesis, an acceleration voltage of 9 kV was used (refer to chapter 3.2.3)

frequency to the sample plate with a capacitively coupled Matching-Unit. This high frequency initially ionizes some process gas atoms.

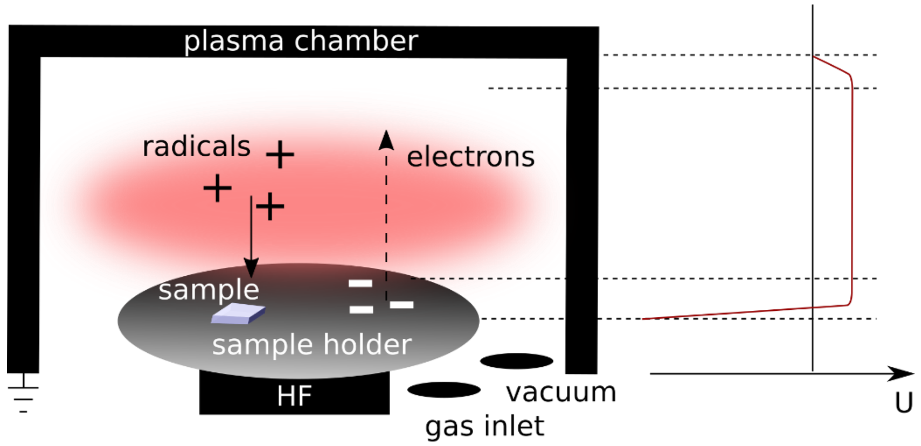

Figure 7: Schematic of a RIE system (modified and based on [46])

The free electrons follow the high frequency field due to their small mass and are accelerated towards the sample plate during the positive frequency half-cycle and the chamber wall during the negative frequency half cycle where they discharge due to the grounding. As the sample plate is only capacitively coupled, it becomes negatively charged to a typical BIAS Voltage in regions of -220 V to -450 V (refer to chapter 3.2.6 for absolute values). In addition, the impact of the primary electrons on the sample plate creates secondary electrons which keep the plasma alive during the next frequency half cycle.

The positively charged radicals are not influenced substantially by the high frequency field due to their higher mass. Instead, they are accelerated towards the sample holder due to the static BIAS Voltage. The impact on the sample leads to a physical material abrasion, just like sputtering (refer to chapter 2.2.2). The result is a physical etching process. [46], [47]

2.2.4. ION BEAM ETCHING

Inside of a chamber recipient, filled with a process gas (usually argon), electrons are provided by a cathode via thermal emission and accelerated towards the anode by an electric field. Collisions with gas molecules generate ions[1]. A second DC BIAS accelerates the positively charged ions towards a negatively charged grid in front of the sample while collimating them. As a result, a collimated, direct ion beam hits the sample surface and knocks out particles of the solid structure. As the sample is bombarded with positively charged ions, a neutralizer can

---

[1] This process is guided by a magnetic field, concentrating the electrons

be activated which balances the charges by introducing additional electrons to the sample surface. [48]–[51]

2.2.5. Atomic Layer Deposition

The process of Atomic Layer Deposition (ALD) relies on two process gases, the precursors, being pumped into a recipient chamber alternately. The first precursor reacts with the surface of the sample and creates a monolayer. This reaction is called half cycle and limits itself in layer growth by chemical adsorption, so that only the creation of a single monolayer is possible. After purging the first precursor with an inert gas, the second precursor is lead in and reacts with the monolayer, created by the first half-cycle, resulting in another monolayer on top (or a single monolayer of the intended material). These two half cycles are repeated until the final layer thickness is reached (Figure 8). Careful selection of the precursors leads to defined materials.

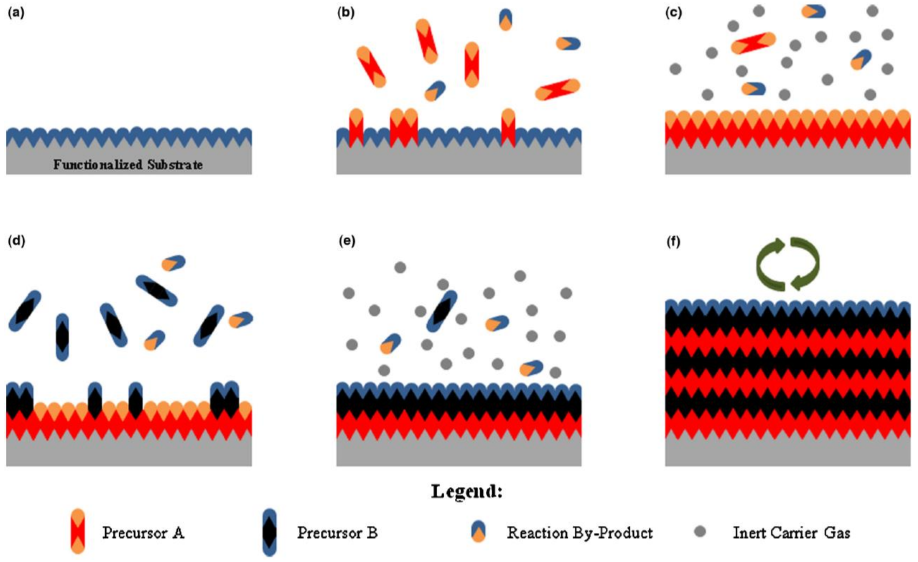

Figure 8: Schematic of ALD process [52]

Each ALD process takes place at an elevated temperature up to 350 °C, whereas the exact temperature and its range is specific to the precursor to induce the described reaction with the sample surface. Temperatures below the specific temperature window lead to incomplete layers due to precursor condensation or due to slow reactions, whereas too high temperatures lead to chemical disintegration. The layer growth rate is temperature independent, if the specific temperature window is maintained. [52]

ALD processes can be classified in pure thermal processes, where the reaction energy is purely given by sample temperature and plasma guided deposition (plasma enhanced ALD, PEALD). By igniting a plasma in the respective half cycle, the temperature window can be reduced greatly, as the reactivity is enhanced by the plasma. All layers in this work are grown with PEALD at 100 °C. [53]

Layers grown by ALD can be tuned very precisely in respect to their layer thickness as the growth is limited to a monolayer per cycle. Furthermore, ALD layers are known to be extremely homogenous and are able to coat high cavities. [54]

2.3. MEASUREMENT TECHNIQUES

As electrical measurements are the main analysis tool in this thesis, the following chapters focus on the theory behind them, beginning with the background theory of transitioning from electron to ion current in chapter 2.3.1. The next chapter 2.3.2 discusses DC measurements in more detail, as these result in very low measureable currents, if at all, when analyzing insulating materials. Next to DC measurements, also impedance spectroscopy is a viable method of analyzing insulators and resistances in fluids and, thus, described in chapter 2.3.3. Finally, as the produced flexible implants contain an electrical strain gauge, the respective theory is found in chapter 2.3.4.

2.3.1. ION AND ELECTRON CURRENTS

Electrical current inside of conductors is described with the classical drude-model and the fermi-gas model which takes a quantum mechanical approach [55]. None of these, however, describe the theory of transitioning from electron-carried current to ion-based current at boundary surfaces. Oxides for example, are negatively charged in water as protons dissociate from surface hydroxyl groups:

$$\sim OH \rightarrow \sim O^{-} + H^{+} \tag{5}$$

A charged, conducting surface adsorbs counter ions due to the electric field it causes. In the simplest case, the adsorbed ions directly bind to the surface and completely neutralize the surface charges within a thickness of a monolayer. This monolayer is called *Helmholtz Layer*, but must be theoretically expanded, as it does not explain the capacitance of an electric double layer. Gouy[1] and Chapman[2], thus, expand this theory with the thermal motion of ions in mind. [56]

In general, charge density and an electric potential are described with the Poisson equation

$$\nabla^2\psi = \frac{\partial^2\psi}{\partial x^2} + \frac{\partial^2\psi}{\partial y^2} + \frac{\partial^2\psi}{\partial z^2} = -\frac{\rho_e}{\varepsilon\varepsilon_0} \tag{6}$$

with ρ_e as the local charge density in C/m^3 which is described with the Boltzmann equation of the local ion density $c_i = c_i^0 \cdot e^{-\frac{W_i}{k_B T}}$, thus, amounting to the following for the simplest case of a planar, infinitely extended surface:

$$\frac{d^2\psi}{dx^2} = \frac{c_0 e}{\varepsilon\varepsilon_0} \cdot \left(e^{\frac{e\psi(x)}{k_B T}} - e^{-\frac{e\psi(x)}{k_B T}}\right) \tag{7}$$

Solving this equation for $e\psi \ll k_B T$ leads to $\psi = \psi_0 \cdot e^{-\kappa x}$, with $\kappa^{-1} = \lambda_D$ as the Debye length, which decreases with increasing salt concentration. In water, λ_D cannot exceed 680 nm due to the dissociation of water[3]. The Debye length for an electrolyte itself is given as

$$\lambda_D = \kappa^{\{-1\}} = \sqrt{\frac{\varepsilon_r \varepsilon_0 k_B T}{2\, N_A e^2 I}} \tag{8}$$

with I as the ionic strength of the electrolyte. [57]

Figure 9 shows how the potential of a diffuse double layer decreases exponentially with increasing distance. The decrease becomes steeper with increased amounts of ions, implying an increased salt concentration. It is also visible, that the electric potential reaches several nanometers into the fluid.

---

[1] Louis George Gouy, 1854-1926, French physicist

[2] David Leonard Chapman, 1869-1958, English chemist

[3] According to $2\mathrm{H_2O} \rightarrow \mathrm{H_3O^+} + \mathrm{OH^-}$, the ion concentration cannot decrease below $2 \cdot 10^{-7}$ mol/L, leading to the given value

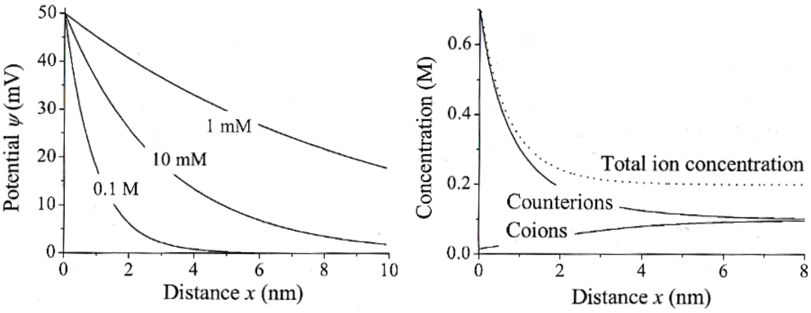

Figure 9: (left) potential-versus-distance for a surface potential of 50 mV and different ion concentrations; (right) local co- and counter-ion concentrations for a monovalent salt at a bulk concentration of 0.1 M [56]

The relation between surface charge σ and the surface potential ψ_0 is deduced by the electro neutrality condition, which means, that the complete charge of ions in the double layer must amount to zero and is therefore calculated as

$$\sigma = -\int_0^{\infty} \rho_e \, dx \tag{9}$$

With this relation, the capacitance of a diffuse electric double layer is derived with the Gouy-Chapman Model as

$$C_{GC}^{A} = \frac{d\sigma}{d\psi_0} = \sqrt{\frac{2e^2 c_0 \epsilon\epsilon_0}{k_B T}} \cdot \cosh\left(\frac{e\psi_0}{2k_B T}\right) = \frac{\epsilon\epsilon_0}{\lambda_D} \cdot \cosh\left(\frac{e\psi_0}{2k_B T}\right) \tag{10}$$

which can be approximated to $C_{GC}^{A} = \frac{\epsilon\epsilon_0}{\lambda_D}$ for sufficiently small surface potentials.

This approach has several limitations, like neglecting the finite size of the ions, the disregard of all non-Coulombic charges and others [58]. This is why Stern[1] proposed a semi-empirical extension to this theory and divided the double layer into two parts: the inner Stern layer and the outer part (Figure 10). Here, the Stern layer describes a layer of immobile ions, which are directly adsorbed to the surface.

---

[1] Otto Stern, 1888-1969, German physicist

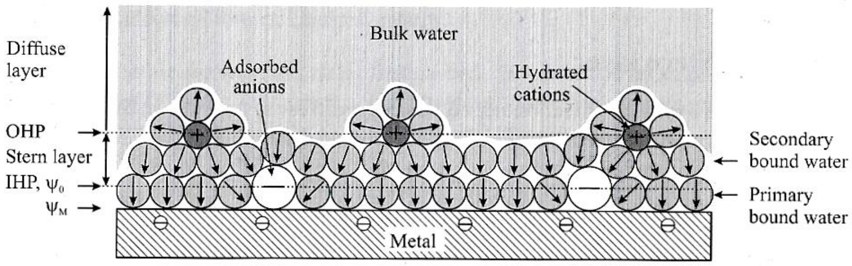

Figure 10: Stern layer at a metal surface [56]

The potential ψ_M is constant over the complete (metal-) volume up to its surface due to the high electrical conductivity. IHP and OHP indicate the inner (IHP) and outer (OHP) Helmholtz planes. The total capacitance is a sum of two capacitors in series, the stern layer C_{St}^A and the Gouy-Chapman layer:

$$\frac{1}{C^A} = \frac{1}{C_{St}^A} + \frac{1}{C_{GC}^A} \tag{11}$$

C_{St}^A can easily be estimated as it calculates to $C_{St}^A = 2\varepsilon_{ST}\varepsilon_0/r_{ion}$ with denoting the radius of hydrated ion by r_{ion} which is in the order of ~ 1 Å. The permittivity at the surface is reduced and can be estimated by $\varepsilon_{ST} = 10$ for water. Thus, a capacitance for the Stern layer of $C_{St}^A = 44\ \mu\mathrm{F\ cm^{-2}}$ is calculated and experimentally often found to be in the range of $10 - 100\ \mu\mathrm{F\ cm^{-2}}$.

Experimentally, this surface-liquid transition is often described with the equivalent circuit, given in figure 11, with R_S as the solution resistance, R_{CT} the coating resistance and a constant phase element Z_{CPE}.

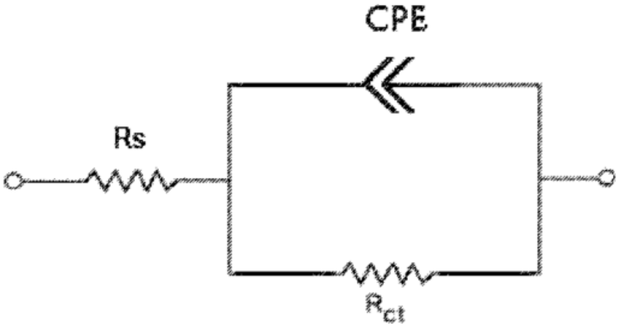

Figure 11: equivalent circuit for a metal-solution interface [59]

The solution resistance is the measured resistance between a working electrode and a reference electrode, both placed in that solution. Under the assumption, that the counter electrode is infinitely large, which is a good approximate for macroscopic electrodes in proportion to a typical MEA electrode, the solution resistance can be determined from the spreading resistance, which is the resistance, encountered by current spreading into solution. It is calculated as follows

$$R_S = \frac{\rho_S}{4\,r} \tag{12}$$

for round electrodes of diameter r with ρ_S as the solution resistivity and given by 72 Ω cm for physiological saline. [60]

The non-faradaic impedance, arising from the interface capacitance, or its polarization, is given by the constant phase element

$$Z_{\mathrm{CPE}} = \frac{1}{Q(j\omega)^n} \tag{13}$$

with $\omega = 2\pi f$, as the angular frequency, Q a measure of magnitude of Z_{CPE} and n a constant $(0 \leq n \leq 1)$, representing inhomogeneities in the surface. In a Nyquist plot (refer to chapter 2.3.3), n gives the angle between the data and the abscissa axis according to $n = (2\,\theta)/\pi$. In the case of a purely capacitive resistance, n is 1. [61]

Model-based values for gold electrodes of defined area are listed in Table 3.

Table 3: Values for the circuit of a gold-pbs contact [59]

Electrode Area [mm²]	**Q [µF s^{n-1}]**	**n**	**R_{ct} [MΩ]**	**R_s [Ω]**
6	0.544	0.85	8.04	110
2	0.258	0.86	27.8	203
0.05	0.036	0.83	209	1137

With smaller electrode areas, the capacitive behavior becomes more negligible, while the purely resistive terms R_{CT} and R_S increase.

2.3.2. DC MEASUREMENTS

Measuring electrical currents by applying a constant, not time-variant voltage results in the resistance, sometimes also called time-invariant impedance. It is quite difficult to obtain the resistance for electrical insulators with values of $10^{12}\ \Omega$ and above while being limited in voltage, as interfering effects like leakage currents, input resistance burden, thermal noise and triboelectric-effects gain in influence. [62], [63]

Leakage Currents

Leakage currents are generated by error currents, flowing over stray resistance paths between the measurement circuit and nearby voltage sources. Especially, in cases of devices with high impedances, leakage currents occur from the insulation resistance. Good shielding over the complete setup, good quality insulators and a reduced level of humidity greatly contribute in reduction of leakage currents.

Input Burden

The ratio of the ammeter's input resistance to the resistance between its input and the outer shield equals the ratio of current loss over the device, caused by the input resistance, and the measured current of the device under test. This error is minimized by using an ammeter with a low input burden, together with a good insulation.

Thermal Noise

Cause of the thermal noise is the temperature dependent Brownian motion, generating short circuit noise in metals, which can be calculated as follows:

$$I_{thermal\ noise,rms} = \sqrt{\frac{4k_b T\Delta f}{R}} \tag{14}$$

In open circuit measurements, the circuit voltage is calculated as follows, with k_b being the Boltzmann constant, T the absolute Temperature and Δf the frequency bandwidth:

$$E_{thermal\ noise,rms} = \sqrt{4k_B TR\Delta f} \tag{15}$$

Generally, the effect of Brownian motion is reduced by integrating over longer time spans and reducing the temperature. Temperature reduction, however, is not always applicable due to change in device properties and not applicable in the case of accelerated aging measurements.

*Triboelectric Effec*t

The effect of induced charged imbalances by bending a cable is called triboelectric effect. It is prevented by avoiding cable movement during measurement in this work.

2.3.3. AC MEASUREMENTS

An AC excitation signal is frequency dependent as follows

$$E_t = E_0 \sin(\omega\, t) \tag{16}$$

with E_t being the potential at the time t and E_0 the original amplitude of the excitation signal. The relationship between the radial frequency ω and the frequency f [Hz] is: $\omega = 2\,\pi\, f$. Applying this signal to a linear system, a response signal I_t with a shifted phase ϕ is obtained. This signal differs from the original I_0 as follows:

$$I_t = I_0 \sin(\omega\, t + \phi) \tag{17}$$

Applying Ohm's law to E_t and I_t leads to the impedance of a system:

$$Z = \frac{E_t}{I_t} = \frac{E_0 \sin(\omega\, t)}{I_0 \sin(\omega\, t + \phi)} = Z_0 \frac{\sin(\omega\, t)}{\sin(\omega\, t + \phi)} \tag{18}$$

with the impedance given in terms with a magnitude Z_0 and a phase shift ϕ. Plotting these two terms against each other, results in a common Lissajous figure, which was the preferred measurement method, bevor Electrochemical Impedance Spectroscopy (EIS) became broadly available. Utilizing Euler's relationship

$$e^{i\,\phi} = \cos\,\phi + i \sin\,\phi \tag{19}$$

the impedance of a system can be represented as a complex number:

$$Z(\omega) = Z_0 e^{i\phi} = Z_{0,\omega}(\cos\phi_\omega + i \sin\phi_\omega) \tag{20}$$

By plotting the real part of eq. (20) versus its imaginary part, a Nyquist Plot is generated, where each point represents the impedance at one frequency (Figure 12).

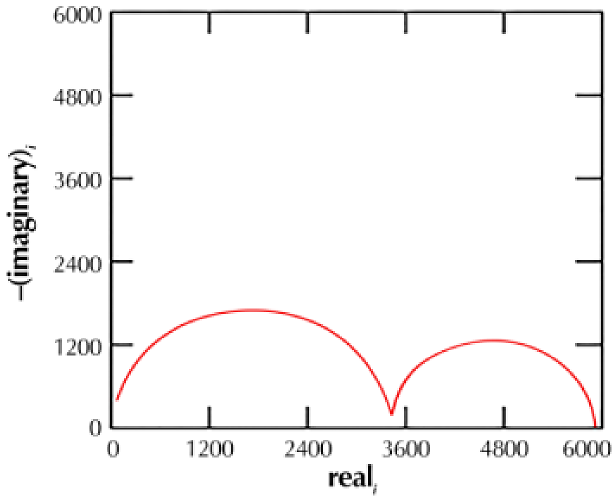

Figure 12: Typical Nyquist Plot of a damaged coating

More information is given in Bode Plots (Figure 13), as Nyquist plots do not indicate the exact frequency for one data point. Only the relation between phase and frequency can be represented. Bode Plots, however, show the complete frequency as well as the phase behavior.

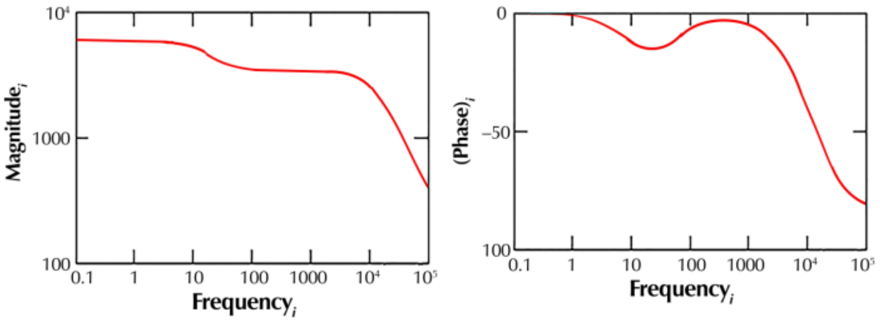

Figure 13: Typical Bode Plot for a damaged Coating

When measuring a resistor of purely capacitive nature, the phase is perpendicular to the excitation signal, resulting in a -90° phase shift and an impedance of $Z = \frac{1}{j\omega C}$. A purely ohmic resistor does not shift the phase, resulting in a 0° phase shift with an impedance of $Z = R$. Inductors, respectively, lead to an impedance of $Z = j\omega L$. A capacitive resistance, responding with anything other than a phase of -90° is evidence of degradation, due to an electrochemical process, water intrusion or corrosion. [64]

Two other special circuit elements are the constant phase element, modeling the behavior of a double layer by simulating an imperfect capacitor, and the Warburg element, which simulates a diffusion process in dielectrics. It is a circuit element, introducing a constant 45° phase shift, while its magnitude is inversely proportional to the square root of the frequency.

When examining degraded coatings against an electrochemically active liquid, like polyimide covering an electrode against a PBS liquid, the resulting impedance behavior is more complex and typically modeled with an equivalent circuit, as one is given in figure 14. Not only the Coating-PBS transition, as well as the capacity of the coating itself, but also the effect of newly created liquid/metal interfaces under the coating by water vapor penetration must be considered now.

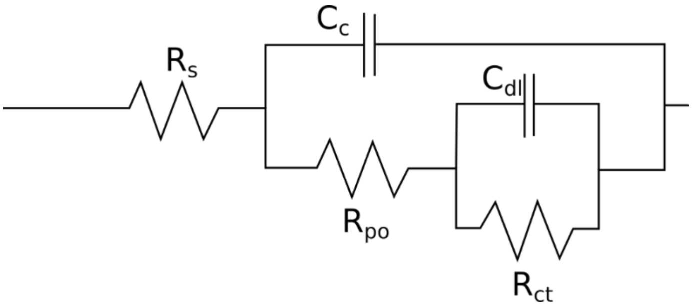

Figure 14: Equivalent Circuit for a Damaged Coating [65]

The capacity as well as the resistance of the original intact coating are characterized by C_c and R_{ct}, respectively, in this model. Eventually developed ion-conducting paths within of the coating are described with the pore resistance R_{po}. It is probable for some parts of the coating to delaminate from the metal, leaving pockets behind, which are filled with electrolyte solution, that may be different from the bulk solution. This interface, between the bare metal and the solution filled pocket, acts a as double-layer and is, thus, modeled with a double-layer capacitance C_{dl}. R_s represents the resistance of the bulk solution over the passivation. [66]–[71]

The previously described given Nyquist and Bode Plots are calculated with the equivalent circuit of Figure 14 and represent a typical degraded coating over an electrode. Generally, finding the appropriate equivalent circuit is not an easy task. [72]

2.3.4. ELECTRICAL STRAIN GAUGES

The resistance of a conducting medium changes with the applied mechanical strain, which causes a relative geometrical change of the conductor. Thus, by determining the electrical resistance of a conducting path, the mechanical strain applied to this path is indirectly measurable. These conducting paths are called strain gauges and are mostly represented as meandering structures in order to maximize the affected conductor length, resulting in a maximal resistance change which again leads to a higher precision of the strain gauge. [73], [74]

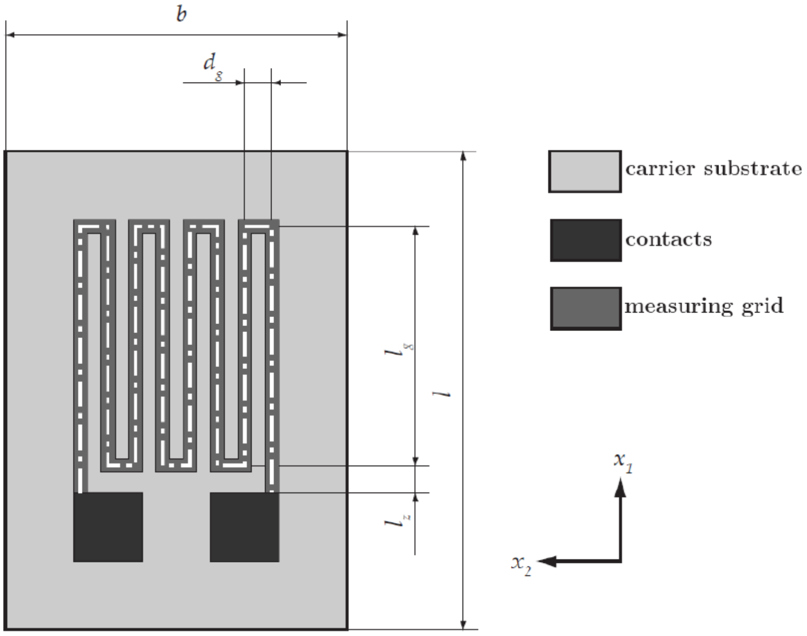

Figure 15: General Structure of a strain gauge with leading wires

Figure 15 shows a typical meandering strain gauge, from which its resistance is calculated after the following eq. (21):

$$\begin{aligned} R_{\text{DMS}} &= 2 \cdot R_{\text{Contact}} + \rho \frac{2 \cdot l_z + n \cdot l_g + (n-1) d_g}{b_g \cdot h_g} \\ &= 2 \cdot R_{\text{Contact}} + \rho \frac{2 \cdot l_{x1} + l_{x2}}{b_g \cdot h_g} \end{aligned} \tag{21}$$

with the parameters of l_z as the feed line length from the contact to the grid, l_g the length of measuring grid, d_g the distance from one feed line to another in the grid, b_g the width of a measuring grid feed line, h_g the height of a measuring grid feed line and n the number of parallel feed lines.

With $l_{x1} = 2 \cdot l_z + n \cdot l_g$ and $l_{x2} = (n-1)d_g$, the specific electrical resistance ρ and poissons's ratio ν, the sensitivity of the strain gauge is calculated as follows:

$$k_l = \frac{\frac{\Delta R_{\mathrm{DMS}}}{R_{\mathrm{DMS}}}}{\varepsilon_l} = \frac{\Delta\rho}{\rho \cdot \varepsilon_l} + 1 + 2 \cdot \nu \cdot \frac{l_{x1}}{l_{x1} + l_{x2}} \tag{22}$$

This sensitivity is also called k-factor. With $\frac{l_{x1}}{l_{x1}+l_{x2}} \approx 1$, as it can be approximated when one direction is disproportionally larger than the other one, a reduced k-factor can be expressed as:

$$k = \frac{\Delta\rho}{\rho \cdot \varepsilon_l} + 1 + 2 \cdot \nu \tag{23}$$

This k-factor only considers the conductor percentage in x_1-direction, resulting in a need of minimizing the conductor length in x_2-direction. k-factors as well as Poisson's ratio for common strain gauge materials are given in table 4.

Table 4: Material parameters for common strain gauge materials [74]

Material	**Poisson's ratio**	**k-factor**
Constantan	0.33	2.044
Platinum	0.39	4.82 [75]
Gold (bulk)	0.42-0.44	4.48 [76]
Gold (300A, sputtered)	0.35 [77]	2.6 [73]

A second k-factor called k_q, describes the relative resistance change to the strain ε_q, in direction x_2, perpendicular to x_1 and is defined as follows:

$$k_q = \frac{\frac{\Delta R_{\mathrm{DMS}}}{R_{\mathrm{DMS}}}}{\varepsilon_q} \tag{24}$$

Naturally, this k_q-factor is to be minimized as much as possible.

(Chapter based on [73] 3.2 and 3.4.1)

3. MATERIALS AND FABRICATION PROCESSES

The following chapters describe the necessary manufacturing processes of all samples in detail, starting with the description of the needed materials and chemicals in chapter 3.1. Every single fabrication process is then further specified in the subchapters of 3.2 , including the specific process parameters for sample production. The complete sample production process requires the combination as well as repetition of several production steps and was developed during this thesis. Thus, the creation of a multilayer sample itself is not handled during Materials and Methods but can be found in the results in chapter 4.1, together with details about necessary hard masks, which were also developed.

3.1. MATERIALS

Polyimide and its properties are described in the following chapter 3.1.1, as it is the main substrate material of nearly all fabricated samples. The enclosed circuitry consisted out of thin layers of titanium and gold, which are both discussed in chapter 3.1.2. The frequently used chemicals are all described in chapter 3.1.3. Titanium dioxide is discussed in the extra chapter 3.1.4 with additional attention, as it represents the desired electrode side wall passivation.

3.1.1. POLYIMIDE 2611

Although Polyimides are widely used in aspects of microelectronics for over 30 years, they were first discussed by Richardson et al. in 1993 in regards to their suitability for encapsulating implantable biosensors and their usage as flexible substrate material [7]. Thus, several workgroups like Akin et al., Sun et al. and Stieglitz et al. examined the biocompatibility and proved the non-toxicity in regards to low cytotoxicity and low hemolytic capacity [6], [78], [79]. Electrical implants with a polyimide encapsulation have also proven to be biostable and fully functional for months in chronic in-vitro and in-vivo studies even though no polyimide has an FDA approval according to ISO 109931 (refer to chapter 2.1.3) until now. [80]–[82]

However, even with the missing FDA certification, a polyimide based sub retinal chip allows blind persons to regain their eyes-sight [12] with the biostability as well as the non-toxicity proven.

Polyimide 2611 (HD Microsystem, Parlin, USA), further abbreviated as PI, is used during this work. It is synthesized by adding a dianhydride as well as a diamine to a dipolar aprotic solvent, resulting in a rapidly forming poly(amic acid)s, which actually is the polyimide precursor. [21]

Table 5: Solution Properties of PI-2610 and PI-2611 [83]

Test	**Units**	**PI-2610**	**PI-2611**
Solids	%	10.5 ± 1	13.5 ± 1
Viscosity	Pa s	0.25 – 0.30	1.10 – 1.35
Chloride Content	Maximum ppm	5	5
Sodium or Iron Content	Maximum ppm	1.0	1.0
Potassium or Copper Content		0.5	0.5
Total Metals	Maximum ppm	10	10
Ash	Maximum %	0.10	0.10
Density	g/cm^3	1.064 ± 0.013	1.082 ± 0.012

PI features a very high viscosity of $1.1 - 1.35\ \mathrm{Pa \cdot s}$ as can be taken from table 5, where it is compared to PI 2610 from the same manufacturer. It is delivered frozen where it remains durable for two years. Defrosted, its shelf life reduces to 2 weeks, as the solvent evaporates continuously. This process is stopped again by freezing the PI. Thus, only the needed amount is to be defrosted in order not to end the shelf life preliminarily.

The high suitability for encapsulation of PI is not only due to its biostability or -compatibility, but also due to its extremely high volume resistivity of > $10^{16}\ \Omega\mathrm{cm}$ (other sources even state an electric resistivity of $1.5 \times 10^{17}\ \Omega\mathrm{cm}$ [84]) which guarantees electrical passivation. The remaining conductivity is described by the work of Deligöz et al., who also analyzed the electrical properties of polyimide under water vapor uptake [85]. With DC Voltages applied, the remaining current flow is described by combination of the Schottky and Poole-Frenkel-type mechanism, with the current density J_{SCH} for the Schottky-type given in eq. (25):

$$J_{\mathrm{SCH}} = A^{*}T^{2} \exp\left(\beta_{s}E^{\frac{1}{2}} - \phi_{s}\right)/k_{B}T \tag{25}$$

with ϕ_s as the Schottky barrier height at the metal-polyimide interface in the absence of an electric field, A^* as the Richardson constant and β_s as:

$$\beta_S = \left(\frac{e^3}{4\pi\varepsilon\varepsilon_0}\right)^{1/2} \tag{26}$$

While the Poole-Frenkel-type current density is given by:

$$J = J_0 \exp\left(\frac{\beta_{PF} E^{\frac{1}{2}}}{2kT}\right) \tag{27}$$

Where, E represents the electric Field, J_0 is the low-field current density and β_{PF} is the Poole-Frenkel field lowering coefficient given as [86], [87]:

$$\beta_{PF} = 2(e^3/4\pi\varepsilon\varepsilon_0)^{1/2} = 2\beta_S \tag{28}$$

The overall resistance in polyimides can be assumed as pure ohmic, until an applied voltage of 25 V is reached [85][1]. Several other physical features are listed in table 6 and, if compared to competitive products clearly show the applicability of PI 2611.

The chemical structure of PI 2611 is given in figure 16 with the specific sequence of benzene rings, imide and ether groups.

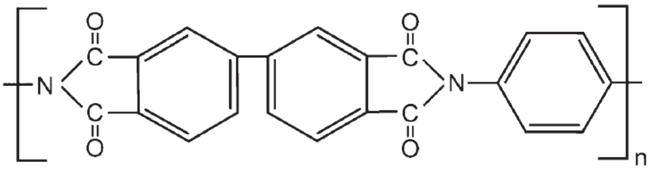

Figure 16: Chemical Structure of PI 2611 [21]

During curing, polyimide loses up to 50% of its mass, which results in a reduced layer thickness, compared to the liquid layer thickness [83]. Several different models as the fringed micelle model, the lamellar models, the adjacent reentry chain-folded models and more all discuss the crystallization procedure or polymers theoretically. A good overview is found in the work of V. Ratta [88]. It is not easily discussable, in which form PI crystallizes, as the result is heavily dependent on process variables [89]. In general, mostly intermolecular rotations and intermolecular chain packing of molecular groups are formed and described by x-ray scattering studies by Ratta et al. [90].

---

[1] Although this value is dependent on the material thickness

Table 6: Comparison of Polyimide 2611 with other polyimides [83]

Feature	**Units**	**PI-2611**	**PI-5878G**	**PI-2525**
Tensile Strength	MPa	350	260	130
Elongation	%	100	120	90
Density	g/cm	1.40	1.42	1.39
Modulus	GPa	8.5	2.3	2.3
Moisture Uptake	%	0.5	2 – 3	2 – 3
Stress (10 µm film)	MPa	2	16	37
Glass Transition Temperature	°C	360	400	325
Melting Point	°C	None	None	None
Decomposition Temperature	°C	620	580	550
Weight Loss (500°C in air, 2hr)	%	1.0	3.6	3.6
Coefficient of Thermal Expansion	ppm/°C	3	20	40
Coefficient of Thermal Conductivity	cal/cm sec °C	25×10^{-5}	37×10^{-5}	35×10^{-5}
Specific Heat	cal/g/°C	-	0.26	0.26
Dielectric Constant (at 1 kHz, 50% RH)		2.9	3.5	3.3
Dissipation Factor (at 1 kHz)		0.002	0.002	0.002
Dielectric Breakdown Field	V/cm	$>2 \times 10^{6}$	$>2 \times 10^{6}$	$>2 \times 10^{6}$
Volume Resistivity	Ω cm	$>10^{16}$	$>10^{16}$	$>10^{16}$
Surface Resistivity	Ω	$>10^{15}$	$>10^{15}$	$>10^{15}$

3.1.2. METALS

All circuitry, as well as the metal intermediate layers of the produced samples consist of a layer stack, consisting of 10 nm titanium, followed by 50 nm gold and topped again with 10 nm titanium. The titanium serves, as an adhesive layer between the gold and the polyimide. Both metals are introduced in this chapter.

Gold

Gold, in the following named Au after its chemical symbol, is chemically inert and an exquisitely good conductor with an electrical resistivity of 23.5 nΩm[1]. This circumstance makes it an ideal circuitry material for micro-technology applications and broadly used in the industry. [91]

Au crystallizes in a face-centered cubic crystal structure with a lattice constant of 4.0782 Å [92]. Initially, Au forms small island-like droplets, which consolidate to a thin film with increasing film thicknesses, as is described with the simplified Volmer-Weber modality (Figure 17). Madey et al. researched the exact growth of thin gold layers in an UHV[2] environment, starting from 0.2 nm thick films [93]. They could confirm single hemispherical Au islands, which percolate with a film thickness of 8 nm. After reaching a thickness of 12 nm, a continuous, closed Au film is formed. [93]–[95]

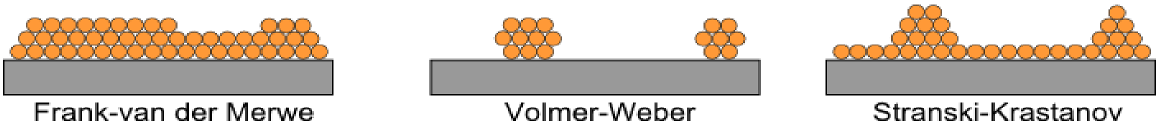

Figure 17: Layer growth possibilities, prior published in [96]

Under normal conditions, the melting temperature amounts to 1063 °C for bulk Au material. However, thin layers of less than 10 nm melt beforehand in temperature ranges of about 1000 K. Temperatures below 1000 K may not lead to melting of thin Au films, but induce spreading of single gold clusters and therefore may break thin film uniformity, which results in a higher surface roughness. [97], [98]

Next to utilizing gold in medical implants for some time [22], [79], [99], the biocompatibility in specific has been topic of studies recently [100]. Fan et al. researched the cytotoxicity of

---

[1] Under normal conditions at 20°C

[2] Pressures under 10^{-7} Pa are defined as UHV

gold particles of various sizes on human hepatoma carcinoma cells (HuH-7). 80% of cell survival was proven for nanoparticles over 15 nm in diameter. Only when decreasing the diameter to less than 15 nm a higher cell death rate was described. Larger clusters and layers did not show any negative impact on the cell cultures. [101]

Biostability on the other hand is more of a problem, as Wolter et al. discussed in [102], where they describe common problems such as crack formation and delamination of gold layers, when exposed to blood plasma in conditions of temperature, flow velocity and pressure, all similar to the human body.

The gold, used to produce the electrode structures via vapor deposition (refer to chapter 2.2.2) were fine gold grains of 999,9 ‰ from Agosi (Allgemeine Gold- und Silberscheideanstalt AG, Pforzheim, Germany), whereas the gold for the intermediate metal layers was sputtered from a solid gold target (see chapter 3.2.4), provided by Lisa$^+$ (Center for Light-Matter Interaction, Sensors & Analytics, Tubingen, Germany).

Titanium

Titanium in the following referred to as Ti, possesses an electrical resistivity of 554 nΩm[1], and thus more than 20 times as much as Au. It has two crystallization phases. The α-phase is a hexagonal close-packaged structure with a lattice constant of 295.08 pm, 295.08 pm and 468.55 pm, respectively, whereas the β–phase takes on a body centered cubic form. Under normal conditions, the α-phase is preferred. At temperatures, exceeding 882.5 °C, however, the β-phase takes over, which shows a greater vulnerability to corrosion. The overall melting temperature amounts to about 1650 °C. [103]–[105]

Ti has previously been used as an adhesive layer between Au and several insulators like silicon or polymers without altering the dielectric properties of the insulator. While researching thin titanium layers, Bottomley et al. also verified the Volmer-Weber growth modality (Figure 17), whereby island coalescence occurs after 1 – 2 nm of film thickness [106]. It was shown, that Ti layers thicker than 2 nm retain a titanium core, while forming a thin oxide surface layer. This thin oxide layer, together with the low electrical conductivity , explains the proven biocompatibility of pure titanium layers. [106]–[110]

---

[1] Measured under normal conditions at 20°C

The addressed thin oxide layer remains at pH values of those in the human body. This aspect, together with the corrosion stability, leads to the biostability of titanium which was first demonstrated by Schiff et al. [111]

The Ti adhesive layers of the electrode structure were evaporated from a crucible with 99.995 % pure titanium, whereas all other Ti layers were sputtered from a solid titanium target, both provided by Lisa$^+$ (refer to chapter 3.2.3 and 3.2.4 for processing steps and chapter 4.1 for detailed fabrication).

3.1.3. CHEMICALS

Chromium Etchant

Chemical wet etching is often utilized for removing sacrificial layers, as it is an undirected and isotropic etching process. Also, by choosing particular etchants, single materials can be dissolved purposefully by breaking their atomic bindings and/or chemically bonding them to a soluble material. Chromium, as well as Ti, are chemically wet etched during sample production. In case of etching chromium, TechniEtch Cr01[1] (Michrochemicals, Ulm, Germany) with a composition of Ceric ammonium nitrate to per-chloric acid to H_2O of 10.9 % : 4.25 % : 84.85 % is used. In general, most chromium etchants consist of parts of ammonium nitrate and per-chloric acid to induce the chemical reaction eq. (29):

$$3\mathrm{Ce(NH_4)_2(NO_3)_6} + \mathrm{Cr} \rightarrow 3\mathrm{Cr(NO_3)_3} + 3\mathrm{Ce(NH_4)_2(NO_3)_5} \tag{29}$$

During the etching process, chromium is transformed into chromium nitrate, which is then dissolved in the etchant and can be easily washed away. The isotropic etch rate amounts to approx. 60 nm/min at room temperature. TechniEtch Cr01 also has a strong impact on silver and vanadium, while it shows little to no influence on aluminum, tungsten, nickel and titanium. (Paragraph based on [112])

Ammonium Fluoride

As Ti is chemically inert due to its oxide layer, very strong acids such as HCl, H_2SO_4 and HF are necessary for etching. HF, in combination with acids, removes the protective oxide layer of a titanium surface and therefore increases the etching rate greatly. However, the

---

[1] formerly known as “Chrome etch n° 1” from the same manufacturer

etching rate of titanium is mostly independent of the concentration of these strong acids, but strongly depends on the concentration of added ammonium fluoride, as Straumanis et al. discuss and suggest the usage of pure ammonium fluoride for etching titanium thin films. [113]

Ammonium fluoride (NH_4F) itself is a colorless solution and a reportedly convenient way of oxide removal and exhibits a strong horizontal under-etching capability. By excluding a strong acid, the etch rate is slightly minimized. However, the constantly forming oxide layers are continuously dissolved. [114]

The used ammonium fluoride is again provided by Lisa+ and originally “Ammoniumfluorid-Ätzmischung AF87,5-12,5” from Merck (Darmstadt, Germany).

3.1.4. TITANIUM OXIDE

Titanium oxide, in the following referred to its chemical formula TiO_2, forms a protective oxide naturally, as previously mentioned. However, it is also the focus of several studies and often deposited on purpose, especially in medical environments, as it has proven to be extremely biostable. [115]–[118]

In addition, the biocompatibility was topic of studies by Nan et al., who evaluated the blood compatibility of thin TiO_2 films by clotting time measurements, platelet adhesion investigations and hemolysis analyses. They conclude, that the blood compatibility of thin films greatly improves by coating them with TiO_2, respectively. [119]

Also, the melting Point of TiO_2 amounts to 1855 °C and it is insoluble in water [120]. Its dielectric breakdown field is measured to approx. $1.5 \cdot 10^8 \frac{\mathrm{V}}{\mathrm{m}}$, which is in the same magnitude of the one of polyimide (refer to chapter 3.1.1) and is experimentally verified in chapter 4.4.1 [121]. An overview of the different properties and the influence of different ALD processes on the resulting TiO_2 layers can be found in the thesis of Dorothea Maier [122].

3.2. FABRICATION PROCESSES

The following chapters each describe a necessary manufacturing process in detail. As the samples are cut from whole wafers, the cutting process is introduced in chapter 3.2.1. The circuitry was produced by optical lithography, which is described in the following chapter 3.2.2. However, as optical lithography just creates the structure, the material itself must be deposited by other means. Therefore, thermal evaporation is used for the electric circuitry, which is explained in chapter 3.2.3 and the metal intermediate layers are sputtered on the thin films, as can be seen in chapter 3.2.4. Polyimide, regardless if used as a substrate material or as a flexible layer, is spin coated in a clean room environment. However, the temperature curing needs detailed parameters, which are given in chapter 3.2.5. The electrodes of the manufactured samples are opened via reactive ion etching in an oxygen plasma, which is the content of chapter 3.2.6. Finally, the electrode side wall is passivated by atomic layer deposition. Therefore, the process is explained in chapter 3.2.7, followed by the recurring and final electrode-opening step by utilizing ion beam etching, explained in chapter 3.2.8.

3.2.1. WAFER DICING

Double sided Borofloat 33 glass wafer from Siegert Wafer (Aachen, Germany) with a diameter of 4 inch were used as substrate material throughout the present work. The samples themselves were much smaller in their dimensions and, thus, the wafer must be cut. A Disco DAD321 dicing saw with the appropriate glass dicing blade Disco P1A851 was used for cutting the substrate material into the desired form factor of (25.225 x 25.225) mm^2 for the non-flexible samples (chapter 4.1.1) and (30.08 x 40.08) mm^2 for the flexible samples (chapter 4.1.2). 80 µm were added to each side due to the wafer saw blade thickness.

The glass wafer was attached to a dicing tape type ULTRON 1008R-9.0 from MINITRON electronic GmbH (Ingolstadt, Germany), which itself was 80 microns thick and attached to an aluminum frame. The alignment of the sample to the tape was accomplished with a template to center the wafer and thus later placing it directly under the cutting saw. The aluminum frame, with the tape and substrate, was placed into the dicer before the blade spun up to 20.000 rpm and cut 130 µm above the dicing tape.

3.2.2. OPTICAL LITHOGRAPHY AND CHROMIUM MASKS

The lithography protocol was mostly independent from the substrate material; may it be a glass wafer or an underlying polyimide layer as it was the case of the flexible samples. However, in both instances, the sample must be heated and therefore was pre-baked for at least 5 minutes at 90 °C on a hotplate before applying the positive photoresist Ma-P 1205 (HD Microsystems, Neu-Isenburg, Germany). 5.5 ml of resist for the 3-inch glass wafer, 1.2 ml for singe 1-inch glass samples and about 1.5 ml for the flexible samples were required. After the resist was applied in a flowing movement without touching the sample surface via a pipette, any enclosed air bubbles were to be removed, as these had a negative influence. A Convac 1001 spin coater with a starting speed of 500 rpm distributed the resist for 5 s, followed by 3000 rpm for 30 s with a 10 s speed-up ramp, which resulted in a 0.5 µm thick resist film [83]. A subsequent pre-exposure bake at 90 °C for 60 s was necessary before patterning the layout, utilizing a Karl Süss Ma/Ba6 Mask Aligner by illuminating the sample for 40 s in hard contact mode with UV light of 350 nm wave length with a power of 210 W. The final structure was acquired by developing the resist with the appropriate developer ma-D 331S, also from HD Microsystems. By carefully swirling the sample in the developer for 35 s and washing the developer off with ultrapure water afterwards, the final lithography structure was established.

Non-flexible Sample Masks

The non-flexible samples could be produced in batches of up to nine units, as the positive mask *bottom electrodes mask* (Figure 18), allowed the exposure of multiple samples simultaneously. It was created in our workgroup by Tanja Martin, for the use of a whole 4 inch glass wafer.

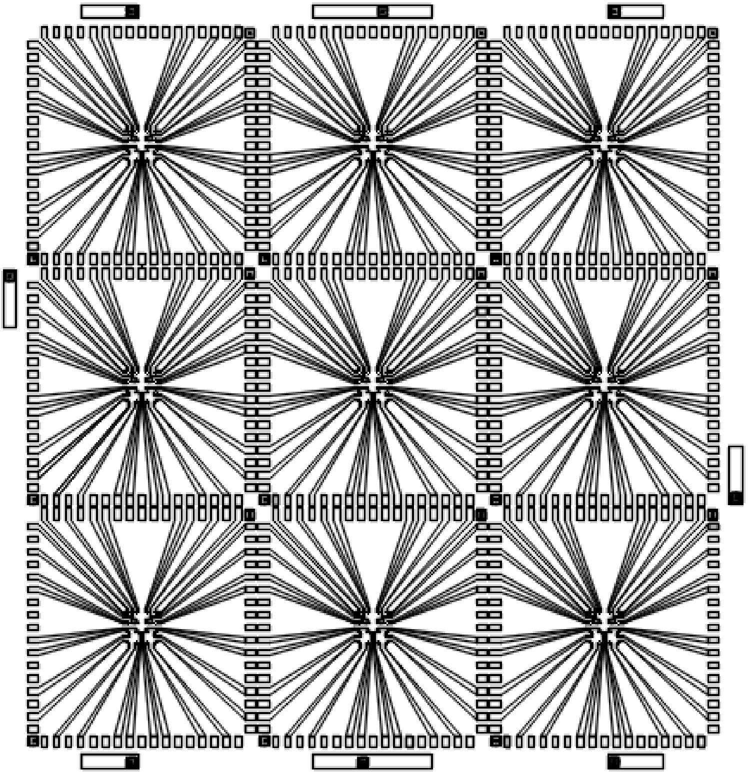

Figure 18: Bottom Electrodes Lithography Mask

A close-up of the electrodes on this mask can be seen in figure 19. The 4 smallest electrodes, located in the corners have a diameter of 100 µm, the 8 electrodes of medium size have a diameter of 250 µm, whereas the 4 largest electrodes are 500 µm in diameter. Every conductive feed line is 50 µm within the electrode square of the array. The mask is rotation-symmetric in a way, that the feed lines do not overlap when rotating the mask by 180°.

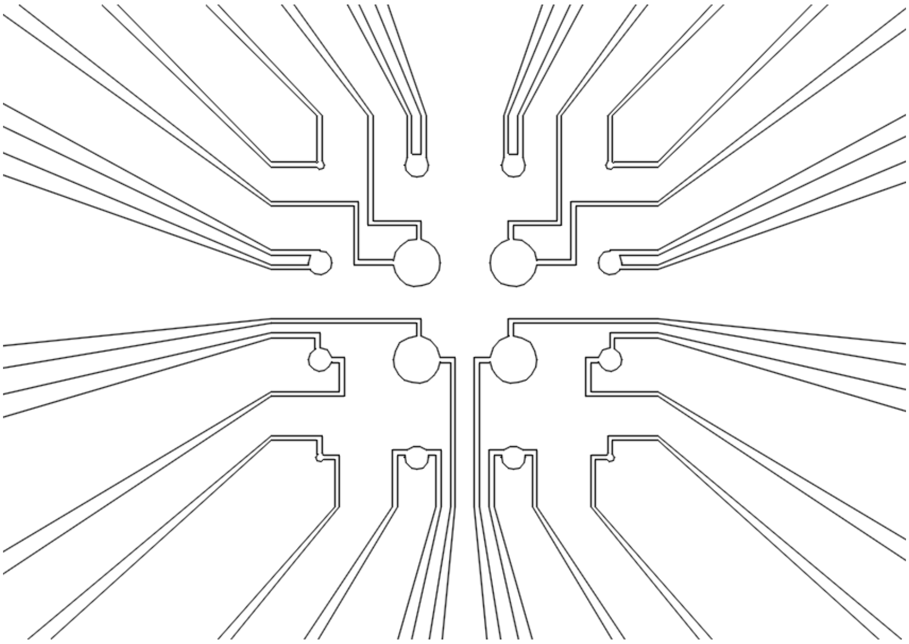

Figure 19: Close-up of the electrode field of the sensor array

Further photolithographic masks, an *ALD Etching Mask* and an *ALD Protection Mask*, were required for the non-flexible samples, and only differ in a small detail. Both are based on the bottom electrodes mask. The ALD Etching mask has the same layout as the electrode mask, just without the feed lines to the electrodes. Thus, a close-up of the important electrode area can be seen in figure 20a.

The ALD Protection mask, also, has the same layout, however, the diameters of the electrode openings are now 80 µm for the smallest electrodes, 200 µm for the medium electrodes and 400 µm for the largest electrode (Figure 20b). It is utilized for opening the ALD passivated electrode surface again (refer to chapter 4.1.2 for detailed sample production).

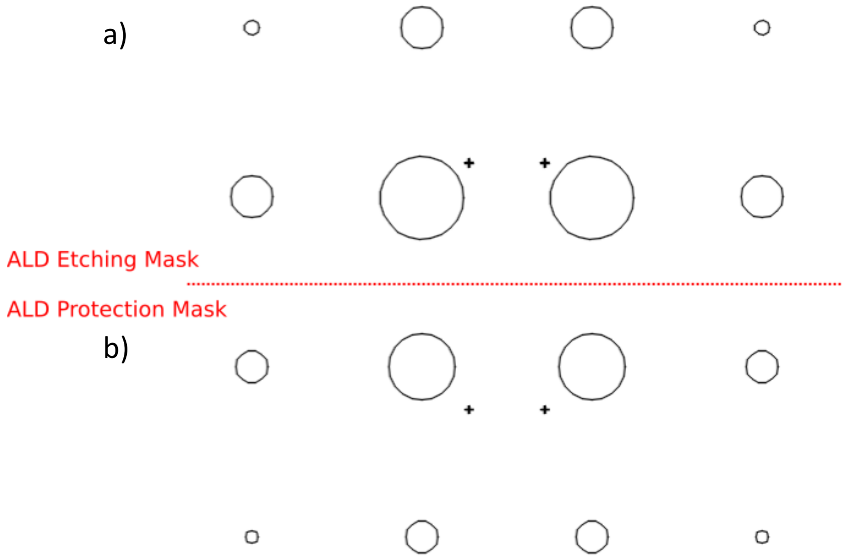

Figure 20: ALD Etching and ALD Protection mask

Flexible Sample Masks

To produce flexible samples, the previously applied parameters for the optical lithography remained unchanged. However, a new mask was designed (Figure 21) for samples sizes of a side length of 28 mm and a height of 40 mm.

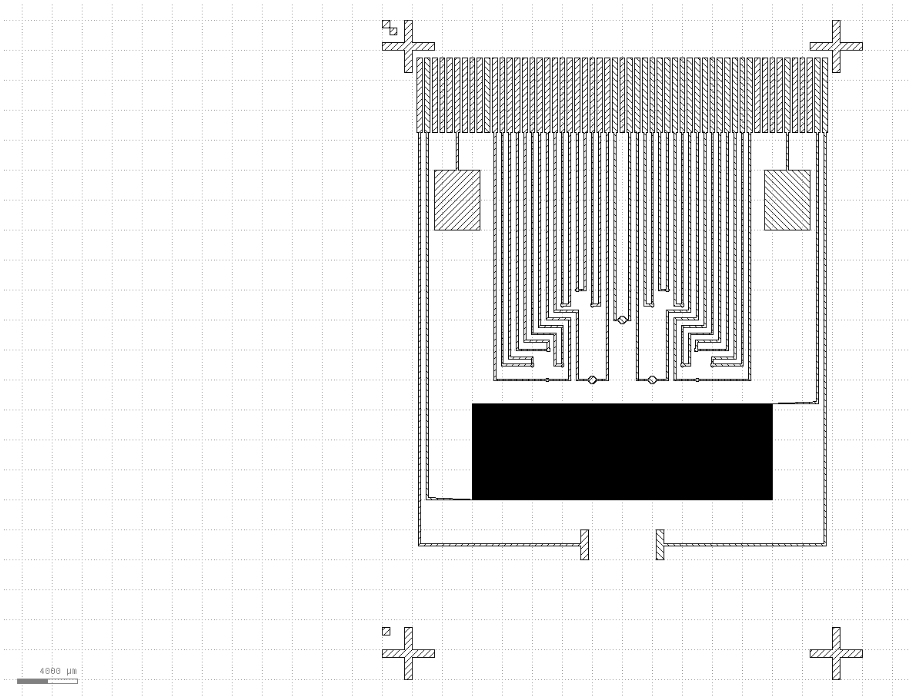

Figure 21: Mask Layout for flexible Samples

As with the non-flexible samples, there were also two etch masks required. The general layout of the etch mask is given in figure 22. The diameters of the electrodes in the first *Flex Mea Etching* mask are 250 µm and 500 µm, which are reduced to 200 µm and 400 µm in the second *Flex Mea Protection Mask*.

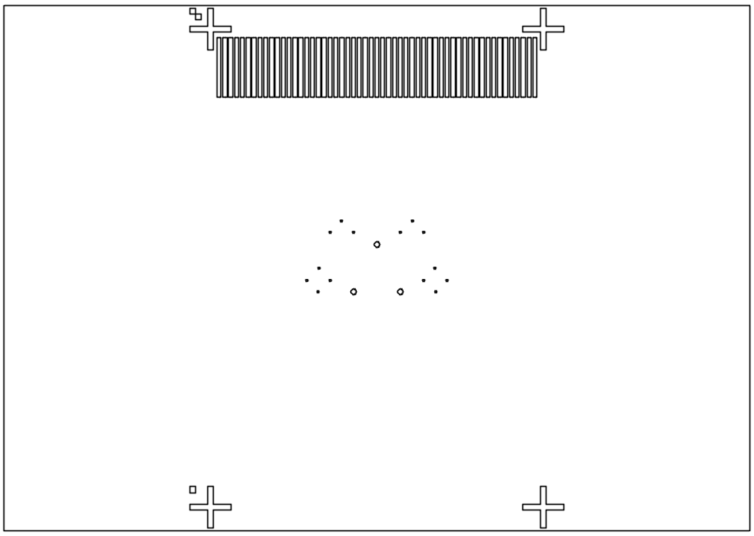

Figure 22: Flexible Sample Etching Mask called “Flex Mea Etching Mask”

In all three masks, orientation guides are provided by incorporating alignment markers in the outer edges. The distances between them are exactly 28 mm and 40 mm. This allows the precise alignment of the mask relative to the sample and therefore guarantees a correct position of the electrode openings onto the electrodes of the sample, created before by the flexible sample mask. The last three Chromium Masks for production of flexible samples were designed and manufactured as part of this thesis.

3.2.3. VAPOR DEPOSITION TECHNIQUES

The Pfeiffer PLS 570 is a vapor deposition machine, capable of holding two evaporation sources, and includes an electron beam physical vapor deposition (EBPVD) module (see chapter 2.2.2 for theoretical information). All electrode structures were produced via vapor deposition in this setup, whereby the gold layers were thermally evaporated from the prior mentioned (refer to chapter 3.1.2) gold nuggets out of an evaporation boat and the titanium adhesive layers were electron beam vapor deposited from a titanium target. By rotating the top plate with the samples attached, a (in situ) switch between thermal evaporation and EBPVD was possible.

In addition, a crystal oscillator with a Model 80 deposition controller from Telemark is positioned inside of the vacuum chamber to control the layer thickness while depositing takes place. As the oscillator was regionally separated from the samples, the material deposition rate it received differed from the one on the samples themselves. Thus, the material to be deposited must be selected in the crystal oscillator control software, which translates the deposition rate to the expected rate on the samples with an appropriate conversion factor[1]. Therefore, the end user does not have to cope with divergent material rates and is able to directly read the layer thickness out of the control software.

Thermal Evaporation

A tungsten evaporation boat (Umicore, Brussels, Belgium) was held in place within two evaporation brackets and filled with 2 to 3 gold nuggets. The samples were fixed to the rotating top plate with sample holders.

After establishing the base pressure of about $4 \cdot 10^{-7}$ mbar by evacuating the recipient chamber overnight[2], the gold nuggets were heated up by applying a current of 2.2 a.U.[3]. The rate was to be controlled with the crystal oscillator and was to be kept in the range of 5 – 11.0 nm/min, until the final layer thickness of 50 nm was reached.

Electron beam vapor deposition (EBPVD)

The titanium adhesive layers to the electrode circuitry were produced via electron beam vapor deposition before and after the gold was applied by thermal evaporation. A skillet, provided by Lisa$^+$, containing solid titanium of 99.95 % purity, served as a target material which was placed at the e-beam target.

All process parameters are summarized in table 7, consecutively.

---

[1] This conversion factor is commonly named “Tooling factor”

[2] A minimal evacuation time of 5 to 6 hours is needed

[3] Arbitrary Unit, as no readout possibility exists

Table 7: Vapor deposition process parameters

Process Parameter	**Unit**	**Gold Layer**	**Titanium Layer**
base pressure	mbar	$4 \cdot 10^{-7}$	$4 \cdot 10^{-7}$
process pressure	mbar	$2 \cdot 10^{-7}$	$2 \cdot 10^{-7}$
DC current	mA		60
	a.U	2.2	
DC voltage	kV	-[1]	9
DC power	kW	-[1]	0.56
deposition rate	nm/min	5 – 11	15 – 22
layer thickness	nm	50	10

To heat the target evenly, an electron beam was accelerated from the cathode by applying an accelerating DC Voltage of roughly 9 kV with a current of 60 mA, resulting in a DC power of 0.56 kW. The beam was also wobbled over the target in the x- and y- direction, which must be verified and, if necessary, corrected with the appropriate magnetic field regulators. The final layer thickness of 10 nm was reached with a deposition rate in the range of (15 – 22) nm/min.

3.2.4. SPUTTERING

The intermediate metal layers, consisting of titanium and gold, as well as the chromium for the etch masks were all sputtered in a Leybold Univex 300 device with two sputter sources, which could be switched during the process. The samples were placed face down opposite to the sputter targets onto a rotating metal plate, which acted as the counter electrode. By rotating the plate, the sample could be moved to face the desired sputter target.

The recipient was evacuated to a base pressure of about $9 \cdot 10^{-5}$ mbar, where an argon gas valve was opened, until a balance between gas flow and pump performance was achieved, which expressed itself in a stable process pressure of approximately $3.3 \cdot 10^{-3}$ mbar. With a missing mass flow meter, the process pressure (and the needed sputtering voltage for keeping the RF power constant), gave insight to the correct argon flow. To start the sputter process, an RF Power of 100 W was applied between the source and the

---

[1] Not applicable, as the only accessible parameter is the applied current (in a.U.)

samples. The needed voltage was then controlled by the argon flow, which may have had to be corrected with the needle valve.

With the etch deposition rates given (Table 8), 80 seconds for the gold layers and 120 seconds for the titanium layers created the desired layer thicknesses of 50 nm and 10 nm. In the case of sputtering the 100 nm thick titanium sacrificial layers, it took 20 minutes to reach the final layer thickness.

Table 8: Sputtering process parameters

Process Parameter	**Unit**	**Gold Layer**	**Titanium Layer**	**Chromium Etch Masks**
Base Pressure	mbar	$< 9 \cdot 10^{-5}$	$< 9 \cdot 10^{-5}$	$< 9 \cdot 10^{-5}$
Process Pressure	mbar	$\sim 3.3 \cdot 10^{-3}$	$\sim 3.3 \cdot 10^{-3}$	$\sim 3.3 \cdot 10^{-3}$
RF Power	Watt	100	100	100
Voltage	V	335	395	370
Time	sec	80	120 / 1200[1]	600
Layer Thickness	nm	50	10	100
Deposition Rate	$\frac{\mathrm{nm}}{(10\,\mathrm{min} \cdot 100\,\mathrm{W})}$	400	50	100

3.2.5. SPIN COATING POLYIMIDE AND TEMPERATURE CURING

The polyimide coating process started with defrosting the frozen polyimide 20 hours before use by placing it in the refrigerator at temperatures of approximately 8 °C.

The liquid, yet extremely viscous PI (see chapter 3.1.1 for material properties) was applied directly to the sample without the use of an adhesion promoter by pouring it slowly and controlled onto the sample until the sample surface was covered completely. While doing so, careful attention had to be paid to avoiding air inclusions in the liquid layer, by holding the vial close to the sample surface to minimize the air drop time. The sample itself was fixated to a Convac 1001 spin coater (see Chapter 3.2.1) via vacuum.

---

[1] The adhesive layer needs to be sputtered 2 minutes and the sacrificial layer 20 minutes

The spin coater parameters remained as laid out in chapter 3.2.2, which resulted in a 5 µm to 6 µm thick layer (Figure 23), as was given in the appropriate material data sheet [83].

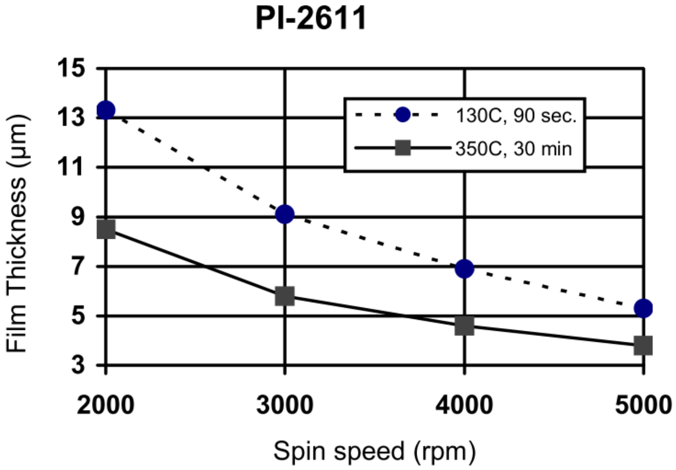

Figure 23: Final Polyimide Thickness, depending on the spin coating speed [83]

Two subsequent baking steps on a hotplate at 90 °C for 90 s, followed by 150 °C for also 90 s greatly decreased the polyimide's flow property and simplified the transportation of the samples. The polyimide covered samples were then placed on a glass tray and set into an oven with an inert atmosphere. The oven Heraeus Eurotherm 2404 (Thermo Scientific, Waltham, MA, USA) with a set nitrogen flow of 800 - 1000 sccm was programmed with a heating temperature ramp of 4 °C/min, until reaching the final temperature of 300 °C, which was then held for 30 minutes. Afterwards a cooling ramp of again 4 °C/min was programmed, which was, however, not reached as the oven itself was not actively cooled and well temperature isolated. As a result, the true cooling ramp was much slower and lasted up to 20 h (Figure 24).

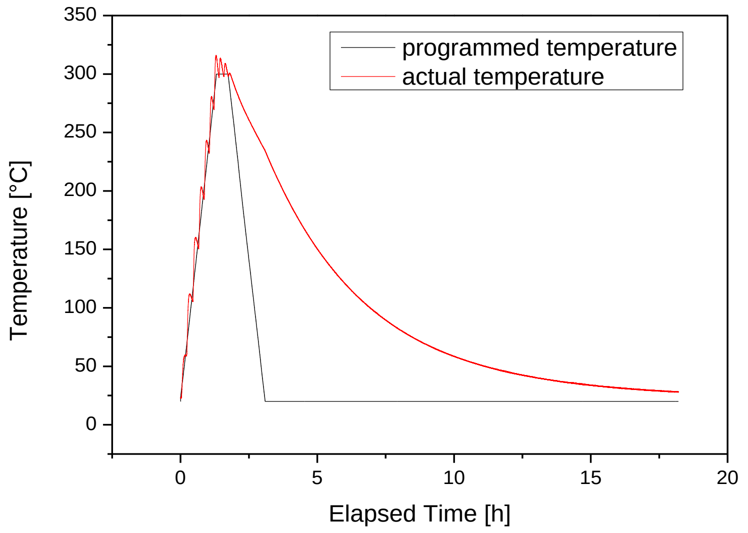

Figure 24: Temperature Ramp of the Polyimide Curing Process with the complete cooling time

3.2.6. PLASMA ETCHING BY RIE

Polyimide is easily etched with oxygen plasma. Plasma enhanced reactive ion etching (RIE) techniques were applied for opening the electrodes, as is industry standard for biomedical applications [123], [124]. A Plasmalab 80 Plus device (Oxford Instruments, Abingdon, Oxfordshire, UK), with several possible gas inlets, was used for etching polyimide and surface activation.

The samples to be etched were placed on the sample plate before evacuating the chamber to its base pressure of 10 mTorr. After reaching the base pressure, the oxygen flow was set to 100 %, which corresponded to a gas flow of 50 sccm, while holding the process pressure at 100 mTorr. The ignition of the oxygen plasma with an RF Power of 100 W started the etching process. All process parameters are listed in table 9.

Table 9: Plasma etching parameters

Parameter	Unit	Polyimide
Base Pressure	mTorr	10
Process Pressure	mTorr	100
RF Power	Watt	100
forwarded	Watt	99
reflected	Watt	0
DC Bias	V	- 395
Oxygen Flow	sccm	50

In the case of activating the sample surfaces, an etching time of 8 s was sufficient. A single polyimide layer, however, required 30 min to be completely etched. WIlliams et al. found a vertical etch rate of 370 nm/min with an RF Power at 400 W [125]. Thus, the etch rate with the parameters used in this work was examined and found to be around 250 nm/min (Figure 25). Etching smaller structures as the electrode openings took longer as described in chapter 4.1 and, thus, the successful electrode opening had to be verified after the etching process.

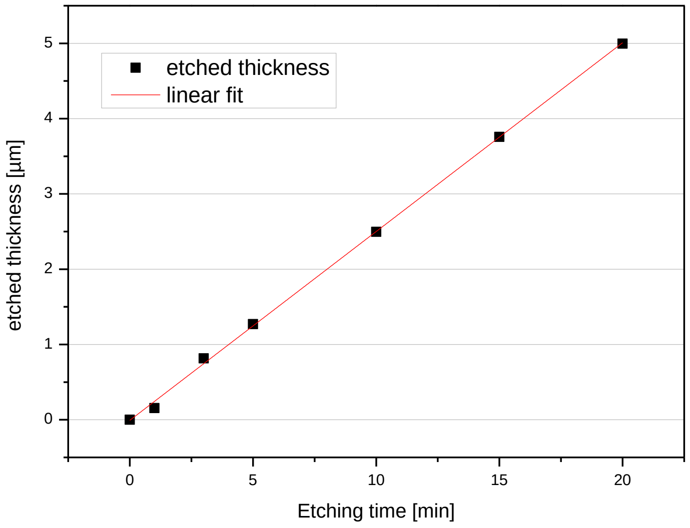

Figure 25: Etching rate of Polyimide 2611 in O2 Plasma

3.2.7. ATOMIC LAYER DEPOSITION

All thin films, deposited with Atomic Layer Deposition (ALD) were produced with a small lab-sized device of the type MyPlas from Plasma Electronic Gmbh (Figure 26) (Neuenburg, Germany) at the *Studienzentrum* Rottweil of the Hochschule Furtwangen, and produced by Michael Metzger.

Figure 26: ALD device used for fabricating electrode side wall passivation layers [126]

The recipient had a volume of 10 liters. The floor and ceiling inside the recipient represented the electrodes for the creation of the plasma, produced by an RF-Generator (13.56 MHz). Various process gases could be pumped into the device, such as oxygen which was not only used as a precursor, but also to initiate the plasma ignition. Argon was used for flushing the process gas (refer to chapter 2.2.5 for theoretical background on the ALD process), whereas nitrogen slowed down the turbo pump after a deposition process. (Paragraph based on [122])

The precursors for the TiO_2 Layers were TTIP (Titan(IV)-isopropoxid) and oxygen, respectively, with the chamber temperature set to 100 °C. With the humidity set to 20%, all parameters lead to a growth per cycle (GPC) of $0.044\,\frac{\mathrm{nm}}{\mathrm{cycle}}$ [127].

The resulting film thickness was controlled by placing an additional Si [111] Wafer into the chamber. Its film thickness was measured via reflectometry or ellipsometry, respectively, which was also done at the *Studienzentrum* in Rottweil. The process parameters are summarized in table 10.

Table 10: Process Parameters for Atomic Layer Deposition

Parameter	Unit	Parameter
Base Pressure	Pa	0.2
Temperature	°C	100
Precursor 1:		TTIP
Precursor 2:		O_2
Flush gas		Ar
GPC	$\frac{\mathrm{nm}}{\mathrm{cyclus}}$	0.044

3.2.8. ION BEAM ETCHING

The device used for ion beam etching (IBE) was an UniLab from Roth&Rau AG, provided by the Institute for Applied Physics from the university of Tubingen. The recipient was evacuated until a base pressure less than $5 \cdot 10^{-6}$ mbar was achieved, where an Argon process pressure of $1.2 \cdot 10^{-3}$ mbar was set via a mass flow controller. The sample itself sat on a rotating sample holder opposite to the ion source with a tilt angle of 0 °. The remaining etching parameters are listed below in table 11.

Table 11: Ion Beam Etching process parameters[1]

Process Parameter	Unit	Parameter
Base Pressure	mbar	$\sim 5 \cdot 10^{-6}$
Process Pressure	mbar	$1.2 \cdot 10^{-3}$
Ion Beam Current	mA	23
Ion Beam Voltage	V	302
Acceleration Voltage	V	700
resulting Current	mA	1 - 8
Cathode Current	mA	17.2
Cathode Voltage	V	11.4
Discharge Current	mA	1.65
Discharge Voltage	V	33
Mass Flow Controller	sccm	3.5 / 1.7
Rotation Angle	°	0
Rotation Speed	Hz	0.715

Determining an Etch rate was complex, as the addressed device showed great variances in the resulting etch rates. Also, the displayed parameters varied during a process.

Prior workgroups estimated the etching speed of several materials at varying parameters, resulting in different ion beam currents per time, called f-cup[2] (Table 12). The data shows the relative etch speed of different materials, even if the actual given speed is not applicable due to different f-cups.

Table 12: Etch rates in comparison with f-cups; Data from University of Tubingen

Material	Etch Rates at different f-cups $[\text{Å}/\text{min}]$			
	0.05	**0.10**	**0.15**	**0.20**
Au	176	352	528	704
Cr	39	78	117	156
Ti	20	39	59	78

---

[1] Given parameters are guidelines. The variance in between several etching processes must be considered.

[2] Parameter of measuring the ion beam intensity (device specific)

The real etch rate of Cr and TiO_2 was measured and resulted to approx. 2 $\frac{\mathrm{nm}}{\mathrm{min}}$ for Cr and 0.7 $\frac{\mathrm{nm}}{\mathrm{min}}$ for TiO_2, respectively[1]. Overall, the etching process had to be monitored precisely and the etching process had to be controlled frequently.

---

[1] using a Dektak 3030ST Auto Surface Texture Profiler

4. RESULTS AND DISCUSSION

This chapter describes and discusses all results gained during this thesis, starting with the sample manufacturing in chapter 4.1, based on the prior introduced fabrication processes. Analysis of the produced samples was done in two self-designed and built setups, both introduced and discussed in chapter 4.2, before the samples are assessed in chapter 4.3.

The use of TiO_2 as electrode side wall passivation is discussed in chapter 4.4, the samples are characterized in the final chapter.

4.1. FABRICATION OF DEVICES

All samples can be roughly divided into the non-flexible multi electrode array group (MEA) or the flexible multi electrode array ones (Flex-MEA), which differ in some manufacturing steps.

In all samples, the gold layer thickness was chosen to be 50 nm, since gold layers thinner than 12 nm do not provide a uniform surface layer (see chapter 3.1.2). A thickness of 50 nm, however, is a good compromise for a guaranteed closed gold surface, while being thin enough for reasonable material usage and maintaining film-flexibility which is a necessity for later measurements. Also, the critical current density of gold amounts to $5 \cdot 10^4 \frac{\mathrm{A}}{\mathrm{cm}^2}$, before surface arrangements and, therefore, negative processes occur [128]. The thinnest circuit path, altogether, is the strain gauge with a width of 20 µm. Thus, a maximal bearable current of 0.05 A can be calculated. As the Keithley's 6517B ammeter upper limit amounts to 0.01 A (refer to chapter 4.1.3 for more information on the setups), which was only reached in case of an electrical short-circuit, gold layer thicknesses of 50 nm were sufficient.

Titanium was chosen as adhesive layer, as gold does not stick well to silicones and polyimides [129], but begins to cluster when heated up way before reaching the melting point (chapter 3.1.2). Good adhesion is only given by interlocking, interdiffusion of the films or chemical bonding between thin films [130]. In case of a Ti layer, diffusion through the Au layer is given, by creating brittle intermetallic phases, such as $TiAu_2$, TiAu and Ti_3Au [131]. Together with the possibility of processing Ti layers in-situ next to Au, this circumstance lead to the choice of Ti as adhesive material.

4.1.1. NON-FLEXIBLE MULTILAYER SAMPLES

No lithographic protocols were established beforehand and every single process had to be established. Early photolithographic produced metal structures had frayed edges and the lift-of process worked reproducibly terrible, leaving resist residues behind. After switching from the negative resist ma-N 2400 from HD Microresist Technology to the positive resist ma-P 1205, the developing and lift-of processes worked well.

All produced samples use 4 inch wide, double side polished Borofloat 33 glass from Siegert Wafer as a substrate material, on which the following multilayer stack is built. The metal layer, containing the electrodes is produced via thermal vapor deposition (Figure 27b), as described in chapter 3.2.3, after the structure itself is established via the photolithography protocol (Appendix A) from chapter 3.2.1 (Figure 27a).

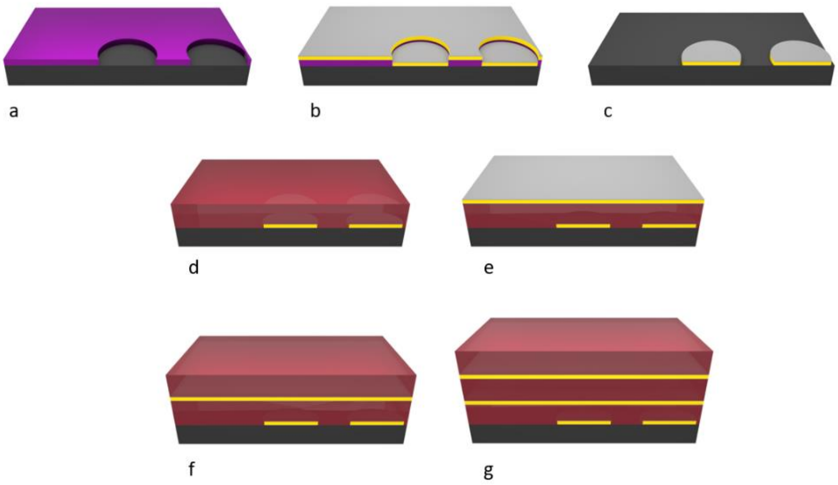

Figure 27: Manufacturing of unopened multilayer samples

After removal of the resist via acetone in an ultra-sonic bath, the sample with the finished electrode structure (Figure 27c) was cleaned with isopropanol. Until now, the wafer could be processed as a whole. However, as the curing oven for the following polyimide process was only about 5 cm wide, the wafer with the 3x3 matrix of electrode structures were separated with a dicing saw, as described in chapter 3.2.1 (Figure 28). In addition, before spin coating the first polyimide layer, the surface was activated in oxygen plasma for 8 s, as described in chapter 3.2.6 and following the recommendations of prior literature. [132], [133]

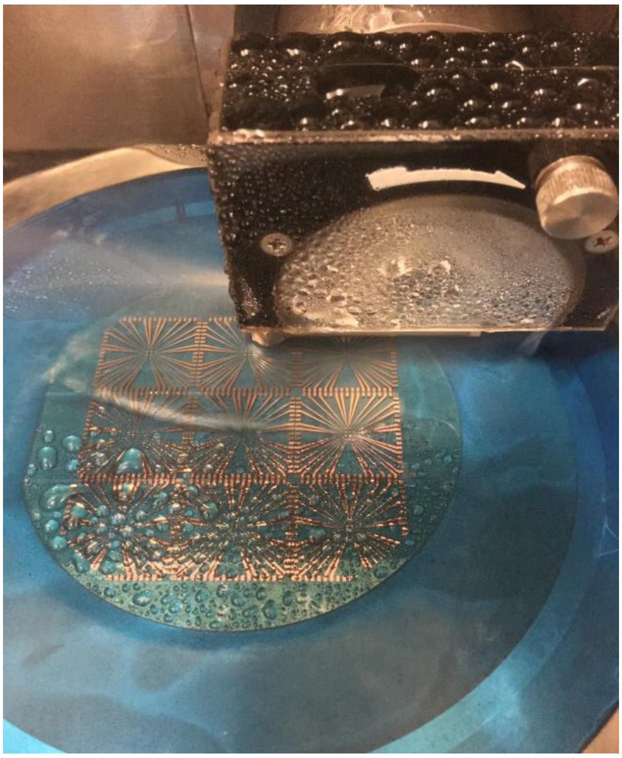

Figure 28: separating the 1 inch samples from the 4 inch wafer with the dicing saw

The following PI layer was fabricated as described in chapter 3.2.5 (Figure 27d). Although HD Microsystems recommends a curing temperature of 350 °C and the usage of an adhesion promoter prior to the distribution of the polyimide, investigations and observations of several parameter variations, lead to the concluding use of a final temperature of 300 °C, as the amount of air inclusions was reduced significantly, and film uniformity looked promising. Also, the application of an adhesion promoter had a disadvantageous effect on the photolithographically processed circuitry and was, thus, excluded. No negative side-effects were observed due to this decision and a uniform polyimide layer could be produced.

Remaining air inclusions on some samples are explained in the work of Shaffer et al. [134], who investigated the stability of titanium adhesive layers at elevated temperatures such as 300 °C. They observed the lack of stability of the self-formed oxide layer, which could lead to oxide inclusions in the upper polyimide layers. This could have been circumvented by very careful oxygen-plasma treatment of the titanium adhesive layers (for adhesion discussion, please refer to chapter 4.3.1).

PI 2611 was chosen over PI 2610 because of its resulting film thicknesses in the ranges of several µm due to its higher viscosity (table 5). This lead to sufficiently high electrode side walls to analyze the electrode side wall passivation. In addition, a minimal sample thickness of about 10 - 15 µm was required for flexible substrates to electrically contact them as discussed in chapter 4.2.2. Also, by comparing it to other possible polyimides (table 6), the lower moisture uptake can be noticed, which resulted in less delamination and prevented negative electrical features like corrosion more reliable. The better (lower) thermal expansion as well as film stress added to the recommendation of its use over the other possible products. [79], [135], [136]

Adding another metal layer stack to the sample via sputtering techniques, again consisting of Ti, Au, Ti (Figure 27e) and repeating the polyimide coating (Figure 27f) twice, finally created the finished multi-layer sample (Figure 27g).

Both intermediate metal layers were created with aluminum shadow masks, which partly covered the sample to protect the contact pads. The dimensions of the produced shadow mask can be taken from figure 29 with the corresponding mask holder being displayed in the appendix E and in figure 30.

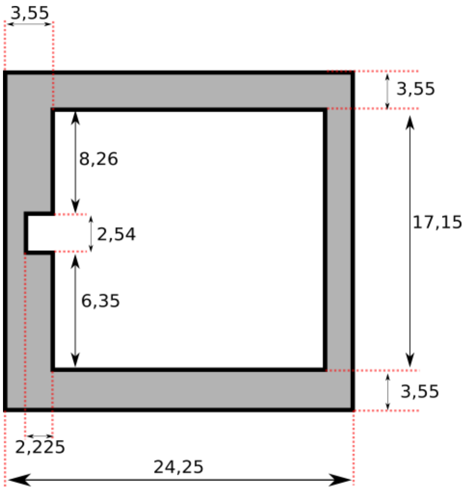

Figure 29: Aluminum shadow mask with the parameters given in mm

The placing of the gap in the mask was calculated in such a way, that the free contact pads 24-26 and 60-62, (see figure 36 for electrode and contact pad layout and table 13 for pad usage) were covered by the sputtered layer. The gap in the mask was necessary for creating an electrical contact possibility to the metal layers, as can be seen in the final sample (Figure 31) and is sketched in figure 32.

The recesses of the sample holder are 2 mm deep, which gave the 1 mm thick substrate glass sample room to sit alongside with the 1 mm thick sputter mask. One also notices the coverage of the contact pads of the electrode structure in figure 31 (right picture), which ensured that no metal was sputtered on them. As a result, the contact pads would later be only covered with polyimide, which was easily etchable with RIE (refer to chapter 3.2.6).

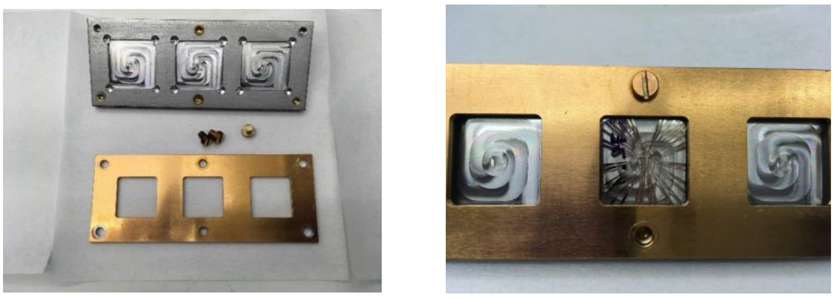

Figure 30: sputter sample holder (left) with sampled mounted inside (right)

After adding a polyimide layer, like the one underneath the metal layer, the aluminum mask was rotated by 90° in either direction for the creation of the top of the two intermediate metal layers, thus, creating two accessible, not overlapping contact pads to the intermediate layers (Figure 31, left image). The opening of the pads of the intermediate layers was done via RIE with etching times of 45 minutes for the top layer and 75 minutes for the lower one, respectively. 5 µm of polyimide is etched in 30 minutes according to the etching rate of 250 nm/min. However, it was noticed, that adding another 15 minutes cleaned the metal surface of residues and guaranteed a good electrical contact, which was achieved by filling the opened hole with conductive silver DAG 1415 (Plano GmbH, Wetzlar, Germany). In the case for the unopened samples, also single electrode contact pads were opened via an aluminum hard mask, containing a hole with 1 mm in diameter, which was placed over the respective pad.

Opening the electrodes:

Unopened samples gave many research opportunities, regarding the stability and delamination of the polyimide passivation layers, as is described in chapter 4.3. As the focus remained on the electrode side wall passivation, the electrodes had to be opened, resulting in a side wall with electrical contact possibilities due to the two intermediate metal layers, forming two ring-electrodes (see figure 32 and the final sample in the right of figure 31).

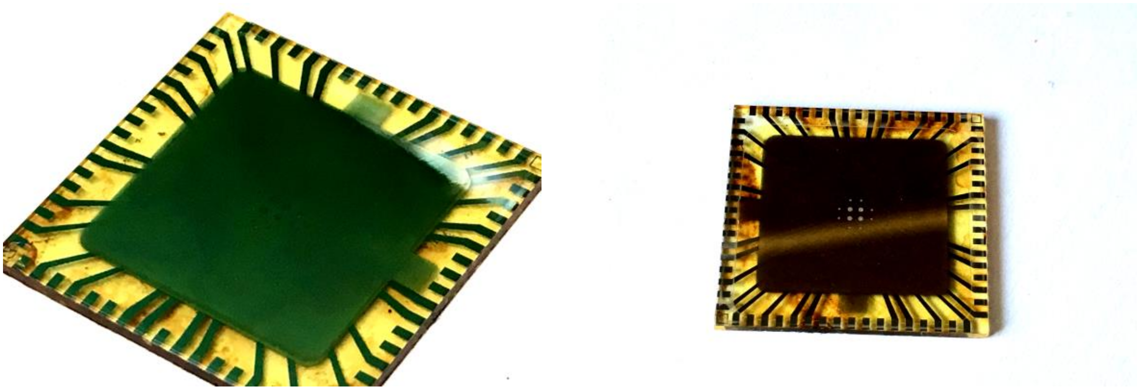

Figure 31: (left) finished 1 in non-flexible sample with the multilayer stack;
(right) similar sample, with electrodes opened

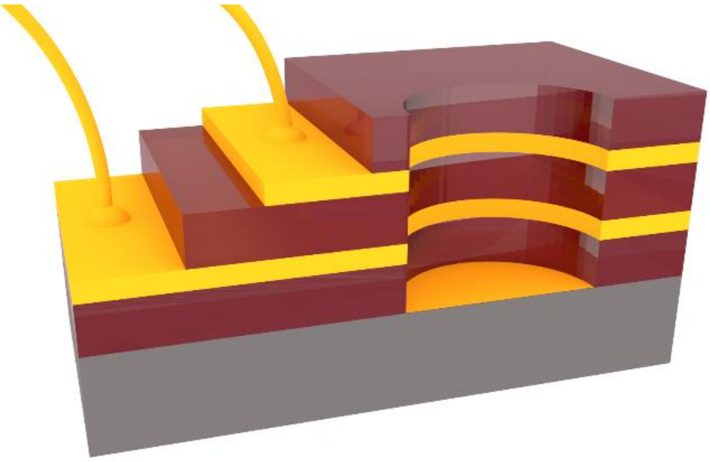

Figure 32: Schematic Image of a (opened) Multilayer System with electrical contacts to the inner metal layers (golden), which sit in between the polyimide passivation layers (red)

A photolithographic mask introduced in chapter 3.2.2, covering only the electrode openings, was created. With it, a 100 nm thick chromium layer was sputtered onto the samples. After lift-off, the complete sample was covered with chromium, excluding holes with the electrodes beneath. Etching the first polyimide layer was easily possible as described.

However, the two intermediate metal layers were now also to be etched through. Early investigations of etching the gold layers with aqua regia ($HNO_3 + 3HCl$) [125], [137] and Lugol's iodine [138] failed, due to the enveloping titanium layers with their extremely stable and inert thin oxide film (refer to chapter 3.1.2). Thus, the titanium layer was first etched with NH_4F (chapter 3.1.3), with a following aqua regia etch process for the gold layer. A final etch with

NH_4F dissolved the underlying titanium layer. Before etching, the Chromium Mask was removed with TechniEtch Cr01, and again applied after etching, in order to etch the next polyimide layer. Trials in this direction were given up quickly, as NH_4F showed great under etching potential and began to dissolve the metal layers underneath the polyimide. In addition, by etching the second metal layer, the opened top metal layer was further etched and thus destroyed.

As a result, the manufacturing process of the unopened samples (Figure 27) was slightly adapted to a complete bottom-up process and now contained recurring photolithographic steps in order to create electrode openings in the intermediate metal layers, as seen in figure 33. Starting with the photolithography (Figure 33a) of the electrodes, fabricating them by vapor deposition (Figure 33b) with a following lift-of step (Figure 33c), still remained the same. Also, the following polyimide process (Figure 33d) was equal to the unopened sample. However, before creating the first intermediate metal layer, the electrode openings were covered with resist (Figure 33f) with the help of the *ALD Etching Mask* (Figure 33e). Sputtering the metal layer (Figure 33g) and lifting the resist (Figure 33h) now created a layer, where only polyimide existed on top of the electrodes. The polyimide layer (Figure 33i) was applied as before. Steps e) to i) were repeated to obtain the final layer stack (Figure 33j).

As now only polyimide was located on top of the electrodes in the bottom layer, they could easily be opened (Figure 33l) with one aluminum etching mask (Figure 33l), created just like the metal layers.

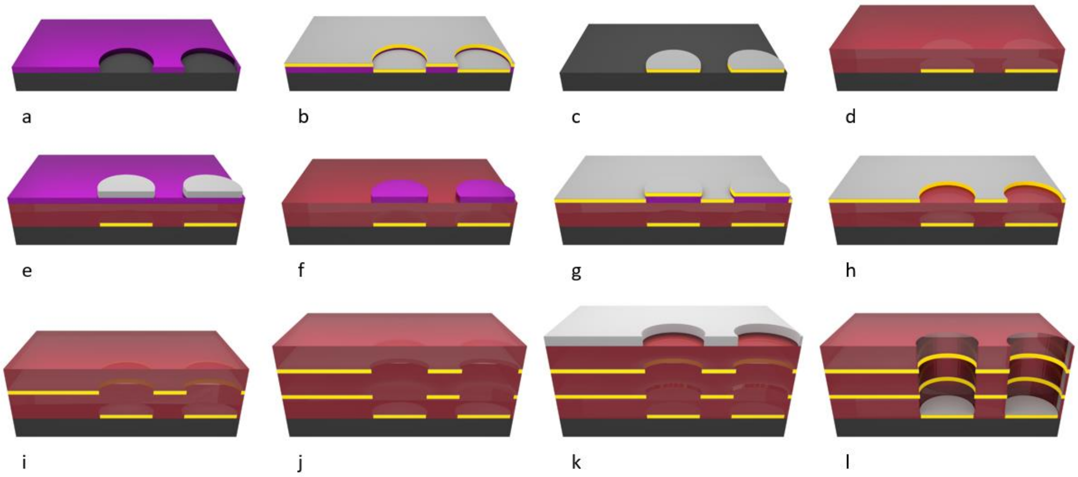

Figure 33: Manufacturing of the opened multi-layer samples

However, as manual alignment of the photolithographic masks was done more than once, the openings of the metal layers are likely to differ from the electrode structures due to misalignment. Figure 34 displays optical microscopy images (Zeiss Axio Scope, with an attached CCD Axiocam from Zeiss, Jena, Germany) of the 250 µm electrode of an opened sample. The upper (1) and middle gold layers (2) are visibly misaligned against the electrode beneath (3). The polyimide layers themselves are not visible due to them being optically translucent.

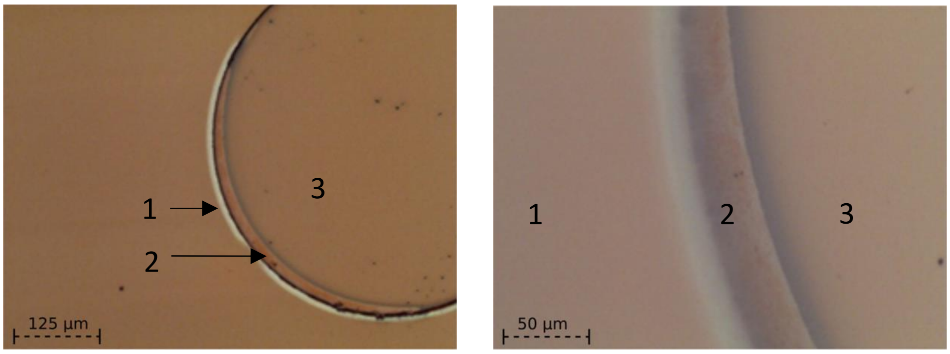

Figure 34: misalignment on the photolithographic process

The newly created circle segment surface is shortly discussed in relationship to the angular side wall electrode surface with basic trigonometrical consideration.

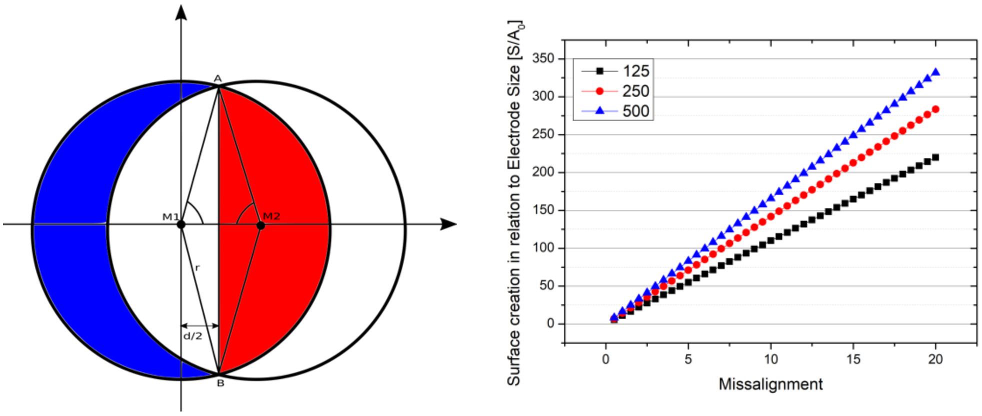

Figure 35 left: trigonometrical schema for misalignment surface calculation;
right: newly created surface S (marked blue in left image) in relation to side wall surface A_0 of the intermediate layers

With the sketch in figure 35 and the angle $\alpha =< \overline{BM_1A}$ follows $\frac{\alpha}{2} = \cos^{-1}\left(\frac{d}{2r}\right)$ with d as the misalignment during photolithography. As such follows

$$S = \pi\, r^2 - \left(\frac{r^2}{2} \cdot \left(2\cos^{-1}\left(\frac{d}{2r}\right) - \sin\left(2\cos^{-1}\left(\frac{d}{2r}\right)\right)\right)\right) \tag{30}$$

for S as the marked blue surface.

Also, in figure 35, S is plotted in relation to the electrode side wall surface of three electrode radii plotted against the misalignment in µm, showing that a slight misalignment of only 10 µm leads to a surface expansion of at least 2 magnitudes.

If the electrode side wall passivation covers the misaligned side wall completely, the only obvious disadvantage is an enhanced circular side wall electrode surface, which prohibits analytical calculation of reference values.

The final pin layout of the non-flexible samples is shown in figure 36 with the electrodes numbered consecutively. Table 13 lists every electrode with the respective pin for electrical contact. The main gap between pad 6 and 12 clearly marks one side of the sample, which was defined as the top side.

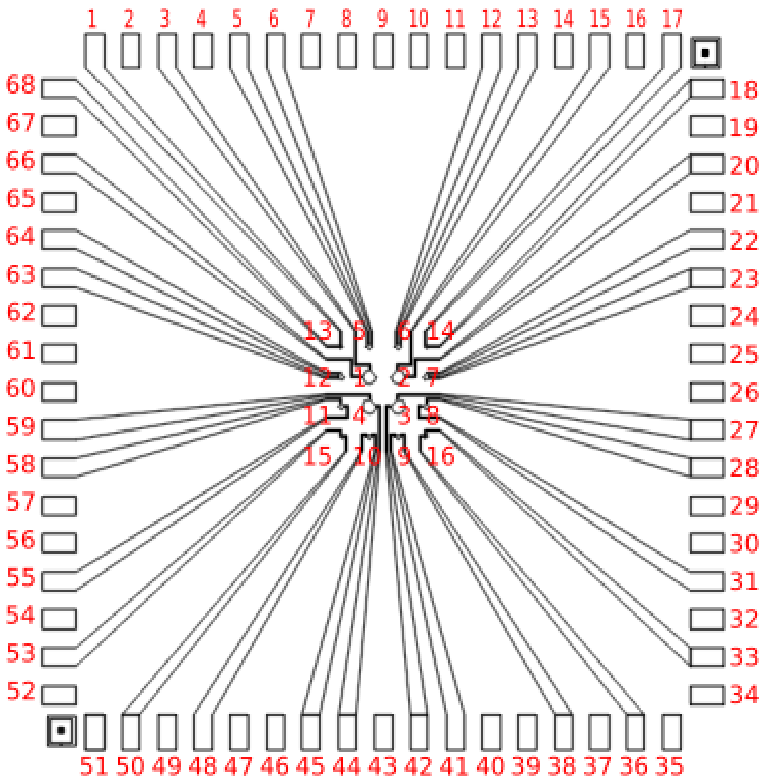

Figure 36: Numbered electrode and pin layout of a produced MEA

Table 13: Pin Layout of non-flexible samples

Pin No.	Function	Pin No.	Function
66 + 3	Electrode 1	38 + 41	Electrode 9
15 + 20	Electrode 2	45 + 48	Electrode 10
27 + 42	Electrode 3	55 + 58	Electrode 11
44 + 59	Electrode 4	63 + 64	Electrode 12
5 + 6	Electrode 5	68 + 1	Electrode 13
12 + 13	Electrode 6	17 + 18	Electrode 14
22 + 23	Electrode 7	33 + 36	Electrode 15
28 + 31	Electrode 8	50 + 53	Electrode 16

4.1.2. FLEXIBLE POLYIMIDE SAMPLES AND ELECTRODE LAYOUT

Flexible layers were created upon plane glass wafer, from which they were separated at some point during the fabrication process. As such, the use of a sacrificial layer was enforced, which was dissolved later on during the manufacturing process, in order to release the flexible multilayer-stack [139]–[142]. Stieglitz even proposes using polyimide itself as a sacrificial layer, which is peeled off a stiff substrate material. [143]

Following the concept of producing the layer stack on top of a sacrificial layer, flexible samples, were built on a 100 nm thick layer of chromium, sputtered before the deposition of the first polyimide layer. As removal of chromium with TechniEtch Cr01 left the other materials untouched, this procedure promised good results. TechniEtch Cr01 provides great vertical etch capabilities, however, the horizontal under etching of the underlying chromium layer was slow and impracticable.

Also, directly peeling the PI off the samples induced tension, resulting in curled thin films, which were already mechanically loaded and, thus, not quantifiable.

Trying to finally dissolve the glass substrate itself with pure HF, lead to the idea of a titanium sacrificial layer, which showed sufficient etching rates in NH_4F. In addition, NH_4F was easier to handle than HF and is known for its under-etching capabilities. The 100 nm thick titanium layer gave a big enough exposed surface to the chemical, such that the samples' sacrificial layers were dissolved within 48 hours by NH_4F.

The resulting manufacturing process for the Flex-Mea is displayed in figure 37, starting with the sputtering of 100 nm of Ti onto the glass substrate (a). As this layer was to be dissolved later, no surface activations and therefore adhesion improving techniques were used. The following polyimide coating (b) was done as introduced in chapter 3.2.5. Figure 37c displays the patterning of the positive resist MaP-1205 with the photolithographic Flex-Mask, which was self-designed and produced. After the resist was developed (d), the circuitry, again consisting of 10 nm Ti, 50 nm Au and 10 nm Ti, was vapor deposited, leaving only the electrode structure behind after a lift off (f). The topping polyimide layer was done just as the one beneath and is seen in figure 37g. Finally, the sacrificial titanium layer was dissolved, leaving only the flexible layer stack behind (h).

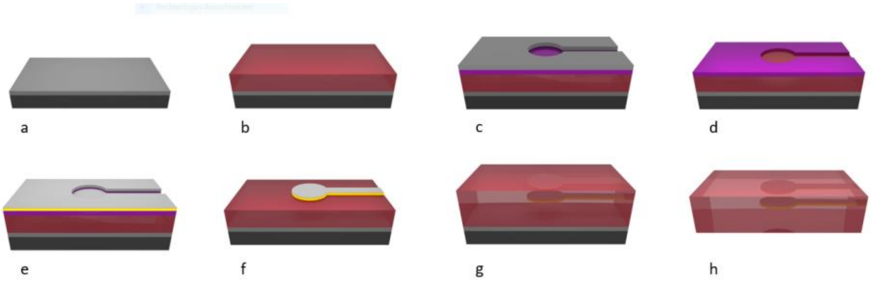

Figure 37: Sketch Images of the manufacturing process of the flexible polyimide test device

A finished and lifted Flex-Mea can be seen in figure 38. The influence of the NH_4F on the PI and the circuity encapsulated in it are discussed in chapter 4.3.4.

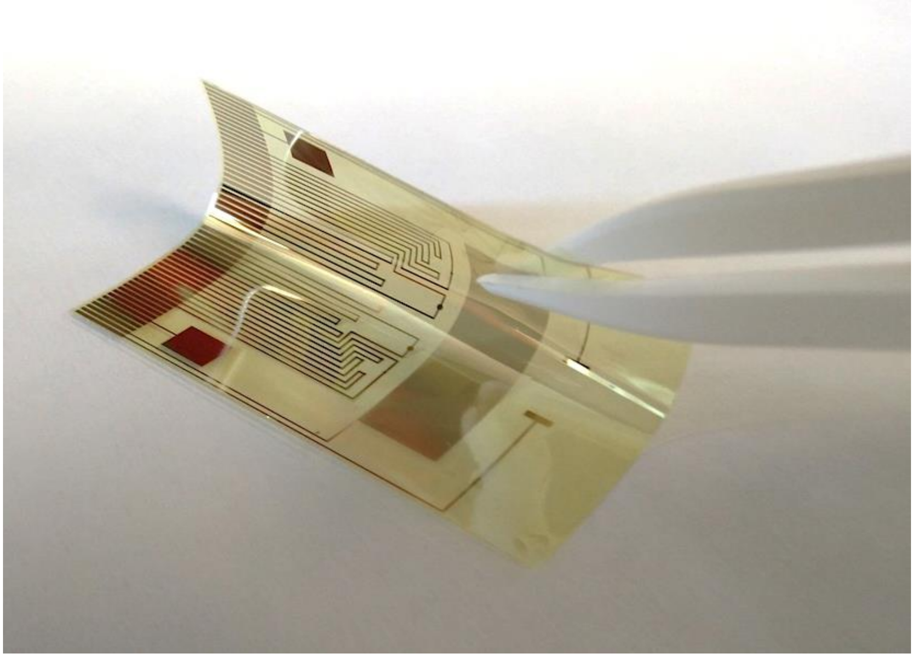

Figure 38: Self-made Flex-Mea Sample on Polyimide Base

Opening the electrodes of the flexible substrates

As the samples had to be removed from the substrate prior to opening the electrodes via RIE, since the NH_4F would also dissolve the titanium adhesive layers, a methodology had to be found to further process the sample. Chapter 4.1.1, together with the process characterization in chapter 3.2.6, describes the etching of polyimide with the help of a chromium etch mask. The layout to be etched was produced via photolithographic processes, which was not feasible with a flexible sample.

A solution was found by applying a WF-20-X4-A (Gel-Pak, Hayward, California, USA) gel film to a non-flexible aluminum substrate. The gel film itself is mounted to a metalized polyester substrate, with pressure sensitive adhesive located at the bottom side [144]. The product is capable of withstanding temperatures up to 150 °C and was found to be chemically inert to TechniEtch Cr01, as well as acetone and isopropanol.

By placing the pressure sensitive adhesive side of the gel-film to a firm aluminum plate, the flexible PI sample was held by the tacky gel surface (Figure 39a). The aluminum substrate with the attached sample could now be processed again as described before. By applying the layout of the *Flex Mea Etching Mask* (refer to figure 22 in chapter 3.2.2) with the standard lithography procedure, a chromium etching mask was sputtered (Figure 39b). An enlarged image of a PI covered electrode with the applied chromium etch mask is seen in figure 39c. Opening the electrode was done via RIE (refer to chapter 3.2.6) with an etching time of 30 minutes. After removal of the chromium etch mask with TechniEtch Cr01, the flexible sample with opened electrodes (Figure 39d), could be peeled off the gel film.

The opened electrodes showed residues, which were not easily removable. These are discussed and described in a separate chapter 4.3.2.

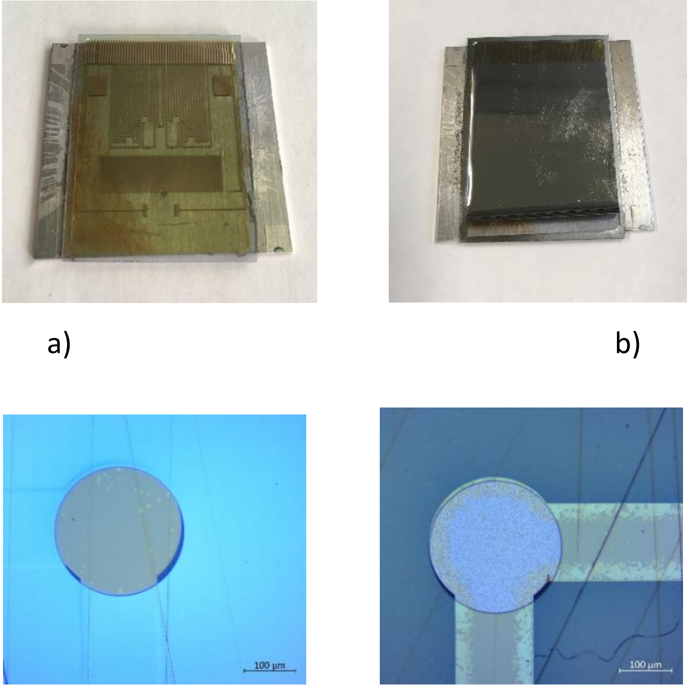

a) b)

c) d)

Figure 39: Etching electrodes of adhered flexible sample

Layout

Figure 40 demonstrates the flexibility of the Flex-Mea. Its circuitry layout was carefully designed and produced with a custom made photolithographic mask, displayed in figure 41.

The mask was adapted for the fluidic-measurement setup, which is introduced in chapter 4.2. The main idea behind the layout was to place all active elements, such as electrodes, the capacitor and a strain gauge inside of a circle with a diameter of 24 mm, as this is the mechanically loaded area in the measurement setup, introduced in chapter 4.2.

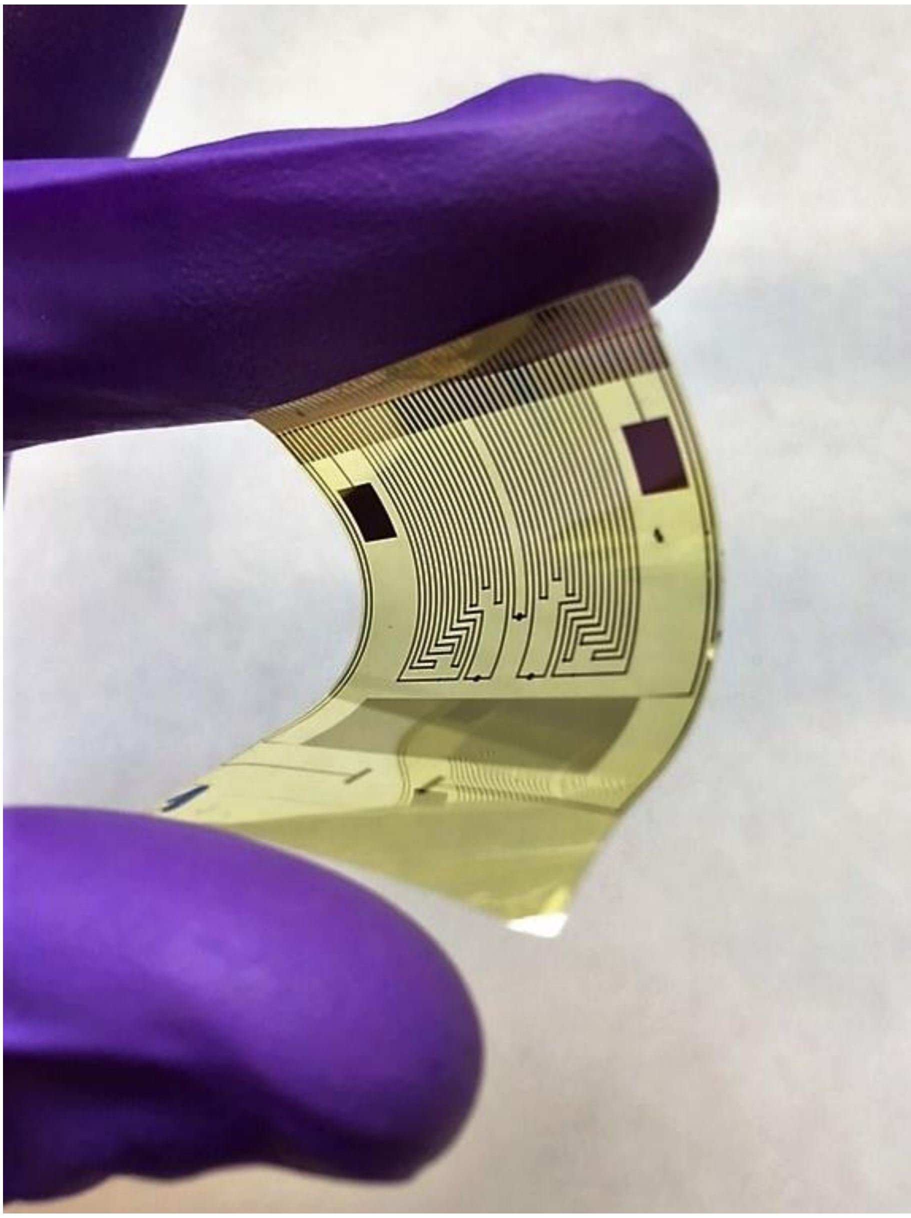

Figure 40: Demonstrating the flexibility of the Flex-Mea

All contact pads were required to sit on one side of the sample, to maximize the flexible area without interfering with external connectors. By using a standard Xf2M-55 connector (Omron, Stuttgart, Germany), 55 contact pads within a length of 28 mm were contactable. The height of the mask, and therefore the sample, was set to 40 mm. Having a fixed limit of 55 contact pads, it was possible to include 17 electrodes with diameters of 250 µm and 500 µm, respectively, and a lead as well as an outlet, two via pads for creation of 3 dimensional structures, a strain gauge and a capacitor. Both, the strain gauge and the capacitor, were intended to be used for monitoring the flexibility of the sample.

Opening the bond pads

One of the Flex-Mea passivating polyimide layers had to be opened over the bond pads, to ensure electrical contact. Therefore, the sample was covered with a silicon wafer, leaving only the contacts exposed. A following RIE (refer to chapter 3.2.6) etch process of 30 min eliminated one passivating PI layer over the contacts.

Table 14 lists the function of every contact pad of a finished flexible sample with the final layout being displayed in figure 43.

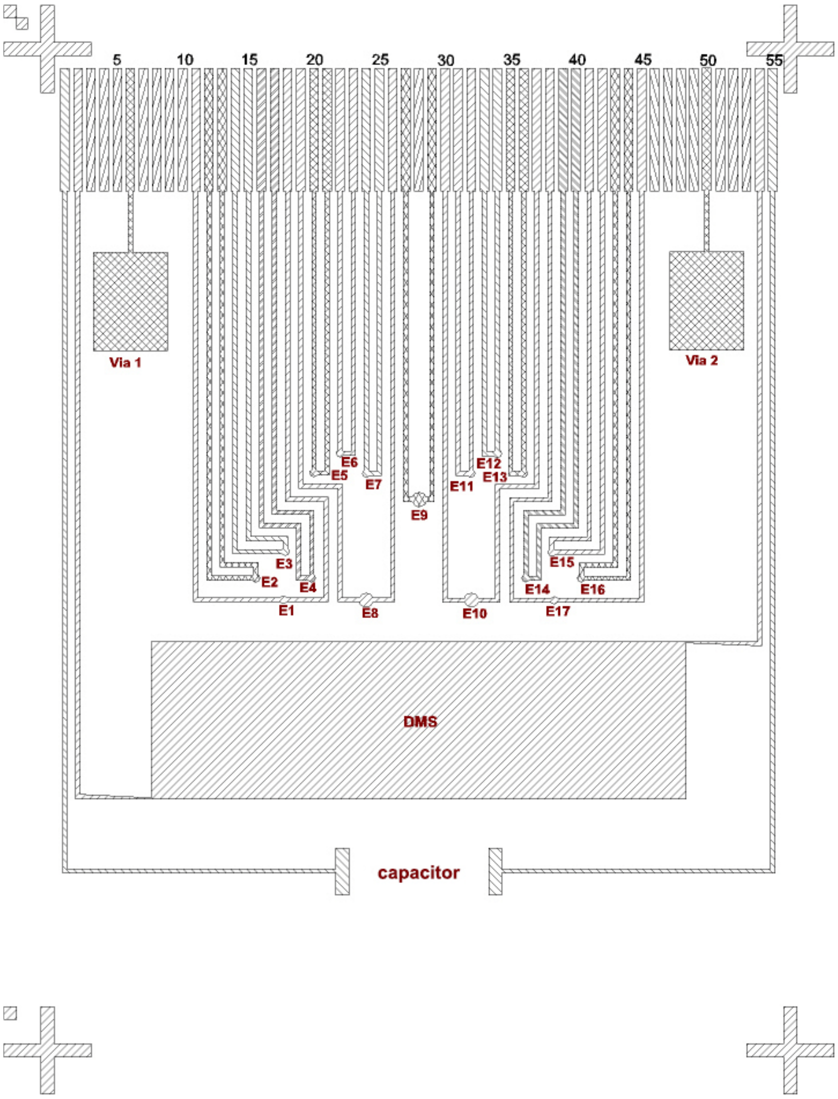

Figure 41: Circuitry Layout of the flexible mask; The respective Pad assignment is listed in table 14

Table 14: Electrode Numbers of flexible mask

Pin No.	Function	Pin No.	Function	Pin No.	Function
1 + 55	Capacitor	11 + 18	Electrode 1	30 + 37	Electrode 10
2 + 54	Strain gauge	12 + 13	Electrode 2	31 + 32	Electrode 11
6	Via1	14 + 15	Electrode 3	33 + 34	Electrode 12
50	Via2	16 + 17	Electrode 4	35 + 36	Electrode 13
3, 4, 5	Not used	20 + 21	Electrode 5	39 + 40	Electrode 14
7, 8, 9, 10	Not used	22 + 23	Electrode 6	41 + 42	Electrode 15
28	Not used	24 + 25	Electrode 7	43 + 44	Electrode 16
46, 47, 48, 49	Not used	19 + 26	Electrode 8	38 + 45	Electrode 17
51, 52, 53	Not used	27 + 29	Electrode 9		

The strain gauge itself, contains 160 loops, each being 20 mm long and 20 µm wide with 20 µm of space between them. The resulting total length of the strain gauge, therefore, amounts to 320 cm.

With the strain gauge principles from chapter 2.3.4 in mind, the dimensions of the DMS are calculated with the introduced equation (21) on page 29 while considering various boundary conditions. The DC Ammeter Keithley 6517B (refer to chapter 4.2 for introduction and more information) offered a maximum resolution of 10 pA while measuring in the 2 µA range. The resulting resistance of the strain gauge is calculated to be within this range. While being able to reproducibly create photolithographic structures down to 20 µm, the following dimensions were determined for the strain gauge:

$$l_z = 28.5 \text{ mm} \,; l_g = 20 \text{ mm}; d_g = 0.02 \text{ mm}; b_g = 20 \text{ µm}; h_g = 100 \text{ nm}^{1}; n = 160$$

As the density of thin films does not correspond to the one of bulk materials, ρ_{Gold} is taken from [145], thus amounting to $\rho_{\text{Gold}} = 40 \text{ µ}\Omega \cdot \text{cm}$, instead of $\rho_{\text{Gold bulk}} = 2.4 \text{ µ}\Omega \cdot \text{cm}$. With these chosen parameters, the strain gauge resistance is calculated to $R_{\text{DMS}} = 652 \text{ k}\Omega$.

As almost all measurements were to be performed within a voltage range of ±1 V to stay within the water window of PBS, the expected current is simply calculated using ohms' law, resulting in a current of $I_{\text{DMS, calc}} = 1.5 \text{ µ}A$, which is at the upper end of the measurement range, but safely within the limits. Thus, a potentially measurable resistance variance can be estimated as: [146]

$$\frac{\Delta I_{\max}}{I_{\text{DMS,calc}}} = \frac{10 \text{ pA}}{1.5 \text{ µA}} = \frac{\Delta R_{\text{DMS}}}{R_{\text{DMS,calc}}} \tag{31}$$

Formula (22) from chapter 2.3.4, together with the then given k-factor of 2.6 (Table 4 in chapter 2.3.4) leads to a calculable minimal possible measurable, longitudinal elongation for this particular strain gauge:

---

[1] Early design decisions assumed a layer height of 100 nm. This was corrected to 50 nm later, which results in a factor 2 for the final calculated resistance and, thus, calculates to $R_{\text{DMS}} = 1.304 \text{ M}\Omega$

$$\varepsilon_l = \frac{\frac{\Delta R_{\mathrm{DMS}}}{R_{\mathrm{DMS}}}}{k_{\mathrm{Gold}}} = 2.56 \cdot 10^{-6} \tag{32}$$

Thus totals in approx. $\varepsilon_l \approx 0.000\,26\,\%$ and can be further translated in a minimal length difference of $\Delta l_{\mathrm{min}} = l_0 \cdot \varepsilon_l = 61\ \mathrm{nm}$ with l_0 amounting to an effective substrate width of 24 mm (refer to chapter 4.2 for discussion on substrate area, which is effectively mechanically loaded), measurable with the given Ammeter. [147]

An optical image of a produced strain gauge on a flexible sample is given in figure 42 (with the feed line visible in the left image). Chapter 4.3.7 discusses the measurements, after the setup has been introduced.

Figure 42 also shows starting delamination over the metal circuitry. This unwanted phenomenon is addressed and discussed in chapter 4.3.1.

The bottom capacitive structure was meant to measure the electrical capacities to the intermediate metal layers. However, the outer feed lines #1 and #55 were defective on every sample due to the lifting process in HF, as can also be seen in figure 43.

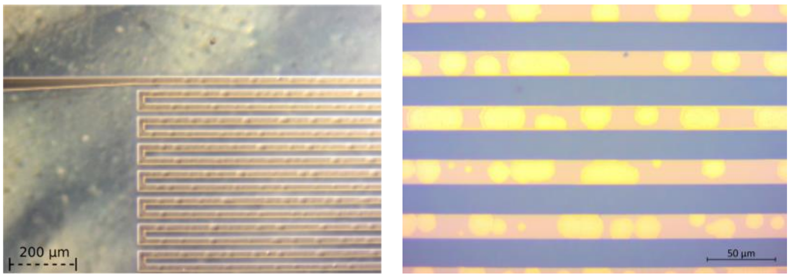

Figure 42: optical Image of the produced strain gauge with 20 microns wide leads (left) and an enlarged view of the strain gauge with visible delamination (right)

4.1.3. FLEXIBLE MULTI-LAYER SAMPLES

The concept of the multilayer samples introduced in chapter 4.1.1 had to be translated to the flexible samples to gain electrical access to the electrode side walls. By combining the bottom-up manufacturing method of the flexible samples with the multilayer stack of the non-flexible samples, a multilayer flexible sample was achieved which can be seen in figure 43 and figure 44.

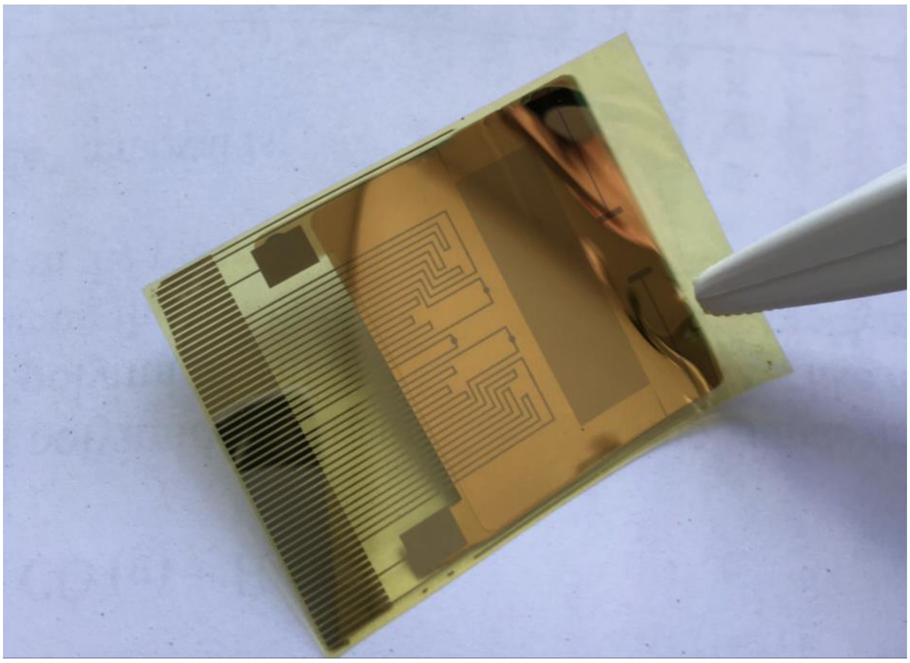

Figure 43: Flexible Multi-Layer Sample with the circuitry visible through both intermediate metal layers

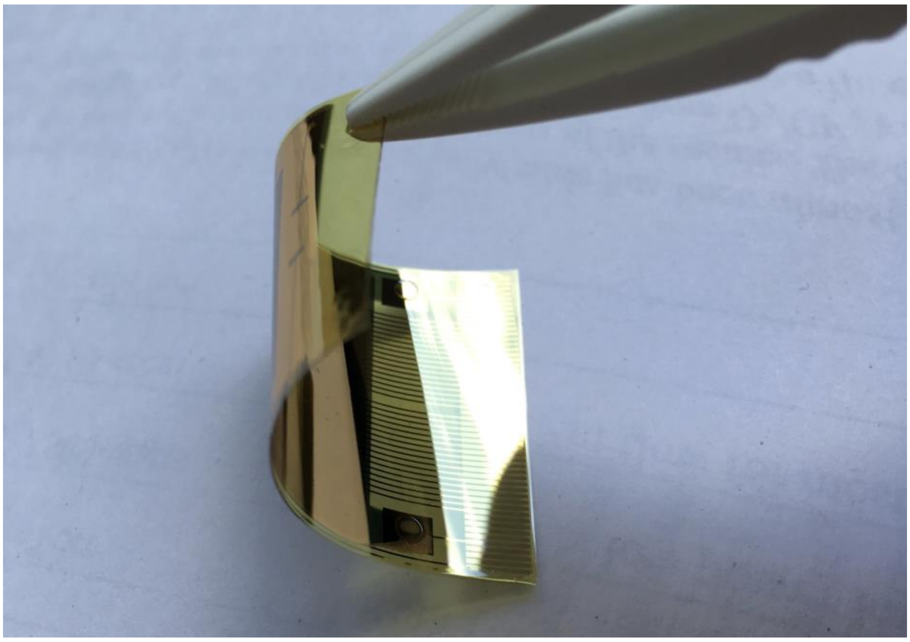

Figure 44: Flexible Multi-Layered Sample, demonstrating the flexibility

Before dissolving the sacrificial titanium layer of the flexible sample, a via was fabricated by opening the PI layer over the via pad #1 of the flexible sample. An aluminum hard mask (refer to right image of figure 45), left a circle of 2 mm in diameter on the PI layer on top of VIA pad #1 exposed to the O_2 Plasma of the RIE, which was utilized again for etching PI. As with the non-flexible samples, the intermediate metal layers, consisting of 10 nm Ti, 50 nm Au and 10 nm Ti layers, were sputtered with the help of another aluminum hard mask (Figure 45), after the electrode openings were ensured by using photolithographic processes and a *Flex Mea Etching mask*. The metal layer had to cover the active electrode area, as well as the strain gauge and be connected to the electrode layer over the opened vias, thus creating a 3-dimensional layer stack, all connectable by the coplanar bond pads.

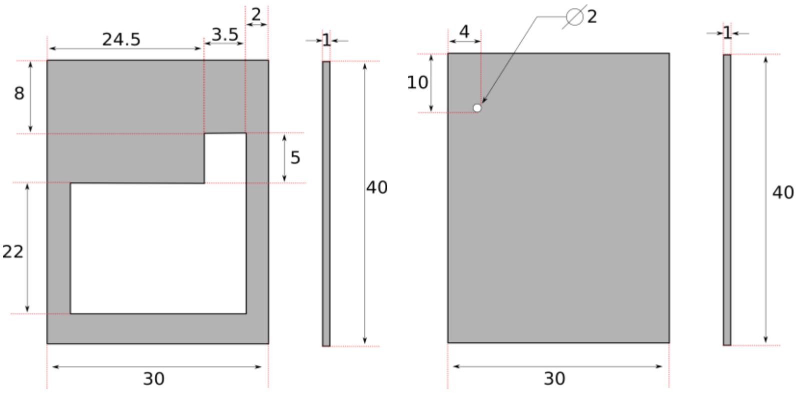

Figure 45: Aluminum hard masks for creating the intermediate gold layers on the flexible samples

Electrical measurements of the bond pad #6, connecting the via to the metal layer resulted in a resistance of 8 Ω, marking the via as functional. By repeating this via creation process mirror-inverted over via pad #2, the final flexible multi-layer stack, seen as a sketch in figure 46 and as real samples in figure 47, with both metal layers connectable by the bond pads, was reached.

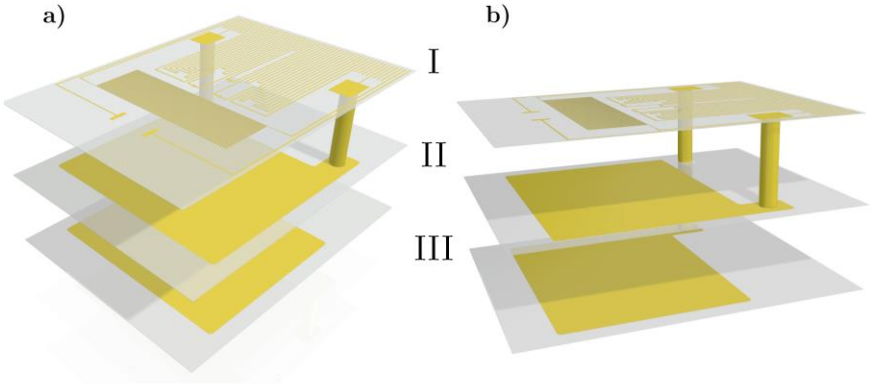

Figure 46: Schematic of flexible multi-layered Sample; Image provided by Marcel Kappel

The second layer also showed a measureable resistance of approx. 8 Ω to the bond pad #50 over the produced via #2. Both intermediate metal layers were therefore sufficiently electrically contacted. By dissolving the sacrificial titanium layer, flexible samples were achieved.

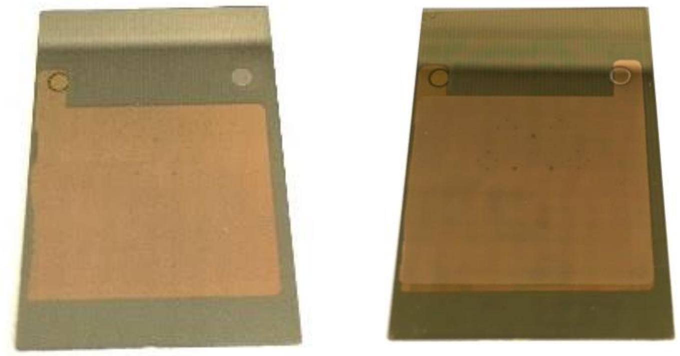

Figure 47: Creation of the multilayered flexible sample, with one (left) and both (right) intermediate metal layers deployed

Figure 48 displays an SEM image of the via bottom with the side wall, while an SEM image (JSM-6500F Scanning electron microscope with an attached EDX Module, both from JEOL, Musashino, Akishima, Tokyo) of the polyimide layer is given in figure 49. The opened via clearly shows artefacts of unremoved polymer strains. This unwanted feature is discussed in more detail in chapter 4.3.2 as it was also seen on the opened electrode surfaces. However, as the metal layers have shown to be electrically connected over this via, these artefacts are not harmful for further sample fabrication. In addition, the via side wall displays the etching progress of the PI. The polymer chains are broken by RIE etching, which can be followed in the via side wall by enlarging the gaps between the polymer strains. The electrodes could be opened similarly, as described with the non-flexible samples in chapter 4.1.1.

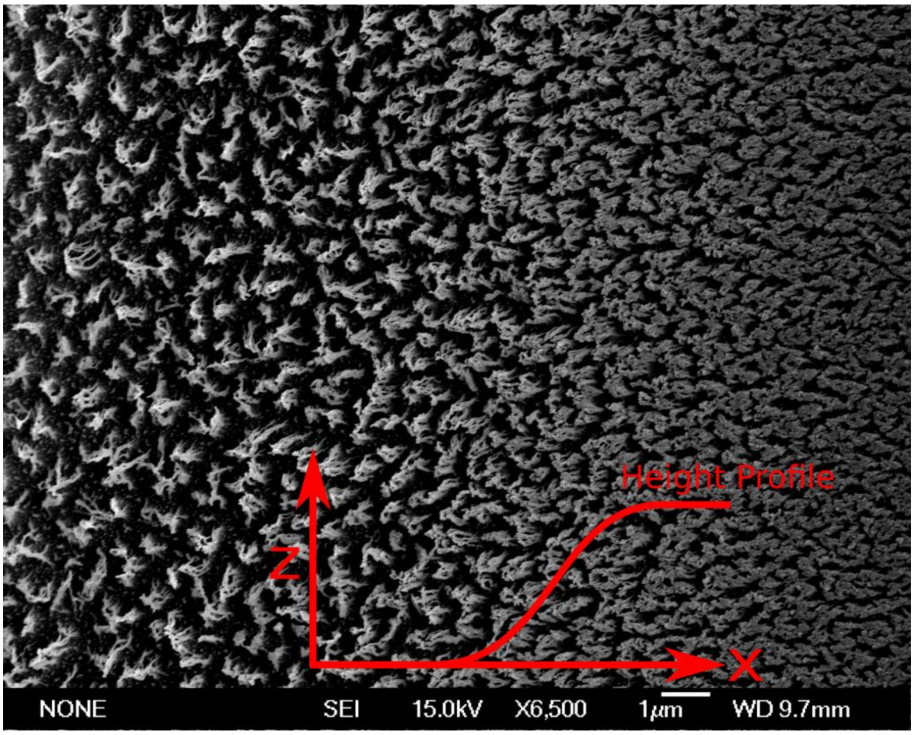

Figure 48: SEM images of VIA side wall

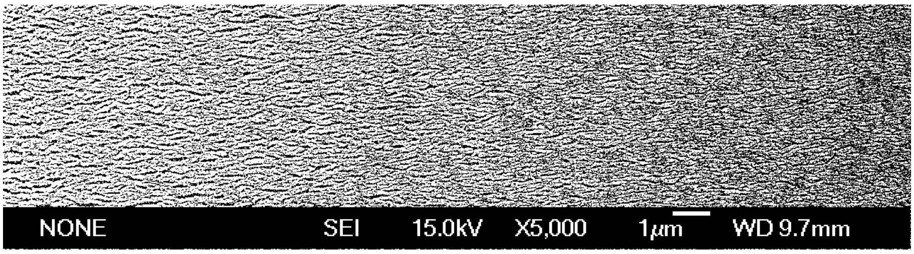

Figure 49: SEM image of top polyimide layer

4.2. MEASUREMENT SETUPS

Two setups were developed, fabricated and validated during this thesis, which are introduced in the following chapters. As the isolating features of the electrode side wall passivation had to be inspected by electrical analysis and polyimide itself is an extraordinary good insulator (see chapter 3.1.1), a measurement setup, capable of detecting very low currents, or high impedances, respectively, was established. In Addition, this setup, called "leakage-setup"[1],

---

[1] The name represents the ability to detect leakage currents over passivating layers

had to be capable of detecting these impedances over several channels on one or several samples, for reasons which are discussed in the following chapter 4.2.1.

Additionally, a second setup was implemented, intended to mechanically stress test the flexible implants of chapter 4.1.2 in a fluidic environment, simulating conditions to those in the human body. The requirements for this “fluidic-setup”, as it is addressed in this work, are also discussed in the following chapter 4.2.1. Finally, the main goal was to combine both into a fully automatic mechanical stress test and electrical analyzation setup which is addressed as FMS (Fluidic Measurement Setup).

The complete manufacturing, as well as software programming is explained in chapter 4.2.2. Also, it is clearly detailed, how a measurement of a non-flexible, as well as flexible sample is performed.

Final validation and verification, together with the capabilities of both setups is laid out in the final subchapter 4.2.3.

4.2.1. SETUP REQUIREMENTS

The prior discussed flexible samples were to be electrically assessed, while being bent to induce the mechanical stress, as would be found in the physiological medium. The electrical measurement setup (*Leakage Setup*) and the bending system (*Fluidic Setup*) were developed separately and combined later on.

Leakage Setup

As delamination and corrosion processes, as well as the isolating electrode side walls with their respective passivation, were to be electrically measured, acquiring minimal resistance variances at absolute values above several GΩ was a hard requirement which was primarily given due to the volume resistivity of polyimide. However, the applied voltage had to stay within the water window of common electrolyte fluids, PBS in particular. Thus, assuming an applied voltage of 1 V, the setup had to be capable of verifiably detecting currents smaller than 10^{-9} A. The smaller the detectable current, the earlier the delamination defects are measurable.

In addition, as corrosion and delamination measurements needed to be traced over longer time spans of several days and even weeks, the setup had to be capable of automatically measuring resistances in constant, but variable time intervals, preferably without user interaction.

To ensure reproducibility, several samples, each again including several channels should be simultaneously analyzed. Thus, the current measurement setup had to include multiplexers, as sketched in figure 50, where the measurement circuitry of a multilayer system with two electrodes is exemplified. By not only measuring the current from a counter electrode to several structures, but also from one layer to others, delamination occurrences could be regionally localized and verified. In the case of measuring several samples in parallel, multiple High lead lines with also multiple Low lead lines became necessary.

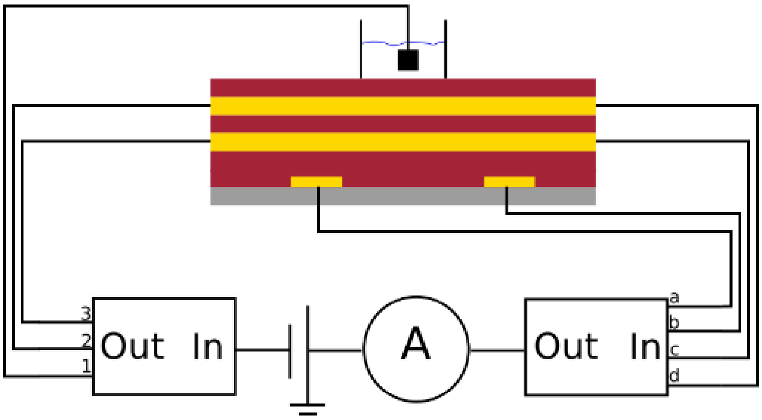

Figure 50: mimic diagram of leakage setup

Fluidic-Setup[1]

Several studies inducing mechanical load on polyimide samples in order to examine delamination and conductor breakages were performed, like the one of Lucchini et al. [148], which examined the deformation and failure mechanisms of metal-polymer interconnections and concluded that tensile stress is a most common cause for interface delamination. Other studies examined the aging influence of PBS on flexible devices, such as the study of Rubehn et al. did [80].

However, currently no study exists, combining mechanical load with electrical access to the samples, all while being embedded in a fluid environment. This was the goal of the FMS to evaluate the produced samples and the electrode side wall passivation. Such a setup would

---

[1] This setup has been published in [180]

be able to mimic body conditions on flexible samples way better than current mechanical stress tests, all while being able to measure electrical effects on the samples.

Further requirements were:

- Fixating the implants securely but also as gentle as possible without leaks occurring in the setup
- Visual assessment to the fixated samples to observe the status of degradation
- Ability of applying mechanical stress precisely, like that in the physiological spectrum of the human body
- Reading out the applied pressure as accurate as possible in order to observe induced micro motions with minimal pressure
- Suitability for temperature-superimposed accelerated aging measurements under mechanical load
- The measurement process must be completely automated, and software controlled

The mechanical stress, expected from realistic physiological conditions like the intracranial pressure (ICP) which varies from 7 – 25 mmHg in a normal adult, converts to 9 - 33 mbar [149]. Therefore, the FMS had to be able of continuously and reproducibly induce as well as record pressures in ranges of some mbar, defining the minimal resolution. In addition, stress test measurements also required pressures up to several 100 mbar.

Figure 51, displays the FMS, where the leakage setup, containing two multiplexers and a Source Measurement Unit, is combined with the fluidic measurement setup. For more detailed information about the Fluidic Setup, refer to the Bachelor thesis of Marcel Kappel [150].

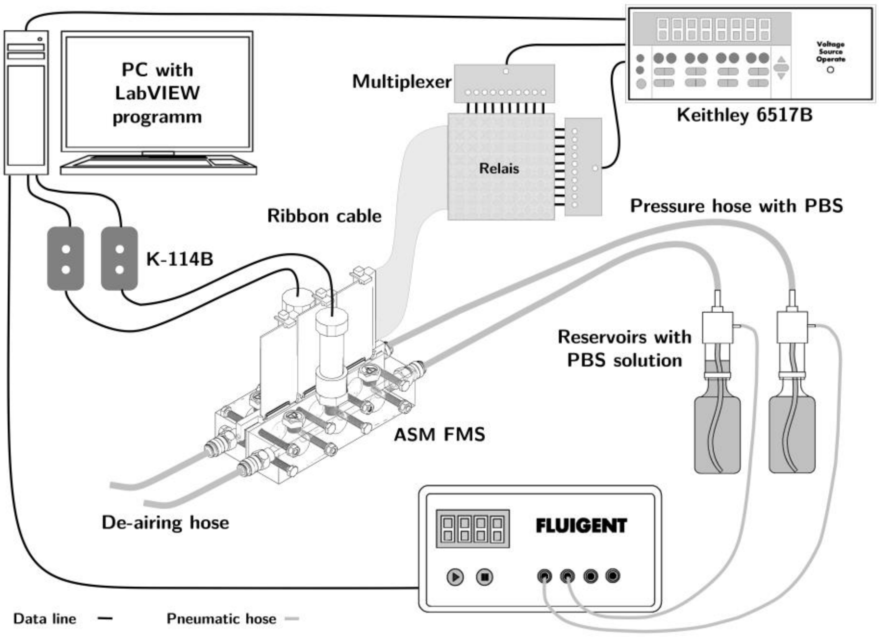

Figure 51: Schematic overview of the whole Fluidic Measurement Setup

4.2.2. MANUFACTURING AND SOFTWARE PROGRAMING

As high resistances in ranges of several MΩ and above are better recognizable by DC measurements [16], a 6517B (Keithley Instruments, Inc., Cleveland, Ohio, USA) Source Measurement Unit (SMU) with a built in ±1000 V voltage source and a low voltage burden of less than 20 µV was acquired. It featured a current measurement range from 20 mA down to 10 aA[1], thus, being able of analyzing resistances up to 10^{18} Ω, when staying inside the electrochemical window of PBS and applying a voltage of 1 V. Computer programmability is given by the GPIB Standard and the included SDK for several programming languages, including LabView (National Instruments, Austin, Texas, USA). An IEEE-488 PCI-GPIB Interface card (Keithley) ensured the connectability to a computer.

Model 7087-TRX-GND Adapters (Keithley) were utilized, translating the Triax Outputs of the SMU to standard female BNC, allowing the SMU to be connected to both multiplexers via standard BNC cables.

The multiplexers were manufactured in house by the electronic workshop of the university of Tubingen, as the Keithley’s integrated 10-Channel Multiplexer 6522 Scanner Card connected the Low of all not activated channels, which allowed not-measurable leakage currents to occur over the multi-layered samples [151]. The self-made multiplexers consisted of DR-SDS relays

---

[1] 10 aA = $1 \cdot 10^{-18}$ A. This measurement resolution will be discussed later in chapter 4.2.3

E48393 from NAIS (Matsushita Eletcric Works, Holzkirchen, Germany) and ensured a floating mass on all not activated channels, thus prohibiting internal leakage currents. Programmability was given by a standard Communication-Port (COM-Port), allowing the switch of single and multiple channels. In addition, the ground of the SMU was looped through the multiplexers, ensuring a standard ground potential over the complete setup, with all connectors being isolated from the multiplexers circuitry. Figure 52 shows a multiplexer, with all channels contacted and 2 of them activated. Each channel features an LED indication of its status.

Figure 52: Image of in-house manufactured multiplexer

The samples are measured inside of a faraday cage (Figure 53), built by the mechanical workshop of the University of Tubingen, ensuring electrical and magnetical shielding. Its backside contains several BNC as well as SMA feedthroughs, contacting the samples.

Figure 53: Electrical measurement Setup with faraday cage and SMU

An Aluminum Plate was designed and built (see Appendix F, G and figure 54) with stainless steel platforms for the Probe Positioners DPP105-Al-S (Cascade Microtech, Beaverton, Oregon, USA) to establish the electrical contact onto the samples themselves. Its dimensions were chosen, so the Probe Positioners reached the sample, which rests in pre-designed recesses.

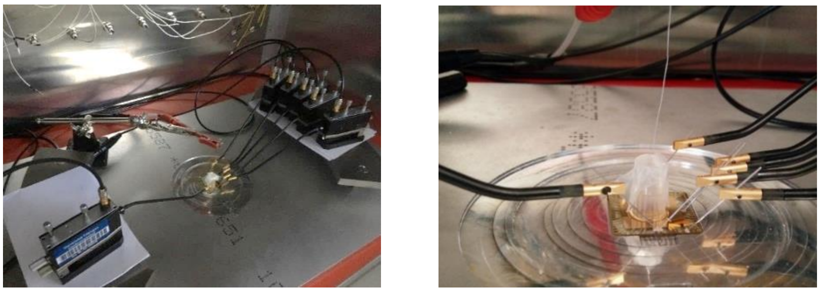

Figure 54: Probe Positioners (left), contacting the sample with the AgCl counter electrode (right)

A 2.0 mm AgCl Pellet Electrode E206 (Hugo Sachs Elektronik, HARVARD APPARATUR GmbH, March – Hugstetten, Germany) was placed inside a plastic cup glued to the sample with Polydimethylsiloxan (PDMS) (Figure 55), and acted as the counter-electrode as described in the mimic diagram in figure 50.

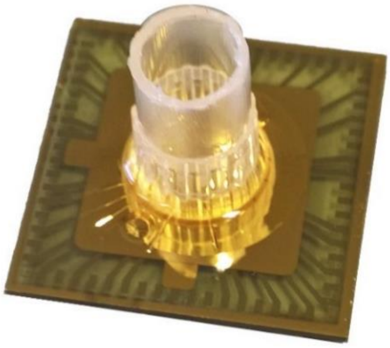

Figure 55: Non-flexible sample with plastic liquid reservoir

Programming the LabVIEW Software

The LabVIEW software was programed with the idea of minimizing electrical noise and eliminating measurement offsets while controlling the complete hardware, being both multiplexers and the 6517B SMU from Keithley at that time. As a result, each measurement took up to several minutes.

Before starting a measurement, the source was set to 0 V while connecting all channels on both multiplexers in order to let any possible capacity discharge. After 10 s, all channels were opened, and the final measurement voltage of 1 V was set. Before applying it to the sample, the Keithley's internal Zero Check with the following Zero Correct functions were called, which internally connected High to Low over a calibrated 10 GΩ impedance shunt. An eventually measured offset was then corrected, ensuring a calibrated ammeter [146]. Now, the appropriate multiplexer channels were opened with the beginning of the resistance measurement. One final measurement value consisted out of 20 single values, over which were averaged.

Fluidic Measurement Setup (FMS):

After several design changes, the final pressure chamber system can be seen in figure 56, alongside its explosion diagram. Both pressure chamber corpuses were manufactured out of single (40 mm x 40 mm x 180 mm) Polymethylmethacrylat (PMMA) blocks. Three connections between both pressure chambers are given by openings with a diameter of 24 mm, respectively, matching the active electrode area of the flexible sample layout (refer to chapter 4.1.2).

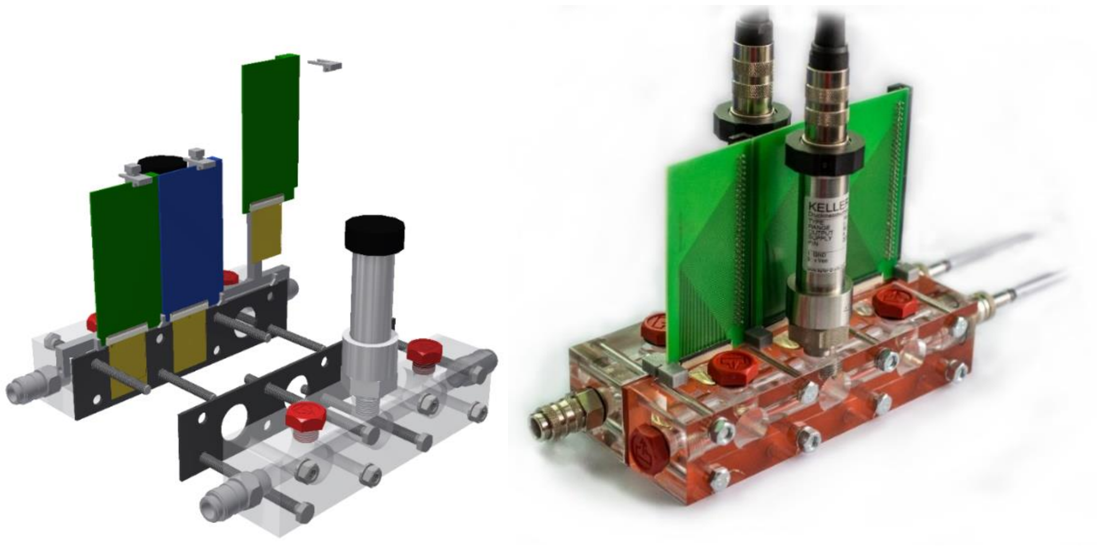

Figure 56: Explosion (left) and real world (right) image of the FMS pressure chambers

The modular design also allows a one-directional pressure build-up. By sealing one pressure chamber corpus with an aluminum plate, the samples are mechanically loaded against the normal conditions (Figure 57).

Figure 57: One sided pressure applied to a Flex-Mea by utilizing one pressure chamber

The bond pads of the flexible sample layout correspond to the Xf2M-55 Omron connector, which were soldered on custom made printed circuit boards (PCB) (also seen in figure 58), featuring an elegant way of contacting the 55 pads. The connector connects thin films up to

300 µm securely while establishing electrical contact, which was another reason in favor of Pi 2610 over 2611, due to its film thickness. However, spacers were needed, to connect the film securely. The PCBs feature a connection for a broadband cable, ensuring contactability to every bond pad on the flexible sample. Another custom-made PCB (Figure 58) translated the broadband cable to a matrix of pins where wires could be attached.

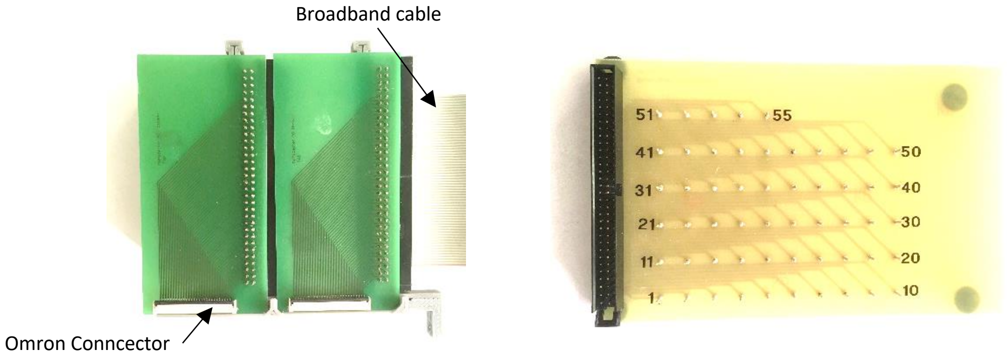

Figure 58: (left) PCB, translating the OMRON connector (bottom) to a standard broadband ribbon cable (right side) to contact the Flex MEA; (right) PCB to contact the broadband wire from the prior PCB

A MFCS[1]-ES Base (Fluigent, Jena, Germany) with two 2000 mbar channels, featuring a resolution of 0.03 % FS[2] and a pressure stability better than 0.1 % CV[3] was chosen as pressure source, as the manufacturer provided a detailed SDK for LabVIEW compatibility. In addition, it only needs a pressured nitrogen source to operate, which was available in the laboratory.

By transferring the nitrogen pressure, originating from the MFCS System Base channels to fluid-filled reservoirs, this pressure was applied to the fluidic setup’s pressure chambers via the liquid. A ventilation at either pressure corpus allowed exhausting the remaining air, allowing the pressure chamber to be completely pressurized by the liquid.

The applied pressure was controlled by the internal pressure sensors of the MFCS Base. However, as they were separated from the pressure chambers by 2 m of tubing, including a medium switch, additional pressure sensors were applied directly to the pressure chamber corpus. The Series 33X pressure sensors (Keller, Jestetten, Germany) feature a 0.01 % FS with

---

[1] Microfluidic Flow Control System

[2] Full Scale; this value translates to 600 µbar with the given values

[3] Coefficient of Variation, also known as “relative standard deviation” (RSD). It is defined as the ratio of the standard deviation to the mean.

an effective range of 0 to 3 bar at -10 °C up to 80 °C and are, thus, capable of withstanding accelerated aging conditions.

Programming

Fluidic setup

Both Keller Sensors, together with the MFCS System Base are initialized at program start. After waiting for several user inputs, including cycle duration and alpha-parameter[1], controlling the MFCS Base sensitivity and pressure values, the de-airing process starts, allowing the user to eliminate any remaining air inside the pressure chambers.

As only liquid remains in the chambers, the test execution program is initiated. A defined high pressure 1 (refer to figure 59) is applied to the first chamber, while a defined low pressure 2 is applied to the second one. After the cycle duration, pressure 1 is switched to a low value while pressure 2 is raised, thus bending the fixated samples. While monitoring all measurement data in real time, the program saves all pressure values, including both MFCS channels and those of both Keller sensors, together with the recorded temperature every 200 ms in a user-definable text file.

Combining the fluidic setup with the leakage setup to the FMS:

By combining the leakage setup with its programing with the fluidic setup and its capabilities, the Flex-Mea Measurement Setup (FMS) setup was achieved, allowing electrical measurement of flexible samples while applying a mechanical load. So far, this is the first known measurement setup, capable of detecting electrical (leakage-)currents over several channels, while mechanically stress testing samples in a liquid environment.

After initialization of all components, definable pressures are applied to the fluidic setup. After these have been established, electrical currents are measured over definable multiplexer channels, with all considerations of the leakage setup. After all measurements for that cycle have been completed, the next cycle begins with applying the next pressure to the fluidic chamber corpuses.

---

[1] Integer from 0 to 255; the value describes the feedback coefficient for the pressure regulation. Higher values correspond to more frequent and nervous pressure regulation by the MFCS Base.

Two main programs were written. The *fluidic-alternate* program applies alternating pressure between electrical measurements, thus bending the samples back and forth. Its Flowchart can be seen in figure 59.

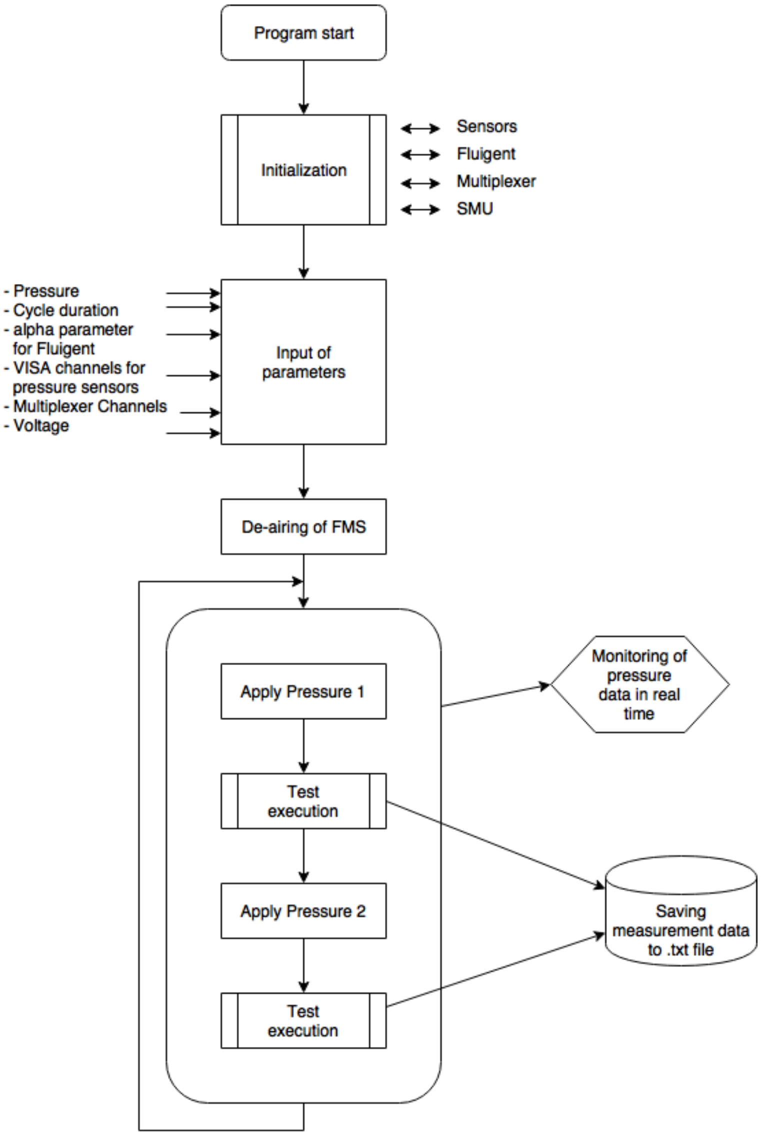

Figure 59: Flowchart for final FMS Program

The *fluidic-sweep* program applies a pressure to one chamber, while holding the second at a base level. After measuring several definable multiplexer combinations, the relative pressure is enlarged by raising the pressure in the first chamber by a fixed value, followed again by the electrical measurements. By doing so, the maximal endurable mechanical load could be determined, before failure in layers and even ruptures of samples occur. In addition, coherences between mechanical load and measurement data are examinable by raising the applied pressure controllably.

Figure 60 shows the control side of the *fluidic-sweep* program, where all user interaction occurs. All initialization values as the GPIB and both Com-Ports can be seen, together with the definable base pressure of the MFCS channel 2. Channel 1 of the MFCS was set to 10 mbar in this example and risen in 10 mbar increments, until the final value of 300 mbar was reached, thus, producing a relative pressure of 280 mbar between both pressure chambers. After each pressure was applied, the channels 1 on both multiplexers were activated and the SMU applied a Voltage of 0 V.

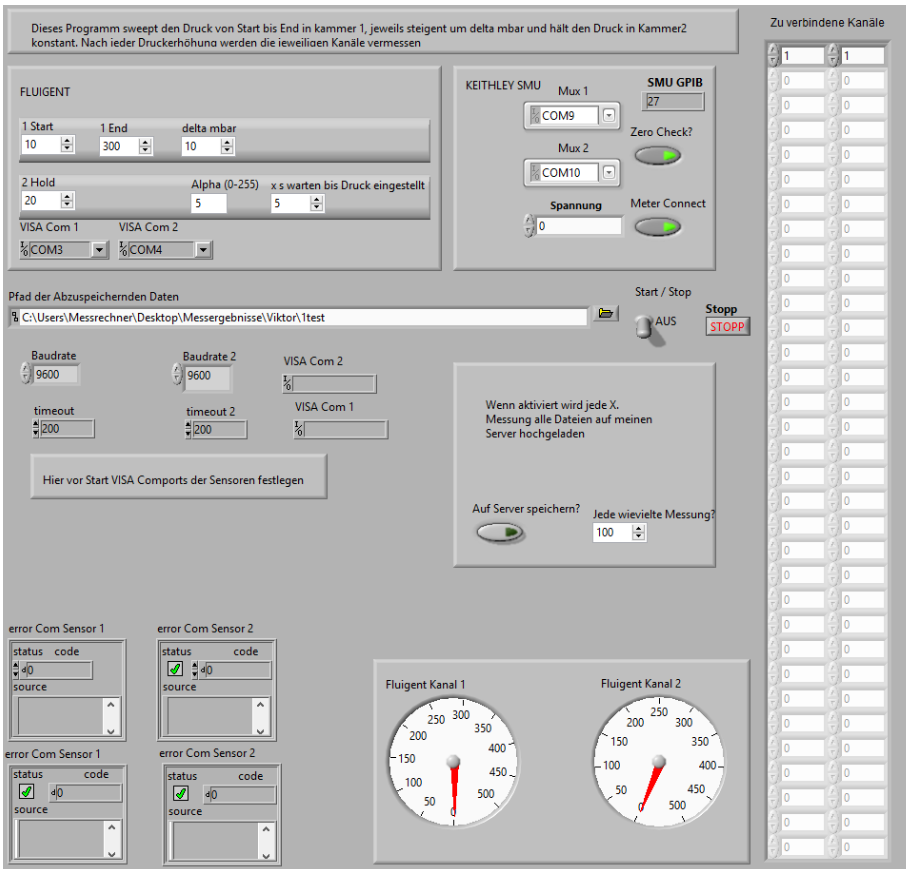

Dieses Programm sweept den Druck von Start bis End in kammer 1, jeweils steigent um delta mbar und hält den Druck in Kammer2 konstant. Nach jeder Druckerhöhung werden die jeweiligen Kanäle vermessen

FLUIGENT
1 Start: 10
1 End: 300
delta mbar: 10
2 Hold: 20
Alpha (0-255): 5
x s warten bis Druck eingestellt: 5
VISA Com 1: COM3
VISA Com 2: COM4

KEITHLEY SMU
Mux 1: COM9
Mux 2: COM10
SMU GPIB: 27
Spannung: 0

Pfad der Abzuspeichernden Daten: C:\Users\Messrechner\Desktop\Messergebnisse\Viktor\1test

Start / Stop: AUS
Stopp: STOPP

Baudrate: 9600
Baudrate 2: 9600
timeout: 200
timeout 2: 200

Hier vor Start VISA Comports der Sensoren festlegen

Wenn aktiviert wird jede X. Messung alle Dateien auf meinen Server hochgeladen

Auf Server speichern?
Jede wievielte Messung? 100

Zu verbindene Kanäle: 1, 1

Figure 60: Parameter Settings of Fluidik Sweep Program

Figure 61 shows the second side of the fluidic-sweep program with the real-time measurement data being displayed to the user. Both MFCS pressure sensors, together with the data of both Keller pressure sensors, sitting in the pressure chambers are displayed. The MFCS sensors report the relative pressure, whereas the Keller sensors report the real pressure. In addition, the temperature is displayed for accelerated aging purposes.

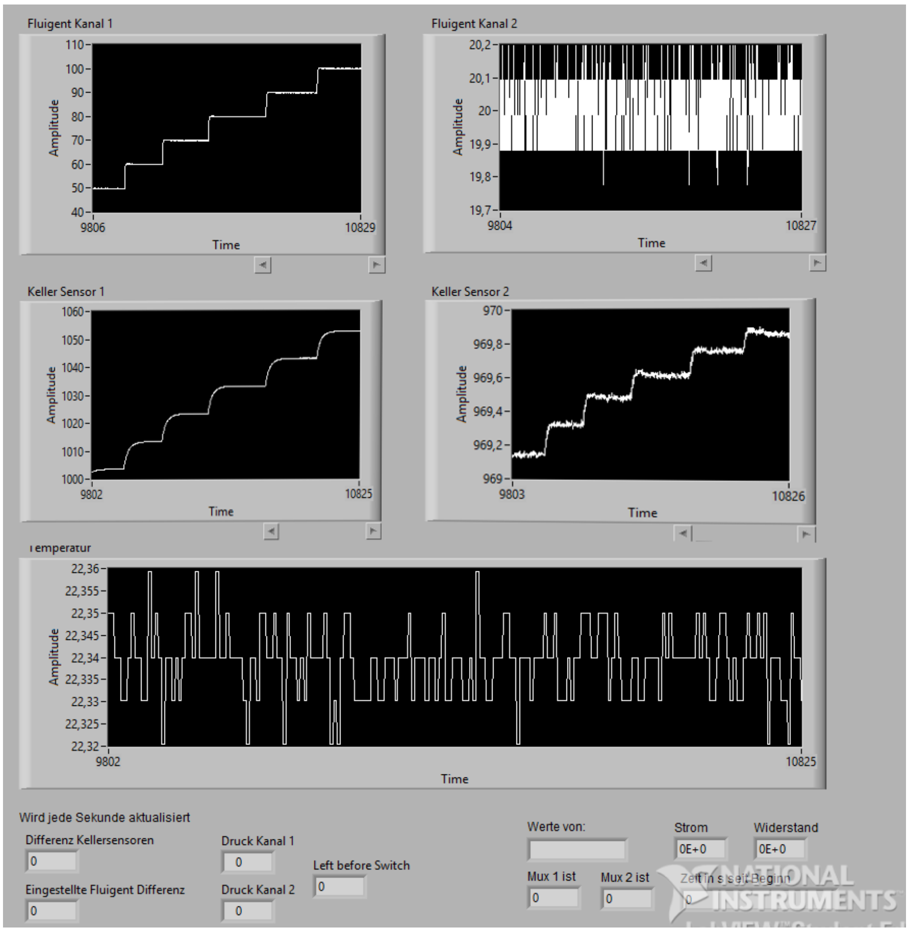

Wird jede Sekunde aktualisiert

Differenz Kellersensoren: 0
Eingestellte Fluigent Differenz: 0
Druck Kanal 1: 0
Druck Kanal 2: 0
Left before Switch: 0
Werte von:
Strom: 0E+0
Widerstand: 0E+0
Mux 1 ist: 0
Mux 2 ist: 0
Zeit in s seit Beginn: 0

Figure 61: Data Display of Fluidic alternate program

In this example of raising the pressure in chamber 1 by increments of 10 mbar, the resulting pressure rise of 0.2 mbar in chamber 2, due to the flexible samples, is also visible. As the Fluigent Channel 1 was set to a fixed pressure value of 20 mbar, being displayed at top right, the rise in the second channel must originate from the flexible sample being bent. This example, thus, confirms the need of monitoring the pressure in the corpus itself.

4.2.3. VALIDATION AND VERIFICATION

It is necessary to validate the setup's capabilities as well as accuracy before measuring possible leakage currents in the produced samples. In case of the Leakage Setup, these accuracy measurements are especially important, as the measurement range of the SMU is lowered by routing currents through two self-made multiplexers. Also, it must be proven, that no electrical leakages occur inside of the multiplexers.

As the main idea of the Fluidic Setup was bending flexible samples most accurately over a long time span, measurements with a focus on pressure accuracy and reliability are conducted.

Also, a correlation between applied pressure and sample bending was to be established to mechanically load the samples very precisely. The main function of bending the samples back and forth by applying alternating pressures is also demonstrated.

Leakage-Setup

To verify the minimal measurable currents and, thus, the maximal detection range, open circuit measurements with the Flex-Mea sample PCB, however without a sample inserted, were performed with both multiplexers, consecutively. These measurements indicate the noise level and therefore the maximal distinctly measurable resistances. In total, 40 measurements per multiplexer channel were performed. The mean value of these measurements, together with the maximal and minimal detected currents, which are given as boundaries in the error bars, are displayed in the following charts. The applied voltage over these measurements was always set to 1 V. Therefore, the detected currents are directly reciprocal with a factor of 1.

Figure 62, displays the open circuit measured resistances over every channel of the first multiplexer. The mean value of all measurements is approx. 74 TΩ, with the all-time lowest detected resistance being still above 1 TΩ over Channel 9. Therefore, the minimal measurable current is lower than $1 \cdot 10^{-12}\text{A}$.

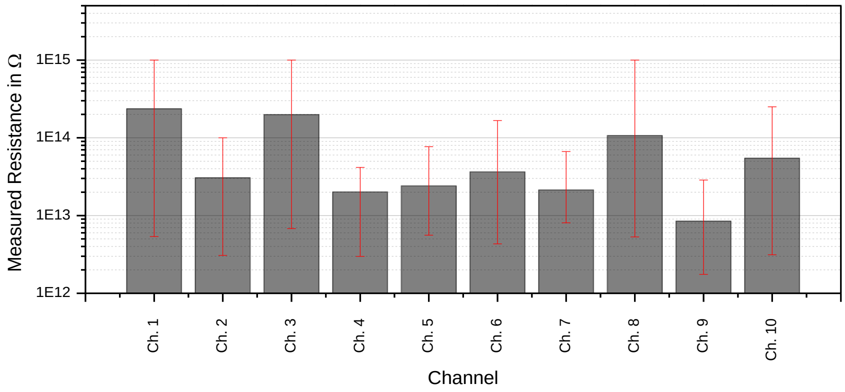

Figure 62: open circuit measurement of multiplexer 1

The range of the second Multiplexer is analyzed in figure 63, which showed a mean open circuit resistance of about 41 TΩ, or a noise current of $4.1 \cdot 10^{-13}\text{A}$, respectively. As in the case of Multiplexer 1, also a minimal resistance of approx. 1 TΩ was measured, this time over channel #1 and #6.

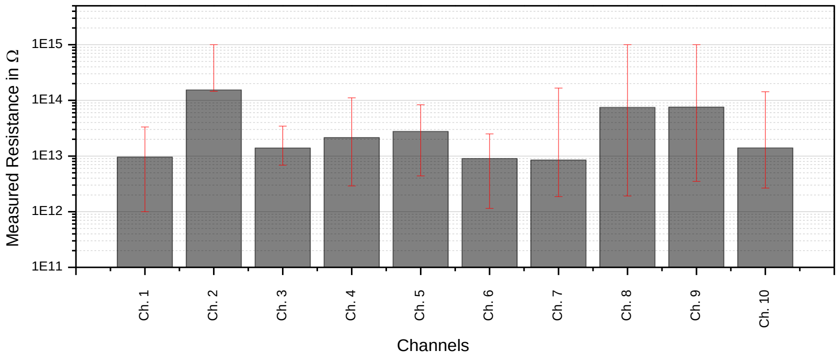

Figure 63: open circuit measurement of multiplexer 2

The consistency and comparability between all channels is analyzed by measuring the DC current over a 10 GΩ resistor by applying a Voltage of 1 V and 5 consecutive measurements done over every channel. The obtained resistances are displayed below with the maximal and minimal detected value, respectively.

Multiplexer 1 showed below 1% scatter for each channel and all obtained values deviated below ±0.3% around the mean of 9.93 GΩ (Figure 64).

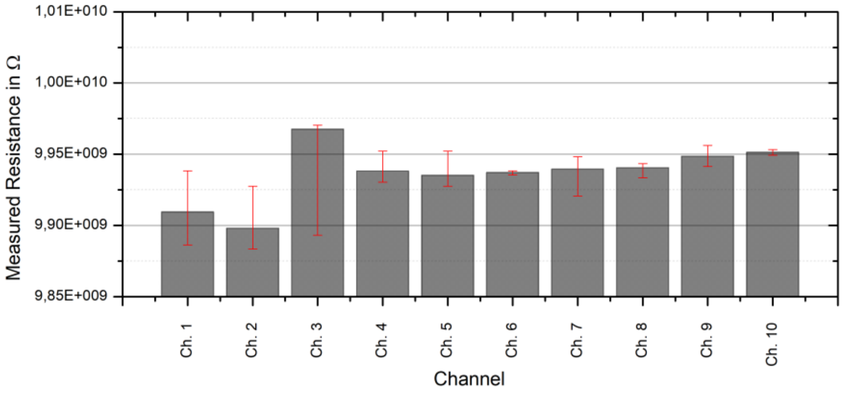

Figure 64: Mux #1 10 GΩ measurements

The same measurement done on Multiplexer 2, showed a scatter below 0.6 % for each channel and a deviation of less than ±0.3% around the mean of 9.95 GΩ for every channel (Figure 65).

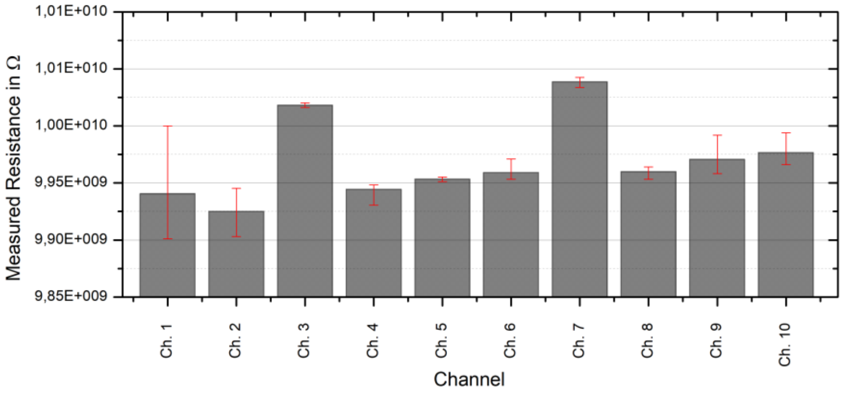

Figure 65: Mux #2 10 GΩ measurements

Both multiplexer feature extremely low noise and, thus, allow the detection of smallest DC current leakages in ranges of 10^{-12} A over any channel. Any currents smaller than that, and therefore, resistances over 1 TΩ are discussed as fully passivating and cannot be detected reliably with this measurement setup. This detection range is only achieved due to measuring all samples within the faraday cage and passing the mass of the SMU through both multiplexers.

Fluidic-Setup:

Leakage tests were executed at a maximum applied pressure of 2 bar and repeated subsequently at three occasions with no leakage of PBS solution detectable. As the flat gaskets and utilized O-rings can withstand this pressure, according to the manufactures' data, the FMS is able to operate at the full Fluigent pressure scale over longer measurement times of several days, or even weeks.

The Keller Sensors are able of recording pressure and temperature every 30 ms with a maximum measuring accuracy of 0.1% FS (full scale)[1] and sending these values to the self-written LabView program in real time. A constant offset of 0.4 mbar was measured between both sensors, which was even present with no pressure applied by the Fluigent and, thus, can be discussed as a systematic calibration error and is easily compensable by the software.

The main goal of the setup was to expose flexible samples to alternating pressure, thus bending them. Figure 66 shows the applied pressure of both Fluigent channels with the

---

[1] 0.1% FS translates to 0.3 mbar for the utilized Keller Sensors

acquired pressure difference of the Keller sensors in the pressure chambers. The resulting pressure switching is clearly visible, with the maximum pressure value according to roughly 90 mbar in the pressure corpus, which differs slightly from the applied 100 mbar. This fact is due to the approx. 2 m of hose length with a medium switch in the pressure supply pipes, originating from the Fluigent. By looping the Keller's sensor pressure value back to the LabView Software in real time, the chamber pressure can be further controlled.

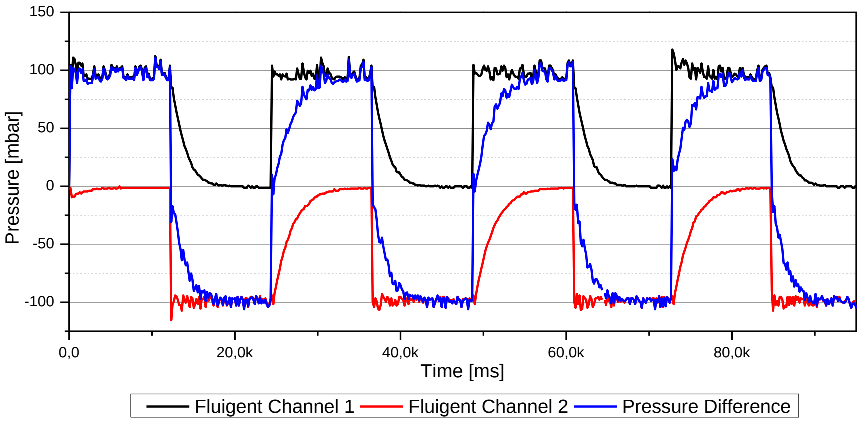

Figure 66: FMS switch verification with 100 mbar applied

Furthermore, the pressure decrease occurs visibly slower than the pressure build up, which originates from the Fluigent MFCS being slower at releasing pressure which is a passive process. It can be circumvented by operating at higher relative pressures, thus, releasing pressure against the lower relative normal ambient pressure. As the speed of the pressure build-up and release is no critical parameter, it was solved by waiting for the final chamber pressure before measuring, thus prolonging the cycle time.

During bending measurements, some samples formed ruptures and ripped, thus connecting the two independent pressure chambers. The resulting pressure diagram is seen in figure 67. The time of rupture is clearly distinguishable by comparing the Keller sensors pressure difference, indicating the hydrostatic setup changing to a hydrodynamic state. The Fluigent MFCS notices the pressure rise in the second channel seconds later, thus underscoring the importance of the Keller sensors.

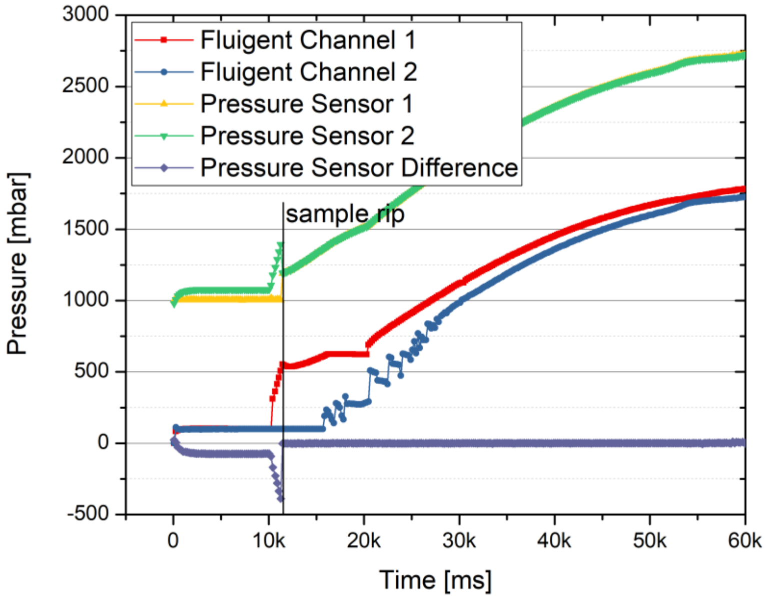

Figure 67: Detection of cracks and samples

The result of applying a constant pressure of one chamber against the other over single polyimide films for a time span of 6 days is displayed in figure 68 with the resulting pressure varying between 189 mbar and 199 mbar with some spikes of $\Delta p = \pm 6 \text{ mbar}$ during working hours on week days. The single spike on Saturday occurs from a system reboot. The pressure stability outside of working hours is visible, together with the inherent sensor noise at maximum measuring accuracy. The other peaks are explained by the nitrogen supply, being shared among other labs. By using the nitrogen supply, its pressure decrease is momentarily overcompensated by the MFCS before returning to the initial base level. This systematic error is not easily avoided, but small enough to be ignored for long term measurements.

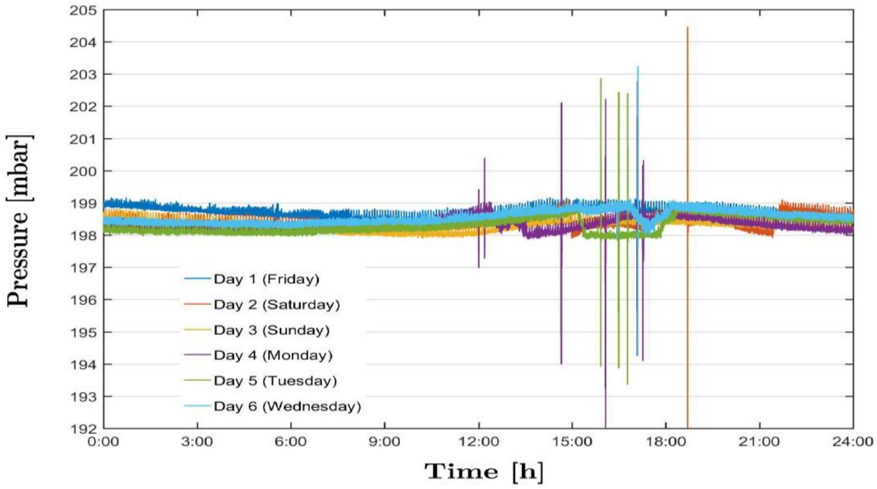

Figure 68: Pressure stability of FMS during 6 consecutive days

An AgCl-Counter electrode was fed through an upper seal, placing it approx. 2 cm before a Flex-Mea inside the PBS solution. The exact positioning is not reproducible; thus, only relative measurements are comparable between multiple samples. Figure 69 and 70 show electrical AC measurements, utilizing a XM FRA 1 MHz Modulab XM ECS (Ametek GmbH, Meerbusch, Germany) impedance analyzer of an unopened and an opened Flex-Mea. In figure 69, those measurements of an unopened one vs the electrode in PBS with an applied Voltage of 1 V and a fixed frequency of 1 kHz are displayed. As the phase is close to -90° for the unopened sample, the overall impedance arises from the capacity due to the polyimide coating, resulting in overall high impedances in ranges of $2-5\cdot 10^6\ \Omega$, clearly marking the Flex-Mea electrodes as covered with the passivation. In addition, the distribution of the impedance values clearly references the location of the single electrodes on the sample (compare to sample layout, shown in figure 41 in chapter 4.1.2). The phase not being exactly -90° is due to degradation effects as the sample was already 3 weeks old and used before for bending measurements (refer to chapter 2.3.3). The behavior of Electrode #1 suggests, that the passivation above this electrode was not completely insulating, resulting in an ohmic behavior, although a short circuit during measurement is also possible.

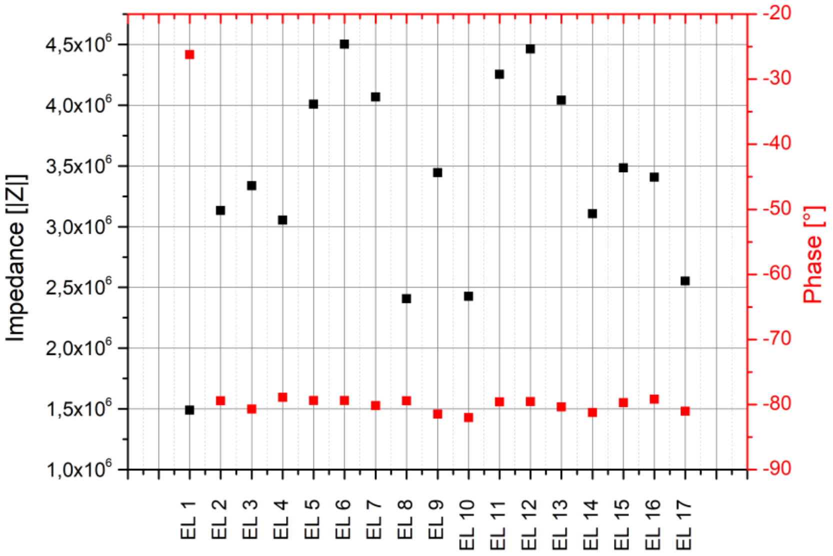

Figure 69: AC measurement of unopened Flex Mea in the FSM (1 V, 1 kHz)

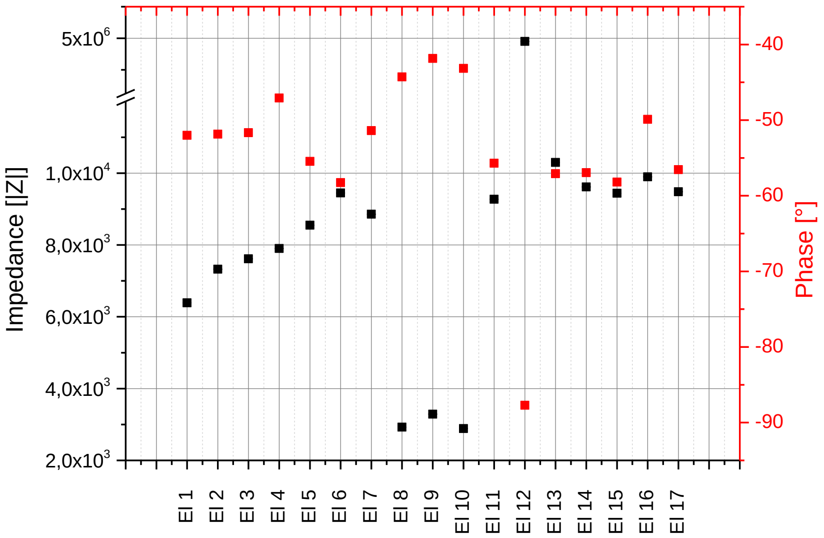

Figure 70: AC measurement of opened Flex Mea against PBS in the FSM (1 V, 1 kHz)

In the case of the opened Flex-Mea, the phase is at lower ranges of - 40° to - 60° due to the Au-PBS contact (refer to chapter 2.3.3). The impedance of approx. $1 \cdot 10^4\ \Omega$ verifies the opened electrodes in contrast to the closed ones. Also, electrode #12 of the opened Flex-Mea is clearly still passivated, resulting in a nearly perfect -90° phase shift and an impedance of $5 \cdot 10^6\ \Omega$, which corresponds with the values of the unopened sample.

By combining the Leakage Setup with the FMS, electrical measurements over several channels while applying a defined pressure load are feasible.

4.3. ASSESSMENT OF MANUFACTURED SAMPLES

Even if the primary focus did not lie on adhesion analyses, the delamination of polyimide from the adjacent layers is shortly introduced in chapter 4.3.1 while etching it is shortly addressed in chapter 4.3.2. Electrical stability and, thus, passivating features however, are of great interest and discussed in chapter 4.3.3.

Short analysis the polyimide foils in regard to fluorine uptake is given in chapter 4.3.4. Bending measurements, gathered from the FMS, are discussed in chapter 4.3.5.

The impact of bending the samples is electrically verified and shown in chapter 4.3.6, as it was shown, that initial sample bending has a positive influence on the electrical features. Chapter 4.3.7, finally, gives a possible explanation for the enhanced electrical capabilities after sample bending.

4.3.1. DELAMINATION OF MULTILAYER SAMPLES

Although Ti was utilized as an adhesion layer between the Au circuitry and the passivating PI Layers, delamination was still present. Figure 71 shows prepared SEM images of a passivation with an intermediate Ti-Au-Ti metal layer, which has partially been opened to the first metal layer over an electrode in the left image. The rough metal surface in the left image of figure 71 is discussed in detail in chapter 4.3.2. A focused-ion beam was utilized to form the cuts, displaying the multilayer system (FIB Strata DB 235 Dual Beam (FEI, Oregon, USA).

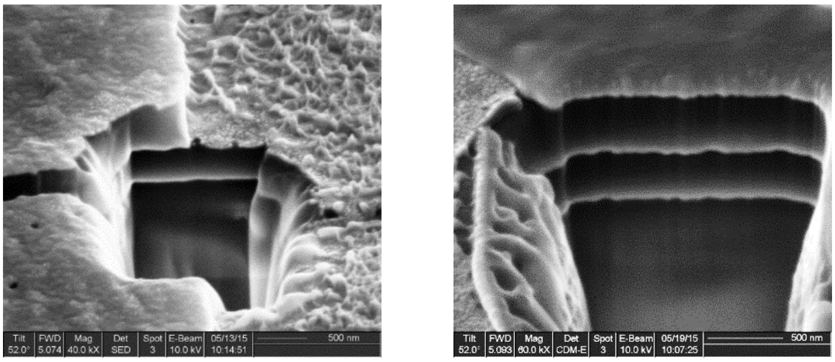

Figure 71: SEM images of multilayer samples, prepared with FIB

During measurements, especially when involving fluids, delamination of single and multiple layers could be observed, resulting in samples like the ones in figure 72. It can be seen, that delamination tends to start from material interfaces, like the metal feed lines beneath the PI passivation, reinforcing the importance of an electrode side wall passivation. If it can spread, complete polyimide passivation layers can delaminate, as seen in the right image of figure 72, thus, leading to complete failure of the passivation system.

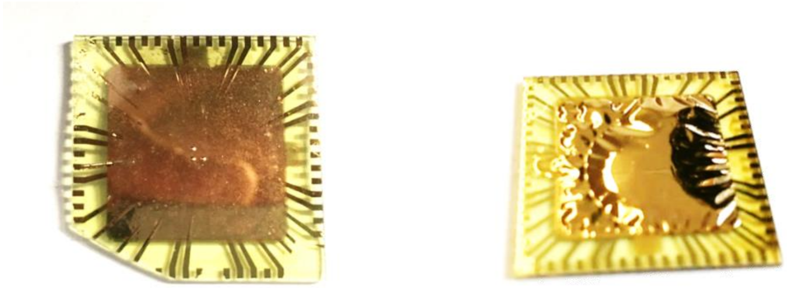

Figure 72: visible delamination between PI and the circuitry (left) or complete Au layer (right)

It is of interest, if this delamination of layers interferes with the structure of the adjacent layer beneath, as future measurements indicate water vapor passing through a metal layer (refer to chapter 4.3.3).

Therefore, atomic force microscopy measurements (using a DI Nanoscope atomic force microscope from Veeco, NY, US) were carried out on several different surfaces, including the standard Ti-Au-Ti layer, as well as a polyimide passivation, leading to surface roughness of 2.95 nm for the metal layer, which was reduced to 0.83 nm after spin coating the polyimide, respectively. The corresponding height profiles can be seen in figure 73.

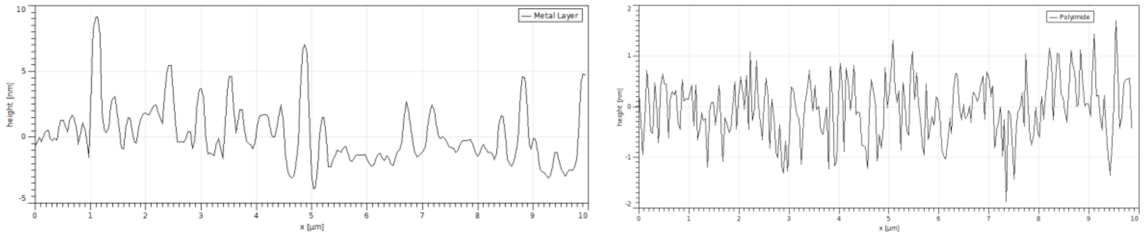

Figure 73: Height profiles of the surface topography of the metal layer (left) and polyimide (right), generated with atomic force microscopy

After the polyimide completely delaminated from the underlying metal layer, the now exposed surface was again analyzed in respect to its surface roughness, resulting in 4.71 nm. The new surface height profile is shown below (Figure 74).

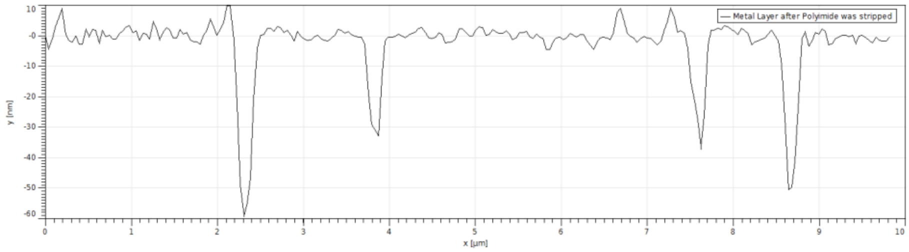

Figure 74: AFM height profile the metal surface after delamination

The surface is now 60% rougher after delamination of the polyimide layer, which is due to the newly created visible dents, which are roughly 50 nm deep. This corresponds to the metal layer thickness. It appears that the delaminated polyimide layer tore complete clusters out of the metal stack, leaving pinholes behind.

One of these pinholes in shown in more detail in figure 75, with its topography right beside. The hole is about 70 nm deep, reaching through the complete metal stack with a gold cluster left behind and still visible.

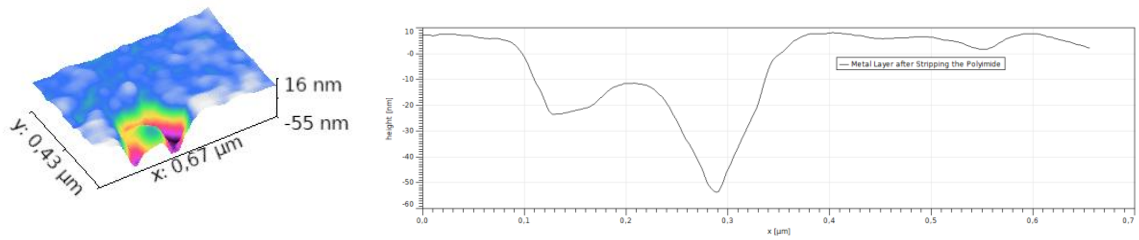

Figure 75: AFM image and height profile of ripped out Au cluster

Figure 76 gives an overview of the metal surface, showing these dents are not rare effects, but commonly distributed over the complete sample, creating many water-vapor permeable pinholes. As minimizing delamination is not the task of this thesis and even necessary for electrical stability measurements in the following chapters, no experiments were conducted in this regard.

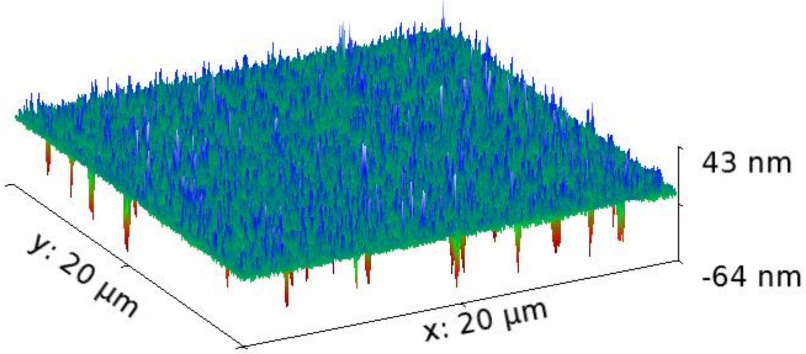

Figure 76: AFM image of metal layer with removed gold clusters

As other workgroups have also noted the insufficient capabilities of titanium as an adhesive layer, several studies have been undergone with alternatives. The workgroup around Stieglitz et al. has shown promising results with SiC and diamond-like carbon (DLC) adhesive layers, resulting in stable samples after 1 year of accelerated aging measurements in saline solution. [152]

4.3.2. ETCHING OF POLYIMIDE

It is shortly addressed in the prior chapter 4.3.1 with the surface of the metal layer above the etched electrode shown in figure 71, that etching the polyimide with oxygen plasma as described in chapter 3.2.6 left residues behind, still covering metal layers and the electrodes.

Figure 77 shows a microscopic image of an opened electrode. It is still coated, while only small areas show the blank metal. This image is translated to grayscale as seen in figure 78 and a histogram, to analyze the share of uncovered metal surfaces.

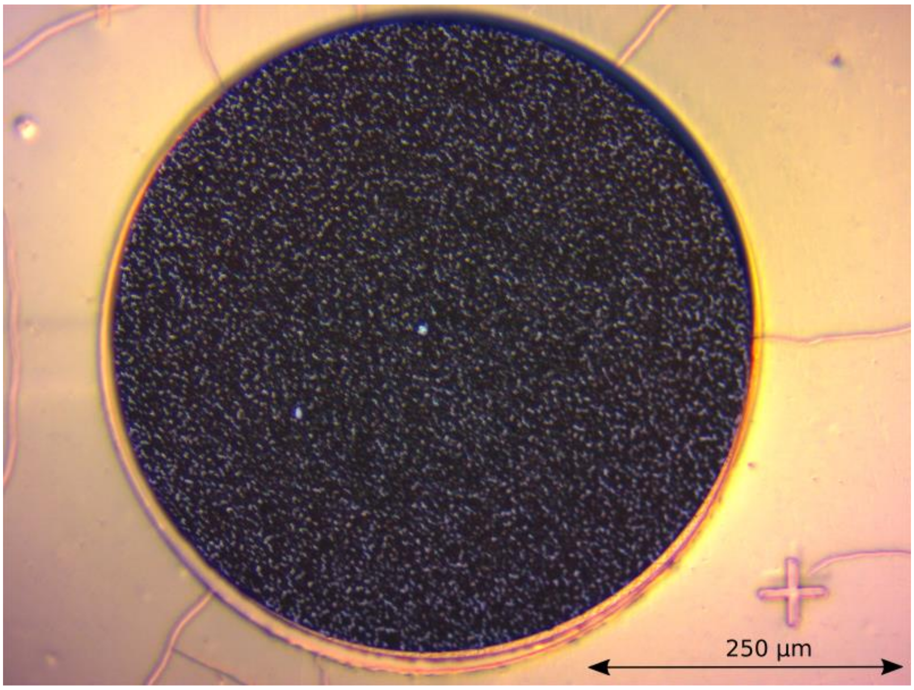

Figure 77: Microscope Image of etched electrode; misalignment is clearly visible

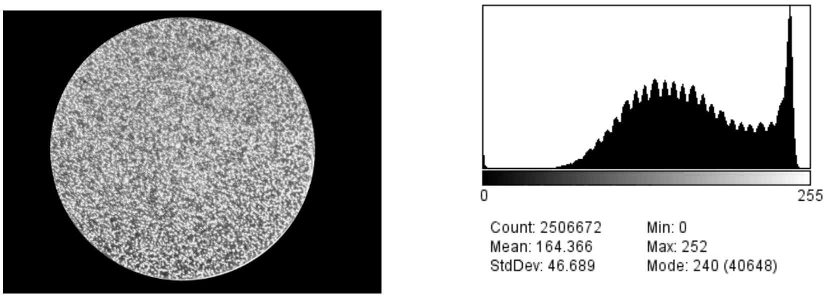

Figure 78: Grayscale image of Figure 77 (left) with its histogram (right)

By analyzing the histogram of the electrode area with the open source software ImageJ (Wayne Rasband, National Institute of Mental Health, Bethesda, Maryland, USA) and setting the threshold to ignore everything, which is not completely white and, thus, metal, it is shown, that 15.8 % of the surface are not covered by the RIE residue and therefore electrically active. This is to be kept in mind for later electrical measurements in chapter 4.3.3.

SEM analysis of such an opened electrode is shown in figure 79. These *RIE grass* called residues are described in literature and occur when the polyimide overheats during the etching process and carbonizes. Normally, the etching process is a simple oxidation of the organics as shown in the following equation (33):

$$CxHy(s) + O_2(g) + plasma \rightarrow CO(g) + H_2O(g) \tag{33}$$

However, in case of overheating, the polyimide carbonizes and leaves typical residues behind, as were shown. [153]

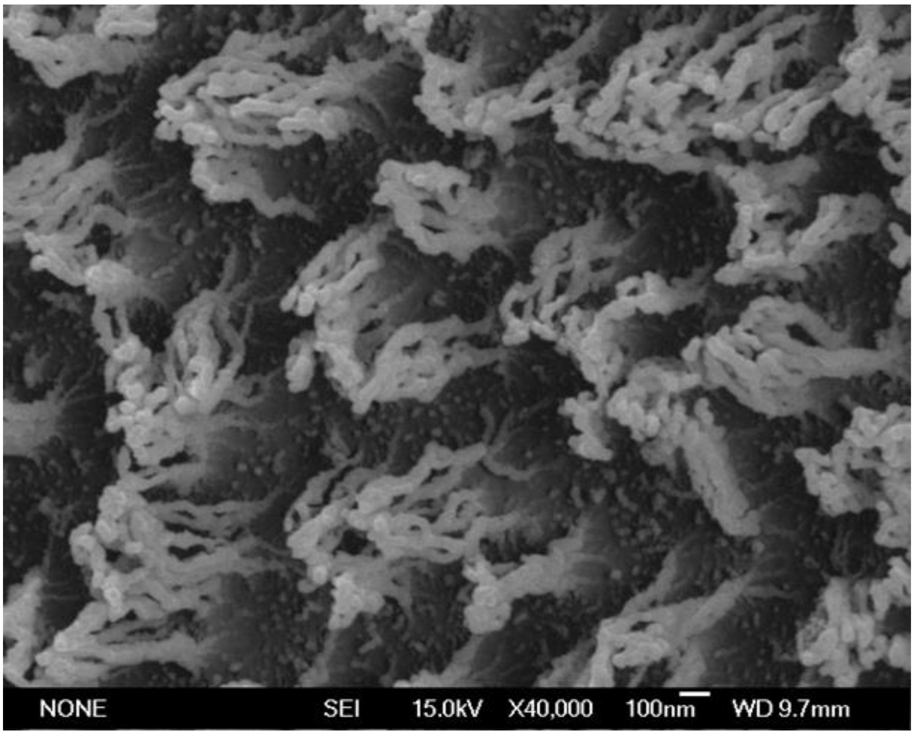

Figure 79: SEM image of RIE etching residues on top of an electrode

It is virtually impossible to remove these residues without using mechanical force. Trials with longer RIE etching times and varying the RF power were unsuccessful as well as trials of removing these residues by wet chemical etching with acetone and even HF. As the electrode is still electrically active, only with a reduced active area of approximately 15 %, these residues have no negative effect on the produced samples.

Other workgroups, like the one of Obermeier et al. suggest an RIE etching atmosphere of oxygen, combined with SF_6 in order to etch polyimide residue-free, but also emphasize that careful attention to the etching parameters is necessary. [154]

4.3.3. ELECTRICAL STABILITY OF POLYIMIDE

The closed non-flexible multilayer samples, introduced in chapter 4.1.1, allow the characterization of the passivating polyimide layers. By measuring the (time invariant) impedance of the metal layers and the electrodes against each other, as well as against an AgCl-counter-electrode, which is positioned in a PBS fluid over the top passivating polyimide layer degradation data can be obtained (refer to chapter 4.2.2).

As the dielectric strength of PI amounts to $2 \cdot 10^6 \frac{\mathrm{V}}{\mathrm{cm}}$ and more, the dielectric breakdown voltage of a 5 µm thick PI layer is approximately 1 kV. More interesting, however, is the behavior of the thin films at an applied voltage of 1 V, which lies in the electric window of PBS and is more applicable for medical implants due to resistance changes of dissipative effects, such as water vapor uptake. In general, absorbed water has a very critical effect on the electrical properties, as water has a very high dielectric constant of 80, so that smallest amounts affect the dielectric constant of PI[1]. Also, as flexible polymers show more water uptake as bulky ones, its effect on the degradation of the produced thin films is measured with the later following flexible samples in mind. [155], [156]

In the following, the two intermediate metal layers inside of the passivation are named *Top Layer* and *Bottom Layer*, in respect of their vertical position. By measuring the resistance between these two electrodes and a counter reference electrode, located in the PBS fluid on top of the sample, the location of degradation inside of the sample could be isolated.

Figure 80 displays measured currents with an applied Voltage of 1 V on a non-flexible sample for three positions against the AgCl-Counter Electrode in PBS. In this sample, the passivation above the electrode was left unopened, to gain data about its quality. After approximately 60 and a half days, suddenly a significant current in the range of 10^{-9} A was measured from the PBS counter electrode against the top metal layer. This indicates the degradation of the top most passivating polyimide layer, most probably due to water uptake from the PBS fluid and electrical degradation. The ongoing, relatively quickly rise of current within a couple of days indicates a progressive delamination of the polyimide layer, thus, enlarging the contacted area of the top layer.

---

[1] Which amounts to 2.9 for PI 2611

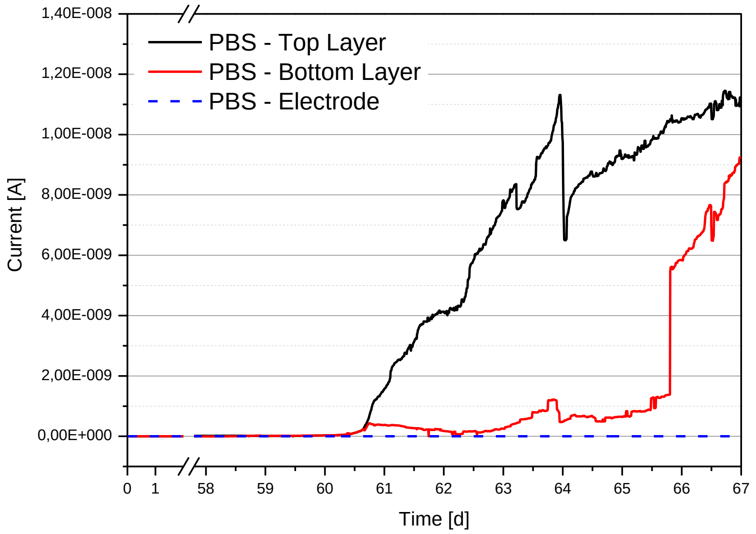

Figure 80: Leakage Current, measured from PBS against metal layers and the electrode (1 V applied)

As no measurable current between the electrode and PBS exists, resulting in an infinite resistance, the passivating system itself is still stable. However, simultaneously with the starting delamination of the top passivating layer, a drop in resistance from the counter electrode to the bottom intermediate layer was detected. As the measured current from PBS to the bottom layer is more constant, it is most probably due to a defective passivating second polyimide layer. Delamination of this layer starts at day 66 with a sudden drop in resistance, resulting in a rise of current flow of about $\Delta I = 5 \cdot 10^{-9}\mathrm{A}$. The defective passivating polyimide layer between the two intermediate metal layers is discussed later in this chapter.

By measuring the resistance of the intermediate metal layers against each other, as well as against an electrode on the circuitry level, the same conclusion of starting degradation inside of the layer stack can be drawn (Figure 81). However, it is now visible without a counter-, or reference electrode in a fluid and is detectable by the sample itself, as the red line indicates. The sample now detects its starting delamination on its own, while still maintaining a fully passivating layer stack, as no measurable current is detected between the intermediate metal layers and the electrode.

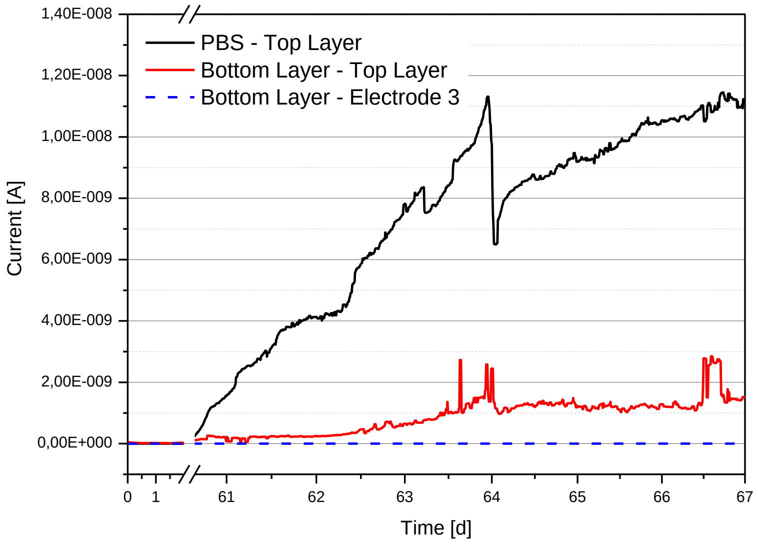

Figure 81: Delamination (measured with 1V applied)

The introduced measurement setup in combination with the multi-layered sample passivation explains the failure of the polyimide passivation layers between the metal layers, which happens simultaneously with the degradation of the top passivating layer.

Figure 82 shows the current of the intermediate layers against each other, as well as the counter-electrode in PBS against several metal layers at the start of the experiment. Here it is visible, that the polyimide film between the metal layers is not fully passivating, which may have several reasons, like air inclusions, microscopic delamination or even pinholes. The resistance amounts to $(2-5)\ \cdot 10^{11}\ \Omega$, which is safely inside of the setup capabilities, ranging up to at least $10^{12}\ \Omega$ (refer to chapter 4.2.3). With this knowledge, the sudden measurable resistance drop between the PBS counter electrode and the bottom layer, occurring together with the degradation of the top metal layer is explained.

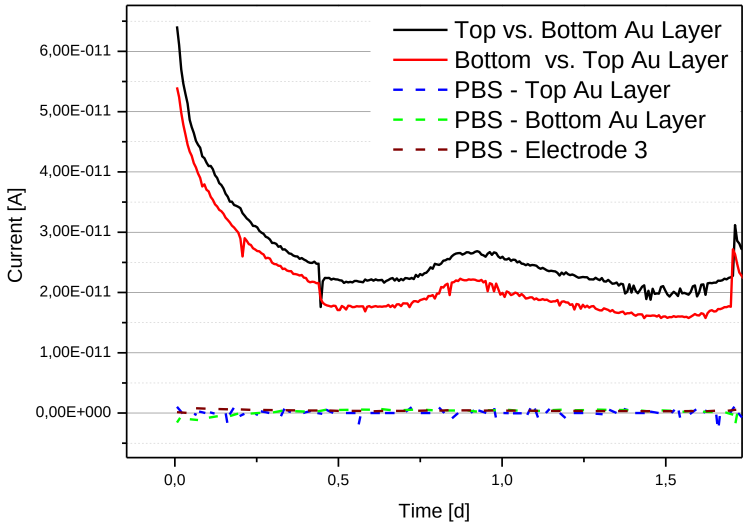

Figure 82: Delamination as seen from beginning (measured with 1V applied)

The current decrement during the first 12 hours is not explained by the creation of Helmholtz layers, as these are formed instantaneously within of a few to several hundred milliseconds [157]. However, starting corrosion and building of an oxide layer are good possible explanations of this often-observed effect. The small peaks at 12 h and approx. 40 hours are both due to the opening of the Faraday Cage.

Figure 83 shows an optical image of the sample surface after the electrical stability measurement, clearly indicating delamination of at least one polyimide layer inside of the curvature of the liquid reservoir. The effect of the delamination was measurable beforehand, thus demonstrating and validating the setups capabilities as well as the sample layout.

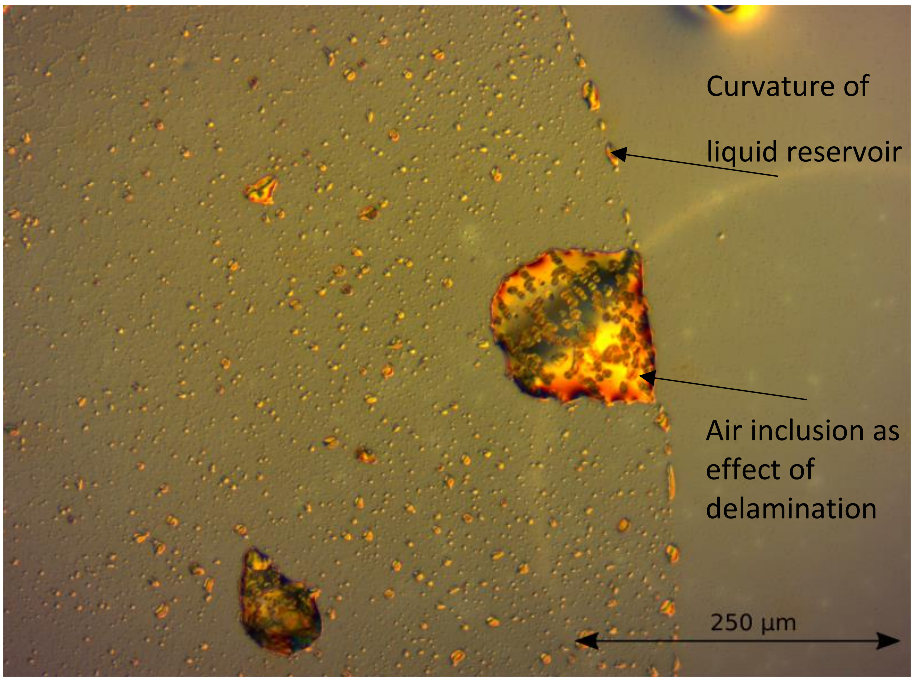

Figure 83: Delamination after long term stability measurement

The intermediate metal layers were intended as an electrical access for later electrode side walls. However, it is shown, that the passivating PI layers are analyzable by utilizing the metal layers as electrical contact, in collaboration with the electrodes.

Starting degradation of the sample was detected, while still maintaining a passivated electrode, thus guaranteeing a fully functional device. This sample layout, combined with opened electrodes featuring a passivated side wall (refer to chapter 4.5), leads to flexible implants, capable of detecting their own degradation (in vivo, as no external access is necessary).

In addition, this simple measurement method allows quick determination of production waste of the multilayer samples, as two of three passivating layers are instantaneously tangible without utilizing external reference electrodes and use of fluid media.

4.3.4. CHEMICAL STABILITY OF POLYIMIDE

The flexible samples are removed from the substrate by dissolving the underlying Ti by wet etching with NH_4F, as is described in chapter 4.1.2. As a result, the toxicity of the polyimide, regarding the uptake of fluorine, is analyzed by energy-dispersive X-Ray spectroscopy (EDX) measurements with the JEOL SEM, provided by Lisa$^+$.

Figure 84 displays the EDX spectrum of a stripped polyimide foil, integrated over a time span of 10 minutes. The three peaks resemble the ubiquitous Carbon, as well as expected nitrogen and oxygen. Table 15 lists the detailed weight percentages for the found substances. Oxygen and nitrogen are found in a ratio of 2:1, which reflects the chemical structure of polyimide as seen in figure 16 in chapter 3.1.1.

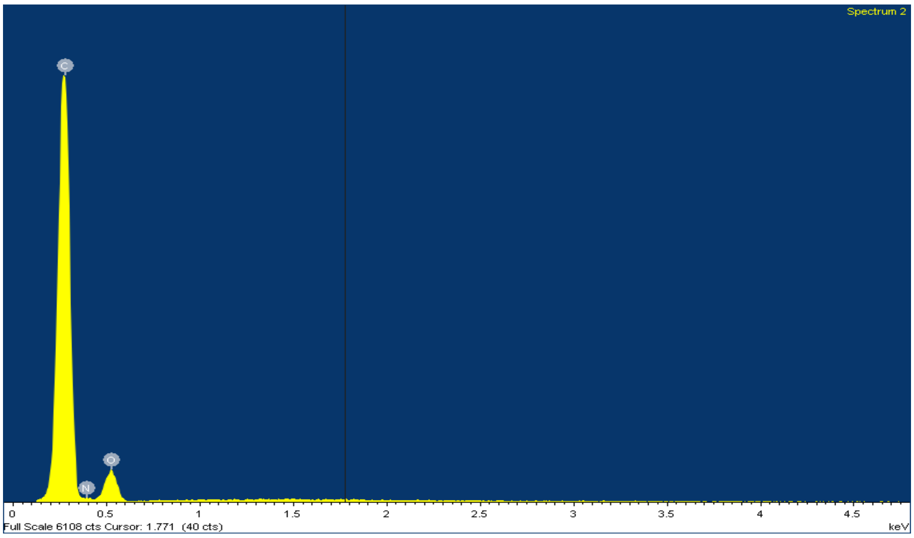

Figure 84: EDX Measurement of pure PI Foil

Table 15: EDX Elements in pure PI Foil

Element	Weight %	Atomic %
C	73.52	78.04
N	7.63	6.95
O	18.84	15.01
F	0.00	0.00
Total	100	100

Primarily, however, no traces of fluorine could be found in the spectrum. Polyimide was previously discussed as chemically very inactive and inert, which is confirmed by this measurement.

The underlying circuitry was also analyzed by EDX, by oxygen etching the topping polyimide layer. It was of interest, whether polyimide may not absorb, but be permeable to it. As a result, fluorine ions would have been detected in the metal circuitry. Figure 85 displays the EDX spectrum of a typical Ti-Au-Ti metal stack with polyimide underneath (and previously above it) and all peaks labelled. In addition, the fluorine position is also marked.

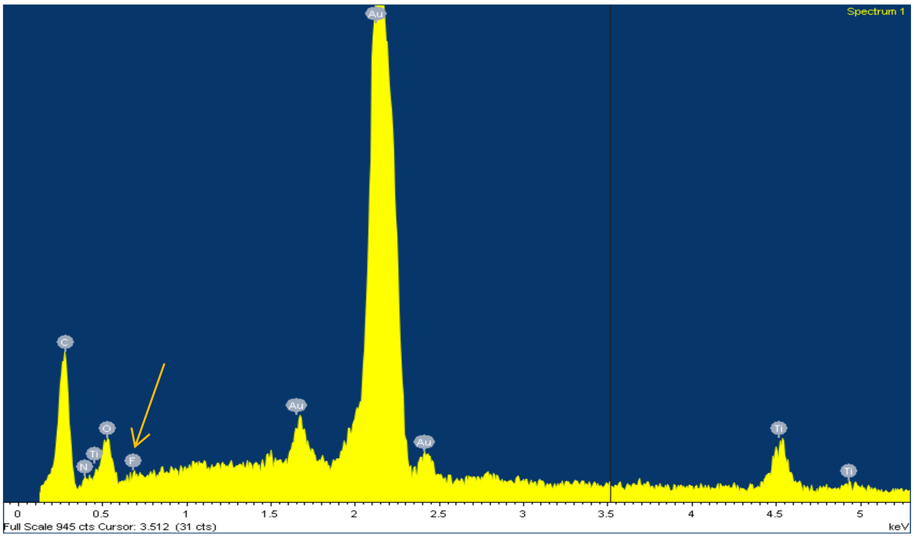

Figure 85 EDX Measurement of Metal Circuitry

The detailed weight and atomic percentages are found in table 16. The data was again obtained by integrating over 10 minutes.

Table 16: EDX Measurement of Metal Layer in PI

Element	**Weight %**	**Atomic %**
C	19.76	65.37
N	0.00	0.00
O	6.76	16.79
F	0.00	0.00
Ti	4.81	3.99
Au	68.66	13.85
Total	100	100

Next to the inevitable carbon, only Ti, Au and oxygen were detected. Thus, the prepared samples are assured to be safe for university studies. The biocompatibility, however should be proven after this process step. As the produced samples are not intended to be implanted, yet the material choice underlies implantability concerns, and the focus of this work lies on an electrode side wall passivation, the missing evidence of fluorine is sufficient for further sample handling.

4.3.5. BENDING OF THIN POLYIMIDE FOILS

Mechanically bending the flexible samples by applying relative pressure differences was the main idea behind the FMS. As the mechanical load is applied uniformly by a fluid, the resulting bending, and therefore the sample elongation were evaluated. The strain gauge introduced and discussed in chapter 4.1.2 was intended to directly give feedback about the sample elongation. Unfortunately, no functional strain gauge, could be established during this thesis, due to micro defects and cracks along the 320 cm long track (Figure 86), or due to defective circuitry at the edge of the samples, where the strain gauges feed lines remain.

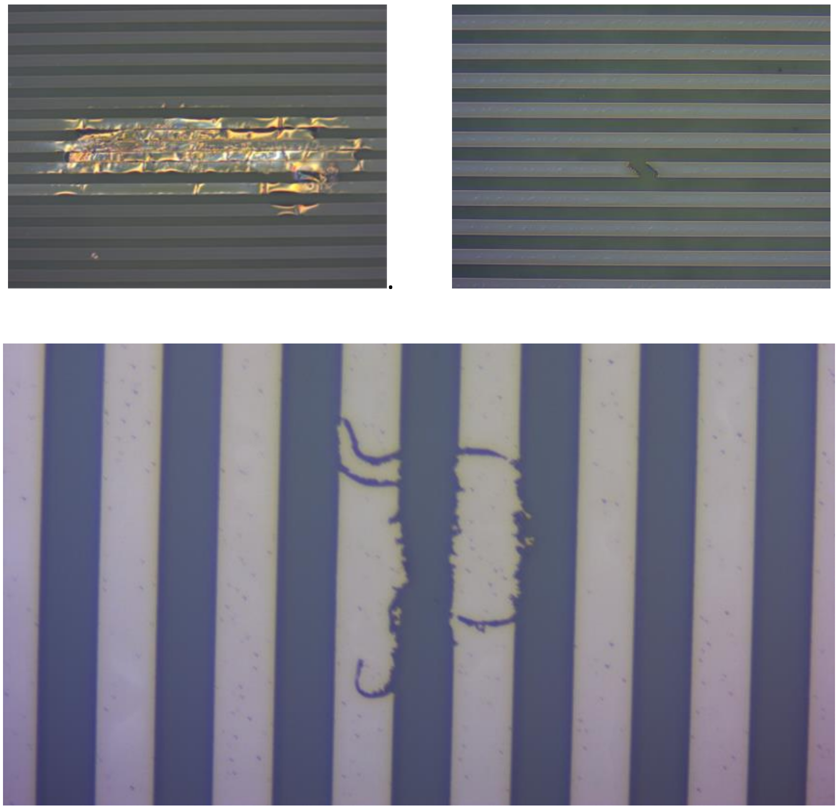

Figure 86: Microscopic Images of visibly defective strain gauges

Therefore, a simulation of sample bending was developed to gain data for expectable surface elongations for variable pressures applied. The simulation was done in ANSYS (ANSYS Inc., Canonsburg, PA, USA) with the flexible sample layout as model and the pressure load within a circle of 24 mm in diameter, placed to match the FMS. The simulation was based on the finite element method. The sample material properties were modeled to match those of PI and Polypropylene (PP) foils.

Figure 87 shows a simulation for a PI foil, being exposed to a relative pressure difference of 50 mbar, resulting in a maximal deformation of 0.7 mm.

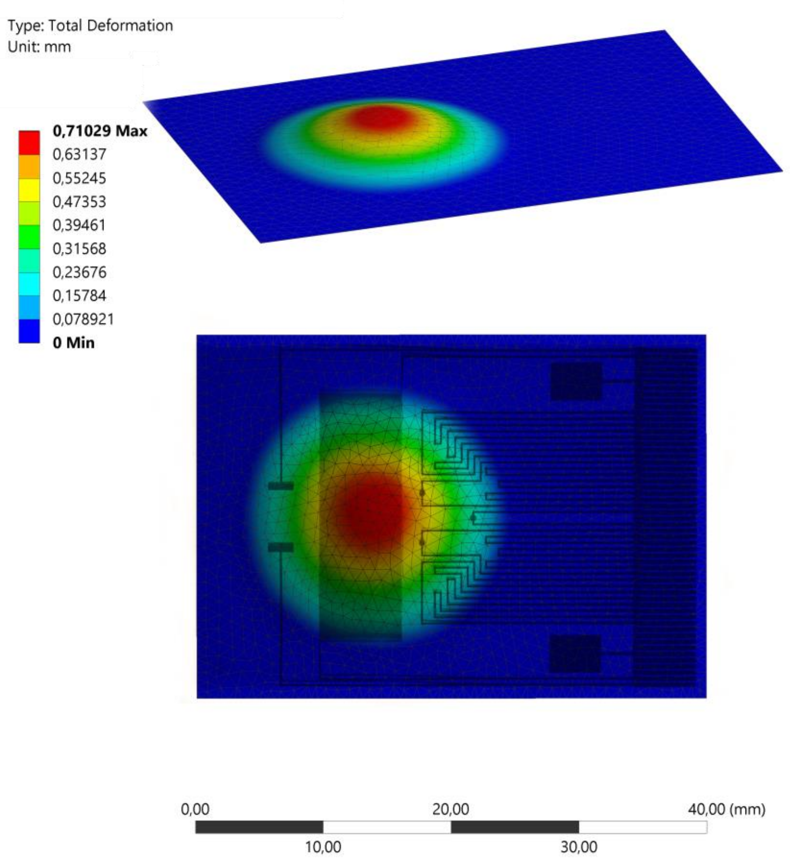

Figure 87: 50 mbar test substrate PI

Bending the polypropylene foils with the FMS resulted in visibly bent samples, as seen in figure 88a, with the surface profile highlighted in figure 88b.[1] By overlaying the appropriate simulation with the same simulation parameters used to bend the sample, the accuracy of the simulation was verified. Figure 88c shows the simulation and figure 88d the simulation overlaid with a photograph of the real bent sample, showing their analogy. Minimal

---

[1] The samples were pressure-exposed for 24 h, after which their surface elongation was measured.

differences may occur due to slight differences in the Young’s modulus or minimal variances in the thickness of the PP foils.

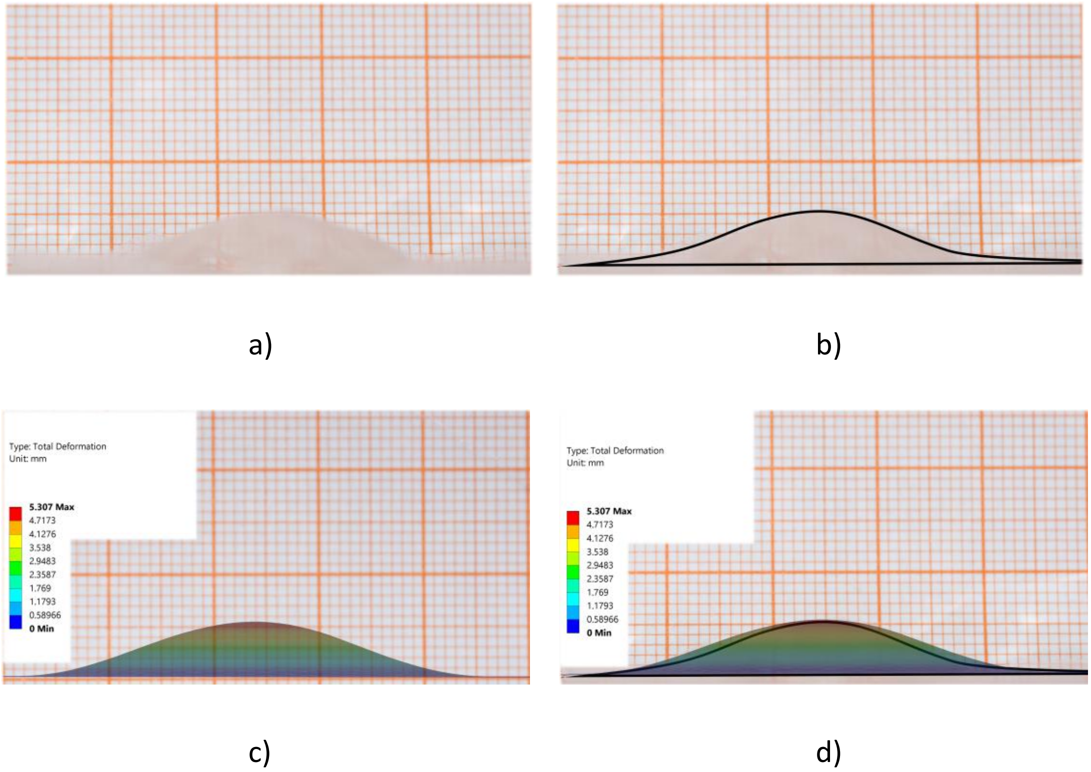

a) b)

c) d)

Figure 88: Comparison between real deformation (PP foil) and FEM simulation at 500 mbar

Bending polyimide and overlaying it with the simulation data results in similar congruent profiles as seen in figure 89. However, as PI bends less due to its higher Young’s modulus, the simulation evaluation is more visible with PP foils. The validation is nonetheless also shown for PI.

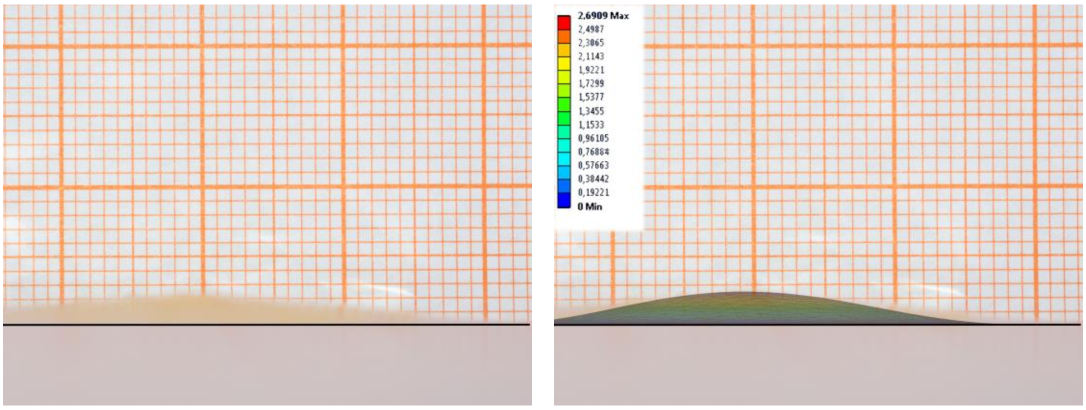

Figure 89: comparison of real deformation and FEM simulation of PI foil 200 mbar

With the simulation being sufficiently accurate, the raw mesh data generated by ANSYS was exported to Matlab (MathWorks, Inc, Natick, MA, USA) where a polynomial equation of the power of 9 was used to fit the raw data (Figure 90).

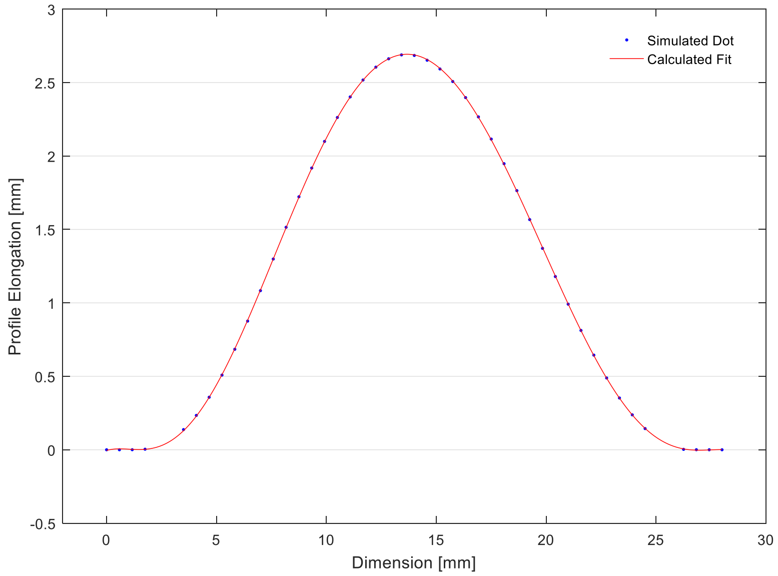

Figure 90: Simulated profile of a polyimide sample with 200mbar pressure applied; the maximal elongation matches that of the real-world sample in figure 89

With the analytical polynomial fitting equation, the resulting surface elongation was calculated with a curve integral. The obtained values are given in table 17 with the profile length set to 24 mm, originating from the FMS pressure chamber diameter of 24 mm. The respective surface elongation Δl is calculated as the difference between the newly created surface length L_s^{ii} with the initial 24 mm and translated to a relative elongation ε_l.

Table 17: Theoretical elongation of PI and PP foil under pressure based on the FEM simulations (l_0 = 24mm)

Material	Pressure (mbar)	L_s^{ii} (mm)	$\Delta l = l_s - l_0$ (mm)	$\varepsilon_l = \Delta l / l_0$
PP Foil				
	500	27.0064	3.0064	12.53 %
	100	24.1308	0.1308	0.55 %
	50	24.0327	0.0327	0.14 %
PI Foil				
	200	24.7411	0.7411	3.09 %
	100	24.1885	0.1885	0.79 %
	50	24.0473	0.0473	0.20 %
	10	24.0019	0.0019	0.01 %

With the theory given in chapter 2.3.4, resistance values can be calculated. More importantly, each pressure difference can now be directly translated to a sample surface elongation and vice versa.

4.3.6. DC MEASUREMENTS WHILE BENDING FLEXIBLE SAMPLES

As discussed in the beginning of chapter 4.3.5, no functional strain gauge could be produced. However, the bending of flexible samples was also visible by DC measurements using both feed lines of single electrodes. Measurements of the surface elongation could not be accomplished by using these feedlines, due to the electrodes being not centered (refer to sample layout - Figure 41 - in chapter 4.1.2) and the greatly reduced sensitivity compared to a fully functional strain gauge. Nevertheless, interesting facts regarding the flexibility of the samples were gathered.

Figure 91 displays the measured resistance R over both feed lines of several electrodes in bend and relaxed sample state, relative to the electrodes' respective maximal resistance R_{bent} in bent state. Bending was achieved by applying a one-sided pressure of 200 mbar. The alternating resistance behavior due to the surface elongation and relaxation is clearly visible, as well as the different impacts this has on the electrodes. The effect of sample bending shows the highest impact on the centered electrode #9, which corresponds to the bending simulations, given in chapter 4.3.5. The further off-centered the electrodes and thus the feedlines are, the smaller the surface elongation in the bend state, and thus the smaller the measured resistance difference in bent and relaxed state. The feedlines and/or bond pads of electrode # 2 on this particular sample were faulty, resulting in the anomalous behavior, which is identified as such, as all other electrodes behaved in a congruent pattern. Overall, an effect of sample bending can be identified by using both feedlines of an electrode.

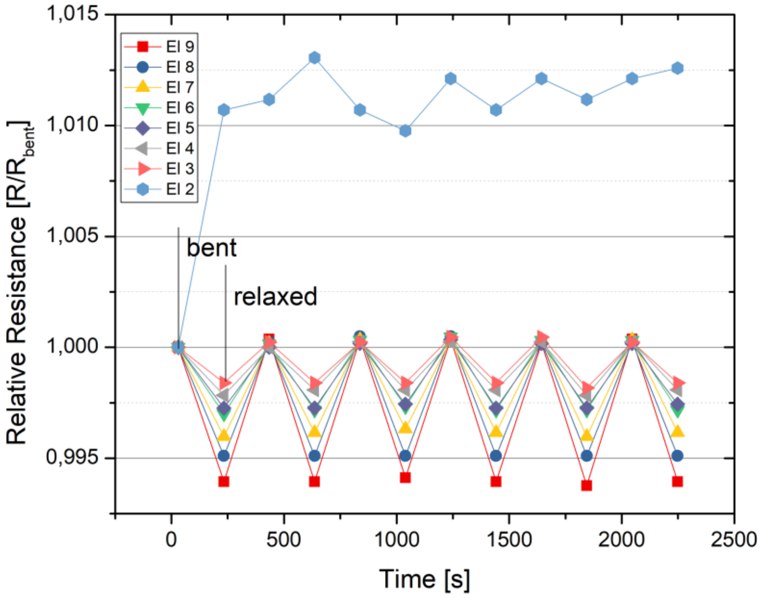

Figure 91: Alternating DC resistivity over electrode feedlines as sample is bend by applying a consecutive pressure of 200 mbar.

Longer alternating sample bending with 50 mbar of pressure applied, lead to the data, displayed in figure 92, where the resistance of electrodes #6 and #12 of a flexible sample in relation to their maximal value in relaxed state is plotted. Similar to figure 91, the resistance in bend and relaxed state was measured and plotted, leading to the alternating data points. However, it is clearly visible, that the overall resistance both, in bend and relaxed state, dropped over time and more importantly with the number of bending cycles.

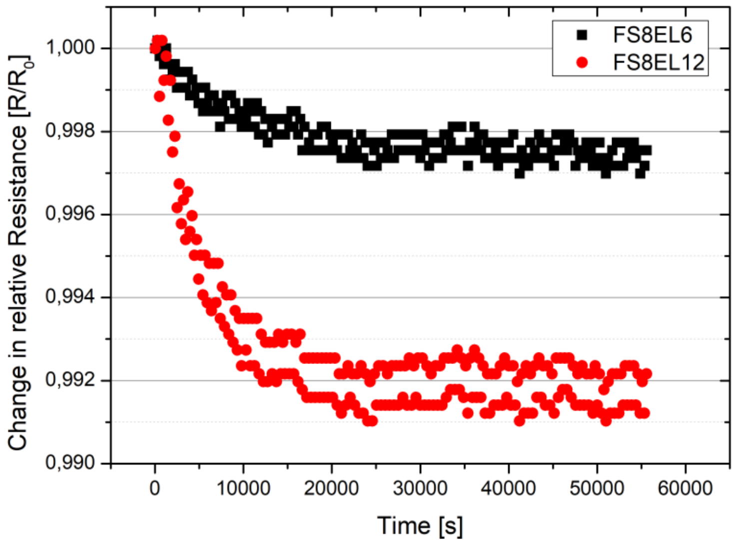

Figure 92: drop in relative DC resistivity during sample bending

The Volmer-Weber layer growth behavior of thin gold films (refer to chapter 3.1.2) with the initial creation of separated clusters is a good first explanation of this result. Mechanically bending the conductive layers quite possible leads to layer stress relaxation as layer growth defects such as grain boundaries and clusters are dissolved and distributed more evenly. The following chapter 4.3.7 presents more details about stress induction and relaxation in thin films.

Closer analysis of the change in resistance, dependent on the number of bending cycles, is given in figure 93, where the average resistance value[1] with its error is plotted. However, with progressive bending, the prior bends are ignored for creation of the averaged value. This results in a fast decrease of the error (as well as the average value) as the main fast drop in resistivity (Figure 92) is quickly ignored. By doing so, the point of reaching final conductivity is visible and reached after about 32 alternating bends. As the remaining dataset gets smaller, the average resistance value becomes vaguer with time (after 90 cycles and more).

---

[1] That is the average of bend and relaxed state, again averaged over all following values

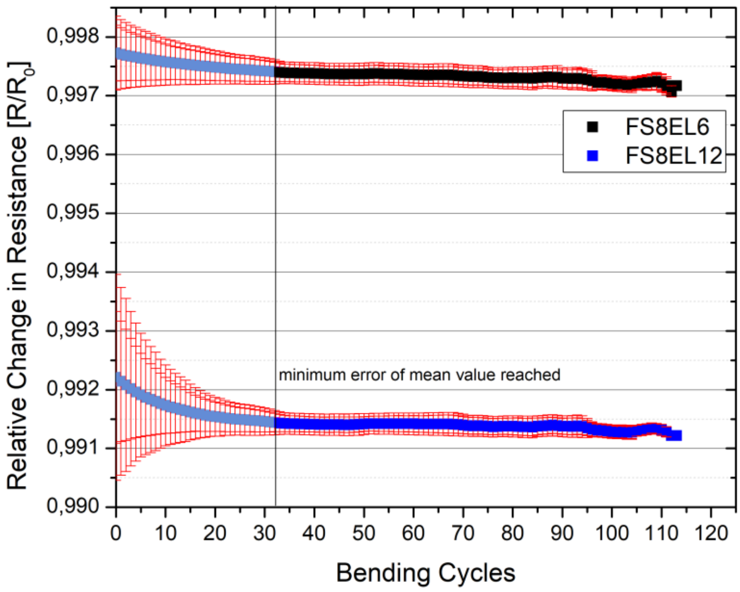

Figure 93: depicting minimal necessary sample bending, until lowest resistance level is reached

Overall, the resistance measured over feedlines increases with progressive sample bending, which was induced by increasing the applied pressure, as can be seen in figure 94. Here, again, the resistance of several electrodes on one FlexMEA is given, all except for one showing similar results (even if electrode #12 also shows increasing resistivity and the overall error is most likeably resulting from a bad connection on the bond pad).

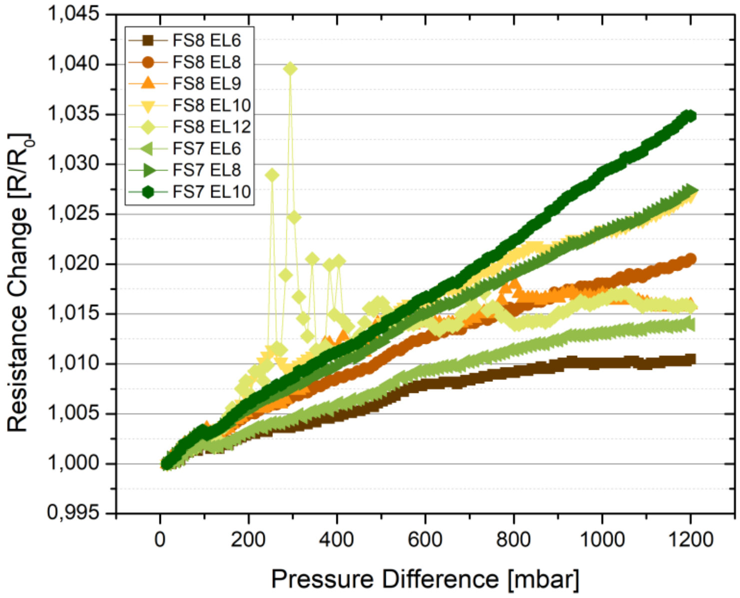

Figure 94: resistivity increases with increased sample bending

Here, a non-linear behavior can be seen after reaching 100 mbar, which corresponds with a surface elongation of 0.79 % (refer to table 17 in chapter 4.3.5). However, the circuitry itself remained stable up to an applied pressure of 1200 mbar, which induced a horizontal sample oscillation of more than 10 mm. Surface elongation simulations in this region must be considered carefully, as no overall valid E-Modulus for polyimide 2611 was found yet.[1]

The surface elongation of 0.79 % at 100 mbar is also congruent with the resistance change of 0.4 %, as the electrodes only experience half of the sample's bending and only a fraction of the feed lines themselves are influenced by the sample bending.

4.3.7. INFLUENCE OF POLYIMIDE TEMPERING ON THE CIRCUITRY

It was hinted, that the increase in conductivity after small initial sample bending is probably due to reduction of the thin film stress of the conductive metal circuitry, which was initially induced during sample production. Normally, thin film stress is measured by disk method, bending beam and X-ray diffraction [158], however, workgroups have also shown to measure it via modified AFM setups [159], [160]. These measurements are not viable for the given

---

[1] Thus, studies like the one of Adrega et. al [145] measure the maximal expandability of gold embedded PDMS, showing it can expand up to 30%, without the circuitry losing its functionality

samples with the gold circuitry being embedded in thin titanium layers and again being enclosed in polyimide, 500 times thicker than the layer itself.

However, AFM measurements (DI Nanoscope AFM, Veeco, NY, US) of a 50 nm thick gold layer on polyimide before and after tempering according to the polyimide process (300° C being held for 30 minutes in N_2 atmosphere) showed the result, given in figure 95. The surface roughness prior to tempering amounted to 0.49 nm and was raised up to 0.74 nm after being temperature exposed. Clearly, tempering the thin film favored the creation of clusters, resulting in a higher surface roughness. It is well known, that grain boundaries, an effect of crystallites coalescence, create thin film stress [161], [162]. This thin film stress is again relaxed by diffusing the created grain boundaries, as Ayas and Van der Giessen conclude [163], which again can be induced by mechanically bending thin films [164].

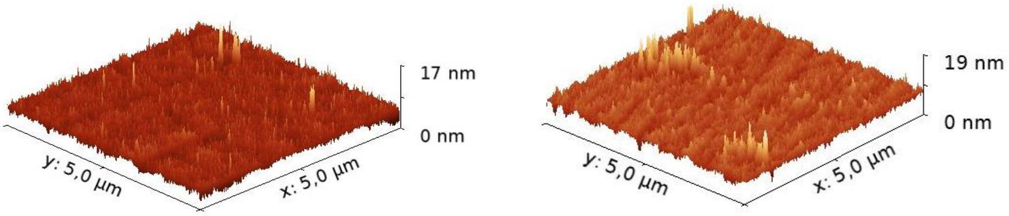

Figure 95: AFM images of a titanium-gold layer not tempered (left) and tempered (right)

Frantlović et al, finally observed the electrical properties of thin film conductive wires regarding their mechanical stress and conclude, that lower thin film stress leads to better electrical conductivity [165], which accords with the apprehension and the data, shown in chapter 4.3.6. This drop in initial electrical resistivity for the first approx. 32 bending cycles of flexible samples must be kept in mind for future measurements.

4.4. ASSESSMENT OF TiO_2 AS ELECTRODE SIDE WALL PASSIVATION MATERIAL

Before passivating electrode side walls, TiO_2 was optically and electrically validated for suitable passivation performance. It was of brief interest, if thin ALD deposited TiO_2 layers uniformly cover the sample surface, as is described in literature, by Kim et al. [166], [167] and reviewed with SEM images on a Ti-Au-Ti metal stack in chapter 4.4.1[1]. In addition, the electrical passivation was analyzed in aspect of estimating the thinnest possible ALD layers

---

[1] Additional afm measurements in chapter 4.4.2 support the results

while still maintaining sufficient electrical passivation. This was quantified by dielectric strength measurements.

As TechniEtch Cr 01 (refer to chapter 3.1.3 and 4.1) was utilized frequently during sample production, its impact on ALD deposited TiO_2 was analyzed by comparing the surface roughness before and after being suspended to the chemical as the electrical abilities of the later sample heavily depend on the TiO_2 layers staying stable when emerged by TechniEtch Cr 01. This is shown in chapter 4.4.2.

4.4.1. OPTICAL AND ELECTRICAL VALIDATION

A standard metal layer (consisting of 10 nm Ti, 50 nm Au and 10 nm Ti) was sputtered onto glass substrates (refer to chapter 3.2.4 for sputtering process) with several ALD layers of varying thickness deposited on top. These ranged from 20 nm to 100 nm, as can be seen in table 18, with the thickness of the 50 nm thick ALD layer being relatively inaccurate according to measurements by reflectometry, as the upper measurement range of the used reflectometer was reached. Thus, all thicknesses above and including 50 nm were analyzed by ellipsometry measurements.

Table 18: Comparison of set and actual layer thicknesses of measured ALD layers

Set layer thickness	**Actual layer thickness measured with**	
	Reflectometry	Ellipsometry
20 nm	19.7 nm	-
50 nm	43.5 nm	53 nm
70 nm	-	60 nm
100 nm	-	125.25 ± 10.53 nm

Figure 96 shows an SEM image of such a 20 nm thick ALD deposited TiO_2 layer on the described metal surface. The TiO_2 layer, visible in the left, covers the metal layer uniformly and even reaches into trenches and scratches. For display purposes, it was partially scratched off during adhesion measurements. This excellent layer conformity is a necessary requirement for the biostable electrode side wall passivation and corresponds with the literature. Thicker layers showed the same uniformity. [166], [167]

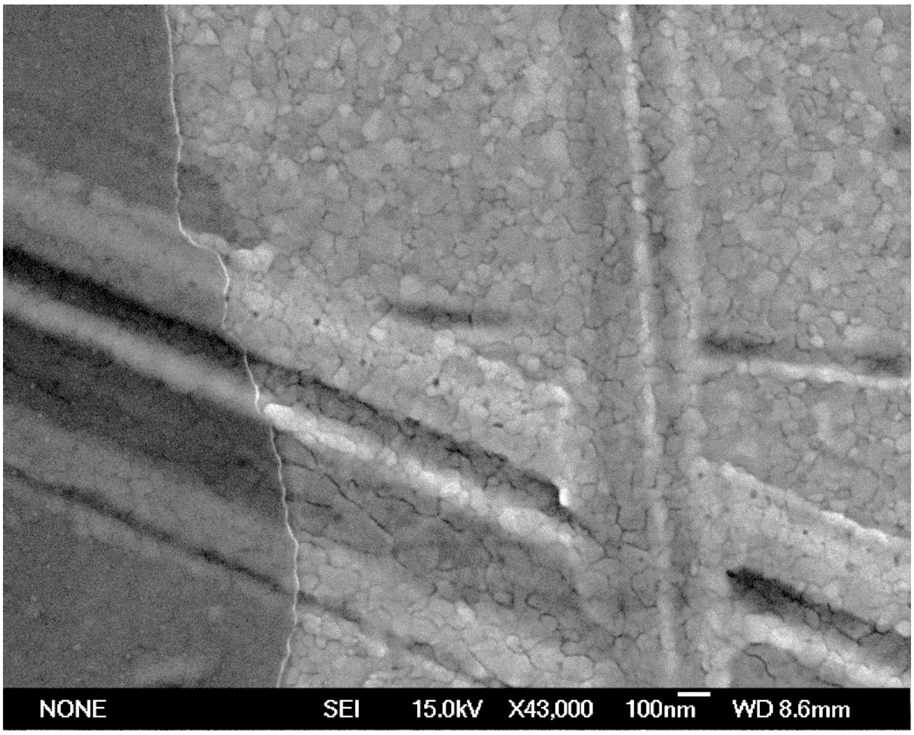

Figure 96: SEM image of a 20 nm TiO_2 Layer (left) on top of a Ti-Au-Ti layer stack

As the primary function of the TiO_2 side wall is electrical passivation, dielectric breakthrough measurements were performed to analyze its strength regarding electric tension. In addition, the thinnest electric passivating layer is identified.

Figure 97 (left) shows a sample for the dielectric breakthrough measurements. It consists of two overlapping standard Ti-Au-Ti metal stacks, which are separated by thin TiO_2 layers of varying thickness, as described in table 18. The TiO_2 layer does not completely cover the sample, to let the underlying metal layer be electrically contactable, as can be seen in figure 97 (right).

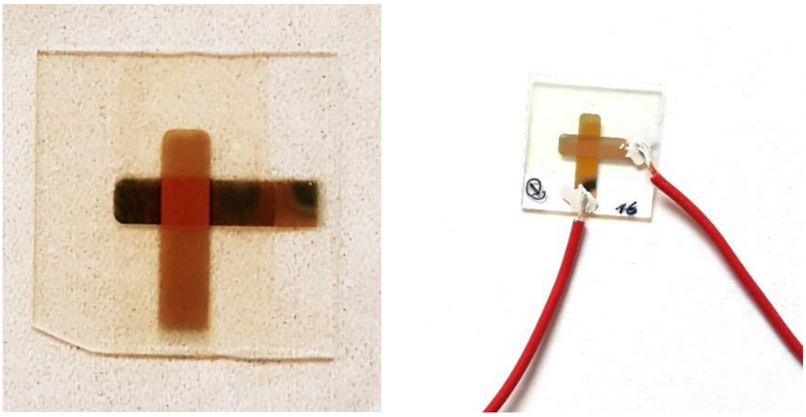

Figure 97: A thin TiO2 Layer between two gold tracks for electrical validation

Figure 98 displays voltage-resistance diagrams of two 20 nm thick TiO_2 layers, showing that both are initially conductive. The SMU reaches its range limit of 10 mA quite quickly with such a low resistance, as is shown with the lower black curve. This results in an apparent linear increase of measured resistance as the current is maxed out with the voltage still rising. Applying Ohm's law, thus, results in a seemingly increasing resistance. The voltage was increased in steps of 10 mV with an error of 20 µV, while the error of the current was $\pm 5 \cdot 10^{-7}\mathrm{A}$, and is, therefore, not visible in the shown scale range.

20 nm thick layers may form a uniform layer, but are not suitable for an electrical passivation, due to probable small defects in the layer, directly leading to an electrical conductivity.

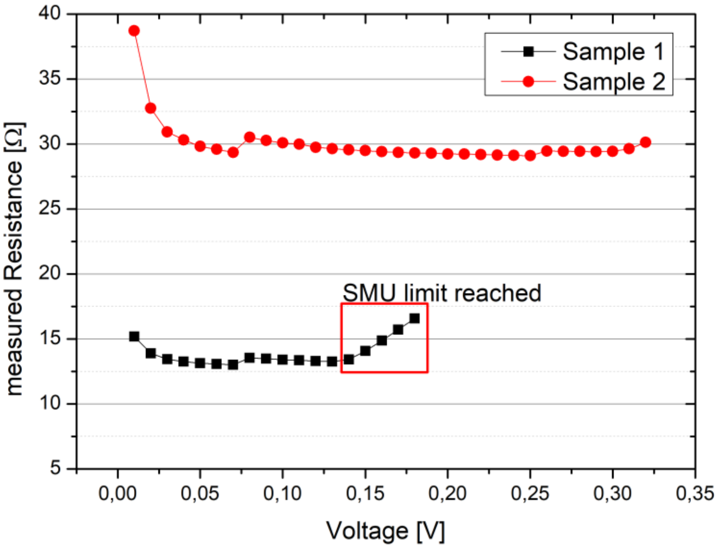

Figure 98: U-R Diagram of two 20nm thick TiO2 Layer; Measurement by Alisa Büttner

Thicker layers, such as the nominally 70 nm (but measured to be 60 nm) TiO_2 layer with its U-R diagram displayed in figure 99 show an initial electric isolation. The dielectric breakthrough occurred at 12.75 V, where a sudden current over the ALD layer was measured. With a layer thickness of 60 nm, this results in a dielectric breakthrough of $2.1 \cdot 10^8 \, \frac{\mathrm{V}}{\mathrm{m}}$, which is in the same range as reported in the literature (refer to chapter 3.1.4). Withstanding an electrical load of 10 V is beneficial for most medical devices, as they typically operate at voltages of 2.5 V – 3 .5 V and a security range is advisable [168]. Thus, TiO_2 layers of 60 nm thickness and above were not only measured to be electrically passivating, but are also capable of withstanding a sufficient electrical load.

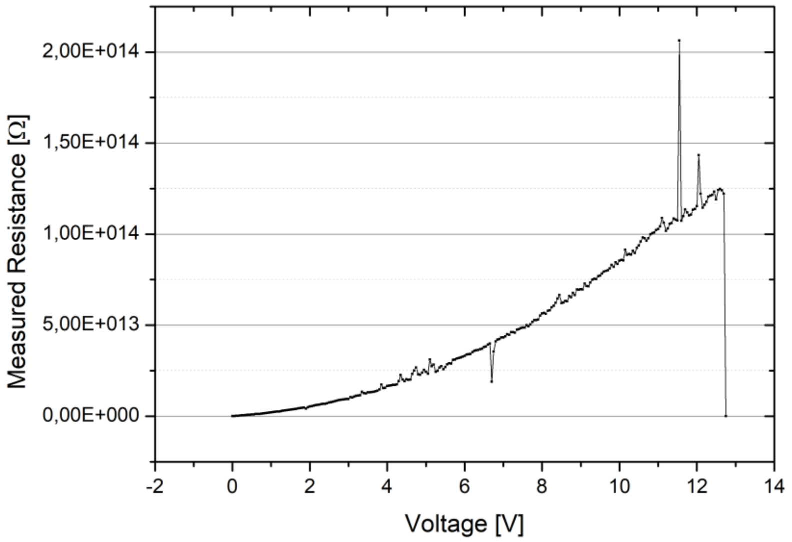

Figure 99: U-R of a 70nm TiO2 ALD Layer; Image by Alisa Büttner

The failure of thinner layers must be considered in this context, as these measurements done here were on a surface area of 5 x 5 mm². The area side length was, therefore, more than 80.000 times larger than the layer thickness, which still formed an electrical passivation over the complete surface. Not only does this feature the capabilities of ALD deposited TiO_2 layers, but also explains the failure of thinner layers, as one small particle or defect in this huge area leads to a complete failure regarding electrical breakthrough. As the later electrode sidewalls offer a fraction of this measured surface, according to $\mathrm{A} = 2 \cdot \pi \cdot r \cdot h = 2 \cdot \pi \cdot 500\ \mu\mathrm{m} \cdot 15\ \mu\mathrm{m} \sim 47 \cdot 10^{-3}\ \mathrm{mm}^2$, an ALD deposited TiO_2 layer leads to very high expectations.

Further data can be found in the work of Alisa Büttner [169].

4.4.2. EVALUATION OF SURFACE STABILITY OF TiO_2 LAYERS

TechniEtch Cr01 from Microchemicals (refer to chapter 3.1.3) is used to strip off the chromium etch mask used to open the electrodes after deposition of the uniform TiO_2 layer. As the side wall passivation must not be chemically attacked, TiO_2 inertness against TechniEtch Cr01 is analyzed. 3 glass samples, with a standard Ti-Au-Ti layer and a 20 nm[1] thick TiO_2 layer deposited on top are measured by atomic force microscopy to evaluate their surface roughness after two of them had been exposed to TechniEtch Cr01. The exposure time was set to 2 min, as it corresponds to the time which is necessary to completely dissolve a chromium etch mask. All measurements were done on a 10 x 10 μm^2 area with a scan rate of 1.19 Hz and 256 measurement points per scan line in hard contact mode.

A 3-dimensional image of the surface of the reference sample is seen in figure 100. These images are obtained with the open source software Gwyddion (David Necas and Petr Klapetek). The surface roughness of this reference surface amounts to (1.0 ± 0.1) nm.

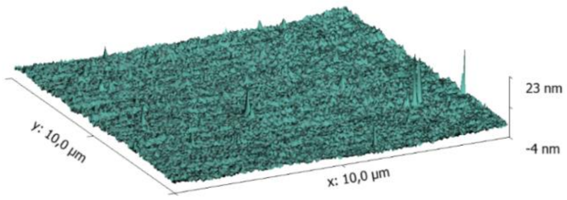

Figure 100: 3D surface image of 20 nm TiO2; Image processed by Alisa Büttner

This excellent surface roughness is typical for an ALD deposited thin film layer and broadly described in literature [167]. Only spin-coated polyimide shows a similar surface roughness in a sub nm scale (refer to chapter 4.3.1).

The second sample with its surface shown in figure 101, was immersed in TechniEtch Cr01 for 2 min, resulting in a surface roughness of (1.7 ± 0.2) nm.

---

[1] it was measured to be 19.7 nm by reflectometry

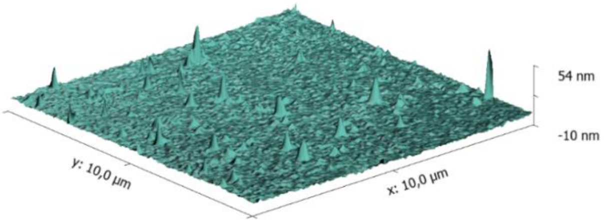

Figure 101: 3D surface image of 20 nm TiO2, immersed in TechniEtch Cr 01 for 2 min; Image processed by Alisa Büttner

The final sample, shown in figure 102, was also immersed for 2 min while being treated with ultra-sonic sound, resulting in a surface roughness of (2.9 ± 0.3) nm.

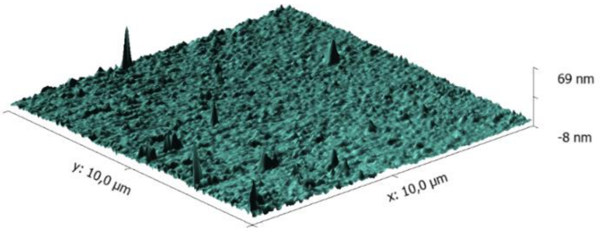

Figure 102: 3D surface image of 20 nm TiO2, immersed in TechniEtch Cr 01 for 2 min in an ultra-sonic bath; Image processed by Alisa Büttner

The lack of obvious dents and cracks in each surface leads to the conclusion, that TiO_2 layers are not significantly affected by TechniEtch Cr01. The change in surface roughness is negligible, considering the treatment. Changes in the nm scale of a surface are expected when in contact with fluids. In addition, different positions in the ALD chamber lead to slightly different surfaces as was shown in prior literature of the work group around Prof. Dr. Bucher [122]. A TiO_2 coated side wall is, therefore, stable enough to withstand the procedure of opening the electrode again, making it highly suitable as an electrode side wall passivation material.

4.5. ELECTRODE SIDE WALL PASSIVATION

This final chapter demonstrates the possibility of passivating electrode side walls with thin atomic-layer deposited TiO_2 layers and validates as well as discusses these. Starting with the non-flexible samples in chapter 4.5.1, the overall possibility is demonstrated. However, the measurement technique delaminated the samples quickly. The flexible samples had to be opened and measured in the FMS to gain reference values, which is shown in the next chapter 4.5.2 with the final electrode side wall passivation on flexible samples discussed in chapter 4.5.3.

4.5.1. VERIFICATION AND VALIDATION OF ELECTRODE SIDE WALL PASSIVATION ON NON-FLEXIBLE SAMPLES

Opened, but non-flexible samples were coated with approximately 100 nm of atomic layer deposited TiO_2, as described in chapter 3.2.7, which completely covered the electrode side walls, as well as the electrodes themselves. Figure 103 shows a Helium-Ion-microscope image of a passivated electrode side wall, after electrical measurements were performed, showing beginning delamination. This delamination is clearly visible with the misaligned top intermediate metal layer. The lower intermediate metal layer is further misaligned back into the polyimide and, thus, not visible in this image. However, when comparing with the upper polyimide side wall, the twice as tall lower one clearly indicates the presence of the included lower intermediate metal layer (also refer to chapter 4.1.1 for misalignment discussion). In addition, the electrode structure of the same sample is completely covered, when compared to an opened electrode with visible RIE residues as was shown in figure 79 in chapter 4.3.2.

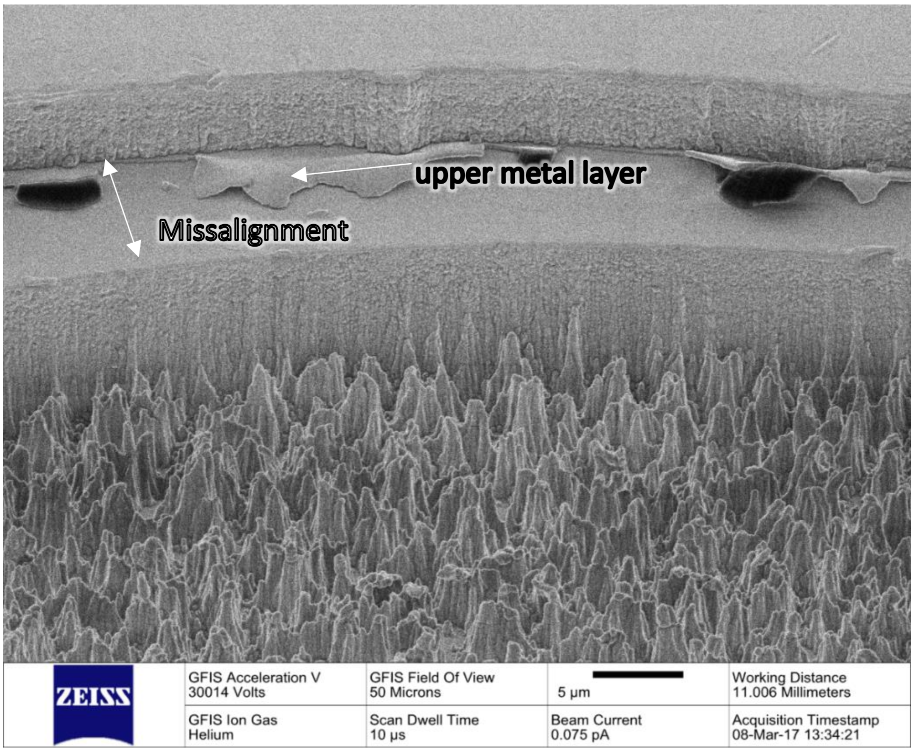

Figure 103: Helium Ion Image of TiO_2 passivated electrode side wall

The ALD process is therefore capable of covering complex 3-dimensional structures, as well as perpendicular electrode side walls.

The delamination of the layers (including the polyimide layers) is explainable with the sample geometry, which is displayed in figure 104. Here, all bond pads are covered with Kapton tape (DuPont, Wilmington, Delaware, US), hindering them of being coated by the ALD process. Removing this Kapton tape for the measurements induced mechanical layer delamination, which is clearly visible in the following electrical measurements.

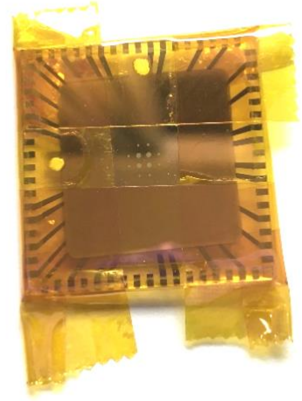

Figure 104: bond pads being covered by Kapton band

Figure 105 shows the DC current, measured from both metal intermediate layers of such a sample, to a reference electrode, located directly above in PBS solution. A linear increase of the measured current is visible due to the ongoing delamination, hence, increasing the electrically active surface. This also explains the sudden rise in current, as the electrode side wall is initially passivated, but layers above it delaminate quickly after the beginning of the measurements. The ongoing increase of the measured current implies ongoing layer delamination.

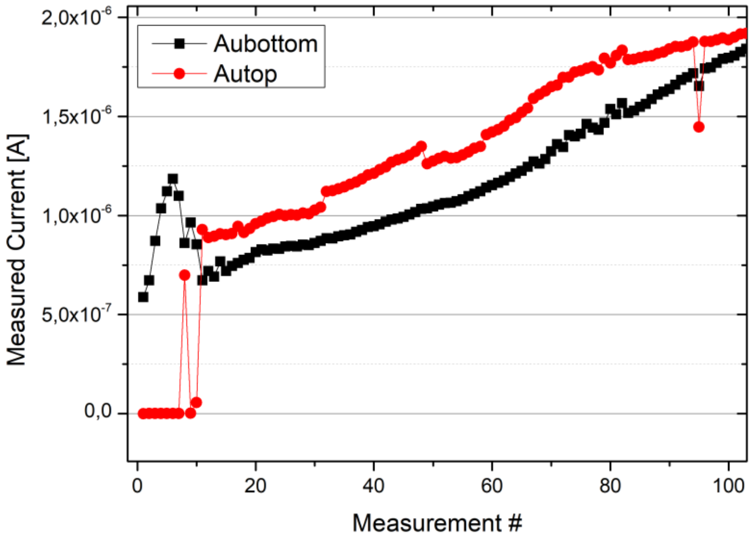

Figure 105: Current measurements during visible delamination

Electrical measurements are given in figure 106 and figure 107 with DC measurements over several indicated positions. The applied voltage was always 1 V. Electrode #6 on the first sample in figure 106 was not electrically contacted due to a bad bond pad and must, thus, be ignored. On the other hand, the data point again displays the detection range of the measurement system. Electrode #2 has a radius of 250 µm, whereas electrode #6 is 125 µm in radius. Assuming an active surface of 15 % of the electrode area (refer to chapter 4.3.2), an approximate electrode surface of 0.03 mm^2 and 0.007 mm^2, respectively, can be calculated. With the calculated gold-PBS transition resistances in ranges of several 100 MΩ (refer to table 3 in chapter 2.3.1), a current of 10^{-6} - 10^{-8} A, with an applied voltage of 1 V is expected and verified in the measurements, indicating opened electrodes prior to the ALD treatment.

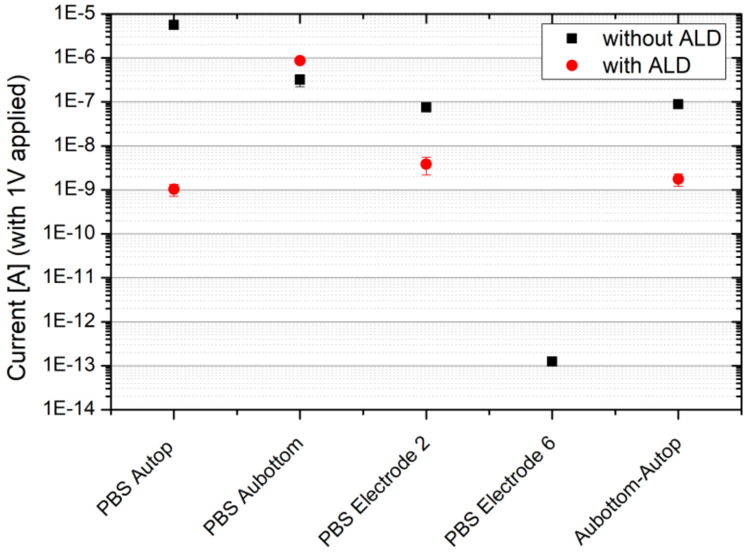

Figure 106: DC Measurements on non-flexible sample #1

On this sample #1, the annular side wall electrodes of the intermediate layer *Autop* are clearly passivated against the PBS solution after ALD treatment, the lower one *Aubottom* however are not, probably due to delamination. The passivation of the electrode sides in height of the top layer is supported by the lower current between both layers themselves.

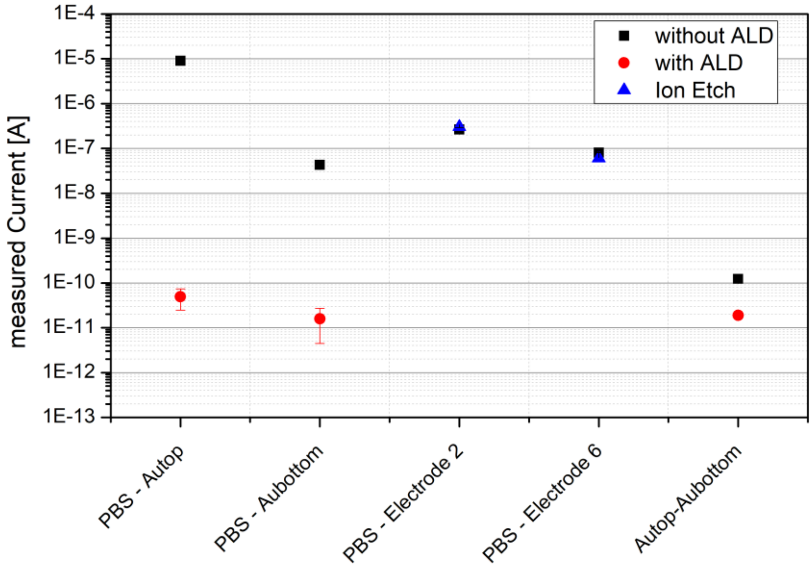

Figure 107: DC measurements on non-flexible sample #2

The second sample, with the measurement data given in figure 107, showed impressive results, as all surfaces were clearly passivated after ALD treatment. Besides, no current was measurable from the PBS reference electrode to the electrodes after ALD coating, which is why those measurement points are non-existent in the graph. All other measured currents were several magnitudes smaller than without coating, clearly showing the electrical passivation of the TiO_2 ALD Layer.

The *Autop* and *Aubottom* cylindrical ring electrodes are both 50 nm high (refer to chapter 4.1.3) and, thus, their electrical surface can be calculated to $\mathrm{A} = 7.85 \cdot 10^{-7}\ \mathrm{mm}^2$ for the electrode with a radius of 250 µm. However, misalignment during the photolithographic process induces errors, which magnify the surface by at least 2 orders of magnitude. Therefore, absolute values for the intermediate layers are not analyzable, but their relative change indicates the quality of the electrode side wall passivation.

Furthermore, the electrodes themselves were opened again by IBE, as described in chapter 3.2.8. Prior to IBE etching, a chromium etch mask was applied by a photolithographic process with electrode openings slightly smaller than the electrodes themselves (refer to the mask design in chapter 3.2.2). The process is sketched on the right page in figure 108, leaving the electrode side wall untouched, while the electrode itself is again opened.

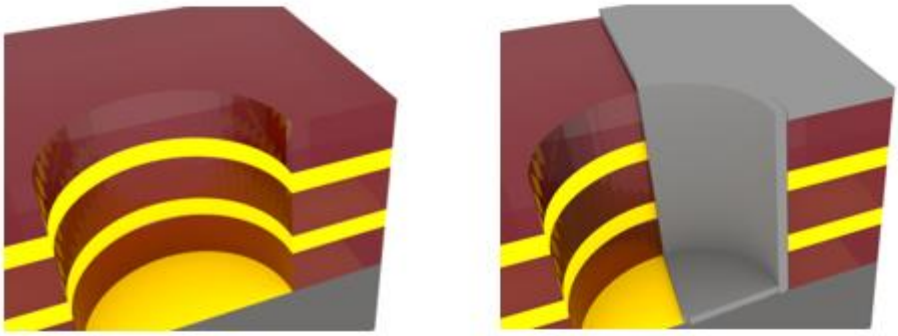

no ALD

ALD covered

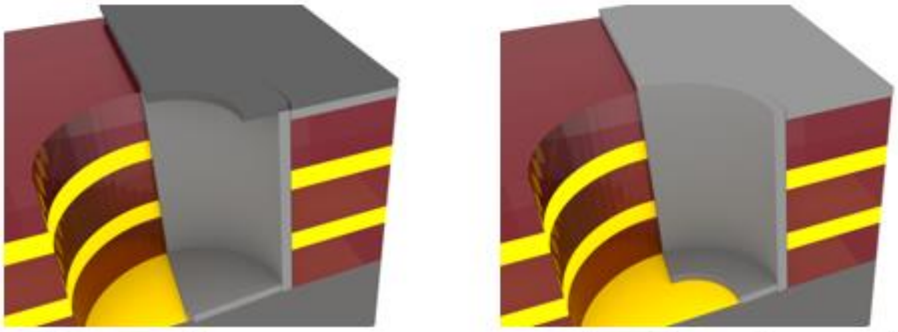

with Cr mask

ALD but electrode opened after ion beam etching

Figure 108: Schematic of ALD coating with subsequent free etching the electrodes

After opening the electrodes again, the current between the PBS reference electrode and the electrodes was measured again and the values are plotted in blue in figure 107. The electrodes side walls showed no measurable current flow[1], while the electrodes themselves regained their value before ALD treatment leading to a proof-of-concept of an ALD based electrode side wall passivation and the possibility of opening the electrode again.

As figure 103 shows a completely passivated electrode, a Helium-Ion microscope image of a final ALD coated side wall with an opened electrode can now be seen in the following figure 109. Like the referenced figure, an electrode surface with the (misaligned) side wall can be seen. In addition, it is clearly visible, how the IBE process opened an inner circle with reduced diameter of the electrode surface as is sketched before in figure 108.

---

[1] This behavior suggests a fully passivated electrode side wall, but may also be the reason of faulty connections/vias to the intermediate metal layers

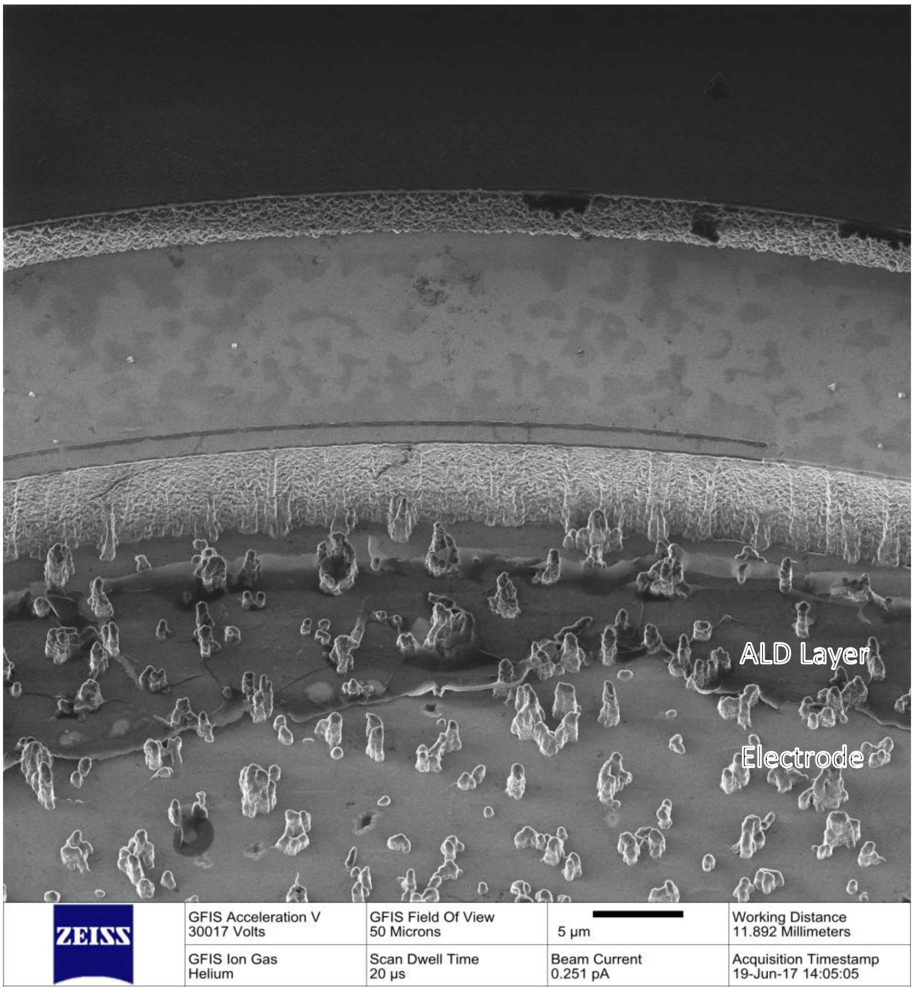

Figure 109: Helium Ion Image of an opened electrode with a passivated side wall

4.5.2. ALD COATING OF ELECTRODES ON FLEXIBLE SAMPLES

The problem of delamination of the intermediate layers due to artificial mechanical stress during measurement is naturally not given in the flexible samples, as all bond pads are located on one side and the sample must not be completely covered during the ALD process. However, reference measurements are not easily feasible, as the sample is not further processable, once it is lifted from the substrate.

As such, several flexible samples with completely covered electrodes (as the polyimide layers were not opened), completely opened electrodes, as well as opened, but ALD covered electrodes are measured to gain reference values for future analysis of electrode side wall measurements.

Figure 110 shows the impedance at 1 kHz, with 1 V applied of all three samples. The lower impedance in magnitudes of $|Z| = 10^4\ \Omega$ on the completely opened sample is clearly visible.

The three center electrodes #8, #9 and #10 are twice as large as the rest and, thus, show a lower impedance (refer to chapter 3.2.2 for mask design). A closed polyimide layer leads to visibly elevated impedances. As the ALD coated flexible sample is mostly passivated except for the first three electrodes, the ability of the ALD layer to completely coat three-dimensional structures is electrically verified.

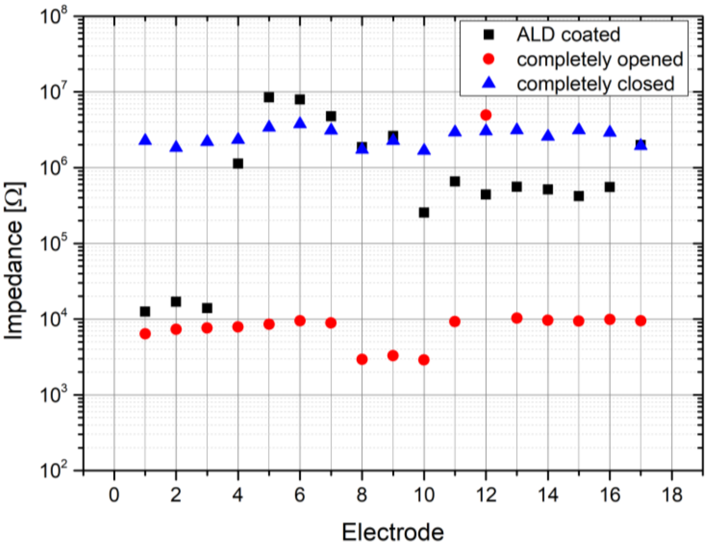

Figure 110: Impedances (1V; 1kHz) of flexible Samples vs the counter Electrode in PBS

The mean values for the small ALD coated electrodes amount to $(2.49 \pm 2.18) \cdot 10^6\ \Omega$, while not counting the first three opened electrodes. The RIE opened flexible sample showed values in the range of $(8.78 \pm 0.94) \cdot 10^3 \Omega$ for the small electrodes[1], clearly marking them as opened. The sample with the unopened, continuous polyimide layer on top of the small electrodes was measured to $(2.75 \pm 0.48) \cdot 10^6\ \Omega$, which is in the same range as the ALD coated. The mean values for the 3 larger electrodes were measured to $(1.58 \pm 0.88) \cdot 10^6\ \Omega$ for the ALD coated, $(3.03 \pm 0.17) \cdot 10^3$ for the completely opened and $(1.89 \pm 0.25) \cdot 10^6\ \Omega$ for the completely closed electrodes, respectively.

An ALD deposited TiO_2 layer, therefore, passivates the electrodes as if they have never been opened.

A similar conclusion is drawn with the phase analysis of these three samples, as is shown in

---

[1] Without electrode #12 which not seems to be opened

figure 111. Here, the mean values for the phase of the standard electrodes amount to $(-67.24 \pm 6.22)\,°$ for the ALD coated [1], $(-56.41 \pm 5.18)\,°$ for the opened and $(-80.02 \pm 3.05)\,°$ for the completely closed, respectively. The 3 larger main electrodes were measured to $(-53.66 \pm 5.79)\,°$ for the ALD coated, $(-43.10 \pm 0.83)\,°$ for the opened and $(-82.96 \pm 1.14)\,°$ for the completely closed ones, respectively. Referring to chapter 2.3.3 for the interpretation of the phase, the polyimide covered electrodes show a capacitive behavior with their phase being close to -90 °. However, the ALD coated, as well as completely opened show a similar phase, with the overall impedance of the ALD coated one being larger, compared to the opened one.

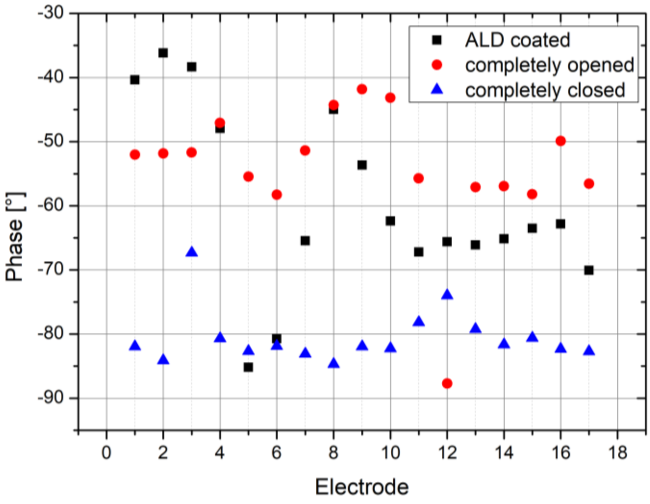

Figure 111: Impedance Phase analysis of flexible samples

The ALD passivation, thus, acts as a mostly ohmic resistance, reaching the same impedances as the capacitive resistance of the polyimide coated sample.

4.5.3. VALIDATION OF SIDE WALL PASSIVATION ON FLEXIBLE SAMPLES

Flexible samples with 2 intermediate metal layers were now analyzed, with one of them having the electrodes opened per IBE and the slightly reduced chromium etch mask, as described in chapter 4.5.1 after the ALD coating. Thus, a sample with opened electrodes (referred to as *No ALD* in the following), a completely *ALD Covered* and an ALD covered with subsequent electrode opening per IBE (*ALD but electrodes opened*) are discussed in the following. The sample mentioned last should only have the electrode side walls passivated

---

[1] Again, the first three electrodes are ignored, as they are clearly not passivated

with the electrodes themselves being electrically active. The resistances were all measured with DC currents, as high resistances are more visible and analyzable with DC measurements.

Figure 112 plots the DC currents of all electrodes vs a reference electrode in PBS solution. Missing values are discussed later in this chapter. The mean values are $(1.21 \pm 1.06) \cdot 10^{-11}\,\mathrm{A}$ for the ALD covered, $(5.34 \pm 2.95) \cdot 10^{-9}\,\mathrm{A}$ for the *No ALD* sample and $(1.37 \pm 2.45) \cdot 10^{-6}\,\mathrm{A}$ (or $(6.20 \pm 3.73) \cdot 10^{-8}\,\mathrm{A}$, by ignoring the large measured current over electrode #11, respectively) for the final ALD treated, with subsequent IBE electrode opening.

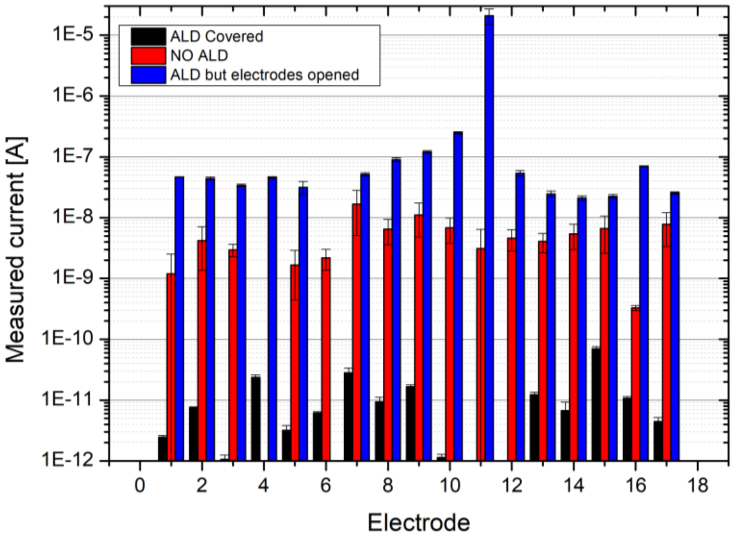

Figure 112: DC measurements (1V applied) on flexible samples of electrodes vs a reference in PBS

In general, a higher measured current is better, as it indicates an opened electrode. Interestingly, the IBE opened electrode showed a smaller resistance to the reference as the initially opened sample. This may be due to enlargement of the electrode surface because of the ion bombardment, which lead to a more 3-dimensional surface or removal in residues. Even if not intended, this result is highly welcomed and confirms the opened electrodes after IBE etching.

The current was also measured between every electrode and the upper intermediate metal layer *Autop* to evaluate the side wall passivation. Figure 113 shows the measured values, however, without the reference values of the ALD covered sample, as the upper metal layer of that sample was not electrically contacted to the via. It is notable, that no measured electrode on the opened sample, without any ALD treatment, shows currents below $10^{-10}\,\mathrm{A}$, whereas 14 out of 17 measured currents on the final ALD treated sample with opened electrodes are below this threshold, marking these electrode side walls as passivated. The first few side walls of the electrodes #1 to #3 are, however, not passivated. A explanation would be the IBE etching of the electrodes themselves. As the electrodes are distributed over the relatively large sample surface of 4 x 3 cm^2, it is most likely for the argon beam to hit the side wall of the outer electrodes. Also, the outer electrodes are more prone to mechanical stress when handling the sample with tweezers. In addition, it cannot be guaranteed, that the ALD layer on these electrode side walls was initially closed, as no measurements before opening the electrodes were possible due to the mechanical stress the sample would have suffered from. The same effect is seen, when measuring the currents between electrodes and the bottom intermediate layer *Aubottom*, displayed in figure 114.

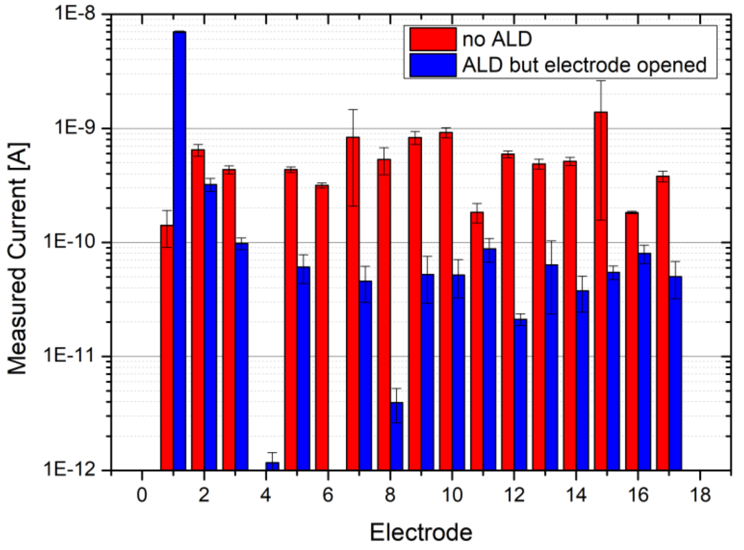

Figure 113: DC measurements (1V applied) of flexible samples vs Autop

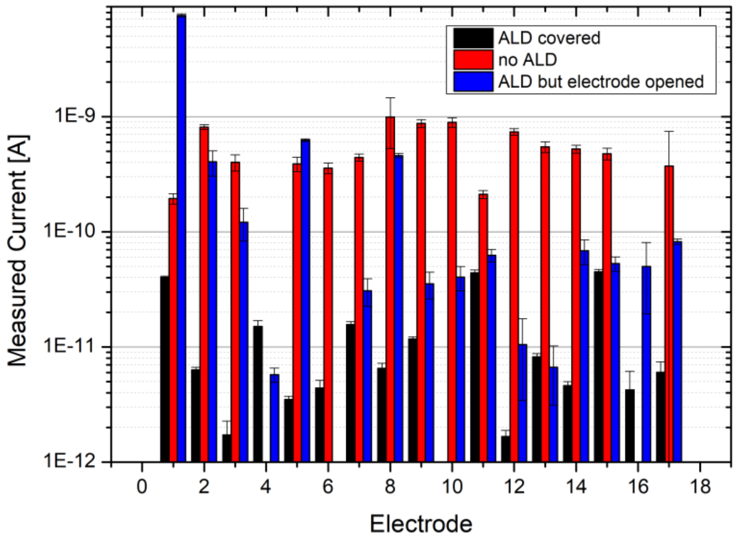

Figure 114: DC measurements (1V applied) of flexible Samples vs Aubottom

Again, the ALD covered sample showed no current above 10^{-10} A. Also, all side walls, excluding those of electrodes # 1, # 2, #3, #5 and #8 are below this threshold, marking them as electrically passivated.

A full analysis of the final sample with opened electrodes, but passivated electrode side walls can be seen in figure 115. All measured values are distinguishable from the background noise, which is below 10^{-12} A and discussed in chapter 4.2.3.

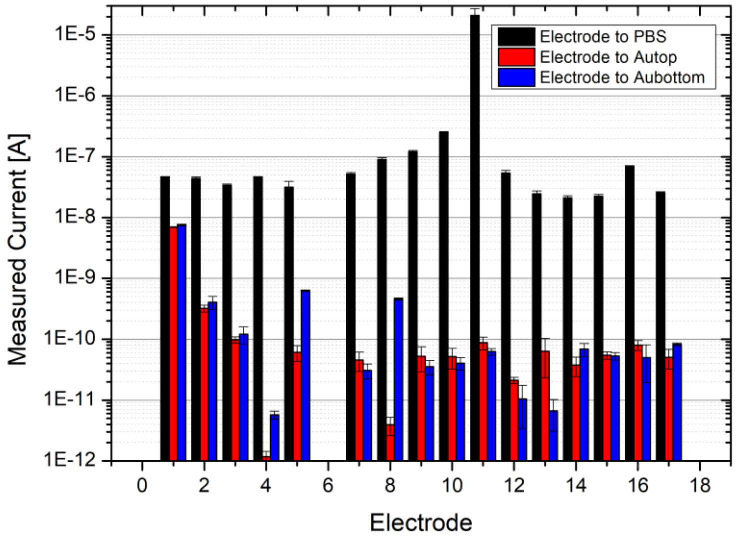

Figure 115: DC Measurements of side wall passivated Electrodes on a flexible Sample

To verify the correctness of these small currents, all measured samples were also characterized by impedance measurements. By doing so, a correct electrical contact to the respective electrode could be verified, as many bond-pads suffered from the manufacturing process with the many wet-chemical processes involved.

Figure 116 shows AC measurements of all bond pads from the final electrode side wall passivated sample against both metal layers as well as the counter reference electrode in PBS solution. The defective bond pads are clearly distinguishable and are marked in the red box. These defective bond pads were not used in the prior DC characterization. This was the reason, why no DC measurements of the ALD covered sample to the upper metal layer are displayed in figure 113. In reverse, a measurable AC current confirms a correct bond pad and as such, validates the extremely low DC currents from before, indicating a passivated electrode side wall.

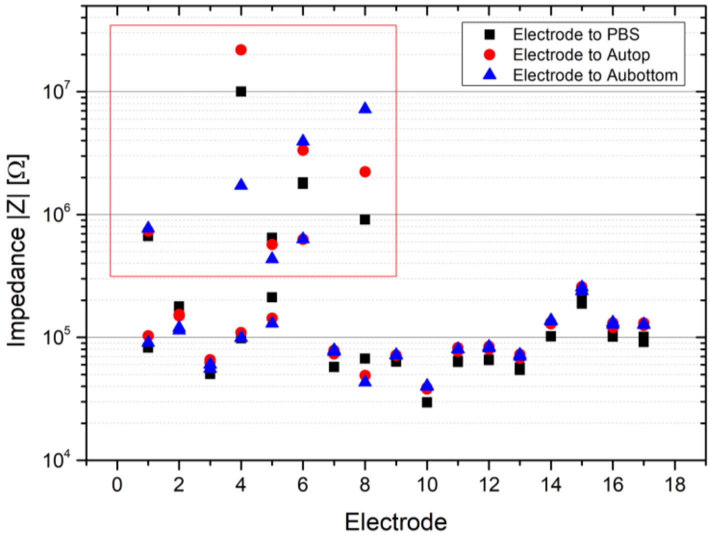

Figure 116: Impedance reference measurements of final ALD covered sample with opened electrodes (1V, 1kHz); The red box marks the measurements of the defective bond pads

In addition, electrical impedance spectroscopy measurements from the ALD covered sample with the opened electrodes facilitate the results. Figure 117 shows the bode plot of electrode #1, which the DC measurements showed to have a non-passivated electrode side wall, while figure 118 displays the Bode Plot of electrode #13 with an intact electrode side wall. Both measurements were performed against the upper intermediate metal layer.

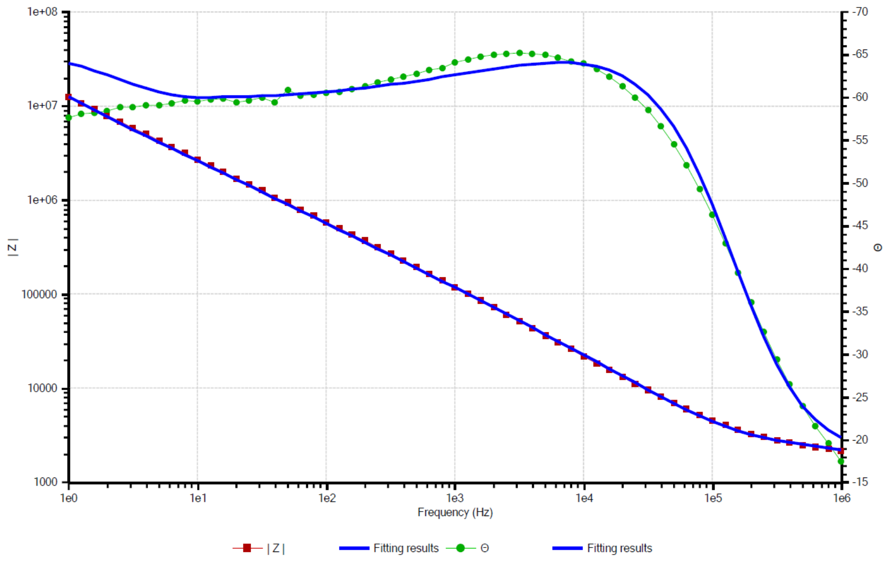

Figure 117: Electrode #1 vs Autop on coated flexible sample with opened electrodes, showing a defective electrode side wall passivation

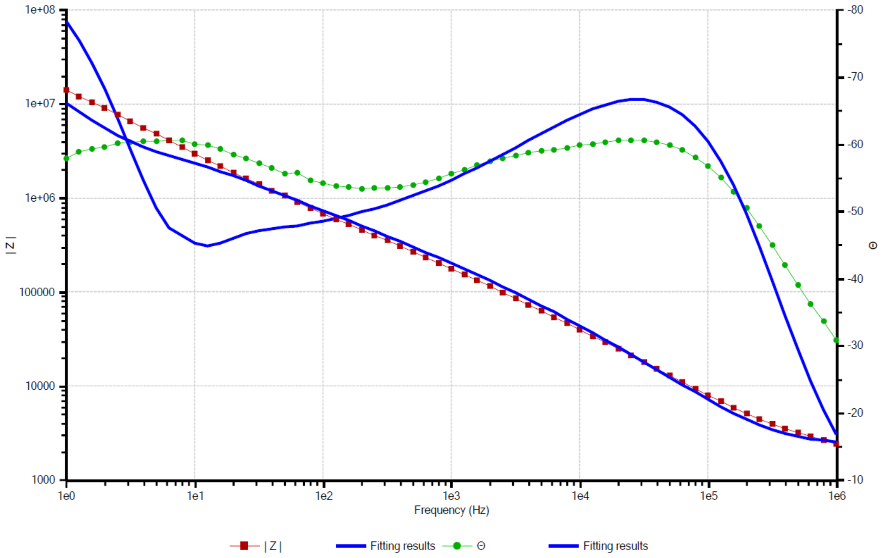

Figure 118: Electrode #13 vs Autop on coated flexible sample with opened electrodes, showing a fully intact electrode side wall, which, therefore, is not truly fitted with the equivalent circuit of a defective coating

Both diagrams are fitted with a slightly modified version of an equivalent circuit for a damaged coating (refer to chapter 2.3.3), shown in figure 119, where R1 stands for the solution resistance and R3 simulates the coating resistance. C1 is the coating capacity, whereas CPE1 and CPE2 are two constant phase elements and W01 a Warburg impedance.

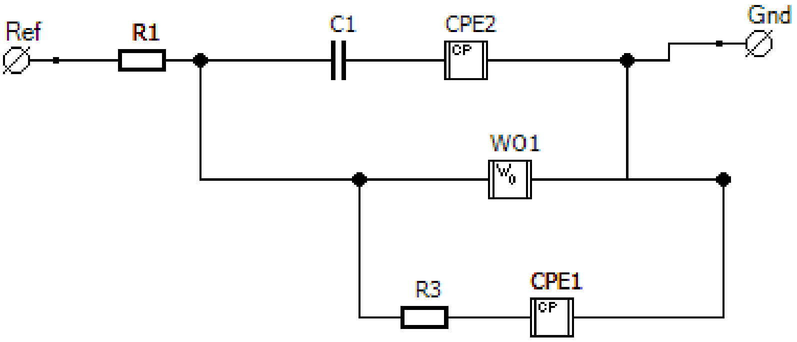

Figure 119: Equivalent circuit for the fits in Figure 117 and Figure 118, based on the circuit in chapter 2.3.3, describing a damaged coating; the fitted values can be seen in table 19

The simulated variables for both diagrams are to be found in table 19, with CPE1, CPE2 and W01 always being -1. The extreme resistance R3 for the coated side wall of electrode #13 explains, why the numerical fit in figure 118 is slightly off. Also, a completely coated side wall is not well fitted with the model of a defective coating. However, by using the same model for both cases and comparing the results, it is clearly visible, that one electrode side wall is completely passivated.

Table 19: Fitted values from the equivalent circuit, displayed in figure 119

		EL #1 vs AuTop		**El #13 vs AuTop**	
Element	**Unit**	**Value**	**Error**	**Value**	**Error**
R1	Ω	1193.3	0,1	2404.2	0,1
C1	µF	0.070	0,309	0.0002	0,0579
R3	Ω	**2704.8**	0,2	$\mathbf{5.912 \cdot 10^{12}}$	$8 \cdot 10^5$

5. CONCLUSION

In this thesis an electrode side wall passivation for flexible MEAs was achieved. This chapter assesses all the prior presented results.

In order to evaluate an electrode side wall passivation, non-flexible as well as flexible MEAs were produced with special attention to the multilayered flexible samples. As no protocols or prior experience in the field of flexible neural implants existed, the first task of this thesis was to implement a manufacturing standard. Beginning with the sample's layout design, the multilayer stack as well as establishment of the fabrication processes, including tuning of equipment parameters, were developed. Critical steps such as the opening of the electrodes were obstacles, which finally could be overcome and did not hinder the development of the flexible samples. Even if the biocompatibility of the produced samples was not especially analyzed, biocompatibility of the produced samples was always kept in mind by careful consideration in material choice. However, as the removal of the flexible samples from the glass substrate is done via HF in this university environment, the final samples are not intended for implantation, even if EDX measurements did not show remaining fluorine atoms inside the samples. As this process step can be circumvented in an industry environment, i.e. by laser-driven delamination [170] and is the only step with unclear consequences to the biocompatibility, it has no disadvantages for medical application.

In general, the presented multilayer passivation with included intermediate metal layers is independent from the substrate removal process, including the HF treatment. It was shown, that the conductive layers in the passivation allow profound in-situ degradation and sample integrity measurements, while the sample is in an active state. This passivation layout allows the creation of neural implants, capable of detecting their own passivation integrity.

Most manufactured samples showed good quality in respect to their passivation and remained stable during testing. However, layer delamination remained a problem with titanium as an adhesion layer. As this thesis did not focus on stabilizing the multilayer stack itself, this was no great disadvantage. In contrary, too stable samples would have given no reference to stability enhancements by the side wall passivation layer. In addition, other workgroups as the one of Stieglitz et al. have shown adhesion layers like SiC, silicon dioxide and silicon nitride to create stable intermediate layers between metal and polyimide, even if stored at 60 °C saline solution for over a year [80]. Their research is transferable to the introduced multilayered passivation, increasing the biostability further.

Furthermore, the flexible samples showed enhanced electrical properties after initial sample bending. It was concluded, that thin film stress relief by mechanical bending leads to increased conductivity, which must be considered for all future measurements of flexible devices, including circuitry, consisting of thin films. A resulting proposal is 30+ initial alternating bending procedures before electrical measurements are concluded.

During this thesis, two measurement setups were designed, fabricated, validated and finally combined to the *Fluidic Measurement Setup* with the possibility of electrical assessment. The electrical setup on its own is called Leakage Setup and was designed in a way to maximize the smallest possible detectable current, as small voltages were needed due to measurements in a fluid medium and, thus, to prohibit electrolysis of the fluid. A detection range down to $10^{-12}\ \mathrm{A}$ was achieved, which was shown to be sufficient to analyze the electrode side wall passivation as well as the polyimide layers themselves. In addition, this measurement range is exceedingly accurate and about 5 times more precise than comparable setups [16]. It was shown, that this accuracy is sufficient to detect a faulty device passivation. It shows great potential as an alternative to industrial standard Ion leakage measurements. Thus, this electrical passivation analysis may act as a device quality control in further device production and research.

In conclusion, the requirements of accurately detecting currents in ranges of few pA was achieved and preserved over the usage of 2 multiplexers, allowing high precision electrical measurements over several channels. Several self-written LabView programs automated these measurements by switching the multiplexer channels and programming the SMU in voltage and detection range, allowing fully automated long-term measurements and, thus, fulfilling all requirements that were defined for the setup.

The Fluidic Setup is the first of its kind, capable of inducing mechanical stress onto flexible samples via an electrolyte fluid while maintaining electrical access to the samples. Several other measurement setups were introduced in chapter 4.2.1, which all fail on at least one of the 6 mentioned requirements. The final fluidic setup not only fulfills the necessary requirements of high precision bending analysis of flexible samples, but also allows further material stress test measurements, like the work of Adrega et. al [145], who elongated PDMS strains by 12 %. This elongation is feasible in our measurement setup with an applied pressure of 500 mbar, which was shown to induce this elongation. The main goal of automatically inducing small loads, in ranges of a few mbar is completely fulfilled and in this form completely novel to the author’s knowledge. Overall, this setup is the first of its kind, combining mechanical bending and electrical measurements all taking place in a fluid medium.

Atomic Layer deposited titanium dioxide was proven to be a suitable material for electrode side wall passivation. Furthermore, samples were covered with 100 nm thin TiO_2 layers, which proved to completely passivate the electrode openings as well as the electrode side walls against each other and against a reference electrode, located outside in an electrolyte fluid. This electrical passivation was stable up to break-through voltages of 10 V, leading to great future expectations for future implants passivation. AC measurements of the thin passivating layer proved its electrical resistance, which confirmed the extremely low DC measured currents. Insufficient electrical contact to the sample could have, thus, been detected, proofing the DC measurements as valid.

Opening the electrodes, while maintaining a passivated electrode side wall was shown to be possible, not only on non-flexible glass based substrates, but also on completely flexible polyimide based multilayered samples. This is a crucial requirement for usage of the shown multilayer passivation in real medical implants with electrode openings.

As such, the electrode side walls (and only those) were validated to be electrically passivated, thus, enhancing the biostability of the complete system. Also, these measurements could distinguish between a correctly passivated electrode side wall and one that is defective, also demonstrating the capabilities of the measurement setups.

This leaves the intermediate metal layers electrically passivated from the electrodes, so that further independent measurements are possible, such as the electric investigation of the polyimide layers. During this thesis, it was proven, that faulty passivating layers as well as starting delamination can be detected directly with these intermediate layers while no visual contact must be given. The only requirement is an intact electrode side wall passivation. Sophisticated in-vivo quality control measurements would be possible with such a system as demonstrated in this thesis.

Finally, the conductivity from the electrodes to an external reference is enhanced by lifting the ALD layer – even if the resulting electrode diameter is reduced, compared to an electrode with no ALD treatment. This effect probably originates from three-dimensional surface enlargements, induced by the IBE treatment to eliminate the ALD layer.

In conclusion, the proof-of concept of an electrode side wall passivation, allowing for highly sophisticated, self-sensing devices, was successfully given. The necessary sample prototypes, as well as measurement techniques were all developed and evaluated during this thesis.

6. OUTLOOK

This chapter provides an outlook to possible future developments, based on the prior presented results. Probable Modifications of the produced samples as well as future applications are given.

All manufactured samples were produced with the clean room environment, provided by the university of Tübingen. The university does provide all necessary technologies to produce flexible implant-like samples, however, the sample quality would benefit enormously from production in an industry standard clean room environment. In addition, this should also lead to fully functional strain gauges, which were not feasible to this point.

All process steps and materials were chosen in regard to the biocompatibility of the final sample. Only the detachment process of he flexible samples with HF is not compatible with this concept, but can be circumvented in an industry production environment (e.g. by laser-driven delamination [170]). The samples have already shown to be biostable over time-spans of several weeks under on-going measurements (refer to chapter 4.3.3). Occurring delamination is caused by the adhesive titanium layers. However, SiC and SiN are in heavy research for adhesives and already show exceedingly good results [171]. As such, the biostability of the produced prototypes could be enhanced greatly by replacing the Ti layers with SiC or SiN layers.

The final electrode side wall passivation was accomplished with atomic layer deposited TiO_2. Other materials, like titanium nitride[1] and silicon dioxide are also viable candidates for passivation.

In general, the next logical step would be in-vitro measurements of the flexible multilayered samples, which would push the prototypes further to a new kind of medical implant with a multilayered passivation. These implants would be capable of self-sensing their future failure, while still remaining fully operational (refer to chapter 4.3.3). Of course, the multilayered passivation must completely surround the implant's electronics. Until now, it was built on one side. Small adjustments during the manufacturing process, such as starting with the bottom multilayer passivation and creating the circuitry way later, would ensure such a novel device.

---

[1] Note, that titanium nitride is conductive. However, it may be a good electrode side wall passivation, but the concept of intermediate metal layers will no longer be applicable

These new devices are only now conceivable with the proof-of-concept of an electrode side wall passivation provided in this thesis.

During this thesis, a fully autonomous measurement setup, capable of mechanically bending flexible devices in a fluid medium, was designed, created and evaluated. This setup can be used for long term measurements, lasting for weeks and even months. With it, more enhanced biostability measurements are possible and also material stress tests can be carried out. Thus, the mechanical stability of the thin ALD layers should be further evaluated [52], [172]. By adding a flow heater, the setup can be easily extended to be capable of accelerated aging measurements. The prior produced samples should greatly benefit by such measurements.

In general this thesis provides flexible prototypes, sophisticated enough to be pushed further to medical implants. The also introduced measurement setup provides a great tool to do so.

7. REFERENCES

[1] G. Jiang and D. D. Zhou, *Technology Advances and Challenges in Hermetic Pachaging for Implantable Medical Devices*. New York, NY: Springer New York, 2010.

[2] J. Comyn and J. Comyn, *Adhesion Science*. Cambridge: Royal Society of Chemistry, 1997.

[3] G. Schmitt, J. Schultze, F. Faßbender, G. Buß, H. Lüth, and M. J. Schöning, “Passivation and corrosion of microelectrode arrays,” *Electrochim. Acta*, vol. 44, pp. 3865–3883, 1999.

[4] W. Betz, “Flexible mikroelektromechanische Implantate für den chronischen Einsatz: Verkapselungskonzuepte und Testverfahren für die Materialcharakterisierung,” Duisburg-Essen, 2011.

[5] M. Kazemi, E. Basham, M. Sivaprakasam, G. Wang, D. Rodger, J. Weiland, Y. C. Tai, W. Liu, and M. Humayun, “A test microchip for evaluation of hermetic packaging technology for biomedical prosthetic implants.,” *Conf. Proc. IEEE Eng. Med. Biol. Soc.*, vol. 6, pp. 4093–4095, 2004.

[6] T. Akin, K. Najafi, R. H. Smoke, and R. M. Bradley, “A micromachined silicon sieve electrode for nerve regeneration applications,” *IEEE Trans. Biomed. Eng.*, vol. 41, no. 4, pp. 305–313, Apr. 1994.

[7] R. R. Richardson, J. A. Miller, and W. M. Reichert, “Polyimides as biomaterials: preliminary biocompatibility testing,” *Biomaterials*, vol. 14, no. 8, pp. 627–635, 1993.

[8] D. Schaubroeck, R. Verplancke, M. Cauwe, D. Cuypers, K. Baumans, and M. Op de Beck, “POLYIMIDE-ALD-POLYIMIDE LAYERS AS HERMETIC ENCAPSULANT FOR IMPLANTS,” in *International Conference on Surface Modification Technologies*, 2017, pp. 1–6.

[9] M. F. Nichols, “The challenges for hermetic encapsulation of implanted devices - a review,” *Crit. Rev. Biomed. Eng.*, vol. 22, no. 1, pp. 39–67, 1994.

[10] M. Op de Beck, Q. Karen, M. Karl, B. Morcos, A. Radisic, and C. Van Hoof, “Biostability and corrosion resistance of a biocompatible encapsulation and interconnect technology for implantable electronics Intro : advanced biomedical packaging,” 2012.

[11] K. Meyer-Waarden, “Der Ursprung bioelektrischer Signale,” in *Bioelektrische Signale und Ihre Ableitverfahren*, Stuttgart: F.Kl. Schattauer Verlagsgesellschaft mbH, 1985, pp. 5–48.

[12] E. Zrenner, K. U. Bartz-Schmidt, H. Benav, D. Besch, A. Bruckmann, V.-P. Gabel, F. Gekeler, U. Greppmaier, A. Harscher, S. Kibbel, J. Koch, A. Kusnyerik, T. Peters, K. Stingl, H. Sachs, A. Stett, P. Szurman, B. Wilhelm, and R. Wilke, “Subretinal electronic chips allow blind patients to read letters and combine them to words.,” *Proc. Biol. Sci.*, vol. 278, no. 1711, pp. 1489–97, May 2011.

[13] D. J. DiLorenzo and J. D. Bronzino, *Neuroengineering*. CRC Press, 2007.

[14] K. W. Horch and G. S. Dhillon, *Neuroprosthetics*, vol. 2. WORLD SCIENTIFIC, 2004.

[15] R. Traeger, “Nonhermeticity of polymeric lid sealants,” *IEEE Trans Parts Hyb Pac*, vol. 13, no. 2, pp. 147–152, 1977.

[16] R. Von Metzen, “Parylene C as a Substrate Material for Micro Implants,” Albert-Ludwigs-Universität Freiburg, 2012.

[17] J. J. Licari, *Coating materials for electronic applications : polymers, processes, reliability, testing*. Noyes Publications, 2003.

[18] J. B. Park and R. S. Lakes, *Biomaterials: An Introduction*. Springer Verlag, 2007.

[19] “DIN EN ISO 10993-1,” no. August. DIN Deutsches Institut für Normung e.V, p. 93, 2009.

[20] E. Wintermantel and H. Suk-Woo, *Medizintechnik - Life Science Engineering*. Heidelberg, Germany: Springer-Verlag, 2008.

[21] C. Hassler, T. Boretius, and T. Stieglitz, “Polymers for neural implants,” *J. Polym. Sci. Part B Polym. Phys.*, vol. 49, no. 1, pp. 18–33, Jan. 2011.

[22] H. Hämmerle, K. Kobuch, K. Kohler, W. Nisch, H. Sachs, and M. Stelzle, “Biostability of micro-photodiode arrays for subretinal implantation,” *Biomaterials*, vol. 23, no. 3, pp. 797–804, 2002.

[23] D. F. Williams, “On the mechanisms of biocompatibility,” *Biomaterials*, vol. 29, no. 20, pp. 2941–2953, Jul. 2008.

[24] D. Flötotto, “Mechanisms of intrinsic stress formation in thin film systems David Flötotto,” no. 246, p. 212, 2013.

[25] M. J. Pryor and D. J. Astley, “Bimetallic Corrosion,” *Corros. Third Ed.*, vol. 1, p. 1:213-1:243, 2013.

[26] Y. Awakuni and J. H. Chalderwood, “Water vapour adsorption and surface conductivity in solids,” *J. Phys. D Appl. Phys*, vol. 1038, 1972.

[27] W. M. Haynes, *Handbook of Chemistry and Physics*. CRC Press, 1995.

[28] J. C. GRIESS, “Crevice Corrosion of Titanium in Aqueous Salt Solutions,” *CORROSION*, vol. 24, no. 4, pp. 96–109, Apr. 1968.

[29] H. Satoh, K. Shimogori, and F. Kamikubo, “Crevice Corrosion Resistance of Some Titanium Materials.,” *Platin. Met. Rev.*, vol. 31, no. 3, pp. 115–121, 1987.

[30] K. C. Kao, “Electrical conduction and breakdown in insulating polymers,” in *Proceedings of the 6th International Conference on Properties and Applications of Dielectric Materials (Cat. No.00CH36347)*, vol. 1, pp. 1–17.

[31] J. C. Fothergrill, “A critical review of water treeing mechanisms,” in *IEE Colloquium*, 1993.

[32] E. Moreau, A. Boudet, C. Laurent, and C. Mayoux, “Recent advance in fine structure of water trees by confocal microscopy,” *6th Int. Conf. Dialectr. Mater. Meas. Appl.*, pp. 488–491, 1992.

[33] P. D. Hoagland and S. W. Fox, “The hydrolysis of polyimides,” *Experientia*, vol. 29, no. 8, pp. 962–964, 1973.

[34] R. Deiasi, “Thermal regeneration of the tensile properties of hydrolytically degraded polyimide film,” *J. Appl. Polym. Sci.*, vol. 16, no. 11, pp. 2909–2919, 1972.

[35] L. E. Stephans, A. Myles, and R. R. Thomas, “Kinetics of alkaline hydrolysis of a polyimide surface,” *Langmuir*, vol. 16, no. 10, pp. 4706–4710, 2000.

[36] “Product Bulletin: ma-P 1200 — Positive Tone Photoresist Series Resists for UV Lithography.” Micro resist technology GmbH, 2017.

[37] C. G. Willson, R. R. Dammel, and A. Reiser, “Photoresist materials: a historical perspective,” 1997, p. 28.

[38] A. C. Mack, “Semiconductor Lithography (Photolithography) - The Basic Process.” [Online]. Available: http://www.lithoguru.com/scientist/lithobasics.html. [Accessed: 17-May-2017].

[39] T. Ono, T. Kenmotsu, and T. Muramoto, *Reactive Sputter Deposition*, vol. 109. Springer, 2008.

[40] I. Langmuir, “The Effect of Space Charge and Residual Gases on Thermionic Currents in High Vacuum,” *Phys. Rev.*, no. 2, p. 329, 1913.

[41] N. Hardy, “What is Thin Film Deposition By Thermal Evaporation.” Semicore Equipment, Inc, 2013.

[42] L. Marton and C. Marton, *Methods of Experimental Physics*. Academic Press, 1979.

[43] K. S. S. Harsha, *Principles of Physical Vapor Deposition of Thin Films*. Elsevier, 2006.

[44] A. Risse, *Fertigungsverfahren der Mechatronik, Feinwerk- und Präzisiosgerätetechnik*. Wiesbaden: Vieweg und Teubner Verlag, 2012.

[45] J. A. Thornton, “Influence of apparatus geometry and deposition conditions of te structure and topography of thick sputtered coatings,” *Vac. Sci. Technol.*, vol. 11, no. 4, p. 666, 1974.

[46] U. Hilleringmann, *Mikrosystemtechnik*. Wiesbaden: Teubner, 2006.

[47] R. Löffler, “Strukturierungsmethoden von Titanoberflächen für biomedizinische Untersuchungen,” Eberhard Karls Universität, 2014.

[48] I. Brenda, I. Prenitzer, W. Brian, W. Kempshall, and L. A. Gianuzzi, *Ion - Solid Interactions*. Springer Science.

[49] L. Todd, *Micro Molding for Medical Applications*. Prototyp. Technol. Int., 1997.

[50] R. Puckett, S. Michel, and W. Hughes, *Ion Beam Etching*. Commonw. Sci. Corp, 1991.

[51] L. A. Giannuzzi and F. A. Stevie, *Introduction to focused ion beams : instrumentation,*

theory, techniques, and practice. Springer, 2005.

[52] R. W. Johnson, A. Hultqvist, and S. F. Bent, “A brief review of atomic layer deposition: From fundamentals to applications,” *Mater. Today*, vol. 17, no. 5, pp. 236–246, 2014.

[53] H. B. Profijt, S. E. Potts, M. C. M. van de Sanden, and W. M. M. Kessels, “Plasma-Assisted Atomic Layer Deposition: Basics, Opportunities, and Challenges,” *J. Vac. Sci. Technol. A Vacuum, Surfaces, Film.*, vol. 29, no. 5, p. 50801, Sep. 2011.

[54] J. Geng and D. Haehnel, “OBERFLAECHEN PEALD – Atomlagenabscheidung mit Plasmaunterstuetzung erschließt neue Anwendungsfelder,” *Womag*, pp. 1–4, 2013.

[55] G. Strobl, *Physik kondensierter Materie*. Berlin: Springer-Verlag, 2002.

[56] H.-J. Butt, K. Graf, and M. Kappl, *Physics and Chemistry of Interfaces*. Wiley-VCH, 2006.

[57] W. B. Russel, D. A. Saville, and W. R. Schowalter, *Colloidal Dispersions*. Cambridge University Press, 1989.

[58] G. Cevc, “Membrane electrostatics.,” *Biochim. Biophys. Acta*, vol. 1031, no. 3, pp. 311–82, Oct. 1990.

[59] E. T. McAdams, J. Jossinet, R. Subramanian, and R. G. E. McCauley, “Characterization of gold electrodes in phosphate buffered saline solution by impedance and noise measurements for biological applications,” *Annu. Int. Conf. IEEE Eng. Med. Biol. - Proc.*, pp. 4594–4597, 2006.

[60] G. T. . Kovacs, *Introduction to the theory, design, and modeling of thin-film microelectrodes for neural interfaces*. London, U.K.: Academic, 1994.

[61] W. Franks, I. Schenker, P. Schmutz, and A. Hierlemann, “Impedance characterization and modeling of electrodes for biomedical applications,” *IEEE Trans. Biomed. Eng.*, vol. 52, no. 7, pp. 1295–1302, 2005.

[62] Keithley, “Low Level Measurements Handbook,” *Book*, p. vi, I-5, 2016.

[63] Keithley, “Model 6517B Reference Manual,” *Keithley Instruments Inc.*, no. June, 2009.

[64] K. Jüttner, “Electrochemical impedance spectroscopy (EIS) of corrosion processes on

inhomogeneous surfaces," *Electrochim. Acta*, vol. 35, no. 10, pp. 1501–1508, 1990.

[65] "EIS of Organic Coatings and Paints," 2017. [Online]. Available: https://www.gamry.com/application-notes/EIS/eis-of-organic-coatings-and-paints/. [Accessed: 13-Apr-2017].

[66] D. Loveday, P. Peterson, and B. Rodgers, "Evaluation of Organic Coatings with Electrochemical Impedance Spectroscopy Part 1 : Fundamentals of Electrochemical Impedance Spectroscopy," *JCT coatings tech*, no. August, pp. 46–52, 2004.

[67] D. Loveday, P. Peterson, and B. Rodgers, "Evaluation of Organic Coatings with Electrochemical Impedance Spectroscopy. Part 2: Application of EIS to Coatings.," *JCT CoatingsTech*, pp. 88–93, 2004.

[68] D. Loveday, P. Peterson, and B. Rodgers, "Evaluation of Organic Coatings with Electrochemical Impedance Spectroscopy. Part 3: Protocols for Testing Coatings with EIS," *JCT CoatingsTech*, pp. 22–27, 2005.

[69] Gamry-Instruments, "Basics of Electrochemical Impedance Spectroscopy." p. 17.

[70] C. Gabrielli, "Use and Application of Electrochemical Impedance Techniques." Solartron Analytical, 1997.

[71] N. D. Cogger and N. J. Evans, "An Introduction to Electrochemical Impedance Measurement," no. 6, p. 11, 1999.

[72] Agilent, "Agilent Impedance Measurement Handbook A guide to measurement technology and techniques," *Measurement*, p. 140, 2009.

[73] U. Nolten, "Entwicklung und Charakterisierung dehnungsbasierter Kraft- und Momentensensoren für medizinische Anwendungen," 2013.

[74] R. L. Parker and A. Krinsky, "Electrical resistance-strain characteristics of thin evaporated metal films," *J. Appl. Phys.*, vol. 34, no. 9, pp. 2700–2708, 1963.

[75] V. K. Pamula, A. Jog, and R. B. Fair, "Mechanical Property Measurement of Thin-Film Gold using Thermally Actuated Bimetallic Cantilever Beams," *Tech. Proc. 2001 Int. Conf. Model. Simul. Microsystems*, pp. 4–7, 2001.

[76] C. Li, “Thin gold film strain gauges,” *J. Vac. Sci. Technol. A Vacuum, Surfaces, Film.*, vol. 12, no. 3, p. 813, 1994.

[77] M. R. Neumann, “Structural Dependence of Strain Gauge Effect and Surface Resistivity for Thin Gold Films,” *J. Vac. Sci. Technol.*, vol. 6, no. 4, 1969.

[78] N. Lago, D. Ceballos, F. J Rodríguez, T. Stieglitz, and X. Navarro, “Long term assessment of axonal regeneration through polyimide regenerative electrodes to interface the peripheral nerve,” *Biomaterials*, vol. 26, no. 14, pp. 2021–2031, May 2005.

[79] T. Sun, W. T. Park, M. Y. Cheng, J. Z. An, R. F. Xue, K. L. Tan, and M. Je, “Implantable polyimide cable for multichannel high-data-rate neural recording microsystems,” *IEEE Trans. Biomed. Eng.*, vol. 59, no. 2, pp. 390–399, 2012.

[80] B. Rubehn and T. Stieglitz, “In vitro evaluation of the long-term stability of polyimide as a material for neural implants,” *Biomaterials*, vol. 31, no. 13, pp. 3449–3458, 2010.

[81] B. Rubehn, C. Bosman, R. Oostenveld, P. Fries, and T. Stieglitz, “A MEMS-based flexible multichannel ECoG-electrode array,” *J. Neural Eng.*, vol. 6, no. 3, p. 36003, Jun. 2009.

[82] H. G. Sachs, T. Schanze, U. Brunner, H. Sailer, and C. Wiesenack, “Transscleral implantation and neurophysiological testing of subretinal polyimide film electrodes in the domestic pig in visual prosthesis development,” *J. Neural Eng.*, vol. 2, no. 1, pp. S57–S64, Mar. 2005.

[83] “Product Bulletin: PI-2600 Series – Low Stress Applications,” no. September. HD Microsystems, pp. 1–4, 2009.

[84] Material Property Database, “Material Property Database MIT (Polyimide),” 2016. [Online]. Available: http://www.mit.edu/~6.777/matprops/polyimide.htm. [Accessed: 17-Nov-2016].

[85] H. Deligöz, T. Yalcinyuva, S. Özgümüs, and S. Yildirim, “Electrical properties of conventional polyimide films: Effects of chemical structure and water uptake,” *J. Appl. Polym. Sci.*, vol. 100, no. 1, pp. 810–818, 2006.

[86] D. Braun, “Electronic injection and conduction processes for polymer devices,” *J. Polym. Sci. Part B Polym. Phys.*, vol. 41, no. 21, pp. 2622–2629, Nov. 2003.

[87] L. I. Maissel and R. Glang, *Handbook of thin film technology,*. McGraw-Hill, 1970.

[88] V. Ratta, “Crystallization, Morphology, Thermal Stability and Adhesive Properties of Novel High Performance Semicrystalline Polyimides,” *Chem. Eng.*, vol. PhD, pp. 29–79, 1999.

[89] M. J. Loboda, R. Singh, S. S. Ang, and H. S. Rathore, *Low and High Dielectric Constant Materials: Materials Science, Processing, And Reliability Issudes*. The Electrochemical Society, 2000.

[90] V. Ratta, A. Ayambem, J. E. Mcgrath, and G. L. Wilkes, “Crystallization and multiple melting behavior of a new semicrystalline polyimide based on 1 , 3-bis (4-aminophenoxy) benzene (TPER) and,” *Polymer (Guildf).*, vol. 42, pp. 6173–6186, 2001.

[91] Material Property Database, “Material Property Database MIT - (Gold),” 2016. [Online]. Available: http://www.mit.edu/~6.777/matprops/gold.htm. [Accessed: 19-Feb-2017].

[92] R. Erlebach, “Einfluss von Gold Nanoclustern auf die strukturellen und supraleitenden Eigenschaften von YBCO,” Friedrich-Schiller-Universität Jena, 2011.

[93] L. Zhang, F. Cosandey, R. Persaud, and T. E. Madey, “Initial growth and morphology of thin Au films on TiO2(110),” *Surf. Sci.*, vol. 439, no. 1–3, pp. 73–85, 1999.

[94] L. Zhang, R. Persaud, and T. E. Madey, “Ultrathin metal lms on a metal oxide surface: Growth of Au on TiO 2 „110…,” *Phys. Rev. B*, vol. 56, no. 16, pp. 549–557, 1997.

[95] F. Silly and M. R. Castell, “Bimodal Growth of Au on SrTiO 3 (001),” *Phys. Rev. Lett.*, vol. 96, no. 8, p. 86104, Mar. 2006.

[96] M. Westerhausen, “Untersuchungen an epitaktischen Schichten mit selbstorganisiert wachsenden Gold-Nanopartikeln,” Friedrich-Schiller-Universität, Jena, 2013.

[97] M. Zinke-Allmang, L. C. Feldman, and M. H. Grabow, “Clustering on surfaces,” *Surf. Sci. Rep.*, vol. 16, no. 8, pp. 377–463, Dec. 1992.

[98] Y.-Q. Xue, M.-Z. Zhao, and W.-P. Lai, “Size-dependent phase transition temperatures of dispersed systems,” *Phys. B Condens. Matter*, vol. 408, pp. 134–139, 2013.

[99] T. Stieglitz and M. Gross, “Flexible BIOMEMS with electrode arrangements on front and

back side as key component in neural prostheses and biohybrid systems," *Sensors Actuators B Chem.*, vol. 83, no. 1–3, pp. 8–14, Mar. 2002.

[100] G. Voskerician, M. S. Shive, R. S. Shawgo, H. von Recum, J. M. Anderson, M. J. Cima, and R. Langer, "Biocompatibility and biofouling of MEMS drug delivery devices," *Biomaterials*, vol. 24, no. 11, pp. 1959–1967, May 2003.

[101] J. H. Fan, W. I. Hung, W. T. Li, and J. M. Yeh, "Biocompatibility Study of Gold Nanoparticles to Human Cells," in *13th International Conference on Biomedical Engineering*, Berlin, Heidelberg: Springer Berlin Heidelberg, 2009, pp. 870–873.

[102] N. Beshchasna, B. Adolphi, S. Granovsky, J. Uhlemann, and K.-J. Wolter, "Biostability issues of flash gold surfaces," in *2009 59th Electronic Components and Technology Conference*, 2009, pp. 1071–1079.

[103] "Technical data for the element Titanium in the Periodic Table." [Online]. Available: http://periodictable.com/Elements/022/data.html. [Accessed: 19-Feb-2017].

[104] "Material Property Data (Matweb) - Titanium." [Online]. Available: http://www.matweb.com/search/DataSheet.aspx?MatGUID=66a15d609a3f4c829cb6ad08f0dafc01&ckck=1. [Accessed: 19-Feb-2017].

[105] F. A. Cotton and G. Wilkinson, *Basic Inorganic Chemistry*. John Wiley & Sons, Inc., 1976.

[106] K. W. Vogt, P. A. Kohl, W. B. Carter, R. A. Bell, and L. A. Bottomley, "Characterization of thin titanium oxide adhesion layers on gold: resistivity, morphology, and composition," *Surf. Sci.*, vol. 301, no. 1–3, pp. 203–213, Jan. 1994.

[107] T. A. Cloud, M. R. Houston, P. A. Kohl, and S. A. Bidstrup, "Evaluation of the Processing and Performance of Noble Metal MCMs," in *International Conference of Multichip Modues Proceedings*, 1993, p. 451.

[108] T. A. Cloud, M. R. Houston, P. A. Kohl, and S. A. Bidstrup, "Processing and performance of gold MCMs," *IEEE Trans. Components, Hybrids, Manuf. Technol.*, vol. 16, no. 7, pp. 724–730, 1993.

[109] T. G. I. Ling, M. Beck, R. Bunk, E. Forsén, J. O. O. Tegenfeldt, A. A. A. Zakharov, and L. Montelius, "Fabrication and characterization of a molecular adhesive layer for micro-

and nanofabricated electrochemical electrodes,” *Microelectron. Eng.*, vol. 67–68, pp. 887–892, 2003.

[110] R. K. Quinn and N. R. Armstrong, “Electrochemical and Surface Analytical Characterization of Titanium and Titanium Hydride Thin Film Electrode Oxidation,” *J. Electrochem. Soc.*, vol. 125, no. 11, p. 1790, 1978.

[111] N. Schiff, B. Grosgogeat, M. Lissac, and F. Dalard, “Influence of fluoride content and pH on the corrosion resistance of titanium and its alloys.,” *Biomaterials*, vol. 23, no. 9, pp. 1995–2002, May 2002.

[112] “Product Bulletin: Chromium Etching Application Notes.” MicroChemicals, p. 2, 2013.

[113] M. E. Straumanis and C. B. Gill, “The Rate of Dissolution and the Passivation of Titanium in Acids with Ammonium Fluoride Added,” *J. Electrochem. Soc.*, vol. 101, no. 1, p. 10, 1954.

[114] P. Walker and W. H. Tarn, *CRC handbook of metal etchants*. CRC Press, 1991.

[115] F. López-Huerta, B. Cervantes, O. González, J. Hernández-Torres, L. García-González, R. Vega, A. L. Herrera-May, and E. Soto, “Biocompatibility and surface properties of TiO2 thin films deposited by DC magnetron sputtering,” *Materials (Basel).*, vol. 7, no. 6, pp. 4105–4117, May 2014.

[116] M. J. Kim, H. J. Lim, B. G. Lee, J. H. Kim, J. Choi, and H. G. Kang, “Establishment of validation methods to test the biocompatibility of titanium dioxide,” *Bull. Korean Chem. Soc.*, vol. 34, no. 6, pp. 1857–1863, 2013.

[117] S. Sangeetha, S. R. Kathyayini, P. D. Raj, P. Dhivya, and M. Sridharan, “Biocompatibility studies on TiO2 coated Ti surface,” in *International Conference on Advanced Nanomaterials & Emerging Engineering Technologies*, 2013, pp. 404–408.

[118] Z. Fei Yin, L. Wu, H. Gui Yang, and Y. Hua Su, “Recent progress in biomedical applications of titanium dioxide,” *Phys. Chem. Chem. Phys.*, vol. 15, no. 14, p. 4844, 2013.

[119] H. Nan, Y. Ping, C. Xuan, L. Yongxang, Z. Xiaolan, C. Guangjun, Z. Zihong, Z. Feng, C. Yuanru, L. Xianghuai, and X. Tingfei, “Blood compatibility of amorphous titanium oxide films synthesized by ion beam enhanced deposition,” *Biomaterials*, vol. 19, no. 7–9, pp.

771–776, 1998.

[120] M. J. O'Neil, *The Merck Index - An Encyclopedia of Chemicals, Drugs and Biologicals.* Cambridge, UK: Royal Society of Chemistry, 2013.

[121] S. Dueñas, H. Castán, H. García, E. S. Andrés, M. Toledano-Luque, I. Mártil, G. González-Díaz, K. Kukli, T. Uustare, and J. Aarik, "A comparative study of the electrical properties of TiO 2 films grown by high-pressure reactive sputtering and atomic layer deposition," *Semicond. Sci. Technol.*, vol. 20, no. 10, pp. 1044–1051, 2005.

[122] D. Maier, "Untersuchung von ALD-Schichten," Hochschule Furtwangen, 2016.

[123] Y. Nakamura, Y. Suzuki, and Y. Watanabe, "Effect of oxygen plasma etching on adhesion between polyimide films and metal," *Thin Solid Films*, vol. 290–291, no. 1996, pp. 367–369, 1996.

[124] N. Gomathi, A. Sureshkuar, and S. Neogi, "RF plasma-treated polymers for biomedical applications," *Cepartment Chem. Eng. Indian Inst. Technol.*, vol. 94, no. 11, pp. 1478–1486, 1988.

[125] K. R. Williams, S. Member, K. Gupta, S. Member, and M. Wasilik, "Etch Rates for Micromachining Processing — Part II," *J. Microelectromechanical Syst.*, vol. 12, no. 6, pp. 761–787, 2003.

[126] "MyPLAS - advanced coating systems." Neuenburg, 2017.

[127] K. Cho, J. Park, and C. Shin, "Atomic Layer Deposition of TiO 2 using Titanium Isopropoxide and H 2 O : Operational Principle of Equipment and Parameter Setting," *J. Semicond. Technol. Sci.*, vol. 16, no. 3, pp. 346–351, 2016.

[128] M. Aguilar, A. I. Oliva, and P. Quintana, "The effect of electrical current (DC) on gold thin films," *Surf. Sci.*, vol. 409, pp. 501–511, 1998.

[129] M.-A. Nicolet, "Diffusion barriers in thin films," *Thin Solid Films*, vol. 52, no. 3, pp. 415–443, Aug. 1978.

[130] V. K. Khanna, "Adhesion–delamination phenomena at the surfaces and interfaces in microelectronics and MEMS structures and packaged devices," *J. Phys. D. Appl. Phys.*,

vol. 44, no. 3, p. 34004, 2011.

[131] J. Pan, R. M. Pafchek, F. F. Judd, and J. B. Baxter, “Effect of Chromium-Gold and Titanium-Titanium Nitride-Platinum-Gold Metallization on Wire/Ribbon Bondability,” *IEEE Trans. Adv. Packag.*, vol. 29, no. 4, pp. 707–713, Nov. 2006.

[132] B. Gupta, J. Hilborn, C. Hollenstein, C. J. G. Plummer, R. Houriet, and N. Xanthopoulos, “Surface modification of polyester films by RF plasma,” *J. Appl. Polym. Sci.*, vol. 78, no. 5, pp. 1083–1091, Oct. 2000.

[133] E. M. Liston, “Plasma Treatment for Improved Bonding: A Review,” *J. Adhes.*, vol. 30, no. 1–4, pp. 199–218, Jan. 1989.

[134] D. K. Shaffer, H. M. Clearfield, and J. S. Ahearn, *Treatise on Adhesion and Adhesives*, vol. 7. New York: Marcel Dekker, 19991.

[135] W. Poppendieck, A. Sossalla, M.-O. Krob, C. Welsch, T. a K. Nguyen, W. Gong, J. DiGiovanna, S. Micera, D. M. Merfeld, and K.-P. Hoffmann, “Development, manufacturing and application of double-sided flexible implantable microelectrodes.,” *Biomed. Microdevices*, vol. 16, no. 6, pp. 837–50, Dec. 2014.

[136] T. Boretius, T. Jurzinsky, C. Koehler, S. Kerzenmacher, H. Hillebrecht, and T. Stieglitz, “High-porous platinum electrodes for functional electrical stimulation.,” *Conf. Proc. IEEE Eng. Med. Biol. Soc.*, vol. 2011, pp. 5404–7, Jan. 2011.

[137] F. Bonaccorso, G. Calogero, G. Di Marco, O. M. Maragò, P. G. Gucciardi, U. Giorgianni, K. Channon, and G. Sabatino, “Fabrication of gold tips by chemical etching in aqua regia,” *Rev. Sci. Instrum.*, vol. 78, no. 10, p. 103702, Oct. 2007.

[138] www.microchemicals.eu, “Gold Etching with KI/I 2,” 2013. [Online]. Available: www.microchemicals.eu. [Accessed: 25-Feb-2017].

[139] S. Metz, A. Bertsch, D. Bertrand, and P. Renaud, “Flexible polyimide probes with microelectrodes and embedded microfluidic channels for simultaneous drug delivery and multi-channel monitoring of bioelectric activity,” *Biosens. Bioelectron.*, vol. 19, no. 10, pp. 1309–1318, 2004.

[140] S. Metz, R. Holzer, and P. Renaud, “Polyimide-based microfluidic devices,” *Lab Chip*, vol.

1, no. 1, p. 29, 2001.

[141] A. Mercanzini, K. Cheung, D. L. Buhl, M. Boers, A. Maillard, P. Colin, J.-C. Bensadoun, A. Bertsch, and P. Renaud, “Demonstration of cortical recording using novel flexible polymer neural probes,” *Sensors Actuators A Phys.*, vol. 143, no. 1, pp. 90–96, 2008.

[142] S. A. Dayeh, D. P. Butler, and Z. Çelik-Butler, “Micromachined infrared bolometers on flexible polyimide substrates,” *Sensors Actuators A*, vol. 118, no. 1, pp. 49–56, 2005.

[143] T. Stieglitz, “Flexible biomedical microdevices with double-sided electrode arrangements for neural applications,” *Sensors Actuators A Phys.*, vol. 90, no. 3, pp. 203–211, May 2001.

[144] www.gelpak.com, “Gel-Pak Product Data Sheet.” HayWard, CA, p. 8, 2017.

[145] T. Adrega and S. P. Lacour, “Stretchable gold conductors embedded in PDMS and patterned by photolithography: fabrication and electromechanical characterization,” *J. Micromechanics Microengineering*, vol. 20, no. 5, p. 55025, 2010.

[146] Keithley, “6517B-900-01 (A - Jun 2008)(User’s).book,” no. June, pp. 1–90, 2008.

[147] H. Dietmann, *Einführung in die Elastizitäts- und Festigkeitslehre*. Kröner Verlag, 1982.

[148] R. Lucchini, E. Cattarinuzzi, S. Maraghechi, D. Gastaldi, A. Adami, L. Lorenzelli, and P. Vena, “Delamination phenomena in aluminum/polyimide deformable interconnects: In-situ micro-tensile testing,” *Mater. Des.*, vol. 89, pp. 121–128, 2016.

[149] L. Rangel-Castillo, S. Gopinath, and C. S. Robertson, “Management of intracranial hypertension,” *Neurol. Clin.*, vol. 26, no. 2, pp. 521–541, 2008.

[150] M. Kappel, “Design and Validation of a Test Setup capable of Simulating and Measuring Mechanical Stress on Polyimide-based Flex-MEAs,” Eberhard-Karls-Universität Tübingen, 2017.

[151] Keithley, “Model 6521 Low Current Model 6522 Voltage / Current.”

[152] J. S. Ordonez, M. Ieee, C. Boehler, M. Schuettler, T. Stieglitz, and S. M. Ieee, “Improved Polyimide Thin-Film Electrodes for Neural Implants,” *IEEE*, pp. 5134–5137, 2012.

[153] A. Crockett and M. Almoustafa, “Plasma Delayering of Integrated Circuits.” Trion Technology Inc., 1999.

[154] U. Buder, J. P. von Klitzing, and E. Obermeier, “Reactive ion etching for bulk structuring of polyimide,” *Sensors Actuators, A Phys.*, vol. 132, no. 1 SPEC. ISS., pp. 393–399, 2006.

[155] C. G. Malmberg and A. A. Maryott, “Dielectric constant of water from 0° to 100° C,” *J. Res. Natl. Bur. Stand. (1934).*, vol. 56, no. I, 1956.

[156] C. Lee, Y. Shul, and H. Han, “Dielectric properties of oxydianiline-based polyimide thin films according to the water uptake,” *J. Polym. Sci. Part B Polym. Phys.*, vol. 40, no. 19, pp. 2190–2198, Oct. 2002.

[157] V. N. Shilov, A. V. Delgado, F. González-Caballero, J. Horno, J. J. López-García, and C. Grosse, “Polarization of the Electrical Double Layer. Time Evolution after Application of an Electric Field,” *J. Colloid Interface Sci.*, vol. 232, no. 1, pp. 141–148, 2000.

[158] H. Adachi, K. Wasa, I. Kanno, and H. Kotera, *Handbook of sputter deposition technology : fundamentals and applications for functional thin films, nano-materials and MEMS*. William Andrew, 2012.

[159] R. Raiteri and M. Grattarola, “Changes in surface stress measured with an atomic force microscope,” *Scanning Microsc.*, vol. 12, no. 1, pp. 243–251, 1998.

[160] M. R. Rosenberger, S. Chen, C. B. Prater, J. P. Killgore, D. C. Hurley, G. Stan, S. W. King, R. F. Cook, G. Stan, R. S. Gates, R. Wagner, J. P. Killgore, and R. C. Tung, “Measuring stiffness and residual stress of thin films by contact resonance atomic force microscopy,” 1882.

[161] R. W. Hoffman, “Thin solid films,” *Phys. Thin Film.*, vol. 3, no. 211, 1968.

[162] R. W. Hoffman, “Thin solid films,” *Phys. Thin Film.*, vol. 3, no. 185, 1976.

[163] C. Ayas and E. Van der Giessen, “Stress relaxation in thin film/substrate systems by grain boundary diffusion: a discrete dislocation framework,” *Model. Simul. Mater. Sci. Eng.*, vol. 17, no. 6, p. 64007, Sep. 2009.

[164] M. N. Shetty, *Dislocations and mechanical behaviour of materials.* PHI Learning Pvt.

Ltd., 2013.

[165] M. Frantlović, I. Jokić, V. Savu, S. Xie, and J. Brugger, “Effects of tensile stress on electrical parameters of thin film conductive wires fabricated on a flexible substrate using stencil lithography,” *Microelectron. Eng.*, vol. 98, pp. 230–233, Oct. 2012.

[166] H. Kim, H. B. R. Lee, and W. J. Maeng, “Applications of atomic layer deposition to nanofabrication and emerging nanodevices,” *Thin Solid Films*, vol. 517, no. 8, pp. 2563–2580, 2009.

[167] H. Kim, “Atomic layer deposition of metal and nitride thin films: Current research efforts and applications for semiconductor device processing,” *J. Vac. Sci. Technol. B Microelectron. Nanom. Struct.*, vol. 21, no. 6, p. 2231, 2003.

[168] S. J. Groiss, L. Wojtecki, M. Südmeyer, and A. Schnitzler, “Deep brain stimulation in Parkinson’s disease.,” *Ther. Adv. Neurol. Disord.*, vol. 2, no. 6, pp. 20–8, 2009.

[169] A. Büttner, “ALD-Seitenwandpassivierung von Mikroelektrodenarrays,” Hochschule Furtwangen University, 2017.

[170] C. C. Chiang, W. C. Chen, Y. P. Chen, R. H. Horng, and D. Wuu, “Flexible TFTs technology using a laser-delamination process,” 2005.

[171] J. S. Ordonez, C. Boehler, M. Schuettler, and T. Stieglitz, “Long-term Adhesion Studies of Polyimide to Inorganic and Metallic Layers,” *Mater. Res. Soc.*, vol. 1466, 2012.

[172] Ultratech/CNT, “ALD Materials,” 2017. [Online]. Available: http://cambridgenanotechald.com/atomic-layer-deposition/ald-materials.shtml. [Accessed: 09-Jun-2017].

[173] M. Westerhausen, T. Martin, and B. Hofmann, “Measuring the long term stability of (flexible) multi layer substrate.” DGBMT, Basel, 2016.

[174] C. Katzer, M. Westerhausen, I. Uschmann, F. Schmidl, U. Hübner, and P. Seidel, “Structural properties of gold modified YBa 2 Cu 3 O 7−δ thin films,” *Supercond. Sci. Technol.*, vol. 26, no. 12, p. 125008, Dec. 2013.

[175] C. Katzer, M. Westerhausen, P. Naujok, H. Bernhardt, G. Schmidl, W. Fritzsche, A.

Undisz, M. Drüe, M. Rettenmayr, and F. Schmidl, “Matrix induced in-situ growth of crystalline Au nanoparticles for photonic applications,” *SPIE Nanosci. + Eng.*, vol. 8807, p. 88070K–88070K–9, Sep. 2013.

[176] C. Katzer, C. Stahl, P. Michalowski, S. Treiber, M. Westerhausen, F. Schmidl, P. Seidel, G. Schütz, and J. Albrecht, “Increasing the sensor performance using Au modified high temperature superconducting YBa 2 Cu 3 O 7-δ thin films,” *J. Phys. Conf. Ser.*, vol. 507, no. 1, p. 12024, May 2014.

[177] M. Westerhausen, C. Katzer, R. Diener, I. Uschmann, F. Schmidl, M. Rettenmayer, and P. Seidel, “Wachstumsbedingungen und Eigenschaften von YBCO-Schichten mit Au-Nano Partikeln.” Deutsche Physikalische Gesellschaft e.V., Berlin, 2012.

[178] S. Koch, P. Michalowski, C. Katzer, M. Westerhausen, F. Schmidl, and P. Seidel, “Grain boundary high-Tc dc-SQUIDs with self-organized nanocrystals.” Deutsche Physikalische Gesellschaft e.V., Berlin, 2012.

[179] D. Purves, *Neuroscience*, 4th ed. Sunderland, Mass. : Sinauer, ©2008., 2008.

[180] M. Westerhausen, T. Martin, M. Kappel, and B. Hofmann, “Stress Testing of Electrically Active FlexMEAs with simultaneous electrical recording in fluidic environment: Introduction of a New Measurement Setup,” *Flow Meas. Instrum.*

I. LIST OF FIGURES

Figure 1: Sketch of Multilayer System with Electrode Openings 2

Figure 2: Schematic of electric active implant. Clearly visible is the artificially created opening in the passivation layer to create an electric access from the electrode to the tissue [10]...... 2

Figure 3: Electrode Side Wall Passivation 3

Figure 4: hybrid sub retinal device with both micro photodiodes and microelectrodes, embedded in a polyimide encapsulation. Developed by Retina Implant AG, Reutlingen, Germany and Zrenner, et al. [12] 6

Figure 5: Water permeability of different materials; the lines depict the timespan in which a humidity of 50 % inside a closed housing of the given material with the respected wall thickness is reached [15], [16] 7

Figure 6: Schematic to evaluate the need for material tests [19] 9

Figure 7: Schematic of a RIE system (modified and based on [46]) 18

Figure 8: Schematic of ALD process [52] 19

Figure 9: (left) potential-versus-distance for a surface potential of 50 mV and different ion concentrations; (right) local co- and counter-ion concentrations for a monovalent salt at a bulk concentration of 0.1 M [56] 22

Figure 10: Stern layer at a metal surface [56] 23

Figure 11: equivalent circuit for a metal-solution interface [58] 23

Figure 12: Typical Nyquist Plot of a damaged coating 27

Figure 13: Typical Bode Plot for a damaged Coating 27

Figure 14: Equivalent Circuit for a Damaged Coating [64] 28

Figure 15: General Structure of a strain gauge with leading wires 29

Figure 16: Chemical Structure of PI 2611 [21] 33

Figure 17: Layer growth possibilities, prior published in [96] 35

Figure 18: Bottom Electrodes Lithography Mask 40

Figure 19: Close-up of the electrode field of the sensor array 41

Figure 20: ALD Etching and ALD Protection mask 42

Figure 21: Mask Layout for flexible Samples 42

Figure 22: Flexible Sample Etching Mask called “Flex Mea Etching Mask” 43

Figure 23: Final Polyimide Thickness, depending on the spin coating speed [83] 47

Figure 24: Temperature Ramp of the Polyimide Curing Process with the complete cooling time 48
Figure 25: Etching rate of Polyimide 2611 in O2 Plasma 49
Figure 26: ALD device used for fabricating electrode side wall passivation layers [126] 50
Figure 27: Manufacturing of unopened multilayer samples 56
Figure 28: separating the 1 inch samples from the 4 inch wafer with the dicing saw 57
Figure 29: Aluminum shadhwo mask with the parameters given in mm 58
Figure 30: sputter sample holder (left) with sampled mounted inside (right) 59
Figure 31: (left) finished 1 in non-flexible sample with the multilayer stack; (right) similar sample, with electrodes opened 60
Figure 32: Schematic Image of a (opened) Multilayer System with electrical contacts to the inner metal layers (golden), which sit in between the polyimide passivation layers (red) 60
Figure 33: Manufacturing of the opened multi-layer samples 61
Figure 34: misalignment on the photolithographic process 62
Figure 35 left: trigonometrical schema for misalignment surface calculation; right: newly created surface in relation to side wall surface of the intermediate layers 62
Figure 36: Numbered electrode and pin layout of a produced MEA 64
Figure 37: Sketch Images of the manufacturing process of the flexible polyimide test device 66
Figure 38: Self-made Flex-Mea Sample on Polyimide Base 66
Figure 39: Etching electrodes of adhered flexible sample 67
Figure 40: Demonstrating the flexibility of the Flex-Mea 68
Figure 41: Circuitry Layout of the flexible mask; The respective Pad assignment is listed in table 14 70
Figure 42: optical Image of the produced strain gauge with 20 microns wide leads (left) and an enlarged view of the strain gauge with visible delamination (right) 72
Figure 43: Flexible Multi-Layer Sample with the circuitry visible through both intermediate metal Layers 73
Figure 44: Flexible Multi-Layered Sample, demonstrating the Flexibility 73
Figure 45: Aluminum hard masks for creating the intermediate gold layers on the flexible samples 74
Figure 46: Schematic of flexible multi-layered Sample; Image provided by Marcel Kappel 74

Figure 47: Creation of the multilayered flexible sample, with one (left) and both (right) intermediate metal layers deployed 75
Figure 48: SEM images of VIA side wall........ 76
Figure 49: SEM image of top polyimide layer 76
Figure 50: mimic diagram of leakage setup 78
Figure 51: Schematic overview of the whole Fluidic Measurement Setup 80
Figure 52: Image of in-house manufactured multiplexer 81
Figure 53: Electrical measurement Setup with faraday cage and SMU........ 82
Figure 54: Probe Positioners (left), contacting the sample with the AgCl counter electrode (right)........ 82
Figure 55: Non-flexible sample with plastic liquid reservoir........ 83
Figure 56: Explosion (left) and real world (right) image of the FMS pressure chambers........ 84
Figure 57: One sided pressure applied to a Flex-Mea by utilizing one pressure chamber...... 84
Figure 58: (left) PCB, translating the OMRON connector (bottom) to a standard broadband ribbon cable (right side) to contact the Flex MEA; (right) PCB to contact the broadband wire from the prior PCB........ 85
Figure 59: Flowchart for final FMS Program 87
Figure 60: Parameter Settings of Fluidik Sweep Program 88
Figure 61: Data Display of Fluidic alternate program 89
Figure 62: open circuit measurement of multiplexer 1 90
Figure 63: open circuit measurement of multiplexer 2 91
Figure 64: Mux #1 10 GΩ measurements 91
Figure 65: Mux #2 10 GΩ measurements 92
Figure 66: FMS switch verification with 100 mbar applied........ 93
Figure 67: Detection of cracks and samples 94
Figure 68: Pressure stability of FMS during 6 consecutive days........ 95
Figure 69: AC measurement of unopened Flex Mea in the FSM (1 V, 1 kHz)........ 96
Figure 70: AC measurement of opened Flex Mea against PBS in the FSM (1 V, 1 kHz) 96
Figure 71: SEM images of multilayer samples, prepared with FIB 97
Figure 72: visible delamination between PI and the circuitry (left) or complete Au layer (right) 98

Figure 73: Height profiles of the surface topography of the metal layer (left) and polyimide (right), generated with atomic force microscopy 98
Figure 74: AFM height profile the metal surface after delamination 99
Figure 75: AFM image and height profile of ripped out Au cluster 99
Figure 76: AFM image of metal layer with removed gold clusters 100
Figure 77: Microscope Image of etched electrode; misalignment is clearly visible 101
Figure 78: Grayscale image of Figure 77 (left) with its histogram (right) 101
Figure 79: SEM image of RIE etching residues on top of an electrode 102
Figure 80: Leakage Current, measured from PBS against metal layers and the electrode (1 V applied) 104
Figure 81: Delamination (measured with 1V applied) 105
Figure 82: Delamination as seen from beginning (measured with 1V applied) 106
Figure 83: Delamination after long term stability measurement 107
Figure 84: EDX Measurement of pure PI Foil 108
Figure 85 EDX Measurement of Metal Circuitry 109
Figure 86: Microscopic Images of visibly defective strain gauges 110
Figure 87: 50 mbar test substrate PI 111
Figure 88: Comparison between real deformation (PP foil) and FEM simulation at 500 mbar 112
Figure 89: comparison of real deformation and FEM simulation of PI foil 200 mbar 112
Figure 90: Simulated profile of a polyimide sample with 200mbar pressure applied; the maximal elongation matches that of the real-world sample in figure 89 113
Figure 91: Alternating DC resistivity over electrode feedlines as sample is bend by applying a consecutive pressure of 200 mbar. 115
Figure 92: drop in relative DC resistivity during sample bending 116
Figure 93: depicting minimal necessary sample bending, until lowest resistance level is reached 117
Figure 94: resistivity increase with increased sample bending 118
Figure 95: AFM images of a titanium-gold layer not tempered (left) and tempered (right). 119
Figure 96: SEM image of a 20 nm TiO_2 Layer (left) on top of a Ti-Au-Ti layer stack 121
Figure 97: A thin TiO2 Layer between two gold tracks for electrical validation 121
Figure 98: U-R Diagram of two 20nm thick TiO2 Layer; Measurement by Alisa Büttner 122

Figure 99: U-R of a 70nm TiO2 ALD Layer; Image by Alisa Büttner 123
Figure 100: 3D surface image of 20 nm TiO2; Image processed by Alisa Büttner 124
Figure 101: 3D surface image of 20 nm TiO2, immersed in TechniEtch Cr 01 for 2 min; Image processed by Alisa Büttner 125
Figure 102: 3D surface image of 20 nm TiO2, immersed in TechniEtch Cr 01 for 2 min in an ultra-sonic bath; Image processed by Alisa Büttner 125
Figure 103: Helium Ion Image of TiO_2 passivated electrode side wall 127
Figure 104: bond pads being covered by Kapton band 127
Figure 105: Current measurements during visible delamination 128
Figure 106: DC Measurements on non-flexible sample #1 129
Figure 107: DC measurements on non-flexible sample #2 129
Figure 108: Schematic of ALD coating with subsequent free etching the electrodes 131
Figure 109: Helium Ion Image of an opened electrode with a passivated side wall 132
Figure 110: Impedances (1V; 1kHz) of flexible Samples vs the counter Electrode in PBS..... 133
Figure 111: Impedance Phase analysis of flexible samples 134
Figure 112: DC measurements (1V applied) on flexible samples of electrodes vs a reference in PBS 135
Figure 113: DC measurements (1V applied) of flexible samples vs Autop 136
Figure 114: DC measurements (1V applied) of flexible Samples vs Aubottom 137
Figure 115: DC Measurements of side wall passivated Electrodes on a flexible Sample 137
Figure 116: Impedance reference measurements of final ALD covered sample with opened electrodes (1V, 1kHz); The red box marks the measurements of the defective bond pads . 138
Figure 117: Electrode #1 vs Autop on coated flexible sample with opened electrodes, showing a defective electrode side wall passivation 139
Figure 118: Electrode #13 vs Autop on coated flexible sample with opened electrodes, showing a fully intact electrode side wall, which, therefore, is not truly fitted with the equivalent circuit of a defective coating 139
Figure 119: Equivalent circuit for the fits in Figure 117 and Figure 118, based on the circuit in chapter 2.3.3, describing a damaged coating; the fitted values can be seen in Table 19 140

II. LIST OF TABLES

Table 1: Overview of material tests regarding the biocompatibility according to DIN EN ISO 109931-1 10
Table 2: Overview of additional material tests according to DIN EN ISO 10993-1 11
Table 3: Values for the circuit of a gold-pbs contact [58] 24
Table 4: Material parameters for common strain gauge materials [72], [74] 30
Table 5: Solution Properties of PI-2610 and PI-2611 [83] 32
Table 6: Comparison of Polyimide 2611 with other polyimides [83] 34
Table 7: Vapor deposition process parameters 45
Table 8: Sputtering process parameters 46
Table 9: Plasma etching parameters 49
Table 10: Process Parameters for Atomic Layer Deposition 51
Table 11: Ion Beam Etching process parameters 52
Table 12: Etch rates in comparison with f-cups; Data from University of Tubingen 52
Table 13: Pin Layout of non-flexible samples 64
Table 14: Electrode Numbers of flexible mask 70
Table 15: EDX Elements in pure PI Foil 108
Table 16: EDX Measurement of Metal Layer in PI 109
Table 17: Theoretical elongation of PI and PP foil under pressure based on the FEM simulations (l_0 = 24mm) 114
Table 18: Comparison of Set and actual layer thickness of measured ALD layers 120
Table 19: Fitted values from the equivalent circuit, displayed in Figure 119 140

III. APPENDIX

Appendix A: Standard positive photolithographic protocol……………………………………………172

Appendix B: Standard Polyimide (2611) protocol…………………………………………………………...173

Appendix C: Standard non-flexible (multilayered) samples protocol……………………..……….. 174

Appendix D: Standard flexible (multilayered) samples protocol…………………………….………176

Appendix E: Sputter Sample Holder…………………………………………………………………………..178

Appendix F: Steel Sample Plate Probe…………………………………………………………………………179

Appendix G: Steel Sample Plate Probe Positioner Holders………………………………………………180

A: STANDARD POSITIVE PHOTOLITHOGRAPHY PROTOCOL

Process Step	Description	Comment
Sample cleaning		using acetone in ultrasonic sound and rinsing with isopropanol
Sample drying	5 min; 90 °C	On hotplate
Resist Deposition	Ma-P 1205; 5,5 ml for 4 in wafer; ~1.5 ml for 1 in sample; 3000 rpm @ 30 sec with 10 sec ramp	
Pre-Exposure Bake	90 °C @ 60 sec	
Exposure	Hard Contact Mode; 40 sec	
Develop	MaD 331 @ 35 sec; then rinse with ultrapure water	While slowly panning

B: STANDARD POLYIMIDE 2611 PROTOCOL

Process Step	Description	Comment
Sample cleaning		using acetone in ultrasonic sound and rinsing with isopropanol
Spin dry	30 s @ 3000 rpm	
Precursor deployment		Carefully drop PI 2611 on sample
Spin coat	5 s @500 rpm followed by 30 s @ 3000 rpm	
Softbake	90 s @ 90 °C followed by 90 s @150 °C	On hotplate
Curing	Heat from RT to 300 °C; ramp 4 °/min N_2 800-1000 sccm; 30 min;	
Sample Cooling	To RT with 4 °/min	Cooling process takes longer due to absence of active cooling unit

C: NON-FLEXIBLE (MULTILAYERED) SAMPLES

Dark Grey steps only necessary for multilayered samples

Light Grey steps only necessary for opening electrodes

Process Step	Description	Comment
Sample Cleaning	4-inch borosilicate glass substrate	using acetone in ultrasonic bath and rinsing with isopropanol
Electrode Structure	Standard positive Lithography with "Bottom Electrodes Lithography Mask"	Appendix A
Electrode Deposition	10 nm Ti by EBPVD 50nm AU by thermal evap. 10 nm Ti by EBPVD	
Lift-off		ultrasonic bath in acetone until structure is visible; rinse with isopropanol
Isolate samples	Cut 4-inch substrate into (24.225x24.225) mm^2 squares	Align by Bondpads
Polyimide	Standard Polyimide 2611 Protocol	Appendix B
Surface Activation	O_2 Plasma; 8s	
Structure of intermediate layer	Standard positive Lithography with "ALD Etching Mask"	Appendix A
Intermediate Layer Deposition	10 nm Ti, 50 nm Au, 10nm Ti; All in situ	sputtering with additional hard mask for Flex creation
Lift-off		ultrasonic bath in acetone until structure is visible; rinse with isopropanol
Surface Activation	O_2 Plasma; 8s	
Polyimide	Standard Polyimide 2611 Protocol	Appendix B
Surface Activation	O_2 Plasma; 8s	
Structure of intermediate layer	Standard positive Lithography with "ALD Etching Mask"	Appendix A
Intermediate Layer Deposition	10 nm Ti, 50 nm Au, 10nm Ti; All in situ	sputtering with additional hard mask for Flex creation; turned by 90°

Lift-off		ultrasonic bath in acetone until structure is visible; rinse with isopropanol
Surface Activation	O_2 Plasma; 8s	
Polyimide	Standard Polyimide 2611 Protocol	Appendix B
Structure of Etch Mask	Standard positive Lithography with “ALD Etching Mask”	Appendix A
Etch Mask Deposition	100 nm Chromium; sputtering	
Electrodes Opening	RIE O2 Plasma (30 min per PI Layer + 15 min)	
Hard Mask Removal	TechniEtch	
Connecting the intermediate Layers	Etch to intermediate Layers by RIE; 30 min per PI Layer, using Aluminum Hard Mask with hole Ø 1 mm, positioned above appropriate Flex	Fill created holes with conductive silver

D: FLEXIBLE (MULTILAYERED) SAMPLES

Grey steps only necessary for multilayered samples

Light grey steps only necessary when opening electrodes

Process Step	Description	Comment
Sacrificial Layer	Sputter 50 nm Ti on 4-inch borosilicate glass wafer	
Isolate substrates	Dice 30.08 x 40.08 mm^2 substrates via Wafer Saw	
Sample Cleaning		using acetone in ultrasonic sound and rinsing with isopropanol
Polyimide	Standard Polyimide 2611 Protocol	Appendix B
Surface Activation	O_2 Plasma; 8s	
Electrode Structure	Standard positive Lithography with Mask for flexible Samples”	Appendix A
Electrode Deposition	10 nm Ti by EBPVD 50 nm Au by thermal evap. 10 nm Ti by EBPVD	
Lift-off		ultrasonic bath in acetone until structure is visible; rinse with isopropanol
Surface Activation	O_2 Plasma; 8s	
Polyimide	Standard Polyimide 2611 Protocol	Appendix B
VIA ETCH	RIE O_2 Plasma; 30 min with aluminum hard mask with Ø 2 mm hole placed above Via # 1	
Surface Activation	O_2 Plasma; 8s	
Structure of intermediate layer # 1	Standard positive Lithography with “Flex Mea Etching Mask”	Appendix A
Intermediate Layer # 1 Deposition	10 nm Ti, 50 nm Au, 10nm Ti; All in situ	sputtering with additional hard mask for Flex creation
Lift-off		ultrasonic bath in acetone until structure is visible; rinse with isopropanol

Surface Activation	O_2 Plasma; 8s	
Polyimide	Standard Polyimide 2611 Protocol	Appendix B
VIA ETCH	RIE O_2 Plasma; 60 min with aluminum hard mask with Ø 2 mm hole placed above Via # 2	
Surface Activation	O_2 Plasma; 8s	
Structure of intermediate layer # 2	Standard positive Lithography with “Flex Mea Etching Mask”	Appendix A
Intermediate Layer # 2 Deposition	10 nm Ti, 50 nm Au, 10nm Ti; All in situ	sputtering with additional hard mask for Flex creation
Lift-off		ultrasonic bath in acetone until structure is visible; rinse with isopropanol
Surface Activation	O_2 Plasma; 8s	
Polyimide	Standard Polyimide 2611 Protocol	Appendix B
Dissolve sacrificial Layer	In NH_4F for approx. 48 h	
Fixate sample	Using gel-Film from Gel-Pack	The gel film itself is adhered to aluminum plate of same size
Electrode Etch Structure	Standard positive Lithography with “Flex Mea Etching Mask”	Appendix A
Deposit Chromium Etch Mask	100 nm Cr by sputtering	
Open Electrodes	RIE O_2 Plasma for approx. 90 min	Check if opened, else add 15 min steps
Lift Off Chromium Etch Mask	TechnieEtch	
Peel from Tape		

E: SPUTTER SAMPLE HOLDER

All Units are given in mm

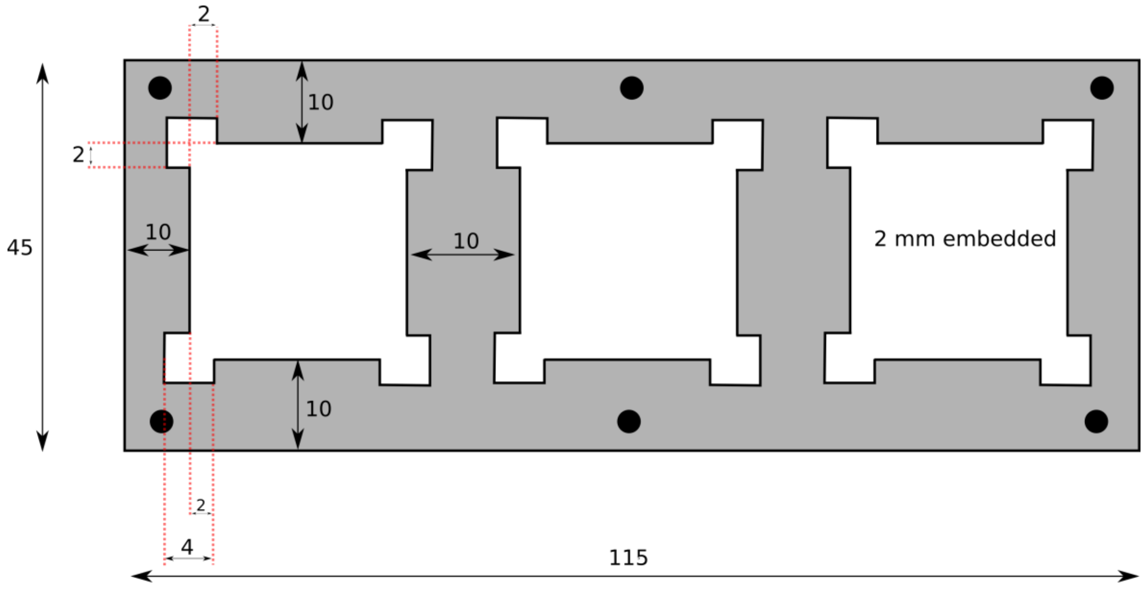

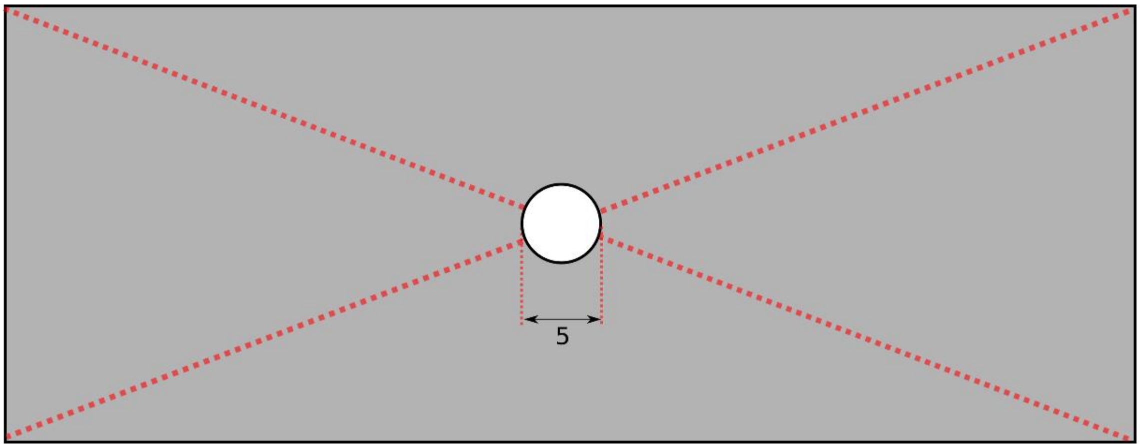

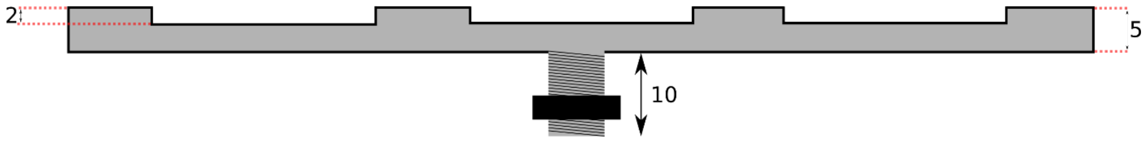

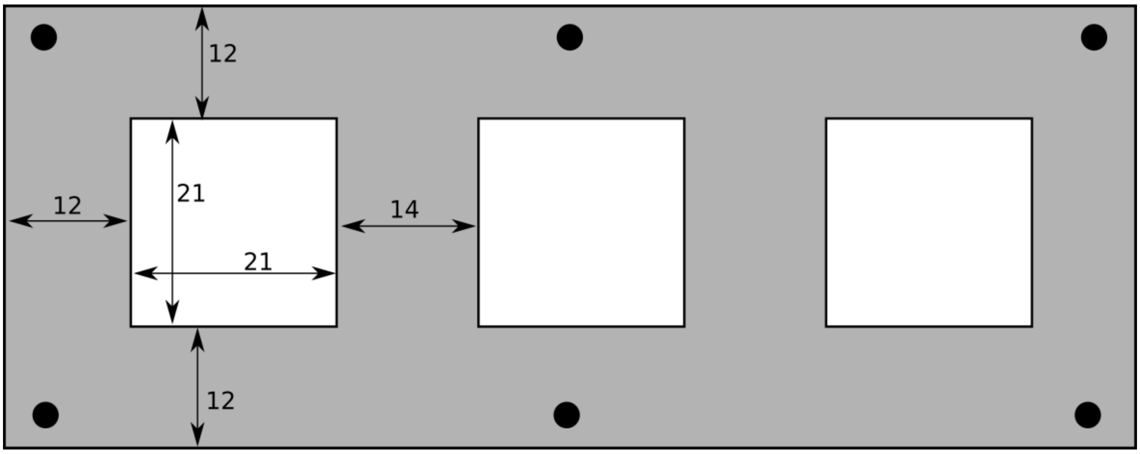

F: STEEL SAMPLE PLATE

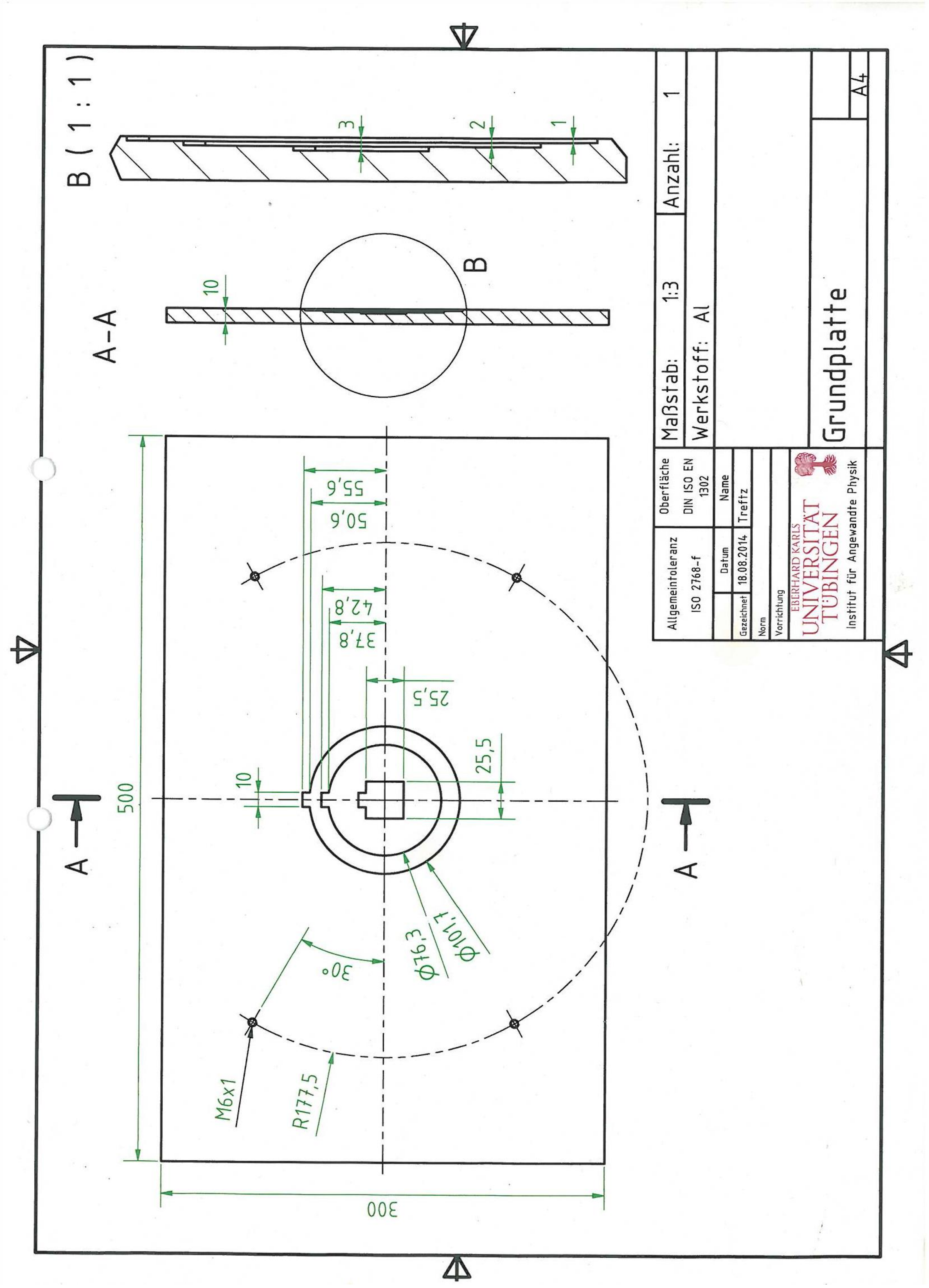

G: STEEL SAMPLE PLATE PROBE POSITIONER HOLDERS

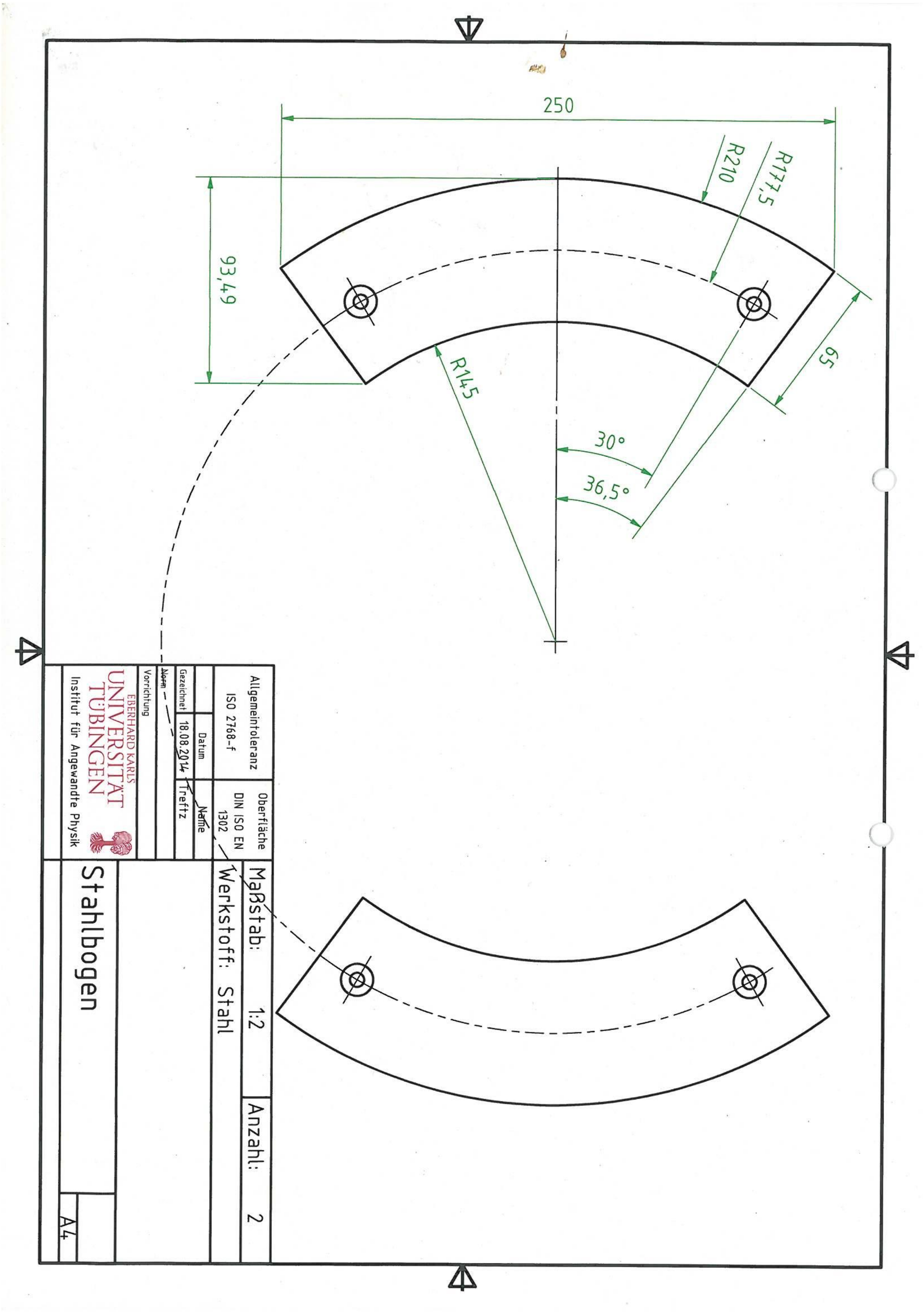

SUPERVISED BACHELOR- AND MASTER THESES

Following Bachelor-, Master thesis and Project modules were supervised during this thesis:

Project modules:

- Alisa Büttner: “ALD-Side Wall Passivation Layer for Microelectrode arrays “, Hochschule Furtwangen - 2016

Bachelor thesis:

- Marcel Kappel: „Design and Validation of a Test Setup capable of Simulating and Measuring Mechanical Stress on Polyimide-based Flex-MEAs”, Eberhard Karls Universität - 2016

Master thesis:

- Alisa Büttner: „ALD-Seitenwandpassivierung von Mikroelektrodenarrays“, Hochschule Furtwangen, 2017

Publications

During Thesis

Paper

- M. Westerhausen, T. Martin, M. Kappel and B. Hofmann, “Stress Testing of Electrically Active FlexMEAs with simultaneous electrical recording in fluidic environment: Introduction of a New Measurement Setup” [173] - submitted
- M. Westerhausen, T. Martin., M. Metzger, V. Bucher and B. Hofmann, “Evaluation of thin atomic layer deposited TiO2 layers as electrode side wall passivation” – in preparation

(International) Presentations

- SurfCoat 2017, Incheon, Rep. of Korea - “Improving the biostability of flexible electrical active implants by passivating the electrode side openings with thin ALD layers”
- NET-Symposium 2017, Tübingen, - “Elektrochemische Sensoren und neuartige Elektrodenöffnungen für flexible Implantate“

Poster Presentations

- M. Westerhausen, B. Hofmann, „New approaches towards electrode openings for long term implantation of flexible neural implants”, Lisa+, Tübingen, 2015
- M. Westerhausen, B. Hofmann, “Messung der Langzeitstabilität von flexiblen Mehrschichtsubstraten”, Frankfurt 2016
- M. Westerhausen, T. Martin, and B. Hofmann, “Measuring the long term stability of (flexible) multi layer substrate.” DGBMT, Basel, 2016 [174]

Older Publications

Paper

- C. Katzer, M. Westerhausen, I. Uschmann, F. Schmidl, U. Hübner, and P. Seidel, “Structural properties of gold modified YBa 2 Cu 3 O 7−δ thin films,” *Supercond. Sci. Technol.*, vol. 26, no. 12, p. 125008, Dec. 2013 [175]
- C. Katzer, M. Westerhausen, P. Naujok, H. Bernhardt, G. Schmidl, W. Fritzsche, A. Undisz, M. Drüe, M. Rettenmayr, and F. Schmidl, “Matrix induced in-situ growth of

crystalline Au nanoparticles for photonic applications," *SPIE Nanosci. + Eng.*, vol. 8807, p. 88070K–88070K–9, Sep. 2013 [176]

- C. Katzer, C. Stahl, P. Michalowski, S. Treiber, M. Westerhausen, F. Schmidl, P. Seidel, G. Schütz, and J. Albrecht, "Increasing the sensor performance using Au modified high temperature superconducting YBa 2 Cu 3 O 7-δ thin films," *J. Phys. Conf. Ser.*, vol. 507, no. 1, p. 12024, May 2014 [177]

Poster Presentations

- M. Westerhausen, C. Katzer, R. Diener, I. Uschmann, F. Schmidl, M. Rettenmayer, and P. Seidel, "Wachstumsbedingungen und Eigenschaften von YBCO-Schichten mit Au-Nano Partikeln." Deutsche Physikalische Gesellschaft e.V., Berlin, 2012 [178]
- S. Koch, P. Michalowski, C. Katzer, M. Westerhausen, F. Schmidl, and P. Seidel, "Grain boundary high-Tc dc-SQUIDs with self-organized nanocrystals." Deutsche Physikalische Gesellschaft e.V., Berlin, 2012 [179]

DANKSAGUNG

Die vorliegende Arbeit zeugt den Abschluss eines sehr prägenden wie auch interessanten Lebensabschnittes, der ohne großartige Unterstützung in dieser Form so nicht möglich gewesen wäre. Daher geht mein herzlichster Dank an meinen Betreuer Herrn Prof. Dr. Boris Hofmann für die hervorragende Betreuung, die guten Ratschläge und die Möglichkeit mich mit diesem Thema auseinandersetzen zu dürfen. Auch danke ich für das entgegengebrachte Vertrauen und die Freiheit verschiedene Prozesse und Lösungsansätze gehen zu dürfen.

Herrn Prof. Dr. Dieter Kern möchte ich für die unverzichtbaren Anstöße in die richtige Richtung sowie die Übernahme der Zweitkorrektur dieser Arbeit danken.

Frau Prof. Dr. Monika Fleischer gebührt mein vollster Dank für den uneingeschränkten Zugang zu allen wissenschaftlichen Geräten Ihrer Arbeitsgruppe, wie auch, dass Sie jederzeit ein offenes Ohr hatte.

Die ALD Schichten wären nicht möglich gewesen, ohne die großartige Unterstützung von Herrn Prof. Dr. Volker Bucher und seiner Arbeitsgruppe in Rottweil, wobei Michael Metzger hier besonders erwähnt wird. Vielen Dank dafür!

Den Instrument Scientists Dr. Markus Turad und Dr. Ronny Löffler gebührt besonderer Dank, die nicht nur die Labore und den Reinraum verwalten und pflegen. Auch die gründliche Einweisung in viele Geräte und einige Anstöße in die richtige Richtung verdanke ich Euch. Vielen Dank dafür!

Martin Ries in der Elektronik Werkstatt hat durch die Konstruktion hervorragender Multiplexer maßgeblich zum Erfolg dieser Arbeit beigetragen, weshalb ihm und seinem Team besonderen Dank gebührt.

Auch die Feinmechanik-Werkstatt unter Leitung von Antje Treftz möchte ich dankend erwähnen, wären doch die hergestellten Aufbauten ohne Sie nicht möglich gewesen.

Meinen Studenten Marcel Kappel, Alisa Büttner und Viktor Schiff möchte ich für die vielen Zuarbeiten zu dieser Dissertation danken.

Meiner Kollegin Tanja Martin gebührt besonderer Dank für die freundschaftliche Zusammenarbeit, aber auch Ihre große Erfahrung in der Photolithographie hat meiner Arbeit sehr zum Erfolg verholfen. Ohne dich wären die vergangenen 4 Jahre ungleich anstrengender gewesen.

Alle anderen Kollegen/innen, wie auch (ehemaligen) Studenten/innen in unserer Arbeitsgruppe möchte ich für die vielen freundschaftlichen Bekanntschaften danken, die den Großteil des sehr angenehmen Arbeitsklimas ausgemacht haben. Namentlich sei hier Yvonne Behres, Saya Heidingsfelder, Silje Völkerath, Melina Becker, Fabienne Röschel und Louisa Bühler erwähnt.

Mein ganz persönlicher und besonderer Dank geht an meine Eltern und meine Schwester, die mich all die Jahre bedingungslos unterstützt haben. Ohne Sie wäre ich heute nicht hier und diese Arbeit ist erst durch Sie möglich geworden. Vielen Dank dafür!

Am allermeisten möchte ich aber meiner Frau Sibel danken, die ich während dieser sehr prägenden Zeit kennen und lieben gelernt habe und die nie das Vertrauen in den Erfolg dieser Arbeit verlor.

LEBENSLAUF

Persönliche Daten:

Vorname / Nachname	Markus Westerhausen
Staatsangehörigkeit	Deutsch
Geburtsdatum	24.03.1987

Berufserfahrung

Zeitraum	August 2013 bis heute
Position	Doktorand / Wiss. Mitarbeiter
Aufgabenbereiche	Dissertation mit dem Thema: “A novel approach towards electrode openings for flexible neural implants”
Arbeitgeber / Adresse	Eberhard-Karls-Universität, Auf der Morgenstelle 10, 72769 Tübingen
Art des Unternehmens	Universität

Zeitraum	Mai 2013 bis Juli 2013
Position	Wiss. Hilfskraft
Aufgabenbereiche	Pulsed Laser Deposition, Reinraumtätigkeiten
Arbeitgeber / Adresse	Friedrich-Schiller-Universität Jena, Helmholtzweg 5, 07743 Jena
Art des Unternehmens	Universität

Schul- und Berufsausbildung

Zeitraum	Mai 2012 bis März 2013
Tätigkeit	Diplomarbeit
Institut/Arbeitsgruppe	Institut für Festkörperphysik Arbeitsgruppe für Tieftemperaturphysik
Thema	„Untersuchungen an epitaktischen Schichten mit selbstorganisiert wachsenden Gold-Nanopartikeln“

Zeitraum	April 2007 bis April 2013
Erworbene Qualifikation	Diplom
Hauptstudium	Physik
Institution	Friedrich-Schiller-Universität Jena Physikalisch-Astronomische Fakultät

Zeitraum	Juli 2006 bis März 2007
	Grundwehrdienst
Ort	Pioniers Kaserne Gera
Zeitraum	2004-2006
Erworbene Qualifikation	Abitur mit den Kernfächern Mathematik und Physik
	Angergymnasium
Ort	Jena
Zeitraum	2001-2004
	Maria-Theresia-Gymnasium
Ort	München
Zeitraum	1997-2001
	Albert-Einstein-Gymnasium
Ort	München
Zeitraum	1996-1997
	Staatliche Grundschule „Rotbuchenschule“
Ort	München
Zeitraum	1993-1996
	Staatliche Grundschule „Am Sonnigen Winkel
Ort	Stuttgart